

Copyright

by

Daniel Cornelius Hatchell

2022

The Dissertation Committee for Daniel Cornelius Hatchell Certifies that this is the approved version of the following Dissertation:

Understanding the stability of Pickering emulsions and foams by manipulating particle-particle and particle-interfacial forces with surface modification

Committee:

Dr. Hugh Daigle, Supervisor

Dr. Wen Song

Dr. Keith Johnston

Dr. Maša Prodanović

Dr. David DiCarlo

**Understanding the stability of Pickering emulsions and foams by
manipulating particle-particle and particle-interfacial forces with
surface modification**

by

Daniel Cornelius Hatchell

Dissertation

Presented to the Faculty of the Graduate School of

The University of Texas at Austin

in Partial Fulfillment

of the Requirements

for the Degree of

Doctor of Philosophy

The University of Texas at Austin

August, 2022

Acknowledgements

I want to thank my advisor, Dr. Hugh Daigle, for his support and guidance throughout my PhD. I cannot understate how important your encouragement and patience were towards building my confidence and experience as a researcher. Thank you for creating such a positive group culture amidst the challenges of graduate research. I'm sure everyone else would say the same.

Thank you to the members on my committee: Dr. Wen Song, Dr. Keith Johnston, Dr. Maša Prodanović, and Dr. David DiCarlo. To Dr. Song, I'm glad I got to properly meet you after being a bit antisocial at Stanford. Thank you for your help, advice, and (thorough!) edits on the emulsion papers, as well as allowing me to use your lab from time to time. To Dr. Johnston, thank you for generously allowing me to use your laboratory equipment in my first few years, and for welcoming me into the group in the last year for the CO₂ foam project. You have given me no shortage of ideas and research perspectives during my time in PhD.

A further thank you to all of the outstanding staff members here at UT. From petroleum engineering, I want to thank Glen Baum, Amy Stewart, Gary Miscoe, Daryl Nygaard, Leilani Swafford, and Angela Scheer; from chemical engineering, Kelly McQueary, Maeve Cooney, Valerie Croft, Randy Rife, and Jason Barborka; and from the Texas Materials Institute, Hugo Celio, Karalee Jarvis, and Raluca Gearba.

Thank you to the various leaders and mentors throughout my life: Omkar Namjoshi, Gary Rochelle, Sally Benson, John Lagasca, and Deniz Dindoruk. I couldn't have gotten where I was today without your guidance.

Thank you to all of my friends and collaborators. Graduate research can be a lonely endeavor in the best of times, but the last two years especially would have been impossible

without your company. From the Daigle group: David Fukuyama, Olin Carty, Ram Disabar, Chris Griffith, Abhishek Bihani, Rita Tian, and Boyang Zhang; from the Song group, Jack Strawson, Artur Davletshin, Sheila Gerardo, Shunxiang Xia, and Qianjun Liu; from the Johnston group, Xiongyu Chen, Mohammed Kawelah, Ceren Atila Dinçer, Taehyung Park, Neha Manohar, Amjad Chowdhury, and Bill Kimball; and also, to Adam Camac, Hanyu Li, Sean Brame, Sercan Gul, Keivan Khaleghi, Cole Speed, Nikhil Garg, Maxim Kolesnikov, and Kent Fischer. There are countless others that I don't have space to name here.

Special thanks to Matthew Hartmann for being a great undergraduate researcher! I couldn't have finished Chapter 5 without your outstanding work.

To Alvan Chen, Matthew Carlson, and Kevin Hankins, for the fond memories and adventures. I'm sure I don't need to say how much you three have helped me this past year. There's a certain word I might use to describe you all; it slips my mind at the moment, but it will come back to me soon.

To Mom and Dad, thank you for the endless support and encouragement you have given me. I'm incredibly fortunate to have grown up in a family that so strongly embraced my goal of graduate school. I love you both. To my siblings, Carly, Peter, and John, for your love and friendship. Thank you for listening (?) to me ramble on about nanoparticles. To all of my Wisconsin relatives, thank you for coming to Texas this past April! It meant a lot to me as someone who has always lived far away.

Finally, I want to thank my wife, Hanbi Liu. I could have never made it through both PhD and several years of long distance without your love and care! You were always there during the most difficult times to cheer me up. I'm grateful for your patience during my lengthy journey through graduate school. I wrote the acknowledgements last, so I'm done now. Let's play *Monster Hunter*!

Abstract

Understanding the stability of Pickering emulsions and foams by manipulating particle-particle and particle-interfacial forces with surface modification

Daniel Cornelius Hatchell, Ph.D.

The University of Texas at Austin, 2022

Supervisor: Dr. Hugh Daigle

This dissertation investigates the stability of nanoparticle-stabilized (i.e., Pickering) emulsions and foams. Nanoparticles – solid objects with one or more dimensions smaller than one micron in size – have enormous surface area inversely proportional to their size, and are consequently active at the fluid-fluid interface. Given the near-irreversible attachment of nanoparticles to an interface, emulsions and foams have the potential for higher stability using nanoparticles than more conventional surfactants. Because of their high stability, Pickering systems have applications in pharmaceuticals, food science, cosmetics, and subsurface flow, including enhanced oil recovery and CO₂ storage.

There are two interactions that greatly influence the stability of a Pickering system: particle-particle forces and particle-interfacial forces. The former interaction can be represented by extended DLVO theory, which considers the interparticle van der Waals attraction, electrostatic repulsion, and steric force; the latter is described by the attachment energy, a function of the particle geometry at the fluid-fluid interface. However, the specifics of these two interactions and their effect on Pickering emulsion and foam stability

are not well understood in the literature, and depend on a number of environmental- and nanoparticle-specific parameters.

Recent developments in nanotechnology have led to the development of nanoparticle surface modification techniques. Performed correctly, surface modification can precisely control different properties at the particle surface, altering the two interactions and allowing us to create “designer” particles that are optimized for a certain set of conditions. There is not much research on studying the role of particle-particle and particle-interfacial forces using surface-modified particles, but the ability to fine-tune particle parameters gives us a novel opportunity to understand these interactions and their influence on stability. The purpose of this dissertation is to use surface modification to manipulate the two interactions, determine the optimal balance of particle-particle and particle-interfacial forces, and generate highly-stable Pickering emulsions and foams.

I use a number of approaches to manipulate the two interactions. Firstly, I surface-modify silica nanoparticles with ring-opened (3-glycidyloxypropyl)trimethoxysilane (GLYMO) ligands and generate Pickering emulsions in both brine and deionized water (DIW). GLYMO is a small but salt-resistant ligand that inhibits particle aggregation in brine. I find that, by reducing electrostatic repulsion at high salinity on a surface-modified particle, I can increase particle-particle attraction, generating stable emulsions without risking particle aggregation.

Secondly, building on the previous study, I investigate a similar phenomenon via the manipulation of the steric force at constant electrostatic repulsion. I graft silica nanoparticles with varying amounts of polyethyleneglycolsilane (PEG-silane), leading to different amounts of steric force that I can confirm with characterization measurements. By controlling the steric force, rather than electrostatic repulsion, I can again increase the particle-particle attraction, generating stable emulsions. Using an energy balance model, I

show that particle-particle interaction can be used to control the stability of emulsions, whereas particle-interfacial interaction can be used to control the emulsion droplet size. The key finding of this study is that stable emulsions can be generated by adjusting PEG ligand surface concentration alone, without needing to modify environmental properties such as salinity.

Having examined the role of particle-particle and particle-interfacial interactions on emulsions, I finally investigate the effect these forces have on CO₂ Pickering foams. I surface modify silica particles with two ligands: (3-trimethoxysilylpropyl)diethylenetriamine (N3-silane), to optimize the particle-particle interaction (prevent aggregation), and dimethoxydimethylsilane (DM-silane), to optimize the particle-interfacial interaction (to improve affinity with CO₂). Taking advantage of our understanding of the two interactions, I generate CO₂ foams with stability at high temperature and high salinity, representing a large advance in foam stability over similar research in the literature.

Table of Contents

Acknowledgements	4
Abstract	6
Table of Contents	9
List of Tables	16
List of Figures	17
Chapter 1: Introduction	33
1.1 MOTIVATION.....	33
1.2 OUTLINE	35
Chapter 2: Literature Review	38
2.1 HISTORY AND DEFINITIONS	38
2.2 APPLICATIONS OF PICKERING EMULSIONS AND FOAMS	41
2.2.1 Enhanced oil recovery.....	41
2.2.2 CO ₂ enhanced oil recovery and storage	44
2.2.3 Other applications	45
2.3 INTERPARTICLE FORCES IN THE BULK FLUID	46
2.3.1 Surface modification of nanoparticles	46
2.3.2 Particle-particle interactions with DLVO theory	49
2.4 FORCES ACTING ON PARTICLES AT THE FLUID-FLUID INTERFACE	52
2.5 STABILITY OF PICKERING EMULSIONS	57
2.6 STABILITY OF PICKERING FOAMS	61
Chapter 3: Examining the role of salinity on the dynamic stability of Pickering emulsions	67
3.1 INTRODUCTION	67

3.2 MATERIALS AND METHODS	69
3.2.1 Materials	69
3.2.2 Functionalization of ring-opened GLYMO nanoparticles	70
3.2.3 Nanoparticle characterization	70
3.2.4 Emulsion generation	71
3.2.5 Centrifugation	72
3.2.6 Microscope imaging and droplet size calculation.....	72
3.3 RESULTS AND DISCUSSION.....	73
3.3.1 Nanoparticle characterization	73
3.3.2 Evaluation of nanoparticle interactions with extended DLVO theory	75
3.3.3 Emulsion imaging	79
3.3.4 Centrifugation	84
3.4 CONCLUSIONS.....	90
Chapter 4: Effect of interparticle forces on the stability and droplet diameter of Pickering emulsions stabilized by PEG-coated silica nanoparticles	92
4.1 INTRODUCTION	92
4.2 MATERIALS AND METHODS	95
4.2.1 Materials	95
4.2.2 Surface modification of silica nanoparticles with PEG-silane to produce PEG-NP.....	96
4.2.3 Measurement of PEG surface density with thermogravimetric analysis (TGA).....	96
4.2.4 Measurement of particle diameter and zeta potential	97
4.2.5 Measurement of particle three-phase contact angle.....	98

4.2.6 Particle imaging with transmission electron microscopy (TEM)	98
4.2.7 Emulsion generation	99
4.2.8 Centrifugation	99
4.2.9 Optical microscopy and droplet size calculation	99
4.3 RESULTS AND DISCUSSION.....	100
4.3.1 Nanoparticle characterization	103
4.3.2 Effect of PEG grafting density on the long-term stability of nanoparticles in brine.....	106
4.3.3 Effect of DLVO interactions on emulsion stability	109
4.3.4 Effect of DLVO forces on droplet diameter	113
4.4 CONCLUSIONS	119
Chapter 5: Stable CO₂/water foam stabilized by dilute surface-modified nanoparticles and cationic surfactant at high temperature and salinity	121
5.1 Introduction.....	121
5.2 Materials and Methods.....	126
5.2.1 Materials	126
5.2.2 Surface modification and preparation of N3-DM NP.....	127
5.2.3 Zeta potential	128
5.2.4 Silane titration to measure protonation of amino groups.....	128
5.2.5 Long-term colloidal stability of N3-DM NP with DLS.....	128
5.2.6 Three-phase contact angle.....	129
5.2.7 Generation of supercritical CO ₂ foam.....	129
5.2.8 Foam apparent viscosity	131
5.2.9 Long-term foam stability	131

5.3 Results and Discussion	132
5.3.1 Preparation and characterization of N3+DM NP.....	133
5.3.2 Three-phase NP contact angle	137
5.3.3 Generation and apparent viscosity of supercritical CO ₂ foam.....	139
5.3.4 Long-term CO ₂ foam stability	141
5.4 Conclusions.....	148
Chapter 6: Conclusions	151
6.1 SUMMARY.....	151
6.1.1 Examining the role of salinity on the dynamic stability of Pickering emulsions	151
6.1.2 Effect of interparticle forces on the stability and droplet diameter of Pickering emulsions stabilized by PEG-coated silica nanoparticles	153
6.1.3 Stable CO ₂ /water foam stabilized by dilute surface-modified nanoparticles and cationic surfactant at high temperature and salinity	156
6.2 FUTURE WORK	157
Appendix A: Nanoparticle surface modification	160
A.1 MATERIALS	160
A.2 SURFACE MODIFICATION	164
A.2.1 GPTMS	166
A.2.2 GLYMO.....	168
A.2.3 PEG	169
A.2.4 N3.....	170
A.2.5 DM	170
A.3 PARTICLE FILTRATION.....	171

A.4 MEASUREMENT OF PARTICLE SURFACE MODIFICATION WITH THERMOGRAVIMETRIC ANALYSIS (TGA)	172
Appendix B: Nanoparticle Characterization	180
B.1 PARTICLE STABILITY	180
B.2 DYNAMIC LIGHT SCATTERING (DLS)	182
B.3 TRANSMISSION ELECTRON MICROSCOPY (TEM)	185
B.4 CONTACT ANGLE MEASUREMENT	187
B.4.1 Spin-coating	187
B.4.2 Contact angle in air	189
B.4.3 Contact angle in decane.....	190
B.4.4 Contact angle in liquid CO ₂	191
B.5 ZETA POTENTIAL	194
B.6 TITRATION.....	195
Appendix C: Emulsion Generation and Measurements	198
C.1 GENERATING EMULSIONS	198
C.2 EMULSION DROPLET IMAGING	200
C.3 EMULSION CENTRIFUGATION.....	204
Appendix D: CO₂ foam apparatus	207
D.1 CO ₂ FOAM APPARATUS.....	207
D.2 LEAK TESTING.....	215
D.3 BEADPACK PREPARATION AND MEASUREMENT OF FOAM APPARENT VISCOSITY	217
D.4 MEASUREMENT OF FOAM COARSENING.....	220

Appendix E: Supporting information for Chapter 4 - Effect of interparticle forces on the stability and droplet diameter of Pickering emulsions stabilized by PEG-coated silica nanoparticles	222
E.1 PROPERTIES OF NYACOL NEXSIL NANOPARTICLES.....	222
E.2 DLVO PAIRWISE INTERACTIONS FOR PARTICLES DISPERSED IN THE AQUEOUS PHASE	223
E.3 EFFECT OF NANOPARTICLE DIAMETER AND AQUEOUS PHASE SALINITY ON EMULSION STABILITY	224
E.4 ENERGY BALANCE EQUATIONS TO MODEL EMULSION DROPLET DIAMETER.....	227
E.5 ENERGY BALANCE MODEL PROCEDURE	228
Appendix F: Supporting information for Chapter 5 - Stable CO₂/water foam stabilized by dilute surface-modified nanoparticles and cationic surfactant at high temperature and salinity	230
F.1 EXTENDED MATERIALS AND METHODS	230
F.1.1 Brine recipe.....	230
F.1.2 Particle grafting reaction and filtration.....	230
F.1.3 Silane titration.....	231
F.1.4 Contact angle and spin-coating.....	232
F.1.5 CO ₂ foam apparatus.....	233
F.1.6 Thermogravimetric analysis	234
F.1.7 NP-CO ₂ dispersity	235
F.2 SUPPORTING RESULTS	235
F.2.1 Thermogravimetric analysis results.....	235
F.2.2 Contact Angle Measurement	236
F.2.3 NP-CO ₂ Dispersity Results.....	238
F.2.4 CO ₂ foam apparent viscosity	238

F.2.3 CO ₂ foam stability images	242
References	245

List of Tables

Table 2.1: Summarized results of selected Pickering emulsion studies, with emulsions from Chapter 3 and 4 added as a comparison.	61
Table 2.2: Summarized results from selected CO ₂ foam studies, with results from Chapter 5 given as a comparison.	65
Table 3.1: GLYMO-nanoparticle parameters measured with DLS and TGA.	73
Table 5.1: Summary of CO ₂ foam stability measurements at 80 °C, 2200 psi, and 22 wt% brine, including comparable results from Chen et al. [180].	144
Table A.1: Properties of NexSil particles.	161
Table A.2: Silane names and structures.	163
Table A.3: Properties of silane chemicals used in our experiments	163
Table A.4: TGA data from PEG-NP series.	179
Table E.1: Properties of unmodified silica nanoparticles.	222
Table E.2: Selected properties of modified silica nanoparticles.	223
Table E.3: Parameters for energy balance model for ~1.75 μmol/m ² PEG-NP emulsions ($L = 2.89 \text{ nm}$).....	228

List of Figures

Fig. 2.1.	Geometry of a solid particle at the fluid-fluid interface. The aqueous contact angle, θ , influences both the attachment energy and the droplet curvature.	39
Fig. 2.2.	Particle gels (yellow) block thief zones in porous media, forcing the flow paths to reorganize and contact new oil (black). Figure modified from Zhang et al. [54].	41
Fig. 2.3.	Traced displacement fronts of a flood in a sand pack, photographed from above. As the mobility ratio, M , increases, the sweep efficiency decreases [61]. P.V. and B.T. refer to the pore volumes of fluid injected and the breakthrough time, respectively.	43
Fig. 2.4.	Field schematic of a CO ₂ -EOR injection process, from Lake et al. [35].	44
Fig. 2.5.	Silanization reaction via hydrolysis and condensation. From Xie et al. [30] and Hubbe et al. [31].	47
Fig. 2.6.	Possible conformations of silane bonded to the silica surface. From Estephan et al. [88] and Worthen et al. [28].	48
Fig. 2.7.	Concentration of hydroxyl groups at the silica surface, from Zhuravlev [86,89]. OH has a concentration of 4-6 sites/nm ² in most cases, regardless of particle surface area.	49
Fig. 2.8.	(a) DLVO interaction potential of bare, ungrafted silica in DIW; (b) DLVO interaction potential of bare, ungrafted silica in 5API brine; (c) DLVO interaction potential of PEG-coated silica in DIW; (d) DLVO interaction potential PEG-coated silica in 5API brine. Only (b) predicts particle aggregation. Inset images illustrate the approach of particles at the given conditions.	52

Fig. 3.1.	(a) DLVO interactions of GLYMO-NP in DI as a function of core surface to core surface particle separation distance, assuming significant electrostatic repulsion; (b) DLVO interactions of GLYMO-NP in 5API brine as a function of separation distance, where electrostatic repulsion is assumed to be zero.	79
Fig. 3.2.	(a) Representative histogram of droplet size distributions of 0.25 wt% GLYMO-NP-5API emulsions. The frequency of droplets at each diameter bin has been normalized to sum to a value of one. Images (b) and (c) show the same 0.25 wt% GLYMO-NP-5API emulsion sample on a microscope slide imaged at 40x and 4x zoom.	80
Fig. 3.3.	(a) D_{32} diameters of GLYMO-NP-DI and GLYMO-NP-5API emulsions as a function of nanoparticle concentration in the original aqueous phase. The geometric minimum line is an estimate of the smallest possible droplet size given the quantity of nanoparticles available to stabilize an emulsion; (b) Estimated fraction of nanoparticles at the surface of a droplet as a function of nanoparticle mass concentration in the aqueous phase.	81
Fig. 3.4.	Volume fraction of oil released during centrifugation for unfiltered GLYMO-NP-DI and GLYMO-NP-5API emulsions as a function of nanoparticle mass concentration. The filtrate concentration is converted into an equivalent nanoparticle concentration for comparative purposes.....	85

Fig. 3.5.	Volume fraction of oil released during centrifugation for filtered GLYMO-NP emulsions in DI and 5API brine as a function of (a) nanoparticle mass concentration on a log scale or (b) emulsion D_{32} diameter in microns. The shaded region represents two standard deviations of uncertainty in the volume fraction of oil released around a linear fit to the data.	86
Fig. 3.6.	Predicted behavior of nanoparticles dispersed in the continuous phase in a Pickering emulsion. In deionized water, the unattached particles repel and remain dissociated. In brine, the particles attract, forming inter-droplet particle networks.....	89
Fig. 4.1.	Illustration of the effect of particle type on emulsion stability. Type I, II, and III particles refer to fast (< 1 minute), slow (days to months), and negligible (> 1 year) aggregation rates, respectively. Type I particles interact too strongly and aggregate, leading to weak emulsions. Type II particles mildly flocculate and produce very strong emulsions. Type III particles are stable in brine and produce moderately strong emulsions; however, because they strongly repel each other with steric forces, they do not exhibit flocculation.	102
Fig. 4.2.	PEG grafting density at the silica surface measured by TGA, plotted as a function of PEG-silane added to the reaction. The black line fits the data to a Langmuir adsorption model with a maximum coverage of 2.37 $\mu\text{mol}/\text{m}^2$	103

- Fig. 4.3.** (a) DLS-measured particle ζ potential in DIW as a function of PEG grafting density for 6 nm PEG-NP; (b) Particle-decane-water contact angle with respect to the aqueous phase (both DIW and brine) as a function of PEG grafting density for 6 nm PEG-NP. The two inset images show aqueous droplets on a spin-coated surface submerged in decane. Along with other measurements, they were analyzed with the sessile drop method to calculate the contact angle.105
- Fig. 4.4.** TEM images of 6 nm, 12 nm, and 20 nm particles grafted with approximately $1.75 \mu\text{mol}/\text{m}^2$ PEG surface density. Each image has an identical scale bar of 40 nm.106
- Fig. 4.5.** (a) DLS-measured Z-average particle diameter in 5API brine over time, plotted for 6 nm, $0.42\text{-}1.90 \mu\text{mol}/\text{m}^2$ PEG-NP. (b) Experimental stability ratio (W) and theoretical pairwise DLVO interaction potential energy barrier of 6 nm, $0.42\text{-}1.90 \mu\text{mol}/\text{m}^2$ PEG-NP, plotted as a function of PEG grafting density. Arrows indicate that the measurement is limited by the timescale of aggregation, and the true value likely lies in the direction specified. Type I, II, and III particles refer to fast (< 1 minute), slow (days to months), and negligible (> 1 year) aggregation rates, respectively.107

Fig. 4.6. (a) Volume fraction of decane released from decane-in-brine emulsions after centrifugation as a function of nanoparticle number concentration in the aqueous phase, plotted for 6 nm, 0.42-1.90 $\mu\text{mol}/\text{m}^2$ PEG-NP. (b) Nanoparticle number concentration in the aqueous phase required to produce an emulsion that releases 50% of its decane by volume after centrifugation, plotted as a function of PEG grafting density. This plot is constructed from the horizontal line drawn across (a). Type I, II, and III particles refer to fast (< 1 minute), slow (days to months), and negligible (> 1 year, extrapolated from the data) aggregation rates, respectively.110

Fig. 4.7. Emulsion D_{32} diameter plotted as a function of nanoparticle concentration (wt%) and presented in the following contexts: (a) all brine emulsions plotted for different particle diameters; (b) all DIW emulsions plotted for different particle diameters; (c) all 6 nm PEG-NP plotted for brine and DIW; (d) all 12 nm PEG-NP plotted for brine and DIW; (e) all 20 nm PEG-NP plotted for brine and DIW. The solid or dashed lines demonstrate the energy balance model fitted to the droplet diameters. Particles with different PEG grafting densities are combined in the above plots where applicable. Images (f), (g), and (h) show microscope images from the emulsions corresponding to the data points indicated in plots (c), (d), and (e). The images are chosen to represent different particle diameters, salinity, and droplet sizes.115

- Fig. 5.1.** Diagram of the apparatus used to generate and measure supercritical CO₂ foams, modified from Da et al. [42]. The NP and surfactant rich H₂O stream combines with the CO₂ stream in a beadpack, shearing to generate foam. The entire flow path is kept at 80 °C and 2200 psi with four heating systems at different locations and with downstream back pressure regulators operating in series.130
- Fig. 5.2.** (a) Zeta potential of 8N3+0DM NP and 8N3+2DM NP plotted as a function of pH. NP are dispersed in a 1 mM KCl solution at a NP concentration of 0.05 w/v%. Error bars are twice the standard error of the zeta potential measurement. (b) pH of 0.01 M N3 silane and 0.01 M N3 + 0.01 M DM silane mixtures plotted as a function of pH. The silanes are mixed into 22 wt% brine at their respective molar concentrations. In both plots, the vertical dotted line indicates the operating pH of CO₂ foam.134
- Fig. 5.3.** (a) DLS-measured volume-average NP diameters of 1 w/v% 8N3+0-2DM NP, dispersed in 22 wt% brine and 1 v/v% RCADA. (b) DLS-measured volume-average NP diameters of 0.2 w/v% 8N3+0-2DM NP, dispersed in 22 wt% brine and 1 v/v% RCADA. (c) DLS-measured volume-average NP diameters of 0.2-1 w/v% 8N3+1.5DM NP, dispersed in 22 wt% brine and 0-1 v/v% RCADA. All NP are kept at pH 4 and 80 °C for up to four weeks. Only the 0.2 w/v% 8N3+1.5DM, 0 v/v% RCADA NP exhibited significant growth over the measured time. .136

- Fig. 5.4.** Three-phase θ_w of 8N3 NP at different interfaces, plotted as a function of DM silane added to the NP grafting reaction. Each data point is an average of measurements from three images. The images to the right show examples of droplets that comprise these averages for the minimum ($0 \mu\text{mol}/\text{m}^2$) and maximum ($2 \mu\text{mol}/\text{m}^2$) cases. The annotated colored lines are approximations of θ_w , but the actual values were determined by software calculations.....138
- Fig. 5.5.** (a) Apparent viscosity of 8N3+1.5DM NP CO₂ foams plotted as a function of CO₂ quality for 0.1-1 v/v% RCADA and 0-1 w/v% NP. (b) Apparent viscosity of 8N3+0-2DM NP CO₂ foams, plotted as a function of CO₂ foam quality with 1 v/v% RCADA and 0.2 w/v% NP. All foams were generated with 22 wt% brine at 80 °C and 2200 psi.140
- Fig. 5.6.** Microscope images of selected CO₂ foams isolated in the view cell at 80 °C and 2200 psi over time. “Discontinued” indicates that the droplets grew too large to properly image at the same scale; at this point, the microscope was shut off. The scale bars are consistent for all images.142
- Fig. 5.7.** (a) D_{SM}^3 of CO₂ foams with 0.2-1 w/v% 8N3+1.5DM NP and 0.1 v/v% RCADA, plotted against time. (b) D_{SM}^3 of CO₂ foams with 0.2-1 w/v% 8N3+0-2DM NP and with 1.0 v/v% RCADA, plotted against time. All foams were generated at 80% CO₂ quality with 22 wt% brine and maintained at 80 °C and 2200 psi. The linear slopes of these data series are the coarsening rates ($\mu\text{m}^3/\text{min}$). The dotted regions indicate two standard deviations of uncertainty in the coarsening rate.143

Fig. 5.8.	(a) Cube of the D_{SM} of CO ₂ foams with 0.2 w/v% 8N3+0-2DM NP and 1 v/v% RCADA, plotted against time. (b) Slope of linear fits to the data (coarsening rates) from both Fig. 5.6 and Fig. 5.8 (a), plotted as a function of DM silane added to the 8N3 NP. Error bars indicate two standard deviations of the coarsening rate. The horizontal solid lines indicate the coarsening rates of 0.1 v/v% RCADA and 1 v/v% RCADA foam without NP at equivalent operating conditions. The horizontal dashed lines are two standard deviations of uncertainty of the coarsening rate in RCADA-only foams.	146
Fig. 6.1.	Illustration of particle-particle networks between oil droplets in deionized water (left) and brine (right). This figure is identical to Fig. 3.6, and provided here as reference.	153
Fig. 6.2.	Illustration of particle-particle interactions for Type I, Type II, and Type III systems at an oil-water interface. This figure is identical to Fig. 4.1, and provided here as reference.	155
Fig. A.1.	Left to right: NexSil 6, NexSil 12, and NexSil 20. Although difficult to see in opaque containers, the NexSil 6 and 12 particles are mostly clear. NexSil 125-40, not pictured, is even cloudier in appearance.	161
Fig. A.2.	TEM image of NexSil 125-40 particles. These particles have been surface modified by PEG before imaging. Particles are spherical and monodisperse.	162
Fig. A.3.	Various N3+DM and PEG particles reacted with an old batch of silica nanoparticles. Every batch failed, despite no changes in the procedures. ...	164

Fig. A.4.	Left: nanoparticle condensation reaction of GPTMS and NexSil 6. While the temperature is not precisely controlled, we get excellent repeatability with this method. Right: evaporation of methanol after silanol condensation (also GPTMS and NexSil 6, but from a different batch).	167
Fig. A.5.	Left: GPTMS and NexSil 6 reacted without methanol. Right: GPTMS and NexSil 6 reacted with methanol.	168
Fig. A.6.	Acid-catalyzed ring opening of GPTMS (left) to form GLYMO (right), from Worthen et al [28]. The epoxy group is converted into a glycerol group by the addition of one water molecule.....	169
Fig. A.7.	Left: TGA instrument. Right: crucibles ready for TGA analysis. The crucibles in positions 16 and 17 contain particles already raised to 800°C, whereas the crucibles in positions 18-20 have yet to be analyzed.	172
Fig. A.8.	Mass fraction of NexSil 6 silica particles during TGA.....	173
Fig. A.9.	TGA mass fraction of various silanes up to 800°C.	174
Fig. A.10.	Diagram of PEG silane (525 g/mol, average), which has an organic fraction of 94% and an inorganic fraction of 6% (31 g/mol). The inorganic fraction is consistent with Si or SiH _x (28-32 g/mol, circled), which we suspect is left behind during TGA.....	175
Fig. A.11.	Diagram of hydrolyzed PEG silane (483 g/mol), which has an organic fraction of 83% (401 g/mol) and an inorganic fraction of 17%. The organic fraction is similar to the circled portion (404 g/mol), which we suspect is removed during TGA.	175

Fig. A.12.	Diagram of hydrolyzed GPTMS (194 g/mol), which has an organic fraction of 63% and an inorganic fraction of 37%. The organic fraction is close to the circled portion (115 g/mol), which we suspect is removed during TGA.....	175
Fig. A.13.	Diagram of hydrolyzed GLYMO (212 g/mol), which has an organic fraction of 60% (127 g/mol) and an inorganic fraction of 40%. The organic fraction is close to the circled portion (133 g/mol), which we suspect is removed during TGA.	176
Fig. A.14.	Mass change of three GLYMO-NP aquilots during TGA runs; normalized mass is defined as a mass fraction equal to one during the second ramp section (beginning at 110 °C), when water is expected to be completely removed.....	177
Fig. A.15.	TGA mass curves of PEG-NP at 16 $\mu\text{mol}/\text{m}^2$ and 1 $\mu\text{mol}/\text{m}^2$ nominal coverage.....	178
Fig. B.1.	(a) DLVO interaction potential of bare, ungrafted silica in DIW; (b) DLVO interaction potential of bare, ungrafted silica in 5API brine; (c) DLVO interaction potential of PEG-coated silica in DIW; (d) DLVO interaction potential PEG-coated silica in 5API brine. Only (b) predicts particle aggregation.....	181
Fig. B.2.	Qualitative stability test of silica particles. From left to right, the cuvettes contain (1) bare, ungrafted silica in DIW; (2) bare, ungrafted silica in 5API brine; (3) PEG-coated silica in DIW; and (4) PEG-coated silica in 5API brine. The second cuvette, (2), is analogous to case (b) from Fig. B.1.....	182

Fig. B.3.	Particle number concentration divided by the initial particle number concentration (N_p/N_o) of PEG-coated NexSil 6 particles in 5API brine, plotted as a function of time (0.66-0.91 $\mu\text{mol}/\text{m}^2$ PEG coating).	184
Fig. B.4.	Left: image of the hot water bath used to store particle samples at high temperature for long-term stability measurements. Right: metal block used to hold and visualize particles during high-temperature storage.	185
Fig. B.5.	TEM images of 1.92 $\mu\text{mol}/\text{m}^2$ PEG-coated NexSil 125-40 particles deposited on a carbon-gold lacey grid. After drying, particles grouped together and could be found along the edges of the carbon “web”.	186
Fig. B.6.	TEM images of 1.84 $\mu\text{mol}/\text{m}^2$ PEG-coated NexSil 12 particles deposited on a carbon-gold lacey grid. Particles were widely distributed around the gaps.	187
Fig. B.7.	Laurell WS-650-23 spin-coater. This specific instrument is located inside a class 100 clean room.	188
Fig. B.8.	Plastic flask used to measure particle-aqueous-decane contact angle. The uppermost face was removed, and a spin-coated microscope slide was placed inside. The bottle was then filled with decane. The clear, flat edges allowed us to take clean, undistorted images of the droplet contact angle.	190
Fig. B.9.	High-pressure contact angle measurement apparatus, including a metal high-pressure vessel and camera. The vessel and camera are mounted onto a tilt cradle.	191

Fig. B.10.	Left: specially-cut glass piece screwed in place on a mount. The mount plugged into the bottom of the high-pressure vessel, sealed with an o-ring. Right: view of glass piece in the direction perpendicular to the camera. The inlet line can be seen hovering closely above the glass surface.....	192
Fig. B.11.	Glass piece attached to microscope slide in preparation for spin-coating. .	193
Fig. B.12.	Three-neck flask used for silane titration. The center neck connects to a burette administering dilute 80 mM HCl; the rightmost neck connects to the pH meter. The leftmost neck, unused in the image, was connected to a condenser for measurements at 80°C.....	196
Fig. C.1.	Branson 450 Digital Sonifier for sonicating oil and water mixtures to form emulsions.....	199
Fig. C.2.	Two batches of stable emulsion following the emulsification process.....	200
Fig. C.3.	Left: initial microscope image of an emulsion. Center: binarized image, segmenting the droplet boundaries as black. Right: final result after running the particle analyzer in ImageJ.....	202
Fig. C.4.	(a) Droplet size distributions of four independently generated, imaged, and analyzed 0.25 wt% GLYMO-NP-5API emulsions to demonstrate repeatability of the imaging process. The frequency of droplets at each diameter bin has been normalized to sum to a value of one for each batch. Images (b), (c), and (d) show the same 0.25 wt% GLYMO-NP-5API emulsion sample from one of the batches on a microscope slide imaged at 40x, 10x, and 4x magnification.....	204

Fig. C.5.	Three emulsions after centrifugation for 15 minutes at 5000 g of acceleration. The leftmost and middle emulsions were unstable and nearly fully coalesced after centrifugation; the rightmost emulsion was more stable, and separated into three distinct phases after centrifugation.	205
Fig. D.1.	Flow diagram of the CO ₂ foam apparatus. This figure is identical to Fig. 5.1 and shown here as a reference.	208
Fig. D.2.	Teledyne ISCO and Series III HPLC pumps were used to flow CO ₂ and the aqueous phase into the foam apparatus. Also imaged is the outlet waste container, which is downstream of the BPRs.	209
Fig. D.3.	Interior of the Thermo Scientific Lindberg/Blue M convection oven. CO ₂ and aqueous lines circulate to bring the fluids up to 80°C, before combining at the indicated connector and shearing in the beadpack. Red arrows indicate the critical flow path.	210
Fig. D.4.	Microscope assembly. The foam flowed from the convection oven (out of image to the right) to the BPRs (out of image to the left), passing through the microscope. Layers of insulation maintain the 80°C environment generated by cartridge heaters and hot water circulation. Red arrows indicate the critical flow path.	211
Fig. D.5.	Interior of the microscope assembly, with some insulation and cartridge heaters removed. Foam passed through a view cell under the microscope. For long-term foam observation, the view cell could be isolated from the rest of the system by operating the valves, rerouting foam through a bypass line. Red arrows indicate the critical flow path.	212

Fig. D.6.	Hot water bath and pump. A water bath was kept at 80°C and continually pumped through annular tubing that jacketed the critical flow path. The bath and hot-water circulation lines were extensively insulated.	213
Fig. D.7.	BPRs and convection bath. We connected two BPRs in series to maintain the system pressure and heated the tubing to 80°C in a water bath. The in-line filter was positioned upstream of the BPRs. The red arrows indicate the critical flow path, leading to the outlet.	214
Fig. D.8.	Absolute pressure sensor and BPR water bath temperature controller.	215
Fig. D.9.	Leak testing of the view cell. While fully connected to the flow lines, we lowered the view cell into a large container (left) and filled the container with water. We then filled the view cell and neighboring lines with pressurized CO ₂ and looked for CO ₂ bubbles (right) to identify leakage points.	217
Fig. D.10.	Left: pressure drop versus time for room temperature water flowed at different flow rates, used to calculate a beadpack permeability of 9.1 darcy (average: 8.6 darcy). Right: pressure drop of 0.1 v/v% surfactant only foam at 80°C and 2200 psi at different foam qualities.	219
Fig. D.11.	Example of manual bubble selection for calculating foam D _{SM} . The pictured foam is 0.2 w/v% 8N3+1.5DM NP with 1 v/v% surfactant after four hours at 80% foam quality, 80°C, and 2200 psi. The calculated D _{SM} for this image was 111 μm (scale bar is 100 μm).	221
Fig. E.1.	DLVO total interaction energy (Φ_T) vs separation distance plotted for 6 nm silica particles in deionized water (left) and 5API brine (right) with varying amounts of PEG coverage at the surface.	224

Fig. E.2.	(a) Volume fraction of decane released from emulsion after centrifugation as a function of nanoparticle number concentration in the aqueous phase, plotted for 6, 12, and 20 nm $\sim 1.75 \mu\text{mol}/\text{m}^2$ PEG-NP in both 5API brine and DI. (b) Nanoparticle number concentration in the aqueous phase required to produce an emulsion that releases 50% of its decane by volume after centrifugation, plotted as a function particle diameter for both 5API brine and DI emulsions. This plot is constructed from the horizontal line drawn across (a).	225
Fig. F.1.	Mass fraction measured by TGA plotted as a function of temperature for 8N3+0-2DM NP. The mass fraction is normalized to equal one when the temperature increases beyond 110 °C (all residual water removed).....	235
Fig. F.2.	Three-phase θ_w of 8N3 NP in pH 4 brine (with or without 1 v/v% RCADA), plotted with respect to air as a function of DM silane added to the NP grafting reaction. Each data point is an average of measurements from three images.	237
Fig. F.3.	Box plot of CO ₂ foam apparent viscosities for all particle-surfactant combinations at 70% CO ₂ foam quality, 80 °C, and 2200 psi. The box indicates the 25 th , 50 th , and 75 th percentiles with red markers representing outliers (1.5 times the 75 th -25 th distance removed from the edge of the box).	239
Fig. F.4.	Box plot of CO ₂ foam apparent viscosities for all particle-surfactant combinations at 80% CO ₂ foam quality, 80 °C, and 2200 psi. The box indicates the 25 th , 50 th , and 75 th percentiles with red markers representing outliers (1.5 times the 75 th -25 th distance removed from the edge of the box).	240

Fig. F.5.	Box plot of CO ₂ foam apparent viscosities for all particle-surfactant combinations at 90% CO ₂ foam quality, 80 °C, and 2200 psi. The box indicates the 25 th , 50 th , and 75 th percentiles with red markers representing outliers (1.5 times the 75 th -25 th distance removed from the edge of the box).	241
Fig. F.6.	Microscope images of CO ₂ foam bubbles (8N3+1.5DM NP, various particle and RCADA concentrations, 22 wt% brine) growing in the foam apparatus view cell at 80 °C and 2200 psi over time. “Coalesced” indicates that the droplets grew too large to properly image at the same scale; at this point, the experiment was discontinued. The scale bars are consistent for all images.....	243
Fig. F.7.	Microscope images of CO ₂ foam bubbles (0.2 w/v% 8N3+0-2DM NP, 1 v/v% RCADA, 22 wt% brine) growing in the foam apparatus view cell at 80 °C and 2200 psi over time. “Coalesced” indicates that the droplets grew too large to properly image at the same scale; at this point, the experiment was discontinued. The scale bars are consistent for all images.	244

Chapter 1: Introduction

1.1 MOTIVATION

Ever since Ramsden and Pickering [1,2] published the original discoveries of solid-stabilized (i.e, Pickering) emulsions, scientists have investigated nanoparticles as candidates for stabilizing Pickering emulsions and foams. Commonly defined as particles that measure 1-100 nm in two or more dimensions [3], nanoparticles have enormous surface area relative to their mass and volume (as high as 500 m²/g). This property makes nanoparticles especially active at a fluid-fluid interface; under the appropriate conditions, they become irreversibly attached, and can stabilize an interface between two otherwise incompatible fluids [4]. Nanoparticles can therefore generate emulsions and foams that are potentially more stable than conventional surfactants, even in challenging conditions (high temperature, high salinity, and high pressure).

Because of their high stability, Pickering emulsions and foams have applications in medicine [5-7], food science [8-10], cosmetics [11,12], and other disciplines [13,14]. In the petroleum space, nanoparticles and Pickering systems have been used or proposed for enhanced oil recovery [15,16] and CO₂ storage [17,18] – the two applications I emphasize in the research presented in this dissertation – as well as aquifer decontamination [19], cleaning of oil spills [20], and more [21-23]. The number of publications on Pickering systems has rapidly increased in the last twenty years with recent developments and reduced cost of nanotechnology [24].

Building from this recent work, the behavior of nanoparticles at a fluid-fluid interface can be expressed as two interactions: interparticle forces, and the forces between a particle and the interface. The former can be described by extended DLVO theory [25-29]:

$$\Phi_T = \Phi_{vdW} + \Phi_E + \Phi_S. \quad (1.1)$$

Here, the total interaction potential between two particles, Φ_T , is expressed as the sum of Φ_{vdW} , the van der Waals potential, Φ_E , the electrostatic potential, and Φ_S , the steric potential.

Particle-interface interaction be described in terms of attachment energy, ΔE [4]:

$$\Delta E = \pi r^2 \gamma (1 - |\cos(\theta)|)^2, \quad (1.2)$$

where ΔE is a function of the particle radius, r , the fluid-fluid interfacial tension, γ , and the contact angle at the particle surface, θ (measured in either the wetting or non-wetting phase). The strength of particle attachment to the interface, therefore, is the product of γ and the area intersected by the particle.

The two interactions depend on both fluid properties and particle-specific parameters, and their effect on emulsion and foam stability is not fully described in the literature. The design of successful Pickering systems for specific applications – for example, stable flow through a high-salinity, high-temperature reservoir – requires an improved understanding of the underlying forces to be commercially successful.

With the recent advances in nanoparticle research, surface modification has risen as an important technique for manipulating particles to better measure these interactions. Through the silanization reaction [30,31], silica particles can be grafted with silane molecules that covalently bond to the particle surface. Grafting reactions can be performed with a variety of compounds to impart particle stability, wettability alteration, and bulk viscosity, among other properties. Techniques such as thermogravimetric analysis and dynamic light scattering allow us to measure particle properties at high resolution, allowing

us to make sensitive changes to particle parameters and measure the resulting impact on emulsion and foam stability. The work presented in this dissertation uses surface modification as the primary goal of probing the two interactions.

There are two main goals of this work: to systematically investigate the effect of the two interactions on the stability of Pickering emulsions and foams, and to use that information to develop stable Pickering systems, ideally at low nanoparticle concentrations. Using surface modification to precisely tune the parameters of our nanoparticles, I evaluate the role of Φ_{vdW} , Φ_E , and Φ_S on the stability and droplet diameters of emulsions, and generate nanoparticles with excellent particle-CO₂ interactions. In doing so, I generate Pickering systems with unprecedented stability and demonstrate new strategies to improve nanoparticle performance.

1.2 OUTLINE

There are six chapters in this dissertation. Following this introduction, Chapter 2 reviews the recent literature on nanoparticles, Pickering emulsions, and Pickering foams. I emphasize papers relevant to particle-particle and particle-interface forces, experimental techniques (including surface modification) and to our target applications (enhanced oil recovery and CO₂ storage).

In Chapter 3, I probe the influence of Φ_E on emulsion droplet size and stability. I surface-modify silica nanoparticles with [3-(2,3-dihydroxypropoxy)propyl]-trimethoxysilane (GLYMO), a low-molecular weight and salt-resistant ligand, and use them to generate emulsions in deionized water (DIW) and brine. The different salinities yield significantly different Φ_E . Measuring the emulsion stability with centrifugation and droplet diameter with microscopy, I demonstrate that a reduction of Φ_E leads to increased emulsion stability through particle-particle interactions. Controlling for differences in

droplet size (DIW emulsions were 50-80% larger), I measure a factor of 78 ± 23 increase in the rate of coalescence for DIW emulsions than brine emulsions.

A key limitation of improving stability by adjusting Φ_E is that Φ_E depends primarily on environmental conditions (such as aqueous phase salinity). As such, a stable system is not necessarily easily applied to reservoirs with different characteristics. A more versatile approach would seek to improve emulsion stability by manipulating either Φ_S or Φ_{vdW} – properties inherent to the particles themselves. Chapter 4 discusses a similar emulsion system to Chapter 3, using silica particles coated with polyethyleneglycol silane (PEG silane). By carefully adjusting and quantifying different surface concentrations of PEG ligands at the particle surface, I precisely manipulate Φ_S ; similarly, I alter the nanoparticle diameter with the goal of changing Φ_{vdW} . Of the two, I show a dramatic increase in emulsion stability at low Φ_S . Specifically, emulsions using particles with $0.5\text{-}1 \mu\text{mol}/\text{m}^2$ PEG coverage – “Type II” particles which aggregate on the order of minutes to months in brine – have higher stability than those with “Type III” ($>1 \mu\text{mol}/\text{m}^2$ PEG, negligible aggregation) or “Type I” ($<0.5 \mu\text{mol}/\text{m}^2$ PEG, instantaneous aggregation) particles. This result emphasizes the importance of balancing attractive particle-particle interactions with particle aggregation for improving emulsion stability. With a model built from extensive droplet diameter measurements, I further show that the size of the emulsion droplets are unaffected by DLVO forces, and depend on particle-interface interactions.

In Chapter 5, to continue the investigation of particle-interface interactions, I graft (3-trimethoxysilylpropyl)diethylenetriamine (N3 silane) and dimethoxydimethylsilane (DM silane) onto silica nanoparticles, and generate high-pressure, high-temperature CO_2 foams. I first confirm the compatibility of N3 and DM as co-ligands with measurements of the particle charge, protonation, and resistance to aggregation. Using DM ligands as a wettability modifier, I manipulate and measure θ and develop stable CO_2 foams. I report

foams at 80°C with a coarsening rate of 2400 $\mu\text{m}^3/\text{min}$ at 0.2 w/v% particle concentration – the best known stability for such a dilute system.

Chapter 6 gives my main conclusions and key innovations. I further discuss ideas for future work. In the appendices, I describe my experimental procedures in detail, as well as some supplemental information that pertains to the previous chapters.

Chapter 2: Literature Review

2.1 HISTORY AND DEFINITIONS

An emulsion is defined as a dispersion of liquid droplets or crystals in another liquid [32]. A foam can similarly be defined as a gas-in-liquid mixture with sufficiently high gas fraction (at low gas fractions they are sometimes called gas emulsions) [33]. Supercritical-fluid-in-liquid mixtures, as in the case of CO₂ at typical reservoir conditions, are often described as foams. Because the two fluids are immiscible, the generation of an emulsion or foam creates significant surface area. This system is normally thermodynamically unstable, and collapses without a stabilizing material [4,34,35].

Solid particles were identified as being able to stabilize emulsions in the initial publications of Ramsden and Pickering [1,2], although authors have found evidence suggesting their use as far back as 1860 [36,37]. In a solid-stabilized (i.e., Pickering) emulsion or foam, solid particles occupy positions on the droplet or bubble interface, separating the two immiscible fluids with a positive attachment energy, as described by Eq. (1.2) [4]. Fig. 2.1 displays a diagram of a particle at the interface.

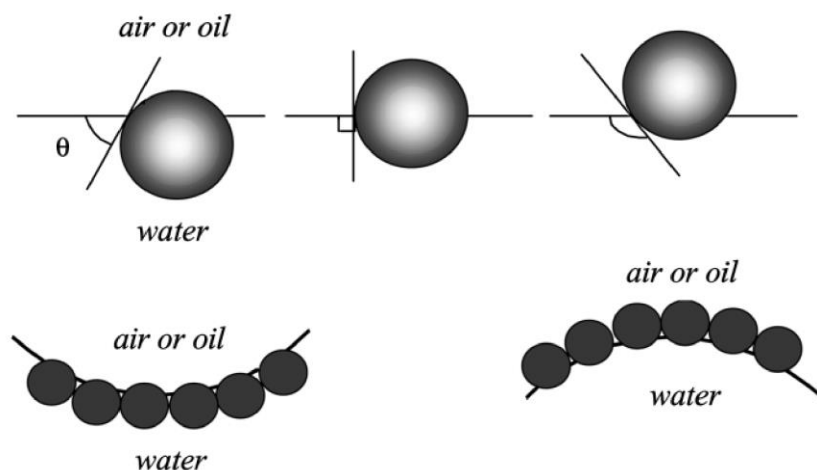


Fig. 2.1. Geometry of a solid particle at the fluid-fluid interface. The aqueous contact angle, θ , influences both the attachment energy and the droplet curvature.

The position of the particle at the fluid-fluid interface (shown in Fig. 2.1) is favorable because the particle (which was already dispersed in one of the phases) reduces the surface between incompatible phases without increasing its own, forming a local energy minimum. The attachment energy, given by Eq. (1.2), is the product of this cross-sectional area with the fluid-fluid surface tension. The particle wettability, measured by its contact angle θ , defines the positioning of the particle at the interface and therefore affects the cross-sectional area and attachment energy. It also influences the droplet curvature, determining which phase will be dispersed and which will be continuous. In practice, however, phase inversion (for example, switching from an oil-in-water to a water-in-oil emulsion) does not occur exactly at 90° [38]. The θ of a solid particle can be measured with direct imaging (39), the Washburn method [40,41], by compressing particles into a flat surface and measuring the contact angle of that surface [42], or by spin-coating particles onto a surface and measuring the contact angle [43,44]. I discuss spin-coating procedures used for this dissertation in detail in Appendix B.

Despite their long history, interest in Pickering systems has only gained widespread focus in the past two decades with advances in nanoparticle technology [24]. Nanoparticles are solid particles with at least two length dimensions measuring between 1 and 100 nm [3] (below this scale are atom clusters; above this scale are microparticles). Some authors consider nanosheets – objects with only one dimension between 1 to 100 nm in length – to be nanoparticles as well. Nanoparticles were first studied by Michael Faraday [45], although they were (perhaps inadvertently) used in glassware manufacturing for their optical properties as far back as ancient times – most famously in the Roman Lycurgus cup [46]. Given their large surface area to volume ratio and negligible mass, nanoparticles occupy an ideal length scale to generate Pickering emulsions and foams. For the purpose of generating Pickering emulsions and foams, the radius of a nanoparticle forms a sufficiently large cross-sectional area at an interface and subsequently large attachment energy that it is considered “irreversibly” attached.

Chemical surfactants, rather than particles, are used to stabilize emulsions and foams in most current applications. Surfactants are amphiphilic chemicals that are interfacially active (literally, surface-active-agents). They bridge the fluid-fluid interface and reduce interfacial tension, lowering the driving force for destabilization and reducing the capillary pressure [47]. While more widely used, surfactants struggle to stabilize foam at high temperature because of thermal fluctuations [4,48], a property that particles with a large attachment energy can excel at. Particles additionally can stabilize foam systems through changes in the interfacial dilational elastic modulus, which I will discuss in a later section [42].

2.2 APPLICATIONS OF PICKERING EMULSIONS AND FOAMS

Pickering emulsion and foams have a variety of applications in various disciplines. While in this dissertation I focus on their use for enhanced oil recovery (EOR) and CO₂ storage, they have been used or studied for several other applications inside and outside the oil and gas industry [49].

2.2.1 Enhanced oil recovery

EOR is the injection of a substance (other than water) into a reservoir to produce hydrocarbons more effectively than a traditional waterflood. The United States, especially, has an abundance of mature fields on which EOR could be applied [50]. Pickering emulsions and foams are promising candidates for EOR because of their potential for conformance and mobility control.

Conformance control refers to the ability of emulsion droplets to block flowing paths through the reservoir and divert flow to less-traveled pathways, improving sweep efficiency [51-53]. Fig. 2.2 illustrates the blockage and rerouting mechanism in a conformance-controlled system [54].

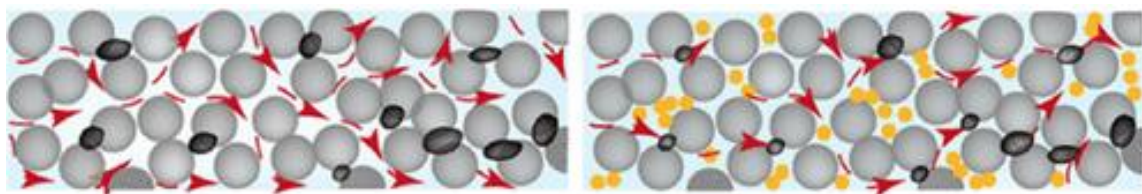


Fig. 2.2. Particle gels (yellow) block thief zones in porous media, forcing the flow paths to reorganize and contact new oil (black). Figure modified from Zhang et al. [54].

According to filtration theory developed by Soo and Radke [55], droplets are trapped by straining (physical blockage of one or multiple droplets at a pore throat) or

interception (droplet adsorption to rock surface from droplet-rock attraction). These mechanisms have been observed in micromodels [56]. Droplet blockage occurs when emulsion droplets are sufficiently large proportional to the pore throat size, which is often true for macroemulsions (emulsions with a droplet diameter of one micron or larger) [57]. Because the high attachment energy of nanoparticles to the fluid-fluid interface can stabilize macro-scale droplets [58,59], as Griffith and Daigle demonstrated [60], this property could be achieved using water-in-water Pickering emulsions, eliminating the need of injecting oil into a reservoir to produce oil. Pickering emulsions have been used in commercial conformance control projects [15,16].

Mobility control is the injection of a viscous fluid into a reservoir to combat viscous fingering and gravity segregation [35]. When a low-viscosity fluid is flooded into a high-viscosity reservoir – such as the use of conventional waterflooding to produce heavy oil – the volumetric sweep efficiency is reduced. Perturbations in the flooding front lead to the development of preferential flow channels, which bypasses sections of the reservoir. These preferential channels – known as viscous fingers – dominate fluid flow through the reservoir and prevent wider distribution of injectant throughout the reservoir volume. Mobility control is described by the mobility ratio, M , given in Eq. (2.1) for a displacing phase (phase 1) injected into a reservoir saturated with phase 2:

$$M = \frac{k_{r1}\mu_2}{k_{r2}\mu_1}, \quad (2.1)$$

where k_{r1} and k_{r2} are the relative permeabilities and μ_1 and μ_2 are the viscosities of phase 1 and 2, respectively. This concept is demonstrated by Fig. 2.3, which shows the development of flooding fronts at different mobility ratios [61].

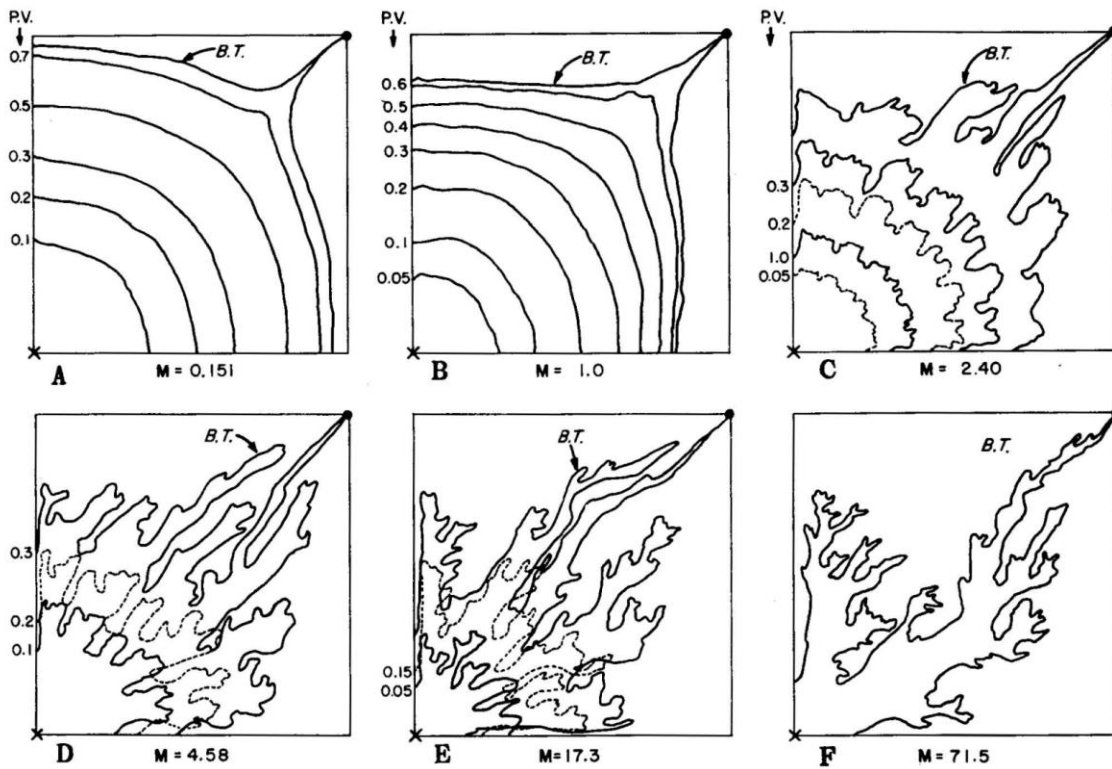


Fig. 2.3. Traced displacement fronts of a flood in a sand pack, photographed from above. As the mobility ratio, M , increases, the sweep efficiency decreases [61]. P.V. and B.T. refer to the pore volumes of fluid injected and the breakthrough time, respectively.

In Fig. 2.3, Habermann constructed artificial sand packs and saturated them with an oil phase. Using different displacing fluids with different viscosities, and therefore different mobility ratios (M), they flooded the sand pack and imaged the front at different pore volumes. The flooding front is defined as P.V. – the amount of pore volumes of displacing fluid injected into the sandpack. The flooding front at displacing fluid breakthrough – denoted as B.T. – occurred at a later P.V. for floods with lower M (better mobility control). With colored dye in the displacing fluid as a marker, they traced the fronts to demonstrate the impact of M on sweep efficiency. Pickering emulsions and foams, by their high viscosity, can benefit from mobility control [62].

2.2.2 CO₂ enhanced oil recovery and storage

CO₂ enhanced oil recovery (CO₂-EOR) is the injection of CO₂ underground to produce hydrocarbons [35,63]. Fig. 2.4 shows a field schematic of a CO₂ injection process [35].

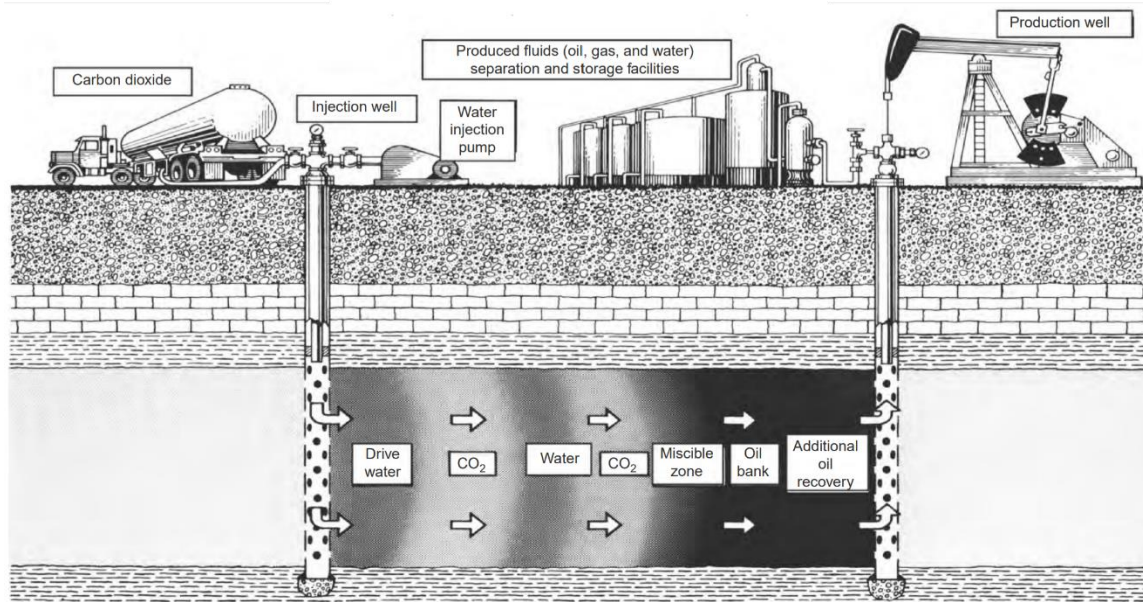


Fig. 2.4. Field schematic of a CO₂-EOR injection process, from Lake et al. [35].

In the given example, alternate slugs of CO₂ and water are injected to produce oil through miscible displacement. Water is used to drive CO₂ into contact with oil. Through a sequence of chemical and physical interactions, CO₂ can partially or fully mix with oil and achieve high displacement efficiency [64], with CO₂-EOR commonly producing 5-15% tertiary recovery of original oil in place [35]. CO₂-EOR is a mature technology and has been commercially successful since the 1970s [65-68]. In addition to producing oil, CO₂-EOR can be co-optimized to both recover oil and keep CO₂ sequestered underground, addressing decarbonization needs in response to climate change [69]. CO₂ storage, then, is

the injection of CO₂ underground with the sole goal of sequestering CO₂ [70,71]. There is significant potential for CO₂ EOR and storage to expand throughout this century to meet climate goals, and ample geologic storage capacity to sequester CO₂ [72-78].

A challenge with CO₂ flooding for both EOR and storage is poor sweep efficiency because of the low viscosity of CO₂ relative to the reservoir fluids. Additionally, the low density of the CO₂ phase can cause gravity segregation, further reducing the sweep efficiency in the vertical direction. As mentioned above, this challenge can be addressed by injecting CO₂ as a viscous foam. With reduced mobility, the CO₂ foam inhibits the formation of viscous fingers; additionally, gravity forces become relatively less important than viscous forces, reducing gravity segregation [35]. Significant research has gone towards Pickering and hybrid nanoparticle-surfactant CO₂ foams [18].

2.2.3 Other applications

Nanoparticles have been examined for other petroleum engineering applications. Sabet et al. studied the use of dense nanofluids to increase the viscosity of the injectant and improve the volumetric sweep efficiency [79]. At sufficiently high concentrations, interparticle attraction can increase the viscosity of an aqueous particle dispersion [80,81]. Particles have also been investigated for improved drilling fluids [82] and tracers [22]. Pickering emulsions have further been studied for water/crude separation with stimulus-responsive “switchable” emulsions [83] and for cleaning oil spills [20]. An especially interesting application is the use of Pickering emulsions for aquifer decontamination. Magnetic particles can be deployed in a reservoir to emulsify oil contaminants in-situ; the emulsions can then be retracted using a magnetic force to remove the oil droplets from the formation [19].

2.3 INTERPARTICLE FORCES IN THE BULK FLUID

An important consideration when selecting nanoparticles for use in a Pickering emulsion or foam is the chemistry of the particle surface. Silica particles are inexpensive and well characterized, but bare silica is challenging to use in a reservoir. The surface silica is densely covered with hydroxyl (OH) groups. Silica is hydrophilic, and prefers to remain almost entirely in the aqueous phase, measured by its low contact angle (θ). As a result, aqueous bare silica does not interact much with the fluid-fluid interface and generates poor emulsions and foams [84]. Additionally, at high salinity, electrostatic forces between the negatively-charged silica particles are screened by ions; absent this force, the particles can aggregate under the influence of the van der Waals attraction [28]. Because petroleum applications require the use of Pickering emulsions and foams in high salinity reservoirs, particles must be designed to resist aggregation.

I will first discuss methods of nanoparticle surface modification to improve wettability and particle stability. Then, I will give a detailed description of the calculation of interparticle forces using extended DLVO theory. A detailed description of particle modification techniques used throughout this dissertation is given in Appendix A.

2.3.1 Surface modification of nanoparticles

There are a few ways to address these issues and use silica to generate stable emulsions and foams. Silica can be brought to high temperature; above 200°C, OH groups at the silica surface are removed via dihydroxylation [85,86]. Ultimately, the removal of surface OH makes the particle less hydrophilic. Particles can also be used in conjunction with a surfactant that adsorbs to the surface [57,87]. However, one of the most robust methods for altering the silica surface is by covalently grafting molecules with favorable properties via the silanization reaction [28,30,31].

Silanization refers to the hydrolysis and condensation reaction used to graft silanes onto the silica surface. Silanol groups on the silica surface react with other silanol groups with a condensation reaction. As such, silica nanoparticles are easily reacted with silanes. Silanes are broadly defined as any molecules with the structure SiR_4 , but the silanes used in most surface modification techniques have one or two functional groups and two or three methanol or ethanol groups. The functional groups are used to impart the desired properties on the particle surface, and the methanol and ethanol groups are hydrolyzed to initiate the silanization reaction. Silanization follows the mechanism described in Fig. 2.5 [30,31]:

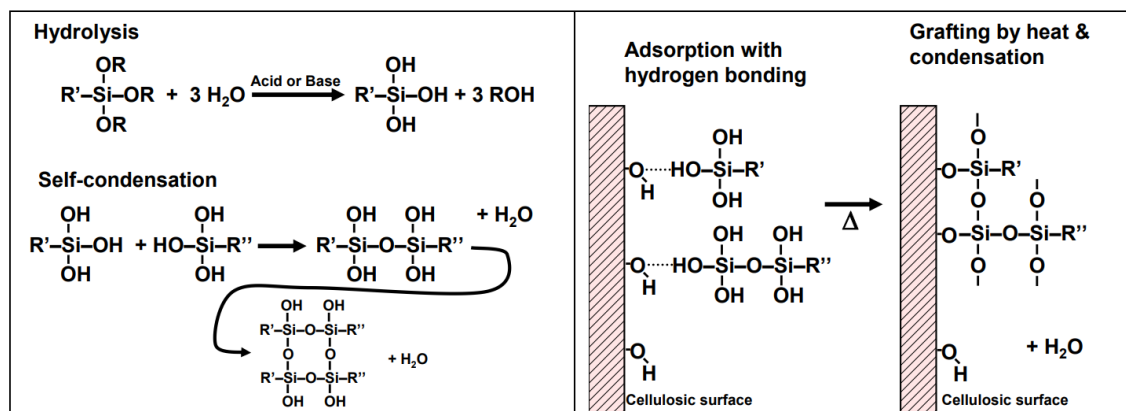


Fig. 2.5. Silanization reaction via hydrolysis and condensation. From Xie et al. [30] and Hubbe et al. [31].

In the presence of water at high or low pH, the methanol and ethanol groups hydrolyze and convert to hydroxyl groups. The hydroxyl groups can react with themselves via a condensation reaction to form dimers or oligomers. At the silica surface, they perform a similar condensation reaction, releasing one water molecule to form a Si-O-Si bond and covalently grafting to the silica surface. The condensation reactions are catalyzed with high temperature.

There are a few possible conformations that silane molecules can adopt as they attach to the particle surface. Fig. 2.6 illustrates the main attachment mechanisms [28,88].

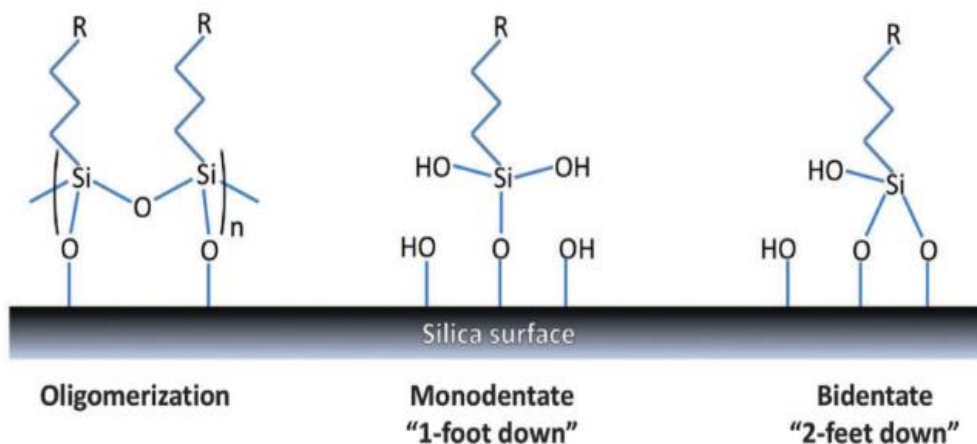


Fig. 2.6. Possible conformations of silane bonded to the silica surface. From Estephan et al. [88] and Worthen et al. [28].

Fig. 2.7 plots the concentration of OH groups at the silica surface for a variety of nanoparticles and surface areas [86,89]. The least-squared error fit to this data, 4.6 OH groups per square nanometer, is taken as a good estimate of the OH coverage of silica. This value is equivalent to $7.6 \mu\text{mol}/\text{m}^2$.

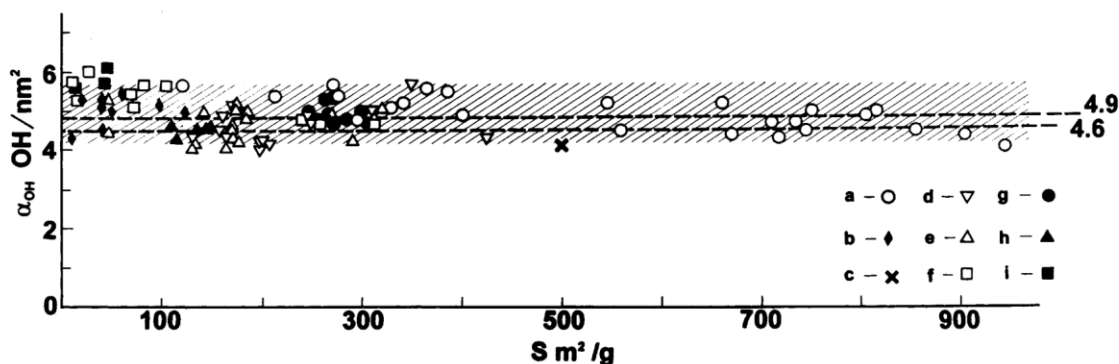


Fig. 2.7. Concentration of hydroxyl groups at the silica surface, from Zhuravlev [86,89]. OH has a concentration of 4-6 sites/ nm^2 in most cases, regardless of particle surface area.

The quantity of silanes grafted to the silica surface are usually measured with thermogravimetric analysis (TGA). I discuss TGA measurements in extensive detail in Appendix A. Given the uncertainty in the number of OH groups occupied per silane molecule, as well as the number of OH groups at the silica surface, it can be difficult to estimate the percentage of surface OH groups occupied by silanes. However, when a percentage is given, it is often reported as monodentate attachment with an OH density of $7.6 \mu\text{mol}/\text{m}^2$ [28,81].

2.3.2 Particle-particle interactions with DLVO theory

As given in Eq. (1.1), the total DLVO interaction energy, Φ_T , is a sum of the van der Waals (Φ_{vdW}), electrostatic (Φ_E), and steric (Φ_S) interactions [25-29]. These calculations can be used to predict particle stability. If Φ_T is sufficiently high, the particles will repel at most distances and should remain stable in dispersion. If Φ_T is negative, the particles will attract and aggregate.

The van der Waals (vdW) interaction of a pair of surface-modified particles is given by Eq. (2.2) [90]:

$$\Phi_{wvdV}(d) = -\frac{(r+L)(\sqrt{A_m}-\sqrt{A_p})^2}{12d}, \quad (2.2)$$

where r is the particle radius, L is the length of the ligand at the particle surface, A_m and A_p are Hamaker constants of the aqueous phase and particle, respectively, and d is the interparticle distance measured from the silica surfaces (neglecting ligand length). The electrostatic interaction is given by Eq. (2.3) [90]:

$$\Phi_E(d) = 32\pi r \varepsilon_o \varepsilon_r b \left(\frac{k_B T}{e}\right)^2 \tanh^2\left(\frac{e\zeta}{4k_B T}\right) e^{-\kappa d}, \quad (2.3)$$

where ε_o is the permittivity of free space, ε_r is the relative permittivity of the aqueous phase, k_B is the Boltzmann constant, T is temperature, ζ is the particle surface potential (assumed to be 0 in concentrated brine because of ion screening), and κ is the inverse Debye length. κ is calculated with Eq. (2.4) [90]:

$$\kappa = \sqrt{\frac{\sum_i \rho_{\infty,i} q_i^2 z_i^2}{\varepsilon_o \varepsilon_r k_B T}}, \quad (2.4)$$

where $\rho_{\infty,i}$ is the density of species i in the bulk, z_i is the valence of species i , and q_e is the elementary charge.

The steric interaction is given as the sum of the osmotic (Φ_o) and entropic/elastic interactions (Φ_{ee}), shown by Eq. (2.5) [91]:

$$\Phi_S = \Phi_o + \Phi_{ee}. \quad (2.5)$$

The osmotic interaction is given pairwise by Eq. (2.6) [91]:

$$\Phi_o(d) = 0, \quad d \geq 2l$$

$$\begin{aligned}\Phi_o(d) &= \frac{4\pi r \varphi^2 (0.5 - \chi)}{v_1} \left[L - \frac{d}{2} \right]^2, & l \leq d < 2l \\ \Phi_o(d) &= \frac{4\pi r v_f^2 (0.5 - \chi) l^2}{v_1} \left[\frac{d}{2L} - \frac{1}{4} - \ln\left(\frac{d}{L}\right) \right], & d < l\end{aligned}\quad (2.6)$$

where v_f is the volume fraction that the ligand occupies at the silica surface, χ is the Flory-Huggins parameter, and v_l is the total volume of a ligand molecule at the silica surface. The entropic/elastic interaction is given by another pairwise function, Eq. (2.7) [91]:

$$\begin{aligned}\Phi_{ee}(d) &= 0, & d \geq l \\ \Phi_{ee}(d) &= \frac{2\pi r N_a \varphi d^2 \rho_p L^2}{M_w} \left[\frac{d}{L} \ln\left(\frac{d}{4l} \left(3 - \frac{d}{L}\right)^2\right) - 6 \ln\left(\frac{3-d/L}{2}\right) + \right. \\ &\quad \left. 3\left(1 - \frac{d}{L}\right) \right], & d < l\end{aligned}\quad (2.7)$$

where ρ_p is the density of the ligand and M_w is the molecular weight of the ligand.

As an example of these calculations, Fig. 2.8 plots the three constituent DLVO interaction potentials, plus the total interaction potential, for a system of 100-nm silica particles in either deionized water (DIW) or 4 wt% NaCl, 1 wt% CaCl₂ brine. The particles are either bare silica, or silica coated with 1.5 $\mu\text{mol}/\text{m}^2$ of PEG-silane.

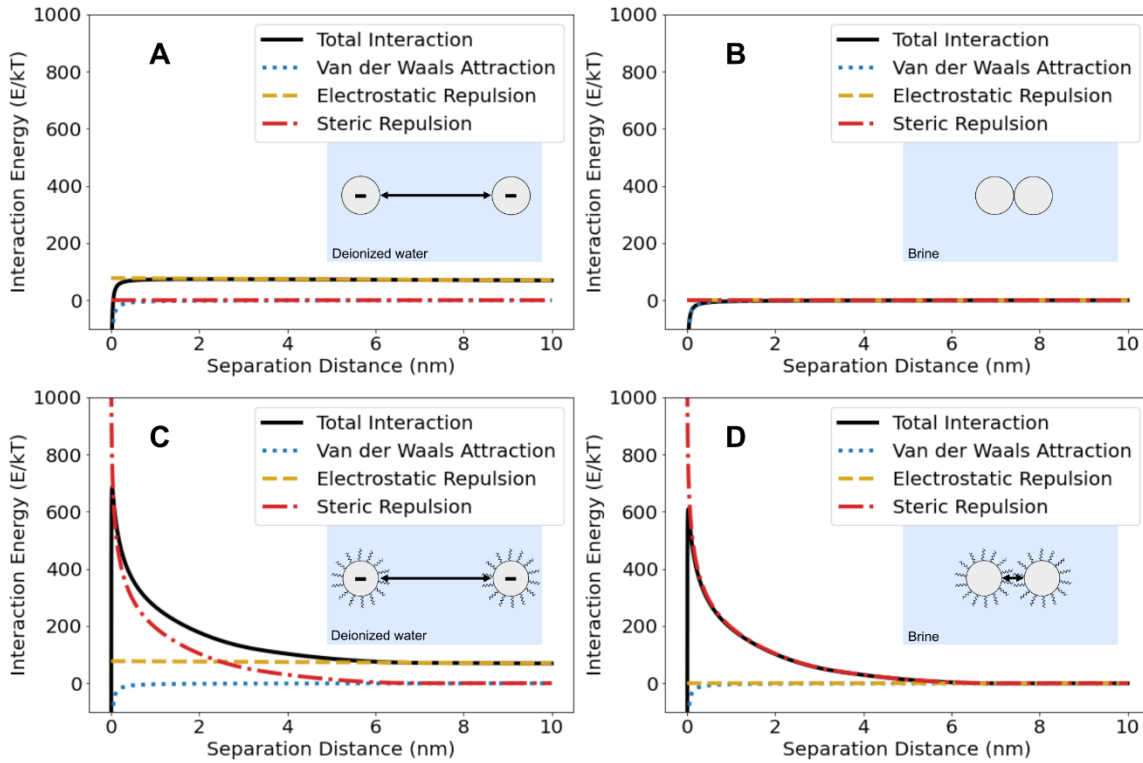


Fig. 2.8. (a) DLVO interaction potential of bare, ungrafted silica in DIW; (b) DLVO interaction potential of bare, ungrafted silica in 5API brine; (c) DLVO interaction potential of PEG-coated silica in DIW; (d) DLVO interaction potential PEG-coated silica in 5API brine. Only (b) predicts particle aggregation. Inset images illustrate the approach of particles at the given conditions.

From these calculations, only case (b) – ungrafted silica particles in brine – have a consistently negative value of Φ_T . Indeed, these particles do aggregate in brine, whereas the other particles remain stable (refer to Fig. (B.2) in Appendix B).

2.4 FORCES ACTING ON PARTICLES AT THE FLUID-FLUID INTERFACE

In a simplified model, a particle positioned at the fluid-fluid interface intersects the interface with a circular cross-section, generating the attachment energy described in Fig. 1.2. However, a more detailed analysis reveals a more complicated energy balance.

Aveyard et al. provide a detailed description of particle-interface interactions and particle-particle interactions at an oil-water emulsion droplet interface [92]. The energy of a single particle attaching to the interface of an emulsion droplet, E_{Total} , is given by Eq. (2.8):

$$E_{Total} = \Phi_{vdW}^{int} + \Phi_E^{int} + \Phi_S^{int} + \Delta_{int}G + \Delta_{demix}G. \quad (2.8)$$

Eq. (2.8) equates E_{Total} to a summation of five energy terms: vdW attraction (Φ_{vdW}^{int}), electrostatic repulsion (Φ_E^{int}), steric repulsion (Φ_S^{int}), reduced oil-water interfacial energy because of area occupied by the interfacial particle ($\Delta_{int}G$), energy associated with the entropic demixing and arrangement of particles from the aqueous phase to the interface ($\Delta_{demix}G$). This equation neglects the energy of curvature considered by Aveyard et al. [92].

Φ_{vdW}^{int} is the energy of vdW attraction between a pair of particles, divided by two to give the contribution from each individual particle. It is assumed that the total vdW interaction of all n particles is expressed as a sum of $n/2$ pairwise interactions. Φ_{vdW}^{int} is given in Eq. (2.9) [92,93]:

$$\Phi_{vdW}^{int} = -\frac{A_{ww}(r+L)}{48d} \left[1 + \frac{(r+L) \cos \theta}{\sqrt{d(r+L)+(r+L)^2 (\cos \theta)^2}} \right] - \frac{A_{oo}(r+L)}{48d} \left[1 - \frac{(r+L) \cos \theta}{\sqrt{d(r+L)+(r+L)^2 (\cos \theta)^2}} \right], \quad (2.9)$$

where A_{ww} and A_{oo} are the combined Hamaker constants of a pair of particles interacting through the aqueous phase and the oil phase, respectively; L is the length of the ligand at the particle surface, r is the particle radius, θ is the three-phase contact angle, and d is the interparticle distance measured from silica surface to silica surface.

Φ_E^{int} is calculated similar to Aveyard et al. 2000 and 2003 [92,94]. First, we need three geometric terms: x , the radius of the circle where a Pickering particle intersects the droplet interface; α , the angle from the center of the intersecting circle to the edge, measured from the perspective of the particle; and ξ , a distance away from the oil-water interface from which electrostatic charges through the oil or aqueous phases are calculated. x is given by Eq. (2.10):

$$x = \frac{rR \sin \theta}{\sqrt{r^2 + R^2 + 2rR \cos \theta}}, \quad (2.10)$$

where R is the droplet diameter. The values of α and ξ are given by Eq. (2.11) and (2.12) [92]:

$$\alpha = \sin^{-1} \left(\frac{x}{r+L} \right), \quad (2.11)$$

$$\xi = r \frac{3 + \cos \theta}{2}. \quad (2.12)$$

Second, using measured values of the ζ potential, we calculate the surface charge, σ , with the Grahame equation, Eq. (2.13) [90]:

$$\sigma = \sqrt{8\epsilon_o \epsilon_{ra} k_B} \sinh \left(\frac{q_e \zeta}{4k_B T} \right) \sqrt{[NaCl]_\infty + [CaCl_2]_\infty \left(2 + e^{-\frac{q_e \zeta}{k_B T}} \right)}, \quad (2.13)$$

where ϵ_o is the permittivity of free space, ϵ_{ra} is the relative permittivity of the aqueous phase, k_B is the Boltzmann constant, T is temperature, q_e is the elementary charge, and $[NaCl]_\infty$ and $[CaCl_2]_\infty$ are the molar concentrations of NaCl and CaCl₂, respectively, in the bulk aqueous phase. This version of the Grahame equation has been adapted for brine with

monovalent and divalent cations. Applying σ to the geometric terms, we calculate the surface charge in the oil phase (σ_{oil}) and in the aqueous phase ($\sigma_{aqueous}$) with Eq. (2.14) and (2.15):

$$\sigma_{oil} = 4\sigma\pi(r + L)^2 \frac{1 - \cos \alpha}{2}, \quad (2.14)$$

$$\sigma_{aqueous} = 4\sigma\pi(r + L)^2 \frac{1 + \cos \alpha}{2}. \quad (2.15)$$

From these terms, we can calculate the electrostatic potential for particles hexagonally distributed across a surface through the oil phase ($\Phi_{E,oil}^{int}$) and through the aqueous phase ($\Phi_{E,aqueous}^{int}$) using Eq. (2.16) and Eq. (2.17) [95]:

$$\Phi_{E,oil}^{int} = \frac{\sigma_{oil}^2}{2\pi\epsilon_0\epsilon_{ro}} \left[\frac{1}{S} - \frac{1}{\sqrt{S^2 + 16\xi^2}} + \frac{1}{S} \ln \frac{1 + \sqrt{1 + \frac{16\xi^2}{S^2}}}{2} \right], \quad (2.16)$$

$$\Phi_{E,aqueous}^{int} = \frac{\sigma_{aqueous}^2}{2\pi\epsilon_0\epsilon_{ra}} \left[\frac{1}{S} - \frac{1}{\sqrt{S^2 + 16\xi^2}} + \frac{1}{S} \ln \frac{1 + \sqrt{1 + \frac{16\xi^2}{S^2}}}{2} \right], \quad (2.17)$$

where ϵ_{ro} is the relative permittivity of the oil phase and S is the distance from particle center to particle center. Eq. (2.17) was calculated using an analogous derivation to the one presented by Aveyard et al. to derive Eq. (2.16) [95]. At this point in the calculation, if we are modeling an emulsion in concentrated brine, we ignore any electrostatic interaction across the aqueous phase (because of significant ionic screening) and assume that our total electrostatic interaction, Φ_E^{int} , occurs only through the oil phase:

$$\Phi_E^{int} = \Phi_{E,oil}^{int}. \quad (2.18)$$

Otherwise, we can calculate Φ_E^{int} as the sum of $\Phi_{E,oil}^{int}$ and $\Phi_{E,aqueous}^{int}$:

$$\Phi_E^{int} = \Phi_{E,oil}^{int} + \Phi_{E,aqueous}^{int}. \quad (2.19)$$

In both cases, Φ_E^{int} is the total electrostatic potential contributed by each nanoparticle in our system.

Third, we determine the steric repulsion. Under close hexagonal packing on a flat surface, we assume each particle independently interacts with six neighboring particles. The steric contribution from each particle, therefore, is triple the pairwise steric interaction, given in Eq. (2.20):

$$\Phi_S^{int} = 3\Phi_S, \quad (2.20)$$

where Φ_S is the pairwise steric potential energy described by Eq. (2.5).

The fourth parameter, $\Delta_{int}G$, is given for each particle by Eq. (2.21) [58]:

$$\Delta_{int}G = 2\pi\gamma_{oa} \left[r^2(1 - \cos \alpha) \cos \theta \left(1 - \frac{\tau \cos \beta}{\gamma_{ow}x} \right) - R^2(1 - \cos \beta) \right] + 2\pi x \tau, \quad (2.21)$$

where γ_{oa} is the oil-aqueous interfacial tension and τ is the line tension associated with the perimeter of the particle-oil-aqueous circle of contact. This equation is a more complex version of Eq. (1.2), in part by factoring in the energy change of the particle itself and line tension. β is another geometric term; analogous to α , it describes the angle from the center

of the intersecting particle-oil-aqueous circle of contact to the edge, measured from the perspective of the droplet. β is given by Eq. (2.22) [92]:

$$\beta = \sin^{-1} \left(\frac{x}{R} \right). \quad (2.22)$$

Finally, $\Delta_{demix}G$, the energy (contributed by a single particle) associated with the entropy of removing a particle from the bulk aqueous phase and arranging it on the droplet surface, is given by Eq. (2.23) [92,95]:

$$\Delta_{demix}G = -k_B T \left[\ln \frac{\varphi_f}{\varphi_i} + \frac{\varphi_f(4-3\varphi_f)}{(1-\varphi_f)^2} - \frac{\varphi_i(4-3\varphi_i)}{(1-\varphi_i)^2} \right], \quad (2.23)$$

where φ_i is the initial volume fraction of nanoparticles in the aqueous phase, and φ_f is the volume fraction of nanoparticles in the aqueous phase after particles have been transferred to the interface.

2.5 STABILITY OF PICKERING EMULSIONS

Unlike surfactant-stabilized emulsions, Pickering emulsions are not stabilized by a reduction in the interfacial tension (nanoparticles often have minimal effect on the interfacial tension). Rather, the irreversible attachment of particles to the fluid-fluid interface generates a physical barrier that prevents droplet coalescence [4]. At rest, emulsions undergo creaming – the separation of the emulsion droplets from the continuous phase due to differences in density [96] – but the physical barrier can prevent the emulsions from coalescing in a realistic timeframe. There are several examples in the literature of Pickering emulsions that are stable at static conditions [38,97-102].

However, for applications in porous media, it is generally better to establish that an emulsion is dynamically stable during flow. Researchers have demonstrated dynamic stability with rheological measurements [81,103] and core floods [104]. Griffith and Daigle [105] demonstrated that stability from centrifugation measurements is a good proxy for the flowing stability of an emulsion. They generated emulsions using silica nanoparticles grafted with [3-(2,3-dihydroxypropoxy)propyl]-trimethoxysilane (GLYMO) at ligand surface coverages and particle concentrations. In a glass capillary tube, they flowed the emulsions at different flow rates. Less stable emulsions exhibited an increase in their droplet diameter at lower flow rates (higher residence time in the capillary tube). They found a strong correlation between their capillary tube stability and de-emulsification pressures calculated from centrifugation experiments. Several other studies report emulsion stabilities in terms of centrifugation [106-109].

The stability of Pickering emulsions is affected by interparticle forces. Studies have shown that some particle attraction can increase emulsion stability [110-114]. Similarly, there is strong evidence in the literature that high salinity can increase the stability of Pickering emulsions [80,105,107,115-118]. This trend has been explained by the existence of inter-droplet particle networks – structures of slightly attracted particles that bridge the inter-droplet space and give additional stability to Pickering emulsions [81,104,119]. As salinity increases, the interparticle electrostatic interaction is screened and reduced, promoting particle attraction [90]. In a recent paper, we showed that this effect could be reproduced by manipulating the particle-particle steric interaction – this concept is the key finding of Chapter 4 in this dissertation.

Table 2.1 summarizes the results from previously mentioned papers on Pickering emulsions. The emulsions described in Chapter 3 and 4 are added to the bottom rows of Table 2.1 as a comparison.

Authors	Particle and emulsion system	Dynamic stability test	Result
Whitby et al., 2011 [80]	Surface modified silica with hexadecylsilane (commercial, Aerosil R816, from Degussa); bromohexadecane-in-brine emulsions with varying NaCl concentration	Sheared at 1-1000 s ⁻¹ for 30 seconds	40 to 0% of oil volume released as NaCl concentration increases from 0.1 mM to 100 mM with 2 wt% particles
Yoon et al., 2016 [103]	Silica particles used with PSS-co-MA (anionic polymer) and DTAB (cationic surfactant); decane-in-deionized water emulsions	Core flooding (qualitative)	Emulsion stability inferred by improved oil recovery and delayed breakthrough of core-flood (1 wt% particles, 0.5 wt% polymer, and 0.1 wt% surfactant)
Katepalli et al., 2017 [104]	Silica particles with adsorbed hexylamine and fumed silica surface modified with hexadecyltrimethoxysilane; bromohexadecane-in-water emulsions with 0.1 and 50 mM NaCl concentration	Sheared at 10-100 s ⁻¹ ; oscillatory strain measured for 0.1-100 % strain	Increased viscosities and higher storage moduli measured for emulsions with 50 mM NaCl and for emulsions with fumed silica, indicating improved emulsion strength (2 wt% particles). Particle-particle networks imaged with cryo-SEM

Griffith and Daigle, 2020 [105]	Surface modified silica with 1.85-4 $\mu\text{mol}/\text{m}^2$ GLYMO (hydrophilic silane); decane-in-deionized water emulsions	Centrifugation at 5000 g for 15 min and slim tube flow at 0.3-68 s^{-1} shear for varying time	0-40 kPa demulsification pressure; 20 kPa (~50% oil released) at 3.4 wt% particles; evidence of destabilization of emulsions with 2.8 wt% or less particles at low shear (0.3 s^{-1} , highest residence time of 80.8 min)
Frelichowska et al., 2010 [106]	Commercial hydrophobic fumed silica particles (HKS D and H30) from Wacher Chemie; water-in-oil and oil-in-water emulsions generated with (2-ethyl)hexyl stearate, DUB SO, and silicone oil.	Centrifugation at 15557 g for 30 min	Emulsions with 7 wt% oil were stable to centrifugation by visual observation at 1.3-3.0 wt% particles
Saha et al., 2013 [107]	Carbon black particles surface-modified by 0.1-4 $\mu\text{M}/\text{m}^2$ PABA (hydrophilic additive); octane-in-water emulsions	Centrifugation at 150-1000 g for 15 min	1.4-4.6 kPa demulsification pressure for 0.0075-0.015 wt% particles; highest stability contained 0.6 M NaCl
Kruglyakov et al, 2004 [108]	Various silica particles (hydrophilic) with 10 ⁻⁶ to 10 ⁻³ M adsorbed CTAB (hydrophobic); decane-in-brine emulsions with 0.1 M KCl	Centrifugation at 500-5000 rpm	With 1% particles and 10 ⁻⁴ CTAB, emulsions are stable for 30 min at 50 kPa pressure and 5 min above 120 kPa

Chapter 3	Surface modified silica with 5 $\mu\text{mol}/\text{m}^2$ GLYMO (hydrophilic silane); decane-in-deionized water and decane-in-brine emulsions with 4 wt% NaCl and 1 wt% CaCl_2	Centrifugation at 5000 g for 15 min	Brine emulsions transition from unstable to stable between 0.1-0.4 wt% particles; deionized water emulsions transition between 2.75-4 wt% particles; 78x decrease in coalescence rate in brine, controlling for droplet diameter change
Chapter 4	Surface modified silica with 0.42-1.90 $\mu\text{mol}/\text{m}^2$ PEG measured by TGA (hydrophilic silane); decane-in-deionized water and decane-in-brine emulsions with 4 wt% NaCl and 1 wt% CaCl_2	Centrifugation at 5000 g for 15 min	50% decane released as low as 1×10^{15} particles/ cm^3 (0.034 wt% particles) for 0.65 $\mu\text{mol}/\text{m}^2$ PEG. Emulsions weaker with different PEG concentrations, in deionized water, and with larger particles.

Table 2.1: Summarized results of selected Pickering emulsion studies, with emulsions from Chapter 3 and 4 added as a comparison.

2.6 STABILITY OF PICKERING FOAMS

Foams, as a gas-in-liquid mixture with a low liquid fraction, have a structure of gas bubbles surrounded by thin liquid lamellae [35]. Like Pickering emulsions, Pickering foams are stabilized by particles positioned at the fluid-fluid interface, although the specific mechanisms of destabilization are different.

Pickering foams destabilize primarily through coalescence and coarsening. In the former case, when gas pressure acting on the lamellae exceeds the disjoining pressure, the lamellae ruptures and the gas bubbles combine. In porous media, this process is dominated by capillary forces [35]. On the other hand, coarsening refers to the shrinkage of small bubbles and growth of larger bubbles over time. This transfer of gas from small to large bubbles occurs because of Ostwald ripening [120-122]. Smaller bubbles, by virtue of their small radius, exhibit a higher capillary pressure (more generally, a higher chemical potential) than larger bubbles. The result is that smaller bubbles release material at a higher rate than larger bubbles and lose volume over time. In a saturated aqueous phase, larger bubbles will receive a net gain in material over time. Nanoparticles help mitigate both coalescence and coarsening by increasing the interfacial elastic dilational modulus, E' . When E' is large, the lamellae are less susceptible to perturbations and collapse, maintaining bubble stability. If E' is larger than half the fluid-fluid interfacial tension, then the bubbles will also exhibit little to no coarsening via the Gibb's criterion [42,123]. Surfactant-stabilized foams do not meet this threshold.

There are a few approaches to measure foam stability. It can be determined through visual observation, and especially by measuring the bulk foam height over time. For high-stability Pickering foams with negligible coalescence rates, however, a more robust measurement of stability is the coarsening rate, often expressed as the cube of the bubble diameter over time, where the bubble diameter is taken as the Sauter mean diameter (sum of bubble diameters cubed divided by the sum of bubble diameters squared). Coarsening rates can be determined via microscopy over time. CO₂ foams are especially challenging to generate stable foams with; owing to its high solubility in water, CO₂ exhibits a higher coarsening rate than many other gases [124,125].

There has been extensive work in recent years to develop CO₂ foams that are stable at reservoir conditions (high pressure, high temperature, and high salinity) for the purposes of CO₂-EOR and CO₂ storage. Li et al. [126] used a combination of HHSB surfactant and unmodified silica to stabilize CO₂ foam at 70°C, 8 mPa, and 100 g/L brine (including divalent ions) with a half-life of six hours – one of the best known stabilities at these conditions. They additionally reported a half-life of 45 minutes at 110°C. Kang et al. [127] used bare silica nanoparticles with an anionic-nonionic surfactant to achieve foam half-lives of up to two hours at 85°C, 14 mPa, and 61.2 g/L brine (including divalent ions). Wang et al. [128] achieved a CO₂ foam half-life up to two hours at 100°C, 14 mPa, and 100000 ppm brine (2000 ppm Ca⁺⁺) using a variety of surfactants. In particularly harsh conditions, Eide et al. [129] generated CO₂ foam at 120°C, 23 wt% brine (including divalent ions), and 100 bar using Levasil CC301 (silica nanoparticles surface-modified with an commercial epoxy silane).

There have been multiple studies on developing stable CO₂ Pickering foams using surface modified particles; many of these papers use commercial and/or proprietary surface coatings. A notable exception is Zhang et al, who have published results developing CO₂ foams with silica particles grafted with various silanes [130-132]. In a recent paper, they grafted silica with GLYMO and generated CO₂ foams in conjunction with ethoxylated amine surfactants. At 60°C, 10 mPa, and 10 wt% brine (including 2 wt% CaCl₂), they report a foam half-life of 75 minutes [132].

Table 2.2 summarizes results from selected CO₂ foam studies described above at their given conditions. CO₂ foams from Chapter 5 are presented in the bottom rows as a comparison.

Authors	Stabilizing agent	Temperature, salinity, and pressure	Stability
Li et al., 2019 [126]	Bare silica nanoparticles and HHSB surfactant (zwitterionic)	Up to 110 °C; up to 100 g/L salinity, including divalent ions; 1160 psi	Half-life ranging from 45 minutes (110 °C, 2 g/L salinity) to 6 hours (70 °C, 10 g/L salinity) with 0.05% HHSB and 0.5% silica
Kang et al., 2021 [127]	Bare silica nanoparticles and EC-1 surfactant (anionic-nonionic)	85 °C; 61.2 g/L salinity, including divalent ions; Up to 1160 psi	Best half-life of 2 hours achieved at 1160 psi with 0.5% EC-1 and 1% silica
Wang et al., 2017 [128]	Various surfactants: nonylphenol polyethoxylate (7-21 EO), alkyl polyglycoside, SDS, SDS' (sulfonate, anionic), SDBS	Up to 120 °C; 100000 ppm salinity, including divalent ions; up to 2031 psi	Best case: 1.5% SDS' surfactant foam with a half-life of almost 2 hours at 100 °C and 2031 psi.
Eide et al., 2018 [129]	Surface modified silica (Levasil CC301) with commercial hydrophilic and steric surface	120 °C; 23% salinity, including divalent ions, as well as other salinities; 1450 psi	CO ₂ foam was generated at 120 °C, 23% salinity, and 1450 psi with 1500 ppm particles by lowering pH below 2; no long-term stability measurement
Zhang et al., 2020a [130]	Surface modified silica with 1 μmol/m ² of silane KH560 (epoxy silane), and C1202 surfactant (ethoxylated amine)	80 °C; 0-15% NaCl; 1450 psi	CO ₂ foams are generated and viscosity is measured; no long-term stability measurement

Zhang et al., 2020b [131]	Surface modified silica with GLYMO (hydrophilic ligand)	35-70 °C; 0-50 g/L salinity; up to 2176 psi	Best case: half-life of 70 min at 50 °C; 15 min at 70 °C.
Zhang et al., 2020c [132]	Surface modified silica with 0.5-2.0 $\mu\text{mol}/\text{m}^2$ GLYMO (hydrophilic ligand) and ethoxylated amine surfactants (C1202, C1205, C1210)	60°C; 8% NaCl + 2% CaCl ₂ ; 1450 psi	Best case: approximately 75 min half-life with 0.5 wt% of 0.5 $\mu\text{mol}/\text{m}^2$ GLYMO particles with 0.2 wt% C1202 surfactant
Chen et al., 2022 [180]	Surface modified silica with N3+N2 (amine ligands) and RCADA surfactant (cationic)	60-80°C; 22 wt% salinity including divalent ions; 2200 psi	Best case at 60 °C: 3 $\mu\text{m}^3/\text{min}$ coarsening rate at 1.0 w/v% NP and 1.0 v/v% RCADA surfactant; best cases at 80°C: 10018 $\mu\text{m}^3/\text{min}$ at 0.2 w/v% NP and 0.1 v/v% RCADA surfactant, 408 $\mu\text{m}^3/\text{min}$ at 1.0 w/v% NP and 0.1 v/v% RCADA surfactant
Chapter 5	Surface modified silica with N3+DM (amine and hydrophobic ligands) and RCADA surfactant (cationic)	80°C; 22 wt% salinity including divalent ions; 2200 psi	Best cases: 2400 \pm 200 $\mu\text{m}^3/\text{min}$ coarsening rate with 0.2 w/v% 8N3+0.5DM particles and 1.0 v/v% RCADA surfactant; 900 \pm 80 $\mu\text{m}^3/\text{min}$ with 1.0 w/v% 8N3+1.5DM particles and 1.0 v/v% RCADA surfactant

Table 2.2: Summarized results from selected CO₂ foam studies, with results from Chapter 5 given as a comparison.

Chapter 3: Examining the role of salinity on the dynamic stability of Pickering emulsions¹

3.1 INTRODUCTION

Solid-stabilized emulsions (i.e., Pickering emulsions) have seen increased focus in literature [5,57,87,133] as a potential alternative to surfactant-stabilized emulsions for applications such as enhanced oil recovery [15,16] and aquifer decontamination [19]. Solid particles stabilize emulsions by attaching to droplet surfaces through interfacial adsorption [1,2]. The particles adsorb to a fluid-fluid interface with high attachment energies and sterically prevent coalescence between adjacent droplets [134,135]. The attachment energy is high enough to stabilize macroemulsions (emulsions with droplets greater than 1 μm), a property that makes Pickering emulsions well suited for both conformance-controlled [55,58] and mobility-controlled [62] flow through porous media, particularly in harsh conditions [97].

The attachment energy is the product of the area a particle occupies at the interface by the surface tension of the two phases, given in Eq. (3.1) for an oil-water emulsion [135]:

$$\Delta E = \pi r^2 \gamma_{OW} (1 - |\cos(\theta_{OW})|)^2, \quad (3.1)$$

where ΔE is the change of energy of the particle transferring from the bulk to the surface, r is the particle radius, γ_{OW} is the oil-water interfacial tension, and θ_{OW} is the oil-water contact angle on the particle surface. The static stability of an emulsion is determined by the attachment energy of its particles. A nanoparticle with intermediate wettability ($\theta_{OW} = 90^\circ$) will achieve the highest ΔE and generate the most statically stable emulsions. Static stability can be controlled by manipulating the particle surface and changing the contact

¹ This chapter was published in the *Journal of Colloid and Interface Science* as: Hatchell, D., Song, W., & Daigle, H. (2022). Examining the role of salinity on the dynamic stability of Pickering emulsions. *Journal of Colloid and Interface Science*, 608, 2321-2329.

angle; various types of particles have been statically stabilized by this method [38,97-102]. Eq. (3.1), however, is not suitable for predicting stability of a flowing emulsion. During flow through porous media, there are more complicated dynamic forces present influencing stability to coalescence. Pickering emulsion stability under dynamic conditions is more difficult to determine and not as well understood.

Dynamic stability is typically measured with either centrifugation [105-109] or rheometry [80,116]. Griffith and Daigle [105] demonstrated that an emulsion's stability to coalescence in a centrifuge was an accurate indicator of its dynamic stability during flow. They generated decane-in-water emulsions stabilized by silica nanoparticles coated with [3-(2,3-dihydroxypropoxy)propyl]-trimethoxysilane (GLYMO), centrifuged the emulsions, and calculated a critical demulsification pressure – the pressure necessary to initiate partial coalescence of the emulsion. They compared these pressures to observations of the coalescence of emulsions flowing through a glass capillary tube, and found them to be good predictors of dynamic stability. Using these methods, some general factors that influence Pickering emulsion dynamic stability have been found. Emulsions with smaller droplet diameters, greater concentrations of nanoparticles, and particles with more intermediate wettability have all been shown to exhibit greater dynamic stability under certain conditions [80,105-109,116]. Dynamic stability also appears to increase with increasing salinity [80,105,107,115-117]. Investigating the role of salinity, Whitby et al. [80] examined the effect of shear force on coalescence in bromohexadecane-in-water Pickering emulsions while altering the concentration of sodium chloride. Using confocal fluorescence images, they demonstrated the tendency for unattached particles in the aqueous phase to aggregate around droplets at increased salinity, accompanied by increasing particle dispersion viscosity and emulsion stability. They were successfully able to destabilize emulsions by applying shear. Their work supported other studies suggesting

the formation of inter-droplet particle networks in the aqueous phase of high-salinity emulsions [81,119,136,137]. These networks are thought to be rigid enough to prevent droplets from approaching and coalescing, and could play a significant role in stabilizing emulsions during flow through porous media.

While particle networks have been qualitatively observed, there is little work in literature attempting to quantify their impact on coalescence in response to compressive stress while controlling for droplet size and nanoparticle concentration. The objective of this work is to quantify the effect of salinity on emulsion formation and coalescence under dynamic conditions with detailed measurements while controlling for droplet size and nanoparticle concentration. We generated and centrifuged emulsions over a range of nanoparticle concentrations and tracked differences in droplet diameter to isolate the effect of salinity. We then combined our observations with calculations of inter-particle forces to infer the presence and impact of inter-droplet particle networks.

3.2 MATERIALS AND METHODS

3.2.1 Materials

NexSil 6 silica nanoparticles were obtained from Nyacol as a nanoparticle core for functionalization. These particles, nominally 6 nm in diameter, have a reported diameter range of 5-7.5 nm and a specific surface area range of 340-545 m²/g. The specific stock used contained 18.8 wt% nanoparticles. (3-glycidyloxypropyl)trimethoxysilane (GPTMS or Ring-Closed GLYMO) was purchased from Sigma-Aldrich (>98% purity). n-decane was obtained from Chevron Phillips (>99% purity). Sodium chloride (NaCl), calcium chloride (CaCl₂), and 12.1 N hydrochloric acid (HCl) were purchased from Fischer Scientific. A Barnstead E-Pure Ultrapure Water Purification System generated 18.2 MΩ·cm deionized water (DI) for use in all experiments.

3.2.2 Functionalization of ring-opened GLYMO nanoparticles

The procedure to functionalize silica nanoparticles with Ring-Opened GLYMO was similar to previous work [28,105,137]. A batch of NexSil 6 stock solution containing 2 g nanoparticles was slightly diluted with DI in a cylindrical vial. 0.03 N HCl, diluted from a 12.1 N stock, was mixed with 4.4 g of methanol in a beaker to give a mixture with a resulting molarity of 0.01 M HCl. Ring-Closed GLYMO was added to the beaker such that there were 5 μmol in solution per m^2 of nanoparticle area based on an average surface area of 445 m^2/g , and stirred for a few minutes to open the epoxy ring and form Ring-Opened GLYMO ([3-(2,3-dihydroxypropoxy)propyl]-trimethoxysilane, referred to from here simply as GLYMO). This GLYMO mixture was then added dropwise to the vial containing 2 g of nanoparticles. The vial was sealed with PTFE tape and stirred overnight at 65° C to graft GLYMO onto the silica surface via hydrolysis condensation. Following the reaction, the mixture was opened to air to allow the methanol to evaporate. The resulting dispersion – approximately 17 g total - was purified in Amicon Ultra-15 30K MWCO centrifugal filters by centrifuging eight times with DI at 5000 g for 30 minutes. The separated particles after this process were redispersed in DI by sonication. The success of filtration was verified by measuring the surface tension of the aqueous particle dispersion with via the pendant drop method in a Ramé-Hart goniometer. The final, filtered dispersion of GLYMO-functionalized nanoparticles (GLYMO-NP) was used for experiments. Multiple batches were prepared by this method.

3.2.3 Nanoparticle characterization

Nanoparticle hydrodynamic diameter and zeta potential were measured with a Malvern Zetasizer Nano ZS. Diameter measurements were taken as the z (intensity) average and number average diameter of a 1 wt% nanoparticle dispersion in a cuvette, both

as reported by the Zetasizer. The zeta potential was measured from a 1 wt% nanoparticle dispersion in a DTS 1070 zetacell. These two measurements were carried out with unfiltered particles.

The coverage of GLYMO molecules on the silica surface was quantified in a Mettler Thermogravimetric Analyzer TGA/DSC 1 using thermogravimetric analysis (TGA). Similar to previous studies [28,81], samples of filtered GLYMO-NP were placed in an alumina crucible and dried overnight in an oven at 80 °C to remove water with the goal of leaving 5 mg of dry sample. TGA measurements were performed by ramping temperature from 30 °C to 110 °C at a rate of 10 °C/min, holding at 110 °C for 20 min to remove residual water, and then ramping up to 800 °C. The percent of organic mass, an indicator of how much GLYMO attached to the silica nanoparticles, was taken as the fraction of mass lost ramping temperature from 110 °C to 800 °C.

3.2.4 Emulsion generation

Oil-in-water emulsions were prepared by combining 20 mL of n-decane with 20 mL of aqueous nanoparticle dispersion in a 50 mL glass beaker. The filtered GLYMO-NP dispersions were diluted in either DI or brine to reach a desired nanoparticle concentration ranging from 0.1 wt% to 7 wt%, depending on the experiment. We formulated brine based on the ions and ionic ratios specified by the American Petroleum Institute [138] (i.e., “API brine”). Our “5API brine” (containing 5 wt% total dissolved solids, rather than the traditional 10 wt%) was prepared by mixing NaCl and CaCl₂ at a four-to-one mass ratio with DI, such that nanoparticles were ultimately dispersed in a 4 wt% NaCl, 1 wt% CaCl₂ aqueous phase. We refer to GLYMO-NP emulsions in DI and in 5API brine as GLYMO-NP-DI and GLYMO-NP-5API emulsions, respectively. The mixtures were emulsified via sonication in a 30W Branson Digital Tip Sonifier using a 5 mm microtip. The sonifier was

set to 50% amplitude with the tip positioned at the oil-water interface and run for 10 s. The mixture was then stirred and the process was repeated two more times, by which point each sample had fully emulsified.

3.2.5 Centrifugation

30 g of emulsion was added to a Falcon 50 mL Polypropylene Conical Tube. The tube was centrifuged in an Eppendorf 5810R Centrifuge at 5000 g of acceleration for 15 min, matching parameters from previous work [105]. Centrifugation caused three phases to form in the tube: a top phase of released decane, a middle phase of concentrated emulsion, and a bottom aqueous phase. For strong emulsions, the top and bottom phases could be negligible or absent; similarly, weak emulsions exhibited only a trace emulsion phase in the middle. Released decane from centrifugation was quickly separated from the top of each sample with a pipette and the mass difference was measured on a scale to determine the extent of coalescence.

3.2.6 Microscope imaging and droplet size calculation

Emulsions were imaged using a Nikon Labophot-Pol microscope and Nikon Digital Sight DS-Fil camera. 40 μL of emulsion, diluted in the appropriate solution (brine or DI), was placed onto a microscope slide under a cover slip. Microscope images were taken at scales of 40x, 10x, and 4x zoom and analyzed by ImageJ to calculate droplet areas. Droplet diameters were determined from the dataset of droplet areas by calculating the geometry of the droplets and accounting for a cover slide height of 50 μm (most droplets had a diameter of below 50 μm and were therefore assumed to be spherical). Emulsion droplet sizes were reported as the Sauter diameter, D_{32} , which is a volume-weighted measure of average droplet size:

$$D_{32} = \frac{\sum_i^n D_i^3}{\sum_i^n D_i^2}, \quad (3.2)$$

where D_i refers to the diameter of the i th droplet in a set of n total droplets.

3.3 RESULTS AND DISCUSSION

3.3.1 Nanoparticle characterization

We characterized the GLYMO-NP and compared them to bare NexSil 6 particles to verify the extent of the grafting reaction. With DLS, we measured the z-average particle diameter, number-average diameter, and zeta potential. With TGA, we measured the organic fraction and calculated a surface coverage fraction and nanoparticle mass. Surface tension was measured with the pendant-drop method. These properties are reported in Table 3.1.

	Bare NexSil 6	GLYMO-NP
Z average diameter (nm)	16.31	15.19
Number average diameter (nm)	4.65	6.44
Polydispersity Index	0.218	0.466
Zeta Potential (mV)	-46±6	-43±6
Organic fraction removed by TGA (f_o)	0.024	0.145
Surface coverage fraction of GLYMO (φ)	0.00	0.33
Estimated mass of single particle (g)	2.5×10^{-19}	3.0×10^{-19}
Surface tension of 1 wt% filtered particle dispersion (mN/m)	n/a	69.22 ± 0.17

Table 3.1: GLYMO-nanoparticle parameters measured with DLS and TGA.

The coverage fraction from TGA was calculated by the following equation, modified from Worthen, et al [28]:

$$\varphi_l = \frac{f_o - f_{o,np}}{(1 - f_o - f_i + f_{o,np})S_A M_{TGA} N_{SiOH}} \quad (3.3)$$

In Eq. (3.3), φ_l refers to the surface coverage of ligand as a dimensionless fraction ranging from 0 (no coverage) to 1 (full coverage). S_A is the specific surface area of the nanoparticle core (445 m²/g for NexSil 6), M_{TGA} is the molecular weight GLYMO removeable by TGA (133.17 g/mol) [28], and N_{SiOH} is the density of silanol sites available for GLYMO grafting at the silica surface (assumed to be 4.6 sites / nm²) [89]. The values f_o , f_i , and $f_{o,np}$ represent different mass fractions of the particle relevant to TGA. The organic fraction of the particle, f_o , is the fraction of the particle mass that is removed at high temperatures during TGA. The organic fraction of the original nanoparticle core, $f_{o,np}$, is the same measurement for bare silica, and is subtracted from f_o to control for mass loss at the bare silica surface during TGA. The inorganic fraction, f_i , is the mass of GLYMO added to the NexSil 6 particle but not removed by TGA.

The calculated surface coverage, 0.33, is consistent with values of 0.38 and 0.35 reported by Worthen, et al. [28], and 0.32 reported by Griffith and Daigle [81] for NexSil 6 particles coated with GLYMO by similar processes. These characterizations altogether were good indicators that GLYMO had successfully grafted to the silica surface.

We finally measured the surface tension of a 1 wt% GLYMO-NP dispersion in deionized water with the pendant drop method to verify the success of particle filtration. The measured value of 69.22 ± 0.17 mN/m was only slightly less than that of pure water (72 mN/m). We further demonstrate successful filtration by comparing centrifugation experiments of unfiltered and filtered particles in Fig. 3.4.

3.3.2 Evaluation of nanoparticle interactions with extended DLVO theory

We can further characterize the properties and interactions of GLYMO-NP using extended DLVO theory [28,29,110]. The original DLVO theory, named for Derjaguin, Landau, Verwey, and Overbeek [25,26], describes the behavior of dispersed particles subject to van der Waals attraction and electrostatic forces. The potential energy (Φ) from van der Waals attraction between two GLYMO-NP is given by the Derjaguin approximation [90]:

$$\Phi_{wdV}(d) = -\frac{(r+l)(\sqrt{A_m}-\sqrt{A_p})^2}{12d}, \quad (3.4)$$

where r is the particle core radius and l is the ligand length, assumed for GLYMO to be 0.95 nm [139]. A_m and A_p are the Hamaker constants for the continuous phase and the particle, respectively. We used Hamaker constants of 3.7×10^{-20} J for the fluid and 6.3×10^{-20} J for the particles, taken from Worthen et al. [28]. The core-to-core separation distance is given by d . Van der Waals attraction between the particles yields a highly negative interaction energy at short distances that approaches zero as distance increases. We assume that this force is not affected by ionic concentration. Electrostatic repulsion can be approximated by Eq. (3.5) [90]:

$$\Phi_R(d) = 32\pi r \epsilon_o \epsilon_r \left(\frac{k_B T}{e}\right)^2 \tanh^2\left(\frac{e\psi_o}{4k_B T}\right) e^{-\kappa d}, \quad (3.5)$$

where T is temperature (equal to 298 K for room temperature), k_B is Boltzmann's constant, and ψ_o is the surface potential of the particle, assumed to be equal to the zeta potential. ϵ_o and ϵ_r are the permittivity of free space and the relative permittivity of the aqueous phase, respectively. The latter term is given for a NaCl/CaCl₂ mixture in Eq. (3.6), following the approach by Chen and Panagiotopoulos [140]:

$$\begin{aligned} \varepsilon_r = & [\varepsilon_{rw} - 16.2c_{NaCl} + 3.1c_{NaCl}^{2/3}] * \left(1 - \frac{3c_{CaCl2}}{2c_{NaCl} + 3c_{CaCl2}}\right) \\ & + [\varepsilon_{rw} - 11.3c_{CaCl2} + 1.9c_{CaCl2}^{2/3}] \\ & * \left(\frac{3c_{CaCl2}}{2c_{NaCl} + 3c_{CaCl2}}\right) \end{aligned} \quad (3.6)$$

The parameters c_{NaCl} and c_{CaCl2} refer to the molar concentrations of NaCl and CaCl₂, respectively, and ε_{rw} is the relative permittivity of pure water. Altogether, we calculate a relative permittivity of 61.2 for 5API brine. The inverse Debye length, κ , is given by Eq. (3.7) [90]:

$$\kappa = \sqrt{\frac{\sum_i \rho_{\infty,i} e^2 z_i^2}{\varepsilon_o \varepsilon_r k_B T}} \quad (3.7)$$

The inverse Debye length is calculated as a function of the number density of ion species i in the bulk solution, $\rho_{\infty,i}$, the species valency, z_i , and the elementary charge, e (as well as k_B , T , ε_o , and ε_r from before). We assume that DI has an NaCl concentration of 0.01 mM, giving an inverse Debye length of $\kappa = 0.0104 \text{ nm}^{-1}$; 5API brine, in contrast, gives an inverse Debye length of $\kappa = 3.80 \text{ nm}^{-1}$.

By the above equations, electrostatic repulsion is some finite, positive value at a separation distance of zero and decreases with increasing distance. The rate that electrostatic repulsion decays is controlled by the Debye length, which itself depends on ionic concentration. In DI, electrostatic repulsion decays slowly with distance, but in 5API brine, due to ionic screening of electrostatic charges, electrostatic repulsion decays almost immediately. As a result, electrostatic repulsion is significant in DI and assumed to be zero in brine. Extended DLVO theory combines these two forces with steric interactions

between GLYMO molecules at the silica surface [28]. Steric interaction Φ_s is modeled as two components: an osmotic contribution, Φ_o , and an entropic/elastic contribution, Φ_e [91]:

$$\Phi_s = \Phi_o + \Phi_e \quad (3.8)$$

The osmotic component of steric energy is described by Eq. (3.9):

$$\begin{aligned} \Phi_o(d) &= 0 & d \geq 2l \\ \Phi_o(d) &= \frac{4\pi r \varphi^2 (0.5 - \chi)}{v_1} \left[l - \frac{d}{2} \right]^2 & l \leq d < 2l \\ \Phi_o(d) &= \frac{4\pi r \varphi^2 (0.5 - \chi) l^2}{v_1} \left[\frac{d}{2l} - \frac{1}{4} - \ln\left(\frac{d}{l}\right) \right] & d < l \end{aligned} \quad (3.9)$$

Eq. (3.9) is a piecewise function of d , the distance measured from the surface of the nanoparticle core. The domain intervals are defined by the ligand length, l , assumed to be 0.95 nm [139]. φ is the volume coverage fraction of GLYMO at the silica particle surface, χ is the Flory-Huggins interaction parameter, and v_l is the volume of one GLYMO molecule at the surface. Following the work of Worthen et al. [28], we used a Flory-Huggins parameter of 0.1 for our calculations, representing good compatibility between the GLYMO ligands and aqueous phase. The entropic/elastic component of steric energy is calculated by another piecewise function:

$$\Phi_e(d) = 0 \quad d \geq l$$

$$\Phi_e(d) = \frac{2\pi r N_a \phi d^2 \rho_p l^2}{M_w} \left[\frac{d}{l} \ln\left(\frac{d}{4l} \left(3 - \frac{d}{l}\right)^2\right) - 6 \ln\left(\frac{3 - d/l}{2}\right) + 3\left(1 - \frac{d}{l}\right) \right] \quad d < l \quad (3.10)$$

The parameters ρ_p and M_w refer to the density of bulk GLYMO and the molecular weight of GLYMO, respectively. At a separation distance close to zero, the total steric repulsion generates a high interaction energy; this energy decreases with increasing distance and equals zero at a distance of 1.9 nm (equal to twice the estimated length of a GLYMO molecule, at which point two particles are no longer in contact). The steric repulsion does not significantly change with a change in ionic concentration of the aqueous phase. Finally, the total interaction energy Φ_T is calculated by combining the van der Waals, electrostatic, and steric terms:

$$\Phi_T = \Phi_{vdW} + \Phi_R + \Phi_s \quad (3.11)$$

Fig. 3.1 plots the interaction energies in dimensionless thermal units ($E/k_B T$) of GLYMO-NP in 5API brine and GLYMO-NP in DI as a function of separation distance between particle cores.

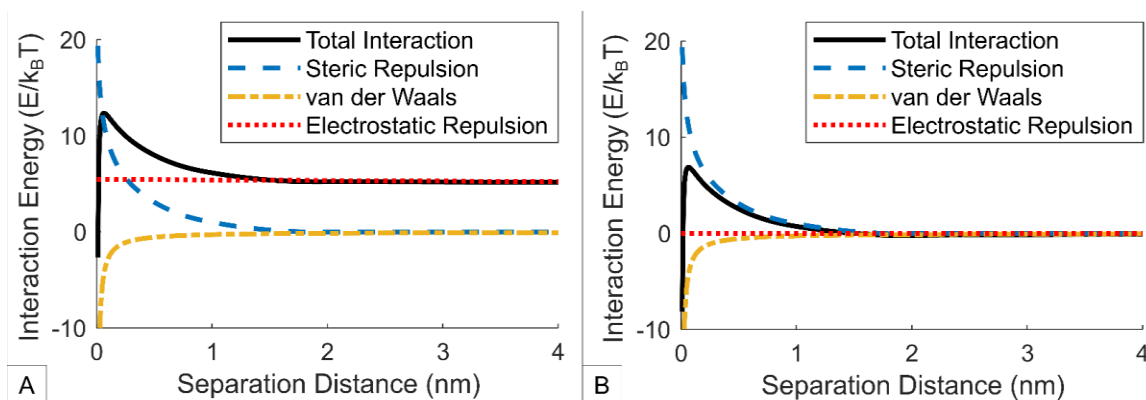


Fig. 3.1. (a) DLVO interactions of GLYMO-NP in DI as a function of core surface to core surface particle separation distance, assuming significant electrostatic repulsion; (b) DLVO interactions of GLYMO-NP in 5API brine as a function of separation distance, where electrostatic repulsion is assumed to be zero.

Fig. 3.1 (a) plots the DLVO interaction energies of GLYMO-NP in DI. These energies are always positive within the domain of interest, suggesting that particles will repel in dispersion. Fig. 3.1 (b) displays the DLVO interaction energies of GLYMO-NP in brine. With electrostatic repulsion absent, the total interaction energy is a sum of the steric and van der Waals forces. Although this energy is strongly negative at near-zero separation distance, the peak observed at approximately 0.1 nm of separation is sufficient to prevent particles from coming into contact and aggregating. Without GLYMO grafted to the surface, these particles would only exhibit van der Waals attraction and therefore be unstable in brine.

3.3.3 Emulsion imaging

To validate our procedure for imaging droplets at different microscope scales and compiling the images into a single D_{32} diameter, we separately generated four 0.25 wt% GLYMO-NP emulsions in 5API brine and independently imaged each batch. A combined histogram of the measured droplet distributions of these four emulsions is plotted in Fig.

3.2, alongside microscope images showing a representative sample of the emulsion at the largest (40x) and smallest (4x) zoom lengths.

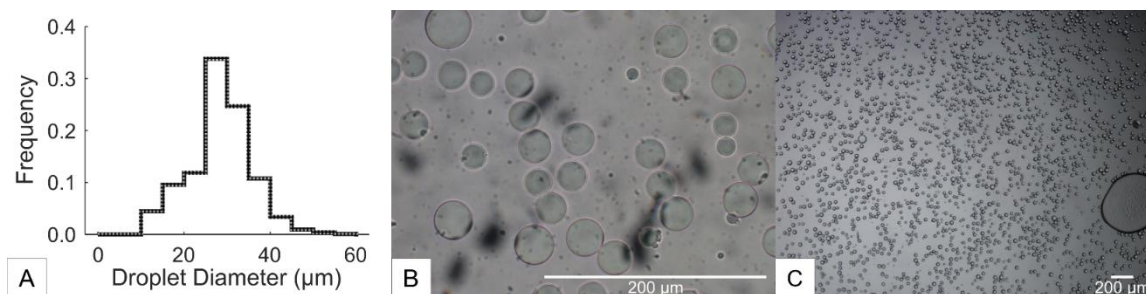


Fig. 3.2. (a) Representative histogram of droplet size distributions of 0.25 wt% GLYMO-NP-5API emulsions. The frequency of droplets at each diameter bin has been normalized to sum to a value of one. Images (b) and (c) show the same 0.25 wt% GLYMO-NP-5API emulsion sample on a microscope slide imaged at 40x and 4x zoom.

The four batches that comprise the histogram in Fig. 3.2 (a) all fell within a similar range. They exhibited D_{32} diameters of 30 ± 4 μm, 31 ± 2 μm, 32 ± 3 μm, and 31 ± 2 μm, respectively. These results help demonstrate the repeatability of the emulsion generation and imaging process.

Two emulsion series were prepared for imaging and centrifugation: GLYMO-NP emulsion in DI and GLYMO-NP emulsion in 5API brine. Each emulsion series contained a wide range of nanoparticle concentrations to observe the effect on emulsion stability and droplet size, and identify any changes between DI and 5API brine. Fig. 3.3 plots the D_{32} diameters of the DI and 5API brine emulsion series in microns against nanoparticle mass concentration on a log-log scale. Error bars are given as a propagated measurement error of ± 1 pixel of droplet diameter for each droplet in the D_{32} calculation.

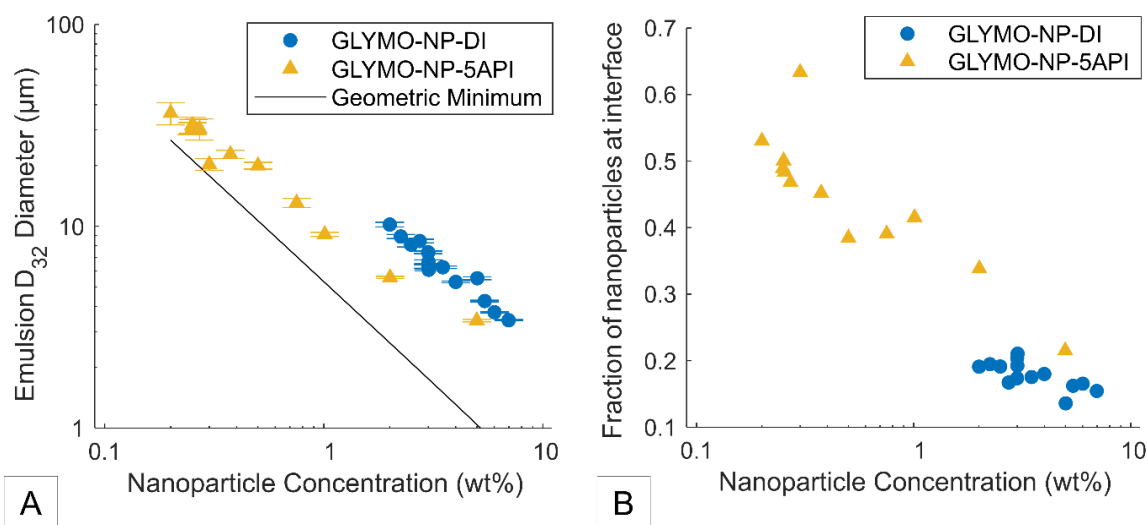


Fig. 3.3. (a) D_{32} diameters of GLYMO-NP-DI and GLYMO-NP-5API emulsions as a function of nanoparticle concentration in the original aqueous phase. The geometric minimum line is an estimate of the smallest possible droplet size given the quantity of nanoparticles available to stabilize an emulsion; (b) Estimated fraction of nanoparticles at the surface of a droplet as a function of nanoparticle mass concentration in the aqueous phase.

GLYMO-NP proved capable of stabilizing smaller, more statically stable emulsion droplets in 5API brine than in DI for the same initial concentration of nanoparticles. As GLYMO-NP concentration increased from 0.2 wt% to 5 wt% in the aqueous phase, the D_{32} diameters of GLYMO-NP-5API emulsions decreased from $36 \pm 5 \mu\text{m}$ to $3.41 \pm 0.05 \mu\text{m}$. A brine emulsion was attempted at 0.1 wt% nanoparticles, but it was not strong enough to remain stable under static conditions. This observation indicates that the critical concentration for stability of GLYMO-NP-5API emulsion lies between 0.1 and 0.2 wt%. GLYMO-NP-DI emulsions generated larger droplets that were only statically stable at higher nanoparticle concentrations. Ranging from 2 wt% to 7 wt% nanoparticle concentration in the aqueous phase, the D_{32} diameters of GLYMO-NP-DI emulsions decreased from $10.2 \pm 0.3 \mu\text{m}$ to $3.42 \pm 0.02 \mu\text{m}$. Another DI emulsion was attempted at 1 wt% nanoparticles, but it too did not remain stable at static conditions, indicating that the

critical concentration for stability of GLYMO-NP-DI emulsion is between 1 and 2 wt%. Holding concentration constant, GLYMO-NP-DI emulsions had 50-80% larger droplet sizes. This difference likely arises from the ability of brine to help particles migrate to the oil-water interface due to electrostatic screening, consequently increasing the total surface area of oil and reducing the droplet diameter. Because larger emulsion droplets are expected to be less stable than equivalent smaller droplets [80,141], it was not surprising that GLYMO-NP-5API emulsion exhibited greater static stability at the same nanoparticle concentration; however, the apparently higher stability of GLYMO-NP-5API emulsion at lower nanoparticle concentrations (when droplet sizes were much higher) suggested a fundamental difference between the two emulsions. We investigated this difference in section 3.3.4 with dynamic centrifugation experiments.

The geometric minimum line representing the minimum droplet diameters expected for a given weight fraction of nanoparticles is plotted in Fig. 3.3 (a). This line corresponds to the droplet size associated with the maximum surface area that the nanoparticles could occupy if every particle in the dispersion was attached to an oil-water interface. For this calculation, we assumed that the particles exhibited hexagonal packing at the interface in a dense monolayer with a diameter of 7.9 nm (the nominal diameter of NexSil 6 plus twice the expected length of a GLYMO molecule). Both the 5API brine and DI series displayed larger droplet diameters than the geometric minimum – an indication that some fraction of the nanoparticles migrated to an interface, but another significant portion remained dispersed in the aqueous phase. This difference was greater at higher nanoparticle concentrations; while the geometric minimum line, by definition, can be fit to an exponential curve with an exponent of -1.0, both the 5API brine and DI curves were best fitted with an exponent of -0.8, suggesting less efficient migration of particles during sonication at higher particle concentrations. Given their smaller diameters at equal

concentration, GLYMO-NP-5API emulsions exhibited more particles at an interface than the GLYMO-NP-DI emulsions, evidence that particles sonicated more efficiently in brine than in DI. Fig. 3.3 (b) plots the estimated fraction of particles at the surface of a droplet as a function of nanoparticle mass concentration, calculated from these results.

The more efficient migration of particles to the interface during sonication in brine can be explained by extended DLVO theory. As seen in Fig. 3.1 (b), GLYMO-NP have sufficiently high total interaction energies at distances up to twice the ligand length to sterically repel other particles and prevent aggregation, despite the absence of electrostatic forces. Beyond the range of steric repulsion, however, the total interaction energy is small and slightly negative. The GLYMO-NP do not repel further than short distances in brine and may even loosely pack together. During sonication, these particles may form dense monolayers at the oil-water interface more easily. Because they migrate to the interface more efficiently, a greater fraction of particles ends up situated at a droplet surface after sonication. The particles stabilize a higher surface area of a finite volume of decane, resulting in smaller droplets. GLYMO-NP form dense monolayers less easily when migrating to an interface in DI. Due to the presence of electrostatic repulsion, as plotted in Fig. 3.1 (a), particles require more energy to approach and pack together at the surface. This tendency prevents as many nanoparticles from situating at a droplet surface after sonication, resulting in less surface area of decane stabilized and consequently larger droplets. The deviation from the minimum lines at higher nanoparticle concentrations in both DI and 5API brine indicated even less efficient sonication as more particles are added to dispersion.

3.3.4 Centrifugation

To measure the dynamic stability of each emulsion, a centrifuge was used to apply a constant acceleration of 5000 g for 15 min to an emulsion to quantify the effect of dynamic force on emulsion coalescence. Following centrifugation, each emulsion separated into three distinct phases. The bottommost layer was an aqueous phase, containing either DI or brine with no decane droplets. This phase likely also contained some number of dispersed nanoparticles, unattached to an oil-water interface. The central layer was a dense, highly-creamed emulsion phase, consisting of multiple decane droplets surrounded by a thin film of the continuous phase (either DI or brine). This central layer was sampled for microscope imaging before and after centrifugation to determine the average droplet size. The uppermost layer was an oleic phase, containing decane released by droplet coalescence events. The volume of this uppermost phase was extracted and measured to determine the fraction of emulsion coalesced, a proxy for emulsion stability. In the case that the emulsion had almost entirely coalesced with only trace amounts of the central layer remaining, the volume fraction was reported as 1. If the uppermost layer was too small to extract with a pipette, the volume fraction was reported as 0.

We first examined the centrifugation behavior of unfiltered GLYMO-NP-DI and GLYMO-NP-5API emulsions to contrast their behavior and to demonstrate the successful filtration of our filtered particles. Fig. 3.4 displays the volume fraction of oil released during centrifugation against nanoparticle concentration for emulsions generated with unfiltered particles, as well as emulsions generated from the filtrate of filtered particles.

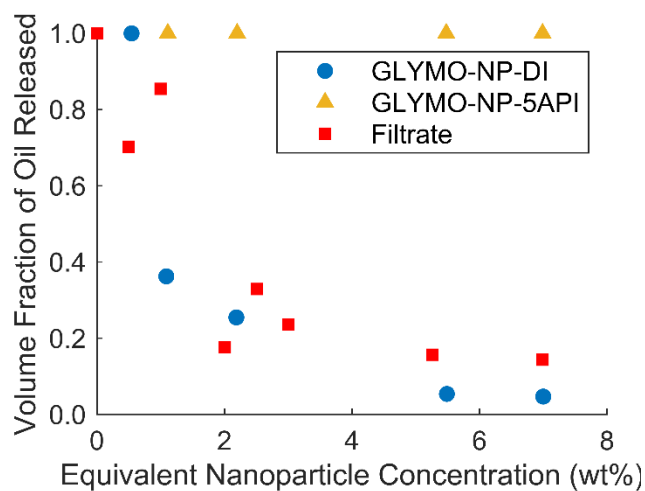


Fig. 3.4. Volume fraction of oil released during centrifugation for unfiltered GLYMO-NP-DI and GLYMO-NP-5API emulsions as a function of nanoparticle mass concentration. The filtrate concentration is converted into an equivalent nanoparticle concentration for comparative purposes.

We assumed that the filtrate had the same chemical composition of the aqueous phase of unfiltered particles. Using the unfiltered GLYMO-NP stock as a basis, we converted this chemical composition into an equivalent nanoparticle mass concentration (essentially, the quantity of unfiltered aqueous phase associated with a given quantity of GLYMO-NP). Unfiltered GLYMO-NP-DI emulsion closely tracked the stability behavior of the filtrate-stabilized emulsion, coalescing easily in the centrifuge at low nanoparticle concentrations but quickly demonstrating high stability as nanoparticle concentration increased to 5-7 wt%. Unlike the emulsions with filtered particles that will be presented in Fig. 3.5, unfiltered GLYMO-NP-DI emulsion exhibited a more gradual decline in stability. There was no critical concentration range for the unfiltered emulsion, and even at low nanoparticle concentrations of 1 wt%, the unfiltered GLYMO-NP-DI emulsion still only partially coalesced in the centrifuge (the filtered GLYMO-NP-DI emulsion was not even

statically stable at 1 wt% nanoparticle concentration). On the other hand, unfiltered GLYMO-NP-5API emulsions were completely unstable at even static conditions.

Fig. 3.5 (a) plots the volume fraction of oil released during centrifugation against nanoparticle concentration for filtered GLYMO-NP-DI and GLYMO-NP-5API emulsions. Fig. 3.5 (b) plots the same volume fraction against emulsion D_{32} diameter in microns (similar to Fig. 3.3, error bars are given as ± 1 pixel of measurement error in the individual droplet diameters propagated through the D_{32} diameter calculation). The shaded regions represent uncertainty in the volume fraction of oil released. This uncertainty is equal to two standard deviations of the repeated values of 3 wt% GLYMO-NP-DI emulsion and 0.25 wt% GLYMO-NP-5API emulsion, respectively, and is centered about a linear fit to the data.

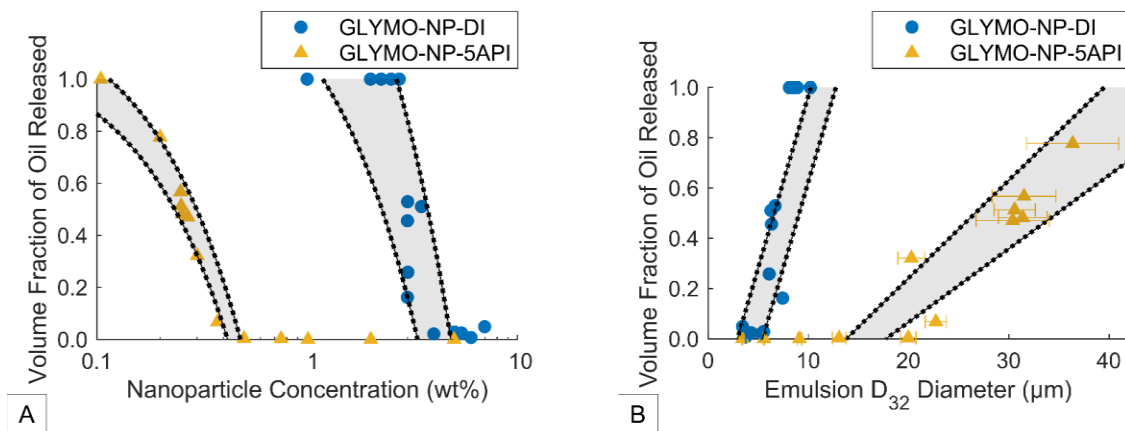


Fig. 3.5. Volume fraction of oil released during centrifugation for filtered GLYMO-NP emulsions in DI and 5API brine as a function of (a) nanoparticle mass concentration on a log scale or (b) emulsion D_{32} diameter in microns. The shaded region represents two standard deviations of uncertainty in the volume fraction of oil released around a linear fit to the data.

Both GLYMO-NP-DI and GLYMO-NP-5API emulsions followed a similar trend, releasing a high volume fraction of decane at low nanoparticle mass concentrations, showing an increase of stability across a critical concentration range, and releasing almost no decane at sufficiently high concentrations. Much of the transition between instability and stability for GLYMO-NP-5API emulsions occurred between 0.2 wt% and 0.375 wt% nanoparticles. A similar transition between 2.75 wt% and 4 wt% nanoparticles was observed for GLYMO-NP-DI emulsions. Approximately 12 times more nanoparticles were required to stabilize the emulsions in DI than in 5API brine. GLYMO-NP-5API emulsion also produced a smoother stability curve with less scatter, indicating a more repeatable stability mechanism.

Because droplet diameter is understood to influence the stability of emulsions [80,141], comparing nanoparticle concentrations directly does not give a complete picture of the difference in emulsion stability. Fig. 3.5 (b) plots the same volume fraction data from Fig. 3.5 (a) as a function of droplet size to account for this difference. The shaded regions again represent two standard deviations of uncertainty in the volume fraction of oil released, centered around a linear fit to the data. Controlling for droplet size, the GLYMO-NP-DI emulsions still coalesced more easily in the centrifuge. The DI emulsions transitioned from stable to unstable at a D_{32} diameter range of 4.3 ± 0.5 times lower than the GLYMO-NP-5API emulsions. Notably, the process of centrifugation did not significantly affect the measured D_{32} diameter for any emulsion. No emulsions exhibited a significant change in D_{32} diameter measured before or after centrifugation. This finding suggests that – after some initial coalesce – droplets coalesced with the bulk separated decane at the top of the centrifuge vial, rather than with other droplets. This outcome is reasonable for a centrifuge system because the compressive force is strongest at the top of the vial.

The observation that emulsion droplets are more stable to coalescence in brine than in DI, together with extended DLVO theory, supports the formation of the particle networks described in literature. As shown in Fig. 3.1 (b), with sufficiently high ionic concentrations in brine screening electrostatic forces, unattached particles in the aqueous phase are slightly attracted by van der Waals forces outside of the range of steric repulsion. These particles interact and form aggregate networks between the emulsion droplets that likely lead to the increased stability observed from our experiments of emulsions in brine. Particle networks were previously observed in a similar GLYMO-NP-Brine system with cryo-SEM imaging [81]. By freezing the emulsion droplets, the authors were able to capture images of white threads (representing dense nanoparticle connections) connecting their emulsion droplets. This process is illustrated in Fig. 3.6. Given the catastrophic loss of stability of our GLYMO-NP-5API emulsions with 0.1 wt% nanoparticles under ordinary gravity, these networks likely formed for our 50% decane emulsions at a critical concentration between 0.1 and 0.2 wt% nanoparticles. Interestingly, as observed in Fig. 3.4, the presence of unfiltered GLYMO appeared to completely destabilize these networks.

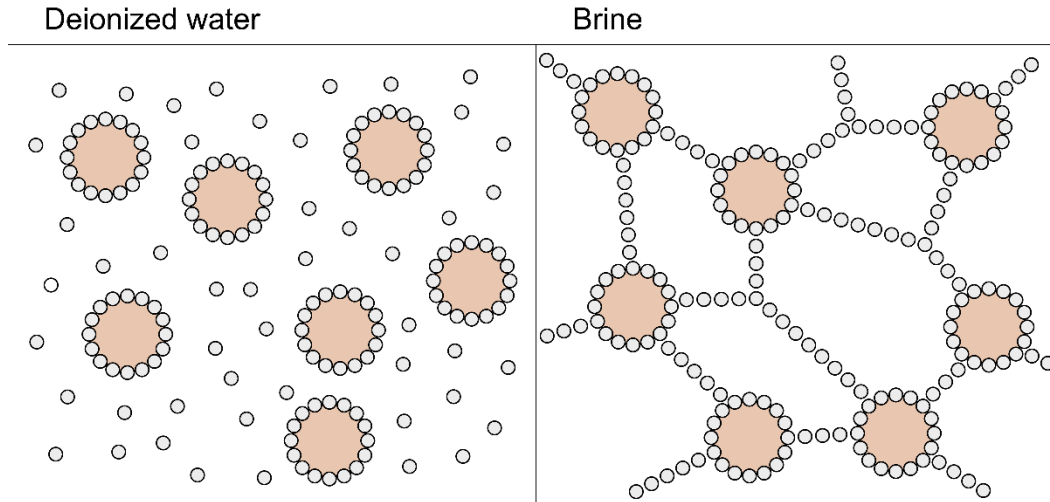


Fig. 3.6. Predicted behavior of nanoparticles dispersed in the continuous phase in a Pickering emulsion. In deionized water, the unattached particles repel and remain dissociated. In brine, the particles attract, forming inter-droplet particle networks.

We can quantify the added stability particle networks contribute to emulsions based on the measured coalescence and D_{32} diameters. GLYMO-NP-DI exhibited a similar stability profile to GLYMO-NP-5API at 4.3 ± 0.5 times smaller D_{32} diameters. Because the orthokinetic rate constant for the coalescence of spherical drops is proportional to the cube of the droplet diameter [80], we calculate that brine-stabilized particle networks reduced the rate constant by a factor of 78 ± 23 , relative to dissociated particles in deionized water. In contrast to other work that examines the presence of particle networks [81,119,136,137], this finding provides a direct quantification of the impact of particle networks on the coalescence of Pickering emulsions in response to compressive forces, accounting for changes in droplet diameter.

3.4 CONCLUSIONS

We measured the relative dynamic stability of GLYMO-NP emulsions over a range of controlled conditions. We found that GLYMO-NP in 5API brine generated smaller, more stable emulsions than in DI. By increasing nanoparticle concentration from 0.2 wt% to 5 wt%, we observed D_{32} diameters of brine emulsion droplets decrease from $36\pm 5\ \mu\text{m}$ to $3.41\pm 0.05\ \mu\text{m}$. The D_{32} diameters of DI emulsion droplets decreased from $10.2\pm 0.3\ \mu\text{m}$ to 3.42 ± 0.02 as nanoparticle concentration increased from 2 wt% to 7 wt%. At the overlapping concentration range of 2 wt% to 5 wt%, emulsion droplets in DI and brine exhibited droplet diameters ranging from $10.2\pm 0.3\ \mu\text{m}$ to $5.52\pm 0.02\ \mu\text{m}$ and $5.57\pm 0.07\ \mu\text{m}$ to $3.41\pm 0.05\ \mu\text{m}$, respectively; controlling for nanoparticle concentration, DI emulsion droplets were 50-80% larger than brine emulsion droplets. The brine emulsions exhibited greater stability, matching the coalescence profile of DI emulsions with 12 times more nanoparticles in dispersion. Controlling for the change of droplet size, the brine emulsions demonstrated the same stability as DI emulsions with 4.3 ± 0.5 times smaller diameters. Based on the effect of diameter on the orthokinetic constant, this result suggests that particle networks slowed the rate of coalescence by a factor of 78 ± 23 . These trends were not present in emulsions with unfiltered particles.

These findings help quantify results from past work showing a link between increased salinity and higher emulsion stability [80,105,107,115-117]. We applied centrifugation methods for determining dynamic emulsion stability [105-107] over a wider particle concentration range in both DI and brine, enabling us to quantify clear stability thresholds for DI and brine emulsions that were similar in behavior but an order of magnitude apart in particle concentration. We found that emulsion stability was highly sensitive to particle concentration, and that high-salinity nanoparticle interactions contributed as much to emulsion stability as a twelvefold increase in particle concentration.

We further expanded on droplet diameter observations in past studies [80,105,116,117] with detailed microscopy measurements over a large range of particle concentrations to infer the effect of DLVO interactions on droplet formation and control for effects of droplet size. The smaller droplet diameters of brine emulsions indicated that the nanoparticles packed more closely during sonication, creating tighter layers at the droplet interface. The diameters of both brine and DI emulsions deviated from geometric predictions at higher particle concentrations, suggesting a tradeoff between the number of particles and sonication efficiency. Based on these droplet diameters, we were able to quantify the extra emulsion stability granted by salinity when controlling for these differences. These results highlight the importance of salinity-dependent particle interactions to both emulsion formation and stability, and are relevant to applications in porous media where salinity is often high. To further examine the role of ligands on nanoparticle bridging, future work will investigate the effect of ligand concentration at the nanoparticle surface on particle interactions and emulsion stability.

Chapter 4: Effect of interparticle forces on the stability and droplet diameter of Pickering emulsions stabilized by PEG-coated silica nanoparticles²

4.1 INTRODUCTION

Nanoparticle-stabilized emulsions (i.e., Pickering emulsions) are a particularly stable form of emulsification and are used broadly [4,5,57,87,133,142], including the petroleum industry (in particular, for enhanced oil recovery and aquifer decontamination) [15,16,19,22,23], food science [8,9], biomedicine [6,12], and other fields [13,14]. Nanoparticles stabilize Pickering emulsions by partitioning to the fluid-fluid interface and physically blocking droplet coalescence [134,135]. This mechanism contrasts with more conventional surfactants that stabilize emulsions by reducing interfacial tension between fluids. The position of solid particles at a Pickering interface is favorable because the particle occupies an area that previously separated two immiscible fluids. The change in energy after particle attachment (the attachment energy, ΔE) is expressed as [4]:

$$\Delta E = \pi r^2 \gamma (1 - |\cos(\theta)|)^2, \quad (4.1)$$

where r is the particle radius, γ is the fluid-fluid interfacial tension, and θ is the contact angle between the two fluids at the solid particle surface, measured from the wetting phase. The potential for high attachment energies and consequently high emulsion stability make nanoparticles attractive alternatives or additives to surfactants as emulsifying agents, especially in extreme conditions (high temperature, pressure, and salinity) [97].

The structure and stability of Pickering emulsions appear to be influenced strongly by particle interactions, although the specifics of these effects are unclear. Several studies

² This chapter was published in the *Journal of Colloid and Interface Science* as: Hatchell, D., Song, W., & Daigle, H. (2022). Effect of interparticle forces on the stability and droplet diameter of Pickering emulsions stabilized by PEG-coated silica nanoparticles. *Journal of Colloid and Interface Science*, 626, 824-835.

observed that mild particle aggregation can improve emulsion stability greatly [110-113,143]. This phenomenon is thought to be caused by interparticle networks [81,104,119], a process where interacting particles arrange into rigid three-dimensional networks between emulsion droplets that increase the emulsion's resistance to creaming and coalescence. The specific conditions that lead to interparticle networks and optimal emulsion stability are not fully understood. There is a demand for very stable Pickering emulsions at low particle concentrations, especially in subsurface applications such as enhanced oil recovery and aquifer contamination. Further study of this behavior is needed to develop new approaches that increase emulsion stability.

Building from the original DLVO theory [25,26], interactions of nanoparticles in the bulk (i.e., unattached) and at the droplet interface (i.e., attached) can be described in terms of an extended DLVO theory [27-29]. Under the extended DLVO theory, the total interactions between two particles arise from the van der Waals (i.e., vdW), electrostatic, and steric forces. The vdW force is a short-range attractive force caused by the sum of interactions driven by fluctuations in electron density between nearby atoms within the two particles. Electrostatic forces act to repel particles with electrical charges of the same sign. The steric force is a repulsive force caused by overlapping electron clouds of atoms on particle surfaces when two particles approach. Altogether, the total interaction potential, Φ_T , is equal to the sum of the energies associated with these three forces, given below:

$$\Phi_T = \Phi_{vdW} + \Phi_E + \Phi_S. \quad (4.2)$$

Φ_{vdW} , Φ_E , and Φ_S refer to the vdW, electrostatic, and steric interaction energies, respectively. A small or negative Φ_T between particles is a predictor for particle aggregation; similarly, particles with large, positive Φ_T are expected to be stable.

The effect of electrostatic interactions on emulsion behavior is well documented in the literature. There is substantial experimental evidence that Pickering emulsion stability increases with increasing aqueous phase salinity [80,105,107,115-118,144]. As salinity increases, the electrostatic field is screened by free ions in the aqueous phase, the Debye length decreases, and Φ_E trends towards zero [80]. As a result, particles flocculate more easily and can produce very stable emulsions [144]. This effect is observed in emulsions with oil-water ratios less than 0.5 [105,116,118], although it appears to be most significant at oil-water ratios of 0.5 or higher [80]. The effects of steric and vdW interactions on emulsion behavior, however, are less clear. Raghavan et al. demonstrated that colloidal interactions between dispersed particles are varied with steric effects by replacing Si-OH groups at the particle surface with non-polar alkyl ligands [136]. Others have shown that steric interactions are altered by surface modifications that induce particle aggregation [145], optimize particle targeting [146], and stabilize uncharged surfactant-stabilized emulsion droplets [147]. While vdW attraction is known to cause particle aggregation in the absence of electrostatic and steric repulsion, it is difficult to manipulate vdW forces in a controlled setting. Studies on the effect of particle diameter on emulsion properties show that larger particles lead to larger, less-stable emulsion droplets, holding particle concentration equal [84,99,148]. From the Derjaguin approximation, attractive vdW forces are expected to increase with increasing nanoparticle diameter [90].

This work examines the effects of steric repulsion on the formation and stability of Pickering emulsions. We hypothesize that interparticle networks can be induced by controlling Φ_S , similar to research demonstrating improved emulsion stability in high salinity conditions with low Φ_E , thought to be driven by the formation of interparticle networks. First, to measure the importance of steric forces, we grafted silica nanoparticles with 3-[methoxy(polyethyleneoxy)6-9]propyltrimethoxysilane (PEG-silane) and adjusted

the grafted surface density to manipulate Φ_S (holding Φ_{vdW} and Φ_E constant). Using centrifugation to measure emulsion stability, we discovered and quantified an intermediate grafting density that maximized interparticle networks while preventing excessive particle aggregation. Second, attempting to measure the influence of vdW forces, we generated Pickering emulsions that kept Φ_S constant while varying Φ_E , and investigated if changes in Φ_{vdW} via different particle diameters affect emulsion stability. Finally, we combined all three DLVO interactions into an energy balance model to calculate emulsion droplet diameter, agreeing with our experimental microscopy data. Our results help explain emulsion stability in terms of interparticle DLVO interactions, but show that emulsion droplet diameter is dominated by particle-droplet interactions. Further, we observe large increases in emulsion stability with careful control of Φ_S , introducing a new consideration of particle design to generate stable Pickering emulsions at low particle concentrations.

4.2 MATERIALS AND METHODS

4.2.1 Materials

NexSil 6, 12, and 20 silica nanoparticles (CAS: 7631-86-9; Lot No. 112820, 110178, and 105704; Nyacol) with average diameters of 6, 12, and 20 nm, respectively, were used as the bare nanoparticles for polymer grafting. Here, the particles are referred to by their diameter, with properties given in Table E.1.

The particles are spherical amorphous silica stabilized in a basic aqueous solution. We used 3-[methoxy(polyethyleneoxy)6-9]propyltrimethoxysilane (PEG-silane, CAS: 65994-07-2, >99% purity, Gelest) to graft PEG ligands to the silica surface. n-decane (CAS: 124-18-5, >99% purity, Chevron Phillips) was used as the oil phase in all emulsions. Sodium chloride (NaCl, CAS: 7647-14-5, 99.5% purity, Fischer Scientific), calcium chloride (CaCl₂, CAS: 7440-70-2, 97% purity, Fischer Scientific), and deionized water

(DIW) were used to make 5API brine (4 wt% NaCl, 1 wt% CaCl₂, 95 wt% DIW). DIW was produced from a Barnstead E-Pure Ultrapure Water Purification System at 18.2 MΩ·cm.

4.2.2 Surface modification of silica nanoparticles with PEG-silane to produce PEG-NP

The reaction to graft PEG-silane to the silica surface followed a similar procedure to past work [28,60]. Stock nanoparticle solution containing 2 g of silica was mixed with DIW and PEG-silane in a vial at a combined mass of 20 g (10 wt% silica). The amount of PEG-silane added to the reaction was proportional to the desired PEG grafting density, and is described in more detail in Section 4.3.1. The vial was sealed with PTFE tape and stirred overnight above 65 °C to hydrolyze and condense the PEG-silane to the silica surface.

Following the reaction, the particle dispersion was pipetted into an Amicon Ultra-15 30k MWCO centrifuge filter and washed with DIW eight times for 30 min at 5000 g. The retentate from the final wash was sonicated in DIW to disperse the clean particles. We refer to the final sonicated product as PEG-NP. Three samples from each batch of PEG-NP produced were extracted, weighed, and heated in an oven for 3 hours at 120 °C to remove water and calculate an average nanoparticle mass concentration (wt%) of the entire batch. We used this reaction and filtration procedure to produce 6 nm, 12 nm, and 20 nm particles with various PEG grafting densities.

4.2.3 Measurement of PEG surface density with thermogravimetric analysis (TGA)

PEG grafting density was measured using thermogravimetric analysis (TGA). We followed a method similar to past studies [28,81,144]. A sample of containing 5-10 mg of PEG-NP was dried overnight in an aluminum oxide crucible at 80 °C. The dried sample and crucible were placed in a Mettler Thermogravimetric Analyzer TGA/DSC 1. Under 50

ml/min of nitrogen (N₂, CAS: 7727-37-9, >99.99% purity, Praxair) flow, temperature was increased from 30 °C to 110 °C at a rate of 10 °C/min and held at 110 °C for 20 min to remove any remaining water. Temperature was then increased from 110 °C to 800 °C, and the change in mass was recorded. The organic fraction, f_o , was calculated as the fraction of mass lost during the transition from 110 °C to 800 °C with respect to the mass at the start of the transition. The PEG grafting density, ϕ_l , was calculated from f_o using Eq. (4.3):

$$\phi_l = \frac{f_o - f_{o,np}}{(1 - f_o - f_i + f_{o,np})S_A M_{TGA}}, \quad f_i = \frac{(f_o - f_{o,np})M_{iTGA}}{M_{TGA}}. \quad (4.3)$$

Eq. (4.3) relates f_o with S_A , the specific surface area of the original silica particles, M_{TGA} , the molecular weight of the segment of PEG ligand removed at high temperature (404 g/mol), $f_{o,np}$, the apparent organic fraction measured from unmodified silica nanoparticles, and f_i , the inorganic mass fraction. The final term, f_i , represents mass from the PEG ligands that remain attached to the silica surface. We assume that the average molecular weight of the segment of PEG ligand that remains at high temperature, M_{iTGA} , is 52 g/mol.

4.2.4 Measurement of particle diameter and zeta potential

Particle diameters and zeta (ζ) potentials were measured using a Malvern Zetasizer Nano ZS. A 1 wt% sample of nanoparticles was prepared in either DIW or 5API brine. Particle diameters were measured in Malvern DTS 0012 cuvettes using dynamic light scattering and reported as the Z-average diameter; ζ potentials were measured in a Malvern DTS 1070 zetacell.

4.2.5 Measurement of particle three-phase contact angle

Particle contact angle was measured via the sessile drop method on a spin-coated glass surface. We prepared microscope slides by stirring them overnight with diluted 0.1 N hydrochloric acid (HCl, CAS: 7647-01-0, 12.1 N, Fischer Scientific) on a hot plate set to 70 °C. We further rinsed the surface with isopropanol (C₃H₈O, CAS: 67-63-0, >99.5% purity, MilliporeSigma) and DIW, and air-dried the slides. Once cleaned, we deposited enough 10 wt% aqueous nanoparticle solution to cover the glass surface and spin-coated the slide for 60 s at 1000 rpm (1000 rpm/s acceleration) in a Laurell WS-650-23 spin-coater.

The spin-coated slide was placed in an empty plastic container with flat edges, into which we pipetted decane as the continuous phase. With a pipette tip positioned above the spin-coated surface and below the decane-air interface, a 7.5 µL droplet of DIW or brine was deposited onto the glass and recorded at 7.6 FPS. The first frame of contact between the settled droplet and particle surface was analyzed by running sessile drop calculations in the OneAttension software from Biolin. Multiple measurements were taken for each batch of filtered particles and averaged into one data point for both DIW and brine.

4.2.6 Particle imaging with transmission electron microscopy (TEM)

Transmission electron microscopy (TEM) was carried out with a JEOL NEOARM electron microscope to visualize particle size distribution and morphology. The imaging was performed using aberration-corrected STEM at 80 kV. To prepare the particles for imaging, a 20 µL sample of dilute PEG-NP (0.1 to 1 wt%) was dropped onto a 300-mesh carbon-gold lacey grid. The grid and particles were heated to 100 °C for 30 min before imaging to mitigate carbon contamination. Imaging was conducted for 6, 12, and 20 nm PEG-NP, but not for ungrafted silica, which was unstable and flocculated when dried.

4.2.7 Emulsion generation

Emulsions were produced with tip sonication, following similar procedures to past work [144]. First, we prepared an aqueous dispersion of DIW or 5API brine containing PEG-NP with the desired diameter, PEG grafting density, and mass concentration in the aqueous phase. We then combined 20 mL of the aqueous dispersion with 20 mL of decane in a 50 mL glass beaker. Sonication was performed with a Branson 450 Digital Sonifier. A 5 mm microtip was positioned in the center of the beaker at the aqueous/oleic interface, and the sample was sonicated three times for 10 s at 50% amplitude. The sample was lightly stirred after each 10 s pulse. The final product was a fully emulsified oil-in-water mixture.

4.2.8 Centrifugation

Emulsion stability was evaluated with centrifugation, similar to previous studies [105,144]. 30 g of freshly sonicated emulsion was transferred to a Falcon 50 mL polypropylene conical centrifuge tube. The tube was then centrifuged for 15 min in an Eppendorf 5810R Centrifuge at 5000 g. Centrifuge forces caused the continuous aqueous phase to separate below the emulsion and caused any coalesced decane to separate above the emulsion. The separated decane was extracted with a pipette and the change in emulsion mass was recorded. Emulsion stability was quantified as the volume fraction of decane separated and extracted during this process, with larger volume fractions of decane being released in weaker emulsions, and smaller or negligible volume fractions separating in stronger emulsions.

4.2.9 Optical microscopy and droplet size calculation

To quantify emulsion size distributions, direct measurements were enabled using optical microscopy. Emulsions were diluted in the appropriate aqueous phase (DIW or 5API brine) to aid droplet visibility and pipetted onto a glass microscope slide with a cover

slip. We used an optical microscope (Nikon Labophot-Pol) and Nikon Digital Sight DS-Fil camera to take at least 10 images for each emulsion at resolutions of 0.271 $\mu\text{m}/\text{pixel}$ (40x magnification), 1.08 $\mu\text{m}/\text{pixel}$ (10x magnification), and 2.71 $\mu\text{m}/\text{pixel}$ (4x magnification). Over 3000 images were captured and analyzed in total. We binarized the images in ImageJ and ran a particle analyzer on the oil droplets to obtain a distribution of droplet diameters from each magnification. The droplet diameters were combined into a single distribution, proportional to their coverage on the microscope slide, from which we calculated the Sauter mean diameter, D_{32} , given in Eq. (4.4):

$$D_{32} = \frac{\sum_i^n D_i^3}{\sum_i^n D_i^2}, \quad (4.4)$$

where D_i refers to the diameter of droplet i in a distribution of n droplets. For the purpose of this calculation, the cover slide height was determined by measurement of focal planes to be approximately 50 μm ; larger droplets that were flattened by this restriction were converted by their apparent shape under the microscope into an equivalent sphere from which their diameter, D_i , was obtained.

4.3 RESULTS AND DISCUSSION

We investigated the effect of Φ_S and Φ_{vdW} on emulsion stability by generating two separate sets of nanoparticles. For the first set, we grafted 6 nm silica nanoparticles with varying amounts of PEG-silane. We expect similar Φ_{vdW} for the particles given their constant diameter, and different Φ_S as the PEG concentration increased. For the second set, we varied the Φ_{vdW} while keeping Φ_S constant by grafting equal amounts of PEG-silane to particles with different diameters.

We characterized both sets of PEG-NP, including long-term stability measurements of the first set dispersed in brine (to observe differences in steric stability) and TEM images

of the second set (to observe differences in particle diameter and polydispersity). These results are reported in Sections 4.3.1 and 4.3.2. From these results, we separated our particles into three categories. Type I particles had low concentrations (0-0.5 $\mu\text{mol}/\text{m}^2$) of PEG grafted to the silica surface, low Φ_S , and consequently poor long-term stability in brine, aggregating in under one minute. Type II particles had moderate concentrations (0.5-1.0 $\mu\text{mol}/\text{m}^2$) of surface PEG, intermediate Φ_S , and intermediate long-term stability in brine, with aggregation on timescales ranging from minutes to months. Type III particles had high concentrations (above 1.0 $\mu\text{mol}/\text{m}^2$) of surface PEG, high Φ_S , and excellent long-term stability in brine, likely requiring longer than one year to aggregate. The first set of PEG-NP (variable Φ_S) consisted of all three types; the second set (variable Φ_{vdW}) contained only Type III particles.

In Section 4.3.3, with our first set of PEG-NP, we show that Type II particles produced the most stable emulsions. Type I and III particles produced weak and moderately stable emulsions, respectively. These results are explained by a trade-off between particle aggregation and repulsion. When introduced to 5API brine, Type I particles aggregate and settle at the bottom of the solution on the order of seconds. These aggregates do not disperse during sonication, and as a result do not transfer to the oil-water interface when emulsions are first formed. The resulting Type I emulsions are weak and coalesce quickly. Type III particles, on the other hand, likely do not interact strongly enough to benefit from the increased stability observed in mildly flocculated particles [110-113,143]. Type II particles have enough surface PEG and Φ_S to resist complete aggregation, but slowly aggregate and mildly interact, leading to very strong emulsions. These three particle types are illustrated by Fig. 4.1. The results for the second set of PEG-NP were less conclusive, and we discuss them in Section E.3 of the appendices.

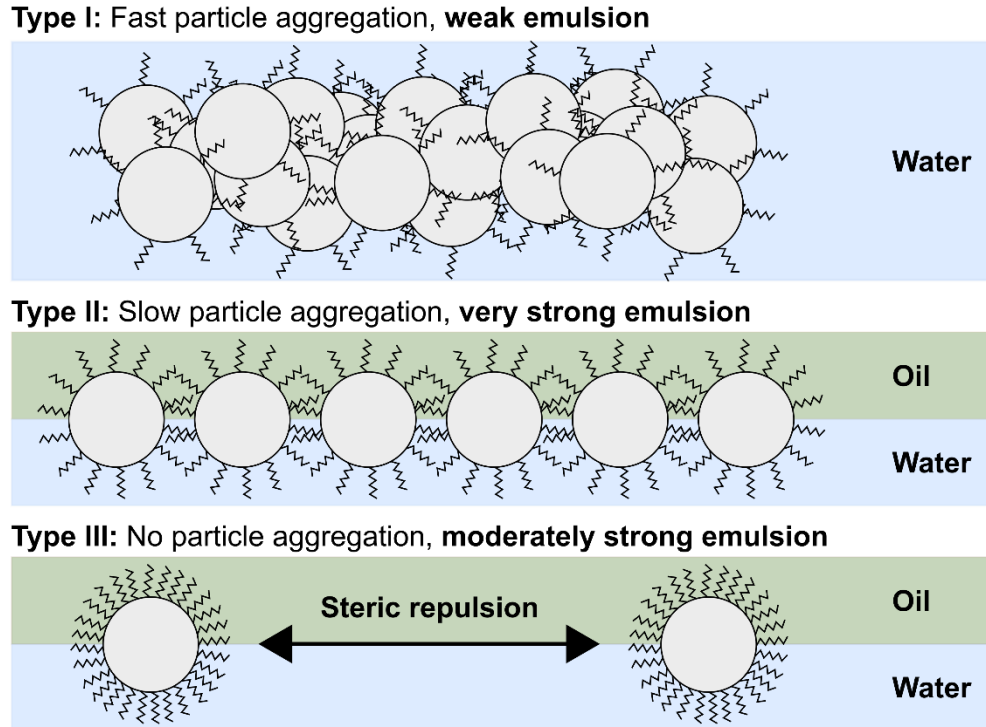


Fig. 4.1. Illustration of the effect of particle type on emulsion stability. Type I, II, and III particles refer to fast (< 1 minute), slow (days to months), and negligible (> 1 year) aggregation rates, respectively. Type I particles interact too strongly and aggregate, leading to weak emulsions. Type II particles mildly flocculate and produce very strong emulsions. Type III particles are stable and brine and produce moderately strong emulsions; however, because they strongly repel each other with steric forces, they do not exhibit flocculation.

In Section 4.3.4, to understand the effect of DLVO interactions on emulsion droplet size, we developed an energy balance model based on DLVO equations to predict droplet diameter. We closely matched our predictions with diameter measurements from microscope images. Using this model, we explain key trends of droplet diameter as a function of particle concentration, particle diameter, and aqueous phase salinity from the perspective of energy balance equations. We show that, by replicating limited coalescence

with an energy balance, emulsion droplet size is controlled by particle-droplet interactions, and not by interparticle forces.

4.3.1 Nanoparticle characterization

We reacted silica nanoparticles in the presence of PEG-silane, ranging from 0.5 to 16 μmol of PEG-silane in the reaction per square meter of particle surface area. Fig. 4.2 plots the TGA-measured PEG grafting density for both sets of particles as a function of PEG-silane added to the reaction [149]. These measurements demonstrate that our reaction conditions are repeatable and capable of small changes in the PEG grafting density, allowing us to precisely control Φ_s . The reaction does not produce a significantly different result at different particle diameters.

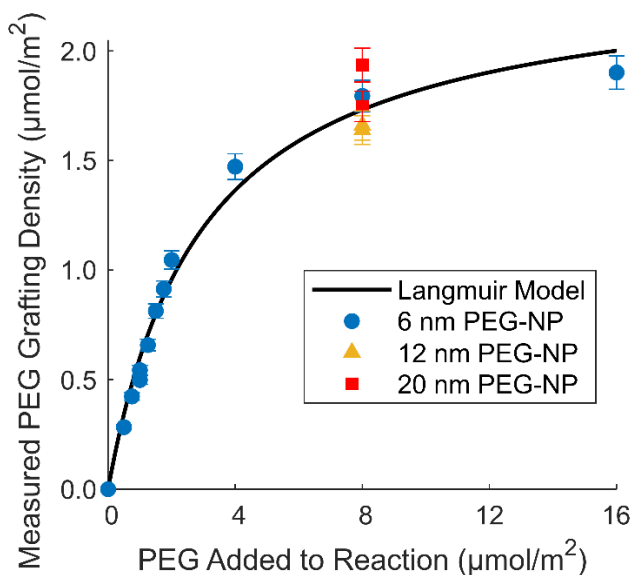


Fig. 4.2. PEG grafting density at the silica surface measured by TGA, plotted as a function of PEG-silane added to the reaction. The black line fits the data to a Langmuir adsorption model with a maximum coverage of $2.37 \mu\text{mol}/\text{m}^2$.

Table E.2 lists the PEG grafting density, Z-average particle diameter, ζ potential, and contact angle for each filtered batch of PEG-NP and stock NexSil particles [149]. The Z-average diameter decreased slightly from the original nanoparticle to the grafted PEG-NP for all particles. This decrease likely resulted from sonication after particle filtration, where aggregated particles were dispersed. Fig. 4.3 plots the (a) ζ potential and (b) three-phase particle-decane-water contact angle of the first set of PEG-NP (6 nm) as a function of the PEG grafting density. We observed a small decrease in the magnitude of ζ potential with increasing PEG grafting density, indicating that neutral PEG ligands replaced negatively charged hydroxyl groups at the silica surface (error bars represent the standard deviation of the zeta potential measurement). The ζ potential does not become positive because there are still several unreacted hydroxyl groups on the silica surface ($7.6 \mu\text{mol}/\text{m}^2$ of surface SiOH sites is often assumed). As described by the interaction potential isotherm, a decrease in the magnitude of ζ potential is associated with reduced hydrophilicity [150]. Correspondingly, as the PEG grafting density increased, we observed an increase in the three-phase contact angle with respect to the aqueous phase for both DIW and brine, indicating reduced hydrophilicity. There was no significant difference between the contact angles measured in DIW or brine. The shaded region represents two standard deviations of uncertainty in the coefficients of linear regression to the combined data.

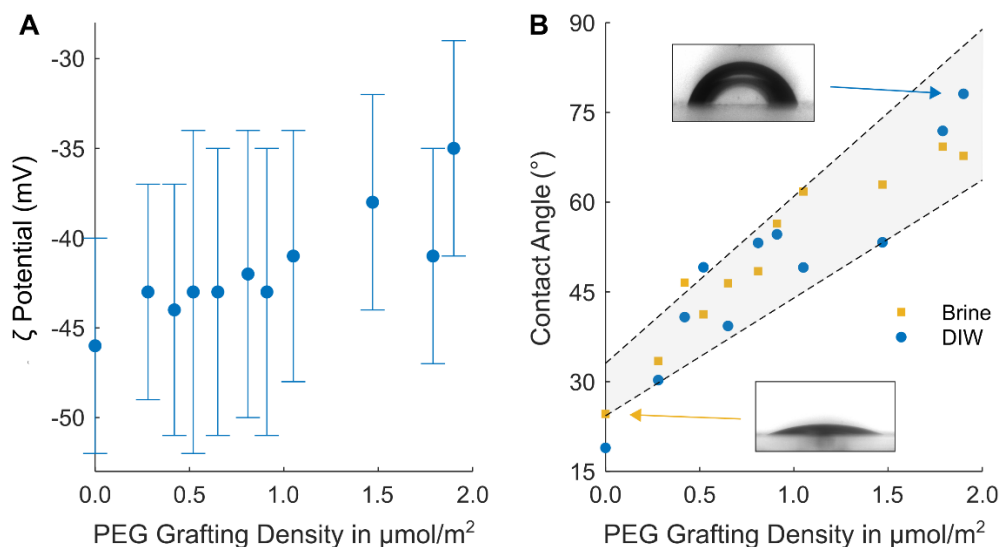


Fig. 4.3. (a) DLS-measured particle ζ potential in DIW as a function of PEG grafting density for 6 nm PEG-NP; (b) Particle-decane-water contact angle with respect to the aqueous phase (both DIW and brine) as a function of PEG grafting density for 6 nm PEG-NP. The two inset images show aqueous droplets on a spin-coated surface submerged in decane. Along with other measurements, they were analyzed with the sessile drop method to calculate the contact angle.

The second set of PEG-NP (constant PEG grafting density of 1.65-1.85 $\mu\text{mol}/\text{m}^2$, varying particle diameter) was analyzed with TEM. Fig. 4.4 displays TEM images of the 6, 12, and 20 nm PEG-coated particles. Each image uses an identical scale for comparison. The particles were monodisperse, with some variance in diameter within each batch but no exceptionally large particles or aggregates present. Particle diameters were approximately consistent with their nominal sizes. These images demonstrate that the particles roughly correspond to spheres with predictable diameters and should be well represented by the extended DLVO equations.

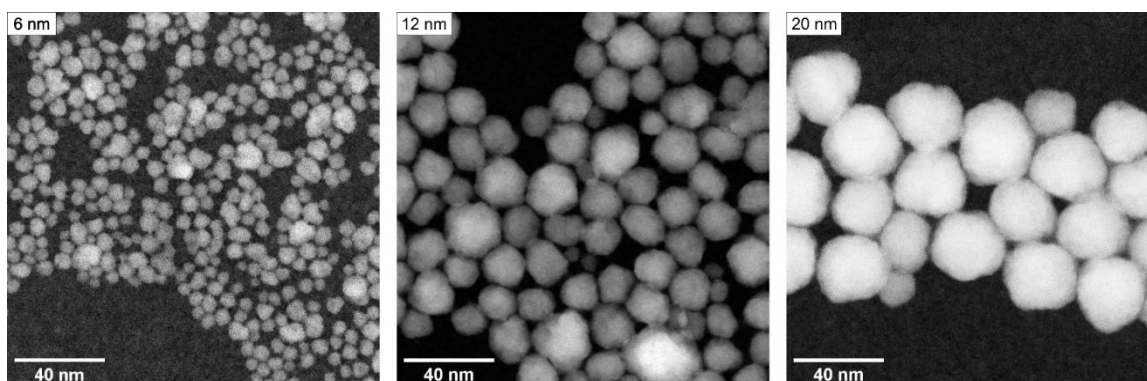


Fig. 4.4. TEM images of 6 nm, 12 nm, and 20 nm particles grafted with approximately $1.75 \mu\text{mol}/\text{m}^2$ PEG surface density. Each image has an identical scale bar of 40 nm.

4.3.2 Effect of PEG grafting density on the long-term stability of nanoparticles in brine

Before using our first set of PEG-NP (6 nm diameter, $0.28 \mu\text{mol}/\text{m}^2$ to $1.90 \mu\text{mol}/\text{m}^2$ PEG grafting density) to study the effect of Φ_S on emulsion behavior, we measured the long-term stability of the particles in 5API brine. We then compared the stabilities to DLVO calculations of the steric interaction to demonstrate that Φ_S was changing significantly with the PEG grafting density.

We mixed 1 wt% particles with 5API brine in a sealed vial and allowed them to sit at room temperature for six weeks, periodically measuring the DLS Z-average diameter of the samples and tracking the growth of particle size over time. Fig. 4.5 (a) plots the particle growth for different PEG grafting densities. The Z-average diameters ranged from 10-20 nm to 10000 nm, the upper limit of our measurement. The error bars for Z-average diameter represent two standard deviations, based on previous repeat measurements of similarly-sized particles. This error is approximately $\pm 10\%$ of diameter for smaller particles and $\pm 40\%$ for larger particles.

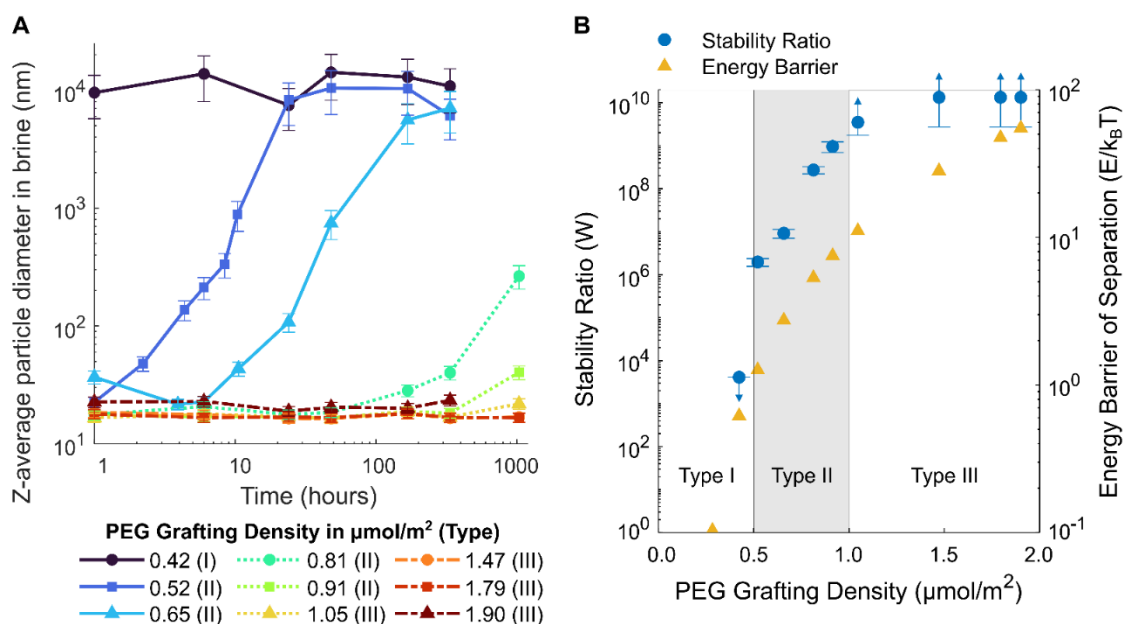


Fig. 4.5. (a) DLS-measured Z-average particle diameter in 5API brine over time, plotted for 6 nm, 0.42-1.90 $\mu\text{mol}/\text{m}^2$ PEG-NP. (b) Experimental stability ratio (W) and theoretical pairwise DLVO interaction potential energy barrier of 6 nm, 0.42-1.90 $\mu\text{mol}/\text{m}^2$ PEG-NP, plotted as a function of PEG grafting density. Arrows indicate that the measurement is limited by the timescale of aggregation, and the true value likely lies in the direction specified. Type I, II, and III particles refer to fast (< 1 minute), slow (days to months), and negligible (> 1 year) aggregation rates, respectively.

Particle stability to aggregation in 5API brine depended on the PEG grafting density. The particles with the smallest amount of PEG ($0.28 \mu\text{mol}/\text{m}^2$ PEG-NP, bare silica) aggregated immediately in brine and were not measured. PEG-NP with $0.42 \mu\text{mol}/\text{m}^2$ PEG grafting density aggregated in less than one minute. As PEG grafting density increased, the timescale of aggregation increased by orders of magnitude, with $0.52 \mu\text{mol}/\text{m}^2$, $0.65 \mu\text{mol}/\text{m}^2$, and $0.81 \mu\text{mol}/\text{m}^2$ PEG-NP respectively taking a day, a week, and several months to aggregate. Above $1 \mu\text{mol}/\text{m}^2$, aggregation was negligible over six weeks.

We calculated a stability ratio, W , to quantify the aggregation rate for each particle, using Eq. (4.5) [151]:

$$W = \frac{4k_B T N_o t_{1/2}}{3\mu}, \quad (4.5)$$

where T is temperature, N_o is the initial number of nanoparticles present, $t_{1/2}$ is the half-life of particle aggregation, and μ is the viscosity of the continuous phase. W describes the random collisions and aggregation of spheres with thermal energy through a viscous medium via the Smoluchowski equation. Because our particles do not aggregate at the same rate, the W term accounts for the longer half-lives caused by PEG molecules at the particle surface. The time for the number of nanoparticles to decrease by half, $t_{1/2}$, is determined by calculating the change in particle volume over time from the Z-average diameter.

Fig. 4.5 (b) plots the stability ratio of each particle as a function of PEG grafting density. Error bars represent the slope error of an exponential fit to particle number versus time when calculating $t_{1/2}$. Below $0.5 \mu\text{mol}/\text{m}^2$ PEG grafting density, particles aggregated too quickly to get an accurate measurement of W ; we refer to the particles that aggregated in less than one minute as “Type I” and plot the upper limit of W (4×10^3) with an arrow indicating the direction of the true value. Between $0.5 \mu\text{mol}/\text{m}^2$ and $1 \mu\text{mol}/\text{m}^2$, particles exhibited aggregation timescales between one day and one year. We measured W values ranging from 2×10^6 to 1×10^9 for these particles with total error bars between $\pm 20\%$ and $\pm 30\%$ of W (large in the absolute sense, but small on a logarithmic scale). We categorized these particles as “Type II”. Above $1 \mu\text{mol}/\text{m}^2$, aggregation occurred too slowly to properly measure; we plot the minimum W (4×10^9) of these “Type III” particles with arrows indicating that the true W is likely far larger. We chose these three categories based on our

ability to measure particle aggregation in brine in a reasonable timescale. Type I particles aggregated so quickly that we could not reliably measure the rate of aggregation. These particles would likely aggregate before emulsion generation, as well. Type III particles aggregated so slowly that we similarly could not measure it – these particles could be considered completely stable for any experiment we performed. The remaining particles – those with measurable aggregation timescales – were grouped into Type II.

Fig. 4.5 (b) also plots the DLVO energy barrier of separation - the difference between DLVO local maximum and local minimum interaction energies (Φ_T) between two identical particles for different separation distances - as a function of PEG grafting density. The calculation of these interaction energy curves is described in Section E.2 and Fig. E.1 in the appendices [90,91,140]. As PEG grafting density increased, steric repulsion increased significantly, resulting in higher Φ_T . The DLVO energy barrier of separation follows the same general trend as the stability ratio, demonstrating that small amounts of PEG added to the particle surface greatly increased both steric repulsion and particle stability to aggregation.

4.3.3 Effect of DLVO interactions on emulsion stability

Using the results from nanoparticle characterization and long-term stability measurements, we verified that our first set of PEG-NP had varying PEG grafting density and Φ_S , while our second set of PEG-NP had different particle diameters, and as a result of the Derjaguin approximation [90], different Φ_{vdW} . With these properties confirmed, we could test the importance of each interaction on emulsion stability.

Our first goal was to use the first set of PEG-NP to determine the effect of Φ_S on emulsion stability. Using PEG grafting densities between $0.42 \mu\text{mol}/\text{m}^2$ and $1.90 \mu\text{mol}/\text{m}^2$, we generated decane-in-water emulsions with our 6 nm particles in 5API brine over a wide

range of particle concentrations. The concentration range was chosen such that emulsions were completely stable to coalescence in the centrifuge on the high end of the range, and completely unstable to coalescence on the low end (with the understanding that increased particle concentration improved emulsion stability to centrifugation). Then, by centrifuging each emulsion across this concentration range, we identified the concentration of nanoparticles required to partially stabilize exactly 50% of the emulsion, and used this midpoint as a point of comparison. The results of this experiment are plotted in Fig. 4.6 (a) and summarized by the midpoint in Fig. 4.6 (b) [149].

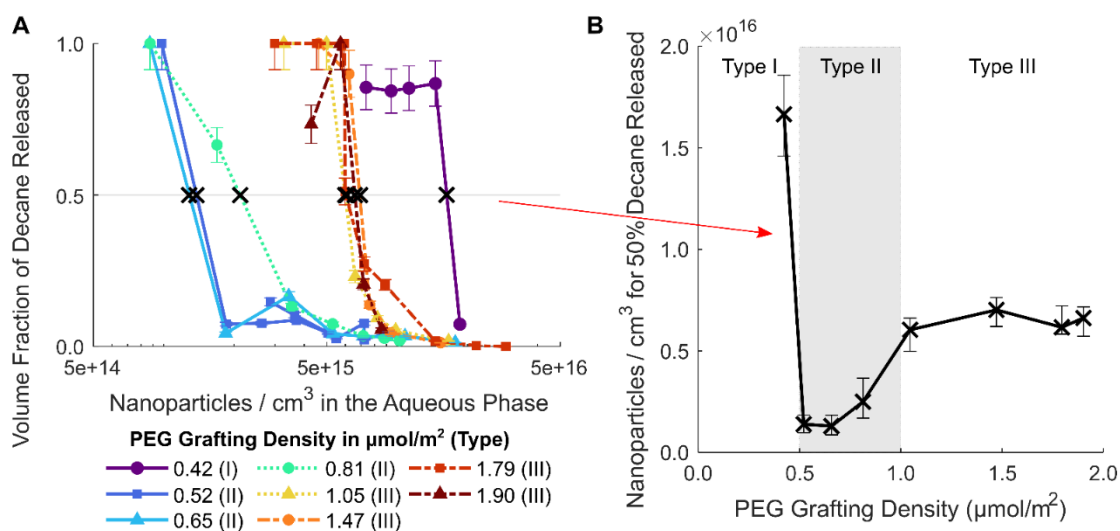


Fig. 4.6. (a) Volume fraction of decane released from decane-in-brine emulsions after centrifugation as a function of nanoparticle number concentration in the aqueous phase, plotted for 6 nm, 0.42-1.90 $\mu\text{mol}/\text{m}^2$ PEG-NP. (b) Nanoparticle number concentration in the aqueous phase required to produce an emulsion that releases 50% of its decane by volume after centrifugation, plotted as a function of PEG grafting density. This plot is constructed from the horizontal line drawn across (a). Type I, II, and III particles refer to fast (< 1 minute), slow (days to months), and negligible (> 1 year, extrapolated from the data) aggregation rates, respectively.

Fig. 4.6 (a) displays stability curves for emulsions from each nanoparticle batch as a function of nanoparticle concentration. “Volume fraction of decane released” refers to the volume fraction of decane that separated out of the emulsion during centrifugation, and is a proxy for emulsion stability: less decane separated from stronger emulsions than from weaker emulsions because there were fewer droplet coalescence events. To account for small amounts of decane evaporating during sonication, if the measured volume fraction of separated decane was above 0.95, the volume fraction was set at 1. Error bars represent two standard deviations in the volume of decane released (approximately $\pm 9\%$), based on previous repeat measurements of comparable emulsions. Nanoparticle concentration refers to the number concentration of particles by volume of the aqueous phase, calculated by dividing the mass of particles in the emulsion by the mass of a single particle (estimated using the volume and density of amorphous silica, as well as the added mass of PEG). We did not produce emulsions from the set of $0.91 \mu\text{mol}/\text{m}^2$ PEG-NP.

Each particle transitioned from an unstable emulsion to a stable emulsion as particle concentration increased. To compare these particles, we took a horizontal slice of the data at 50% volume fraction of decane released and plotted the result in Fig. 4.6 (b), which shows the particle concentration required for 50% stability as a function of PEG grafting density. Error bars in Fig. 4.6 (b) represent the concentration of the nearest emulsions that released more than 60% or less than 40% of decane after centrifugation. The emulsions exhibited an interesting trend: at low PEG grafting densities (Type I particles), the emulsions were weak, with $0.42 \mu\text{mol}/\text{m}^2$ PEG-NP requiring 1.7×10^{16} particles / cm^3 for 50% stability; $0.28 \mu\text{mol}/\text{m}^2$ PEG-NP and bare silica failed to stabilize emulsions in brine at all. At moderate PEG grafting densities (Type II particles), the emulsions were very stable, requiring 1 to 3×10^{15} particles / cm^3 for 50% stability. Particles with higher PEG

grafting densities (Type III particles) were less stable, needing $6-7 \times 10^{15}$ particles / cm^3 to achieve the same stability.

If we only considered the interaction between a particle and the droplet interface, as described by Eq. (4.1), we would expect emulsion stability to increase monotonically with increasing PEG grafting density and consequently increased contact angle (as observed in Fig. 4.3 (b)). However, the trend from Fig. 4.6 (b) is better explained by coupling between steric repulsion and flocculation. Type I particles had low steric repulsion and likely aggregated too quickly in 5API brine to act as effective emulsifiers. As a result, the Type I emulsions were comparatively weaker. Type III particles, on the other hand, strongly resisted aggregation with high steric repulsion. The stability of Type III emulsions was higher than Type I emulsions. Type II emulsions were the strongest of the three; the Type II particles sufficiently resisted aggregation over the timescale required to generate an emulsion, but steric repulsion was low enough to allow for significant interparticle attraction, which is associated with high emulsion stability [110-113,143]. The improved emulsion stability was likely caused by interparticle networks [81,104,119], where electrostatic repulsion is sufficiently screened to allow particles to interact and flocculate partially. These findings are the first known quantification of a particle surface coverage that optimizes emulsion stability via changes in steric repulsion, and present a new approach for optimizing Pickering emulsion stability at low particle concentrations.

Our second goal was to evaluate the effect of Φ_{vdW} on emulsion stability. We repeated similar centrifugation experiments for our second set of PEG-NP, which are described in detail Section E.3 and Fig. E.2. We found that smaller particles required a greater number concentration per volume of aqueous phase to stabilize an emulsion to the same extent as larger particles. We further observed that emulsions in DIW required a greater number concentration of particles to achieve the same stability as emulsions in

5API brine. This finding supports past work suggesting that reduced electrostatic repulsion in 5API brine promotes interparticle networks and increases emulsion stability [144]. Controlling for these two factors, we found that emulsions with 6 nm particles exhibited the smallest improvement in stability (1.5-2.4 times fewer nanoparticles) when switching from DIW to 5API brine, compared to emulsions with 12 nm (2.5-5.6 times fewer nanoparticles) or 20 nm particles (2.7-4.3 times fewer nanoparticles). This smaller improvement in stability with 6 nm particles may be evidence of smaller vdW attraction leading to weaker particle flocculation in brine, although the trend is unclear and needs additional study.

4.3.4 Effect of DLVO forces on droplet diameter

In addition to evaluating emulsion stability, we examined emulsion droplet diameter using microscopy. We took multiple microscope images at different magnifications from each emulsion presented in the previous sections and processed the images into a single representative measure of diameter, the Sauter diameter (D_{32}). Fig. 4.7 (a) through (e) plots D_{32} values as a function of nanoparticle mass concentration for different contexts: (a) varying particle diameter in brine, (b) varying particle diameter in DIW, (c) 6 nm PEG-NP in brine and DIW, (d) 12 nm PEG-NP in brine and DIW, and (e) 20 nm PEG-NP in brine and DIW. The solid and dashed lines are an energy balance model fit to the data, explained below. There was no significant trend in D_{32} for 6 nm particles with varying amounts of PEG grafting density, so those data points were combined into a single “6 nm, brine” curve in Fig. 4.7 (a) and (c). Fig. 4.7 (f), (g), and (h) represent emulsions generated particles with different characteristics (1 wt%, 6 nm, brine, $D_{32} = 9.34 \mu\text{m}$; 1 wt%, 12 nm, DIW, $D_{32} = 45.9 \mu\text{m}$; and 0.185 wt%, 20 nm, brine, $D_{32} = 135 \mu\text{m}$,

respectively). These three emulsions are highlighted to demonstrate the range of particle properties and emulsion diameters observed under the microscope.

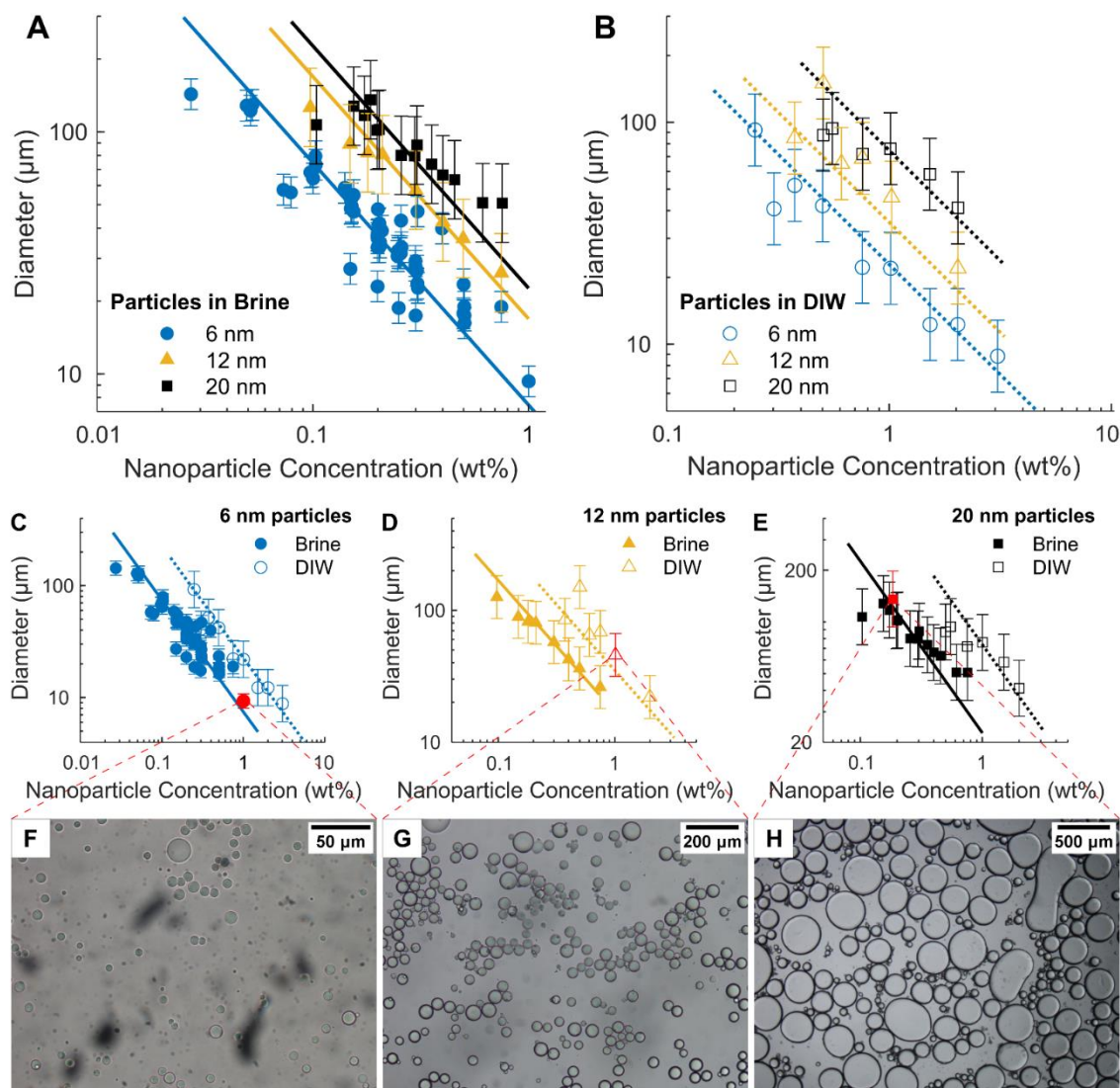


Fig. 4.7. Emulsion D_{32} diameter plotted as a function of nanoparticle concentration (wt%) and presented in the following contexts: (a) all brine emulsions plotted for different particle diameters; (b) all DIW emulsions plotted for different particle diameters; (c) all 6 nm PEG-NP plotted for brine and DIW; (d) all 12 nm PEG-NP plotted for brine and DIW; (e) all 20 nm PEG-NP plotted for brine and DIW. The solid or dashed lines demonstrate the energy balance model fitted to the droplet diameters. Particles with different PEG grafting densities are combined in the above plots where applicable. Images (f), (g), and (h) show microscope images from the emulsions corresponding to the data points indicated in plots (c), (d), and (e). The images are chosen to represent different particle diameters, salinity, and droplet sizes.

A few trends stand out from the D_{32} measurements. Emulsion droplets were larger in DIW than in 5API brine, holding particle diameter and concentration constant. Emulsion droplets also decreased in size with increasing particle concentration, and with decreasing particle diameter. Plots of D_{32} against particle concentration fit reasonably well to linear relations on a log-log scale. These observations agree with previous measurements [144], and are consistent with the particle-poor systems considered by limited coalescence models and experiments [152-154]. In limited coalescence models, the area occupied by an individual densely-packed nanoparticle forming part of an interfacial monolayer is multiplied by the number of particles at the droplet interface. The product is the total droplet surface area, and can be combined with the total volume of the dispersed phase to calculate an average droplet diameter. The number of particles at the droplet interface can range from 0-100% of the total. Salt ions in the aqueous phase act as a “promoter” and increase this percentage by suppressing electrostatic repulsion and assisting the transition of particles from the bulk to the droplet interface [152,153].

To determine the importance of interparticle forces on limited coalescence, we fitted a numerical energy balance model to the data based on DLVO interaction potentials at the oil-water interface. The energy balance model considers a starting condition of small decane droplets dispersed throughout the aqueous phase, analogous to assumptions made in emulsifier-poor limited coalescence models [152-154]. At the starting condition, all nanoparticles reside in the aqueous phase; no particles are present in the decane or at the brine-oil interface. We assume this starting condition is caused by sonication, where the oil phase is broken into a collection of small droplets. Without nanoparticles, these droplets coalesce rapidly (in a few seconds) into a continuous decane phase.

From the starting condition, we assume that a fraction of the particles transition from the aqueous phase to the brine-oil interface, until an energy equilibrium is achieved.

The migration of particles to the interface in our model is governed by five energy terms: (1) vdW attraction between closely packed particles at the interface (Φ_{vdW}^{int}), which favors particle migration; (2) electrostatic repulsion between closely packed particles at the interface (Φ_E^{int}), which hinders particle migration; (3) steric repulsion between closely packed particles at the interface (Φ_S^{int}), which hinders particle migration; (4) reduced oil-water surface energy because of area occupied by the interfacial particle ($\Delta_{int}G$), which favors particle migration; and (5) energy associated with the entropic demixing and arrangement of particles from the aqueous phase to the interface ($\Delta_{demix}G$), which hinders particle migration. The total energy E_{Total} of bringing a particle from the aqueous phase to the interface can be described as the sum of these five terms, using Eq. (4.6):

$$E_{Total} = \Phi_{vdW}^{int} + \Phi_E^{int} + \Phi_S^{int} + \Delta_{int}G + \Delta_{demix}G. \quad (4.6)$$

The derivation of these five energy terms, as well as specific parameters used in our calculations, are described by Eq. (2.8) through Eq. (2.23) in Section 2.4 of the appendices, based primarily on research by Aveyard et al. [92] and other past work [93-95]. In practice, Φ_{vdW}^{int} and Φ_E^{int} are often insignificant in the final summation; E_{total} is typically negative because of the large magnitude of $\Delta_{int}G$, and particles transition to the interface until there are no more particles to attach to the interface ($\Delta_{demix}G$ approaches infinity) or particles can no longer be packed into the surface area available by sonication (Φ_S^{int} approaches infinity). The two cases represent the particle-poor and particle-rich regimes, respectively, of limited coalescence models.

Once the equilibrium distribution between particles at the interface and in the aqueous phase has been determined, we consider the density of particles at the interface of our initial sonication-generated oil droplets. For particle-rich systems, the equilibrium

density of particles at the interface already forms a dense monolayer. In particle-poor systems, we assume that limited coalescence occurs, in which the sparsely-coated droplets coalesce and increase in diameter until the adsorbed particles form a dense monolayer [152-154]. The oil droplet diameter required to pack the equilibrium number of interfacial particles into dense monolayers, D_{model} , is the output of our model. A detailed list summarizing the specific steps involved in our model is presented in Section E.5 of the appendices.

The solid and dashed lines in Fig. 4.7 (a) through (e) display the results of our model fitted to the data, with three fitting parameters: L , the ligand length; AF_{DIW} , the particle attachment fraction in DIW; and AF_{Brine} , the particle attachment fraction in brine. Based on the structure of PEG, L should be less than 4 nm. AF_{DIW} and AF_{Brine} represent the fraction of particles permitted to transition to the droplet interface by the model, and are introduced to explain the differences of DIW and brine emulsions, as described in previous work with the concept of salt “promoters” [152,153]. Particle radii are obtained from DLS measurements. The exact parameters used to generate the model are listed in Table E.3.

We see good agreement between our energy balance model and the data. While the cases of DIW and brine were fitted separately using AF_{DIW} and AF_{Brine} , the differences in droplet diameters predicted by 6 nm, 12 nm, and 20 nm particles arise naturally from the model. Holding the particle concentration constant, larger particles have less available cross-sectional area to form a monolayer, and therefore can only stabilize larger droplets. We find that Φ_{vdW}^{int} and Φ_E^{int} are too small in proportion to $\Delta_{int}G$ to meaningfully affect emulsion droplet size, and can be neglected. As a result, our model simplifies to a geometric limited coalescence model with particle-poor (controlled by $\Delta_{demix}G$) and particle-rich (controlled by Φ_S^{int}) regimes. Given our low particle concentrations, all of our measurements exist inside the particle-poor regime. One consequence of this simplification

is that the model is insensitive to changes in θ , explaining the lack of measurable trend of D_{32} as a function of PEG grafting density for 6 nm PEG-NP. The energy balance model demonstrates that – unlike emulsion stability, which is strongly affected by interparticle forces – droplet diameter appears to be dominated by particle-droplet interactions, with Φ_S^{int} and $\Delta_{demix}G$ functioning only as boundary conditions.

4.4 CONCLUSIONS

We created PEG-coated silica nanoparticles with varying particle diameters and PEG grafting densities. We hypothesized that, in a manner analogous to studies that show improved emulsion stability with increasing salinity by reducing electrostatic repulsion [80,105,107,115-118,144], we could improve emulsion stability by reducing steric repulsion.

By modifying the PEG grafting density of 6 nm nanoparticles, we generated Type I (0 to 0.5 $\mu\text{mol}/\text{m}^2$ PEG), Type II (0.5 to 1 $\mu\text{mol}/\text{m}^2$ PEG), and Type III (1 to 2 $\mu\text{mol}/\text{m}^2$ PEG) particles that aggregated in timescales of less than one minute, from one minute to one year, and several years, respectively. We found that Type II emulsions were the most stable in 5API brine, requiring $1\text{-}3 \times 10^{15}$ particles / cm^3 to achieve 50% stability to centrifugation. Type III emulsions required $6\text{-}7 \times 10^{15}$ particles / cm^3 to achieve the same stability, and were less stable than Type II emulsions, even though Type III particles have higher contact angles and attachment energies. This difference is explained by the reduced steric repulsion and improved interparticle attractions between Type II particles, likely leading to interparticle networks and improved emulsion stability. The relative instability of Type I particles made Type 1 emulsions far less stable or completely unstable with 5API brine. These results are consistent with past research showing that particle flocculation can be controlled by surface modification [136,145], and that particle flocculation can lead to

emulsion stability [110-113,143]. To our knowledge, these findings represent the first quantification of an optimal intermediate surface grafting density that balances particle flocculation with Pickering emulsion stability. These results introduce a new strategy for designing particles to generate stable Pickering emulsions, especially at low particle concentrations. Future work will attempt to reproduce these results on different grafting chemicals to see how the optimal coverage changes as a function of ligand chemistry. We repeated these experiments using particles with different diameters in DIW and 5API brine to isolate the influence of vdW attraction; however, we did not see a conclusive trend of improved emulsion stability at higher particle diameters. More sensitive experiments will be required in the future to determine if increased vdW attraction can improve emulsion stability.

We finally measured droplet diameters of our emulsions and fit them with an energy balance model, achieving a close match to the data. These measurements demonstrate that droplet diameter tends to increase with increasing particle size and decreasing particle concentration, consistent with past work [144]. This work adapts interfacial DLVO equations described by past studies [92-95] to a large experimental dataset, and builds on past limited coalescence models [152-154] by taking the perspective of energy equilibrium. Altogether, these results demonstrate that emulsion stability can be greatly impacted by particle interactions, whereas droplet diameter is unaffected by changes in Φ_{vdW}^{int} and Φ_E^{int} , and is influenced by Φ_S^{int} only as a particle-rich boundary condition. Both conclusions are important for informing particle selection for applications.

Chapter 5: Stable CO₂/water foam stabilized by dilute surface-modified nanoparticles and cationic surfactant at high temperature and salinity

5.1 INTRODUCTION

CO₂ enhanced oil recovery (EOR) and storage are promising technologies to mitigate greenhouse gas emissions. Under appropriate conditions, anthropogenic CO₂ can be injected into geologic formations and sequestered from the carbon cycle, either as a secondary objective of oil production (CO₂-EOR) [35,63], as the primary objective of CO₂ storage [70,71], or as a co-optimization of the two [69]. Future energy scenarios that meet climate goals call for increased carbon storage activity by orders of magnitude this century [72-75], and there is potentially vast storage capacity for CO₂ in geologic formations [76-78]. Successful commercial CO₂-EOR and storage projects date back to the 1970s [65-68].

At reservoir conditions, CO₂ is a supercritical fluid with low viscosity relative to oil and reservoir brine. This viscosity difference results in an unfavorable mobility ratio, M , given by Eq. (5.1):

$$M = \frac{k_{r,CO_2}\mu_{brine}}{k_{r,brine}\mu_{CO_2}}, \quad (5.1)$$

where k_{r,CO_2} and $k_{r,brine}$ are the relative permeabilities and μ_{CO_2} and μ_{brine} are the viscosities of CO₂ and brine, respectively (assuming that brine is the reservoir fluid). A high mobility ratio causes viscous fingering and exacerbates gravity segregation of the CO₂ phase, leading to inefficient sweep of CO₂ throughout the reservoir [35,155-157]. CO₂ has been deployed in the field as a viscous foam to lower M and mitigate these issues [157-159]. Significant research has gone into developing viscous, stable, and economic CO₂ foams for this purpose [160,161]. Foams are gas-in-liquid or supercritical-fluid-in-liquid mixtures, and also have substantial research interest outside of petroleum applications [162-164].

The stability of foams in a reservoir is an important consideration for successful EOR and storage applications because they are thermodynamically metastable [35]. Foams are susceptible to two main destabilization mechanisms: coalescence, involving the rupture and failure of liquid lamellae between gas bubbles; and coarsening, the preferential growth of larger bubbles at the expense of smaller bubbles via Ostwald Ripening [120-122]. There are numerous challenges with deploying stable, viscous CO₂ foams in harsh reservoir conditions, ideally with low material costs. Successful examples are rare in literature [18], but the potential impact of developing such a foam is broad.

Candidates for successful foam systems are evaluated by measuring their stability. Foam stability has been quantified through visual observation [165], by measuring the foam bubble coarsening rate via microscopy [42,166,167], and by measuring the bulk foam half-life [126-128,132,168-170]. The coarsening rate is a useful metric for stable foams that could take weeks or longer to exhibit visual changes. It is defined as dD_{SM}/dt , which is the rate of change with time of the volume-weighted Sauter mean diameter of the foam bubbles (D_{SM} , the sum of bubbles cubed divided by the sum of bubbles squared), often expressed in units of $\mu\text{m}^3/\text{minute}$. Surfactants are traditionally used to stabilize foams by reducing the interfacial tension of the gas-liquid interface [128,167-169]. Nanoparticles (NP) are potentially more effective at stabilizing foams (i.e., Pickering foams) through multiple mechanisms [4,123,171,172]. Solid NP occupy the gas-liquid interface with a large and essentially irreversible attachment energy [4]. The attachment energy depends in part on the NP-brine-CO₂ aqueous contact angle (θ_w), which itself depends on the NP affinity for the CO₂ phase (hydrophilic/CO₂-phillic balance) [171,172]. NP interactions at the interface can increase the interfacial elastic dilational modulus, E' , reducing coalescence by inhibiting lamellae collapse and slowing coarsening via the Gibbs criterion ($E' > \gamma/2$ where γ is the interfacial tension) [42,123]. Systems using both surfactants and

NP are especially promising: surfactants aid in generating foams at low shear rates, and NP contribute to long-term stability [42,126,127,132,165,170].

Several factors must be taken into account when designing CO₂ foams with surfactants and NP, especially at common reservoir conditions of high temperature, pressure, and salinity. High salinity screens electrostatic repulsion between NP and can cause aggregation. Bridging of two silica surfaces with divalent ions such as calcium is particularly destabilizing [18,28,173,174]; this problem can be solved by surface modifying NP with sterically stable ligands [28]. On the other hand, high salinity helps screen the repulsion between NP at and with the CO₂-brine interface, improving NP adsorption [42,172,175]. NP must have enough affinity with the CO₂ phase to transition to the gas-liquid interface and stabilize CO₂ foams. Surfactants and molecules at the NP surface can become insoluble in water at high temperature and salinity [28,35], and must be selected to ensure compatibility at the operating conditions [18]. Finally, the solubility of CO₂ in reservoir brine at high temperature and pressure is much higher than that of N₂ or air, accelerating the coarsening rate [124,125]. As a result, systems proven effective with other gases may not produce stable foams with CO₂.

There are a number of approaches to address these challenges and optimize NP and surfactant selection for foam stability. Studies have examined the effect of NP material [176], NP size [177,178], NP concentration [176,178], surface treatment [165,179], and surfactant adsorption onto NP [127,170]. Chemical surface modification via covalent bonding of ligands to the NP surface is another useful and versatile strategy. Through the silanization reaction [28,42], silanes react easily with a silica surface. Different ligands have been shown to increase colloidal stability by increasing interparticle steric repulsion [28] and increasing the affinity of the NP for the CO₂ phase [171,172]. Past work has demonstrated success grafting two ligands to the same NP to meet these different goals

[42,132,180]. Authors have generated CO₂ foams with like-charged NP-surfactant combinations [18,42], opposite-charged NP-surfactant combinations [42,181,182], non-ionic surfactants [176,183], and zwitterionic surfactants [126,165]. The transition of charged NP and surfactants to the interface is assisted by the screening of electrostatic repulsion. Like-charged systems have the advantage of reduced surfactant adsorption on NP at high surfactant concentrations, and reduced surfactant or NP adsorption to a like-charged reservoir rock surface [180]. Switchable amine surfactants protonate at low pH (dissolved CO₂ reduces pH) and transition from non-ionic to cationic [132,166,180] and may thus be soluble in CO₂ or water.

There has been extensive research in recent years on developing stable foams. “Ultra-stable” foams - with coarsening rates of about 100 μm³/min - have been designed with N₂ at room temperature with an anionic surfactant [184], having coarsening rates of 28 μm³/min at 50°C with cationic surfactant and sulfonated NP [185], and 97 μm³/min at 80°C with anionic surfactant and silica NP modified with ether diol and dimethoxydimethylsilane (DM silane) ligands [42]. In the latter case, Da et al. explained their slow coarsening rate with the Gibbs criterion, measuring an increased elastic dilational modulus of an analogous NP-rich air/brine interface. Unfortunately, differences in chemistry and solubility make N₂ results difficult to translate to CO₂ foams. Stable CO₂ foams have been reported at room temperature [166] (135 μm³/min, diamine surfactant) and at high temperatures in DIW [165] (3.5 day half-life at 65°C and 18 hour half-life at 85°C with fumed silica NP and zwitterionic surfactant); however, most high salinity, high temperature CO₂ foams in literature exhibit half-lives of just a few hours [126-128,132,168-170].

Li et al. [126] reported a CO₂ foam with a half-life of over six hours at 70°C in 10 wt% brine with divalent ions, using unmodified silica NP and zwitterionic surfactant.

Wang et al. [128] generated foam with a half-life of 2 hours at 100 °C in 10 wt% brine with divalent ions, using anionic surfactant without NP. In especially extreme conditions, Eide et al. [129] reported a viscous CO₂ foam at 120°C and 23 wt% brine with divalent ions using silica NP surface-modified with an epoxy silane, although they did not measure the stability. These short half-lives highlight the difficulty of generating stable CO₂ foam systems at high temperature. In 2022, Chen et al. [180] investigated an ultra-stable CO₂ foam at 60°C and 22 wt% brine with divalent ions using a cationic surfactant, RCADA, using silica NP modified with both (3-trimethoxysilylpropyl)diethylenetriamine (N3 silane) and 3-(N,N-dimethylaminopropyl)aminopropylmethyldimethoxy-silane (N2 silane), switchable amines intended to increase colloidal stability and CO₂-affinity, respectively. The most stable foam reported had a coarsening rate as low as 3 μm³/min at 60°C; the same foam exhibited a larger coarsening rate of 408 μm³/min at 80°C. These high stabilities may indicate the development of *in-situ* Janus NP, in which the brine-facing switchable N2 and N3 ligands protonated whereas the CO₂-facing ligands remained nonionic [180,186]. Unfortunately, the Pickering foams reported by Chen et al. did not become more stable at higher RCADA concentration, meaning that the most stable result relied on a high concentration (1 w/v%) of NP (NP are often far more expensive than surfactants, and lower NP concentrations are desirable). Additional research is needed to develop stable CO₂ foams at 80°C and higher for application in high-temperature reservoirs.

The objective of this work is to develop a surfactant-NP system that can generate stable CO₂ Pickering foams at extreme reservoir conditions (80°C, 22 wt% salinity with divalent ions, and 2200 psi). Unlike Chen et al., we emphasized generating stable foam at dilute NP concentration (0.2 w/v%), with the goal of making more economical foams. We planned to achieve this goal by identifying an NP-foam system that benefited from higher

RCADA concentrations. We hypothesized that DM ligands (known wettability modifiers) would be compatible with N3 ligands (salt-tolerant and steric ligands at low pH) at the NP surface and produce stable CO₂ foams with RCADA. First, we verified that DM ligands did not destabilize the N3-coated NP using a combination of zeta potential, amine titration, and hydrodynamic diameter measurements. We then assessed the NP affinity to air and to liquid CO₂ with measurements of θ_w . In a high-pressure, high-temperature foam apparatus, we confirmed satisfactory viscosities ranging from 10-30 cP of CO₂ foams with the N3+DM ligands and RCADA system under various conditions. Finally, we measured long-term foam stabilities in a view cell at 80°C and 2200 psi. We found that the addition of a small amount of DM ligands enabled the NP to reduce foam coarsening, lowering the coarsening rate by up to a factor of ten. 8 $\mu\text{mol}/\text{m}^2$ N3 + 1.5 $\mu\text{mol}/\text{m}^2$ DM (8N3+1.5DM) NP at 1 w/v% concentration with 1 v/v% RCADA had the lowest foam coarsening rate of 900 $\mu\text{m}^3/\text{min}$ (extrapolating to 340 μm foam bubbles at one month), while less-concentrated 0.2 w/v% 8N3+0.5DM NP with 1 v/v% RCADA had a coarsening rate of 2400 $\mu\text{m}^3/\text{min}$ (470 μm at one month). Although not ultra-stable, these foams report 2-4x lower coarsening rates at dilute (0.2 w/v%) NP concentration than Chen et al. [180] at 80°C, which is beneficial for economics. These results show the potential of N3+DM NP and RCADA for generating stable CO₂ foams, and demonstrate the utility of DM ligands as an additive to increase NP affinity to CO₂ while not interfering with colloidal stability.

5.2 MATERIALS AND METHODS

5.2.1 Materials

Aqueous, 6 nm silica NP (NexSil 6, CAS: 7631-86-9, Lot No. 112820, Nyalcol) were used as the basis for ligand grafting. The NexSil 6 NP are spherical, bare silica that come dispersed in water at pH 10 and 18.8 wt% concentration (specific surface area of 445

m²/g). N3 silane (CAS: 35141-30-1, 95% purity, Gelest) and DM silane (CAS: 1112-39-6, 95% purity, Arcos Organics) were used to add N3 and DM ligands to the NP surface to improve colloidal stability and CO₂ affinity, respectively. A cationic surfactant, C₈₋₁₆-NH-(CH₂)₃-N(CH₃)₂ (RCADA, 100% purity) was received as a gift from TotalEnergies SE. Potassium chloride (KCl, CAS: 10035-04-8, ≥99% purity, Fischer Scientific) was used in zeta potential measurements. We diluted hydrochloric acid (HCl, CAS: 7647-01-0, 12 N, Fischer Scientific) and sodium hydroxide (NaOH, CAS: 1310-73-2, ≥97%, Fischer Scientific) to various concentrations for pH control in all experiments. 2-propanol (C₃H₈O, CAS: 67-63-0, >99.5% purity, MilliporeSigma) was used to wash glass before spin-coating. Sodium sulfite (Na₂SO₃, CAS: 7757-83-7, ≥98% purity, Fischer Scientific) was added to the NP/surfactant foam mixture as an oxygen scavenger. Pressurized carbon dioxide (CO₂, CAS: 124-38-9, 99.99% purity, Praxair) was used to generate CO₂ foams. At 80°C and 2200 psi, CO₂ is supercritical with a density of 434 kg/m³ and a viscosity of 0.0325 cP. DIW was generated from a Barnstead Nanopure II. We produced 22 wt% TDS brine (including divalent ions) using a recipe given in Section F.1.1 of the appendices.

5.2.2 Surface modification and preparation of N3-DM NP

The procedure to react silica NP with N3 and DM silanes and generate N3 and DM surface ligands was similar to previous research on silica NP surface-modified by a silanization reaction [42,144,180,187]. The process was performed in three steps: first, we grafted N3 ligands to the silica surface; second, as necessary, we grafted DM ligands to the N3-coated NP; finally, we filtered surface-modified NP to remove ungrafted silanes. We refer to the final filtered NP with the notation 8N3 NP or 8N3+2DM NP, with the numbers (if present) indicating the quantity of silane added to the reaction in units of μmol/m². Full details of the NP grafting and filtration are given in Section F.1.2 of the appendices.

5.2.3 Zeta potential

Zeta potential measurements were performed similar to past work [42,180] with a ZetaPALS (Brookhaven Instruments), using the Smoluchowski model under the ZetaPals mode. NP were dispersed at 0.05 w/v% in 1 mM KCl solution, and were titrated with diluted HCl and NaOH from an initial pH of 5 to a pH range of 2-12. We measured pH with a calibrated Mettler Toledo Seven2Go pH meter S2 with ± 0.01 accuracy. 1.7 mL of titrated NP dispersion was placed in a clear cuvette and measured with an electrode connected to the ZetaPALS instrument. The zeta potential was measured six times on each sample and reported as an average.

5.2.4 Silane titration to measure protonation of amino groups

Silane titration curves were determined by a method similar to previous studies [165,180,188]. Briefly, N3 silane, DM silane, and brine were combined in a three-neck glass flask. The container was then stirred and slowly titrated by adding dilute HCl dropwise through a burette. The pH was measured to determine the concentration of H^+ ions and calculate Θ , the fraction of switchable amine groups protonated for a given pH. Titration curves were measured at room temperature and at 80°C. Specific details of the titration method and calculation of Θ are given in Section F.1.3 of the appendices.

5.2.5 Long-term colloidal stability of N3-DM NP with DLS

NP colloidal stability was measured for up to four weeks at 80°C in a water bath, following the same methods as past studies [44,180]. 0.2-1 w/v% NP were dispersed in pH 4 brine at a desired surfactant concentration, sealed in glass vials with PTFE tap, and placed in a specially-designed metal block to sink the samples to the bottom of the water bath. The water bath was maintained at 80°C, fitted with insulation, and periodically refilled to prevent excessive evaporation. PTFE tape was replaced weekly and no samples

experienced seal failure in the water bath throughout the experiment. At regular intervals, 1 mL was extracted from the samples and analyzed with dynamic light scattering (DLS), running ZetaPALS in the NP sizing mode with the BI-MAS configuration and NNLS model. The volume-average NP diameter was measured as the average of at least two runs.

5.2.6 Three-phase contact angle

We measured DIW-NP-air, brine-NP-air, and brine-NP-CO₂ θ_w by imaging a fluid-fluid interface on a spin-coated glass surface, following a similar method to past work [44,187] with some notable differences. We performed spin-coating on microscope slides using 10 w/v% NP dispersion. Spin-coating was carried out at 1000 rpm (1000 rpm/s) with a Laurell WS-650-23 spin-coater. Droplet images were captured and analyzed with the OneAttension software from Biolin. Given the transient nature of droplets on our spin-coated surface, the first frame of a 76 FPS video after droplet deposition was used for analysis.

We measured θ_w in air and in liquid CO₂. For the latter measurement, we spin-coated a specially-cut glass piece and placed it in a high-pressure vessel, which we filled with 950 psi liquid CO₂. The operation of the pressure vessel was similar to a past studies [189,190]. Droplet deposition was controlled with an ISCO pump. We captured images of the droplet-surface contact through view cells in the high-pressure vessel. A more detailed description of these methods is given in Section F.1.4 of the appendices.

5.2.7 Generation of supercritical CO₂ foam

The apparatus used for generating and studying CO₂ foams is illustrated in Fig. 5.1, modified from Da et al. [42].

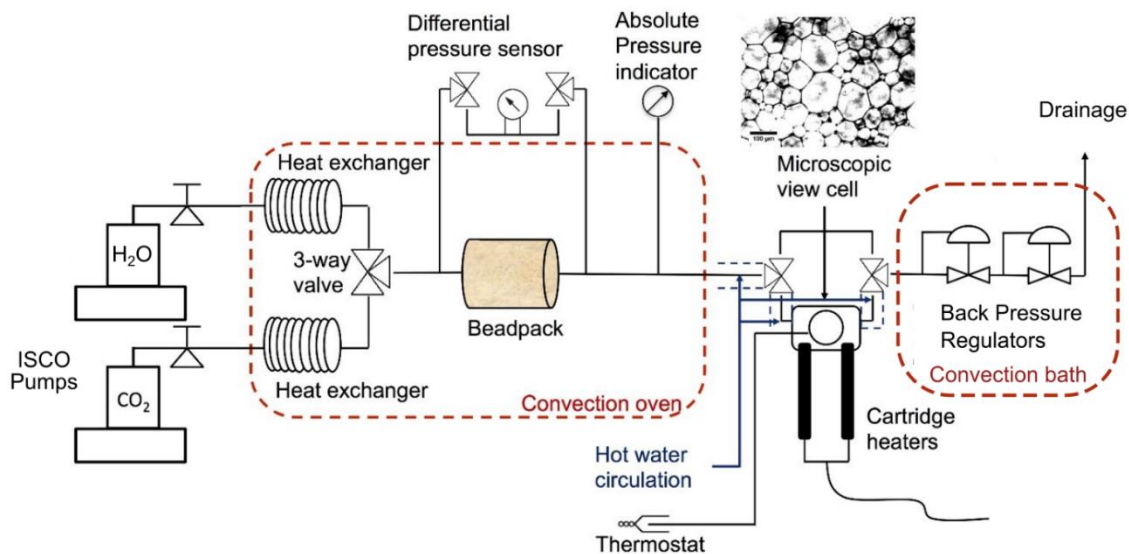


Fig. 5.1. Diagram of the apparatus used to generate and measure supercritical CO₂ foams, modified from Da et al. [42]. The NP and surfactant rich H₂O stream combines with the CO₂ stream in a beadpack, shearing to generate foam. The entire flow path is kept at 80 °C and 2200 psi with four heating systems at different locations and with downstream back pressure regulators operating in series.

Our procedure was also similar to Da et al. and others [42,180]. Briefly, we combined a brine, NP, and RCADA stream with a CO₂ stream in a beadpack, shearing to generate foam. Leaving the beadpack, the foam entered a view cell which could be isolated at high temperature and pressure for long-term stability imaging (described below). The flow lines were maintained at 80°C and 2200 psi with multiple heating elements and back pressure regulators. A notable addition to our procedure from past work was the addition of an 80°C convection bath around the BPRs, which we used to prevent tubing from freezing during CO₂ depressurization. Detailed operation of the foam apparatus is described in Section F.1.5 of the appendices.

5.2.8 Foam apparent viscosity

Following the same procedures as past work [44,180,191], we calculated the apparent viscosity, μ_{app} , from the differential pressure across the beadpack during flow, using Darcy's law:

$$\mu_{app} = \frac{kA}{QL} \Delta p, \quad (5.2)$$

where Q is the volumetric flow rate (1 mL/min), k is the permeability of the beadpack (8.6 darcy), A is the cross-sectional area of the beadpack ($7.31 \times 10^{-2} \text{ cm}^2$), L is the length of the beadpack (10.6 cm), and Δp is the pressure drop across the beadpack. Time-series pressure drop was monitored until an equilibrium was established, indicating fully-developed flow across the beadpack. The beadpack permeability was measured using Eq. (5.2) by flowing DIW through the system. Apparent viscosities were measured for various NP and surfactant concentrations at 70%, 80%, and 90% CO₂ foam qualities. Everything upstream of the back pressure regulators was maintained above 2200 psi during foam generation and apparent viscosity measurements.

5.2.9 Long-term foam stability

Long-term foam stability was measured by the same method as past studies [42,44,122,180,185]. Once isolated in the view cell, foam was observed over time with a Nikon microscope camera. Images were saved every two seconds for the first 30 minutes of foam growth, and every 30 minutes after that. The bubbles in foam images were manually analyzed in Fiji ImageJ [192] to determine the volume-weighted diameter, D_{SM} (the Sauter diameter), given by Eq. (5.3):

$$D_{SM} = \frac{\sum_i^n D_i^3}{\sum_i^n D_i^2}, \quad (5.3)$$

where D_i represents the diameter of the i^{th} foam bubble from a set of n foam bubbles. With the exception of the view cell, cartridge heaters, and hot water circulation, the foam apparatus was shut down, depressurized, and cleaned during long-term foam stability measurements.

The view cell was rigorously tested for leaks multiple times throughout these experiments by submerging it in a room-temperature water bath, filling it with 3000 psi liquid CO₂, and observing for bubbles. No indication of view cell leaks were found during our experiments.

5.3 RESULTS AND DISCUSSION

We investigated 8N3+DM NP and RCADA-surfactant systems as suitable candidates for viscous, stable CO₂ foams in high-temperature, high salinity conditions (80°C, 2200 psi). In Section 5.3.1, we demonstrate successful grafting of both N3 and DM ligands to the silica surface. We further show that the addition of DM does not interfere with the ability of N3 to protonate at low pH and stabilize NP in a high-temperature, high salinity environment. In Section 5.3.2, we show the effect of added DM ligands on the θ_w of N3+DM NP. We find that θ_w increases in the presence of liquid CO₂, and slightly increases following the addition of DM ligands. In Section 5.3.3, we demonstrate that CO₂ foams with N3+DM NP and RCADA-surfactant exhibit a sufficiently high apparent viscosity at a variety of tested conditions. DM ligands do not significantly influence the apparent viscosity. Finally, in Section 5.3.4, we discuss the long-term stability of N3+DM Pickering foams. Foams are stabilized for several days at 80°C, 2200 psi, 22 wt% brine, and low NP concentration with the addition of a small amount of DM ligands. In total, DM

ligands appear to be an excellent NP additive to improve CO₂ foam stability without affecting colloidal stability (a prerequisite for generating stable foams).

5.3.1 Preparation and characterization of N3+DM NP

We generated N3+DM NP with the hope of creating colloidally stable NP that are interfacially active with the CO₂ interface. N3, a switchable amine ligand, protonates at low pH and sterically prevents NP aggregation [132,166,180]. DM ligand, a known wettability modifier [42], was selected to increase NP CO₂-philicity. Together with RCADA, a switchable amine surfactant, our objective was to produce viscous, stable CO₂ foams at harsh conditions (80°C, 2200 psi, and 22 wt% brine with divalent cations).

We used thermogravimetric analysis (TGA) to confirm the presence of surface ligands at the silica surface. We measured an N3 ligand grafting density of 2.0 μmol/m² (25% of the 8 μmol/m² N3 silane used in the reaction) at the silica surface and qualitatively observed the presence of DM ligands, although we could not accurately quantify the surface ligand concentration. These results are discussed in greater detail in Section F.2.1 and Fig. F.1 in the appendices [28,44,144,193].

While N3 ligands are known to give colloidal stability to silica [132,166,180], it was unclear if hydrophobic DM ligands would inhibit NP stability at the reservoir conditions; if the NP were not colloidally stable, they would not produce effective CO₂ foams. Part of the effectiveness of N3 ligands at stabilizing NP comes from its switchable characteristic to protonate at low pH, becoming hydrophilic, salt-tolerant, and solvated to provide steric stabilization [180]. We measured the zeta potential and titration curves of N3 and N3+DM systems at different pH to determine the influence of DM on the charge and protonation of the N3+DM NP. Fig. 5.2 (a) plots the zeta potential of 8N3 and 8N3+2DM NP dispersed in 1 mM KCl at 0.05 w/v% concentration as a function of pH,

and Fig. 5.2 (b) plots the fraction of protonated amino groups, θ , as a function of pH for ungrafted N3 and DM silanes dispersed in brine, both at room temperature and 80 °C. θ was calculated using Eq. (F.1) in the appendices.

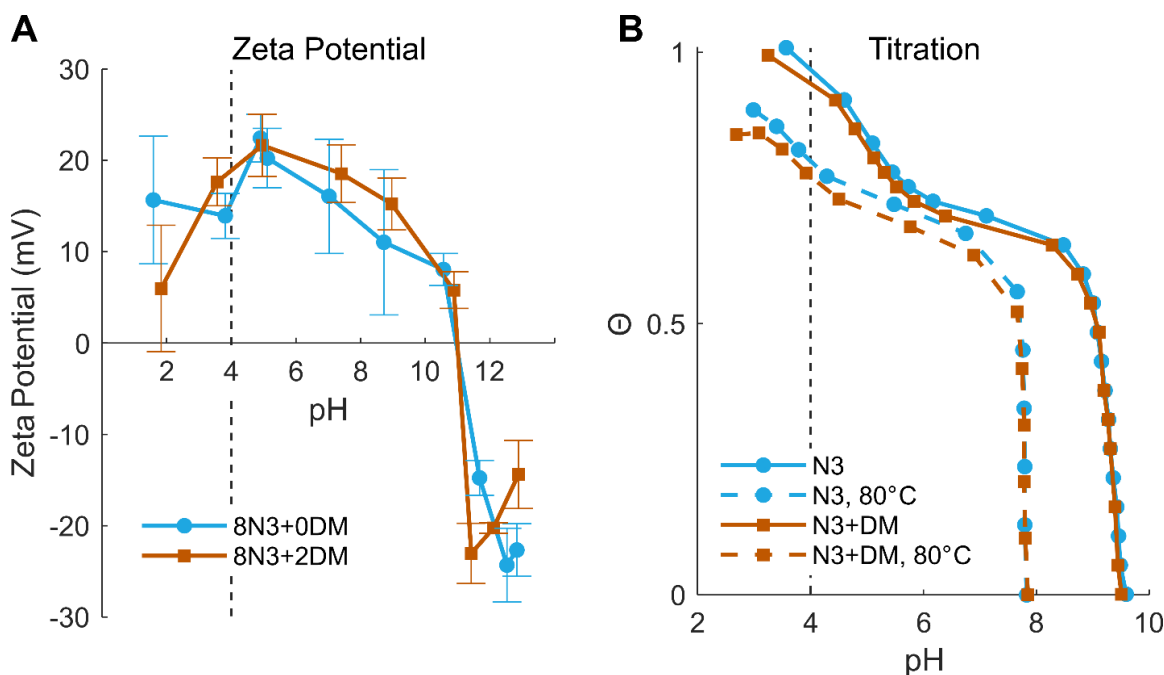


Fig. 5.2. (a) Zeta potential of 8N3+0DM NP and 8N3+2DM NP plotted as a function of pH. NP are dispersed in a 1 mM KCl solution at a NP concentration of 0.05 w/v%. Error bars are twice the standard error of the zeta potential measurement. (b) pH of 0.01 M N3 silane and 0.01 M N3 + 0.01 M DM silane mixtures plotted as a function of pH. The silanes are mixed into 22 wt% brine at their respective molar concentrations. In both plots, the vertical dotted line indicates the operating pH of CO₂ foam.

As seen in Fig. 5.2 (a), the NP zeta potential is positive for most of the pH range. As pH increased, the NP passed through an isoelectric point of approximately pH=11 and transitioned to a negative zeta potential. The zeta potential measurements were consistent with the room-temperature titration curve plotted in Fig. 5.2 (b). Starting near pH 10, the silanes rapidly protonated as they were acidified by dilute HCl. The increase in θ

corresponded to an increase in the NP zeta potential. Protonation required lower pH when measured at 80°C, with titration curves for both silane mixtures shifting leftwards. The vertical dotted lines at pH 4 in both Fig. 5.2 (a) and (b) correspond to the measured pH of our CO₂ foam effluent, and indicate that our operating conditions are acidic given CO₂ dissolved in the aqueous phase at high concentrations. At pH 4, the NP exhibited a high θ , even at 80°C, and a positive zeta potential – good indications that the NP would be colloidally stable. The addition of DM had no measurable effect on the NP charge or protonation, suggesting that DM ligands will not interfere with the switchable behavior of N3 ligands.

We measured the volume-average NP diameter of 8N3+0-2DM NP at a variety of NP and surfactant concentrations using DLS. The NP were dispersed in 22 wt% brine, adjusted to pH 4, sealed in individual vials, and heated to 80°C in a water bath for up to four weeks (a desirable length of time for CO₂ foam deployment in a reservoir). Fig. 5.3 (a) through (c) plots the NP diameters over time at different conditions.

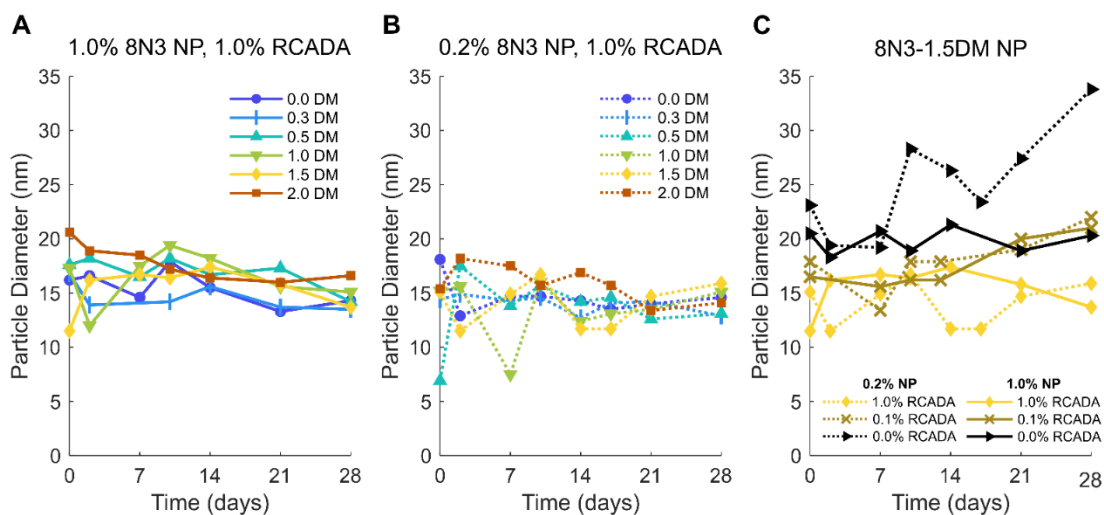


Fig. 5.3. (a) DLS-measured volume-average NP diameters of 1 w/v% 8N3+0-2DM NP, dispersed in 22 wt% brine and 1 v/v% RCADA. (b) DLS-measured volume-average NP diameters of 0.2 w/v% 8N3+0-2DM NP, dispersed in 22 wt% brine and 1 v/v% RCADA. (c) DLS-measured volume-average NP diameters of 0.2-1 w/v% 8N3+1.5DM NP, dispersed in 22 wt% brine and 0-1 v/v% RCADA. All NP are kept at pH 4 and 80 °C for up to four weeks. Only the 0.2 w/v% 8N3+1.5DM, 0 v/v% RCADA NP exhibited significant growth over the measured time.

The 8N3 and 8N3+DM NP were consistently stable in the presence of RCADA, regardless of NP concentration or the concentration of DM ligands. 5.3 (c) displays NP stability over time with different RCADA concentrations. Of all measurements, only the 0.2 w/v% NP + 0 v/v% RCADA series showed any significant NP diameter growth over four weeks, perhaps from the modest loss of hydrophilicity from the added DM ligands relative to Fig. 5.3 (b). Thus, at all but one condition, the addition of DM ligands did not influence the colloidal stability of 8N3 NP, consistent with the data presented in Fig. 5.2 (a) and (b).

5.3.2 Three-phase NP contact angle

Having confirmed that the addition of DM ligands did not negatively affect the NP colloidal stability, our next goal was to measure the impact of DM ligands on the NP affinity for the foam interface. Using a glass surface with spin-coated NP, we measured three-phase θ_w of N3 and N3+DM NP with respect to different fluid-fluid combinations. Fig. 5.4 plots the three-phase θ_w as a function of DM silane added during surface modification for NP at a DIW and air interface, at a 22 wt% brine and air interface, and at a 22 wt% brine and liquid CO₂ interface. The brine used in these measurements was adjusted to pH 4 (the operating condition of the CO₂ foam). Liquid CO₂ was pumped into a high-pressure vessel and maintained at 950 psi to match the density of supercritical CO₂ at reservoir conditions as closely as possible.

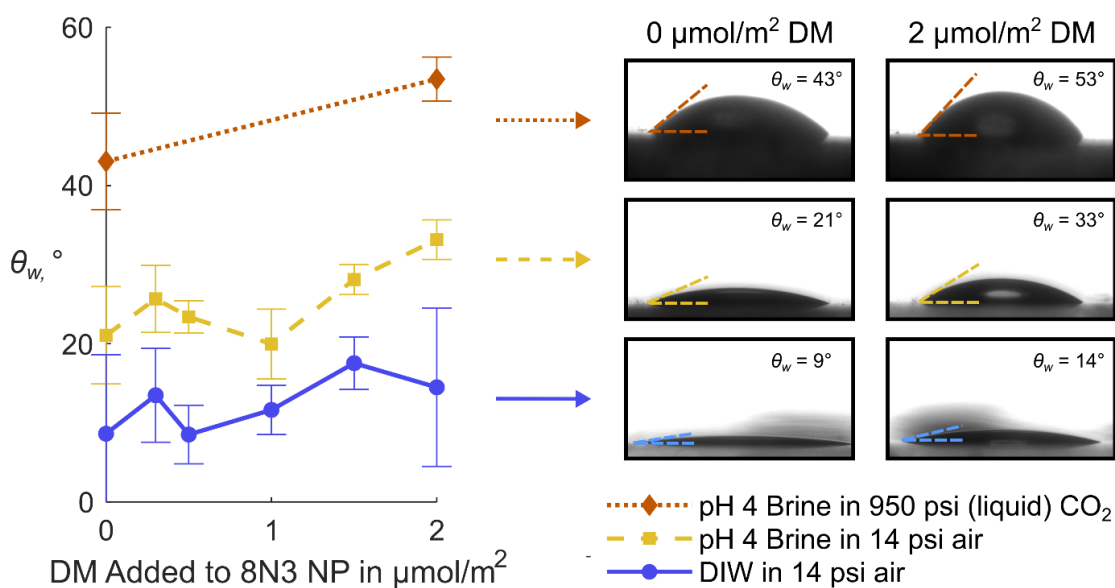


Fig. 5.4. Three-phase θ_w of 8N3 NP at different interfaces, plotted as a function of DM silane added to the NP grafting reaction. Each data point is an average of measurements from three images. The images to the right show examples of droplets that comprise these averages for the minimum ($0 \mu\text{mol}/\text{m}^2$) and maximum ($2 \mu\text{mol}/\text{m}^2$) cases. The annotated colored lines are approximations of θ_w , but the actual values were determined by software calculations.

Two notable trends were observed. Firstly, the NP θ_w increased by an average of 9° from $0 \mu\text{mol}/\text{m}^2$ to $2 \mu\text{mol}/\text{m}^2$ DM silane added to the grafting reaction for all conditions tested. DM ligands are hydrophobic and somewhat CO_2 -philic. This change is significant given the small amount of DM ligands relative to N3. Secondly, θ_w was strongly influenced by the non-wetting phase. Switching from DIW and air to pH 4 brine and air increased the θ_w by an average of 13° , averaged across all DM silane concentrations. These brine measurements were comparable to similar θ_w reported for amine-coated particles in brine. Alzobaidi et al. reported 14° for silica NP coated with quaternary amine in brine [194]; Chen et al. measured 15° for 4N3 NP and 38° for 4N3+4N2 in brine (the latter containing a hydrophobic modifier with dimethyl groups, similar to DM [180]). Moreover, going to

950 psi liquid CO₂ increased the θ_w another 21° for a total 37° increase from DIW to liquid CO₂. The increase of θ_w from DIW-air to brine-air is consistent with previous measurements of air-water-silica and CO₂-water-silica systems [195]. The large increase of θ_w in liquid CO₂ (reaching a maximum of 53°) versus air likely arises from the compatibility of N3 and DM ligands with the CO₂ phase and is promising for generating stable CO₂ foams. Amines exhibit acid-base interactions with CO₂ molecules that contribute some degree of CO₂-philicity [196]. The addition of a small amount of DM ligands further increases θ_w with CO₂, although not proportionally more than with DIW or pH 4 brine. We additionally measured θ_w for pH 4 brine with 1 v/v% RCADA in air. These results had significantly greater variance than without RCADA and are plotted in Fig. F.2 in the appendices.

We used the same high-pressure vessel to observe the dispersity of dried 8N3+2DM NP in condensed CO₂ at up to 4000 psi and 80°C. We did not measure any significant dispersion of particles into the CO₂ phase; our results are detailed in Sections F.1.7 and F.2.3 of the appendices.

5.3.3 Generation and apparent viscosity of supercritical CO₂ foam

We used the 8N3+0-2DM NP with RCADA in 22 wt% brine to generate foams at 80°C and 2200 psi in the foam apparatus illustrated in Fig. 5.1. Fig. 5.5 (a) and (b) plots the apparent viscosity as a function of CO₂ foam quality for 8N3+DM NP at different NP, surfactant, and DM silane concentrations.

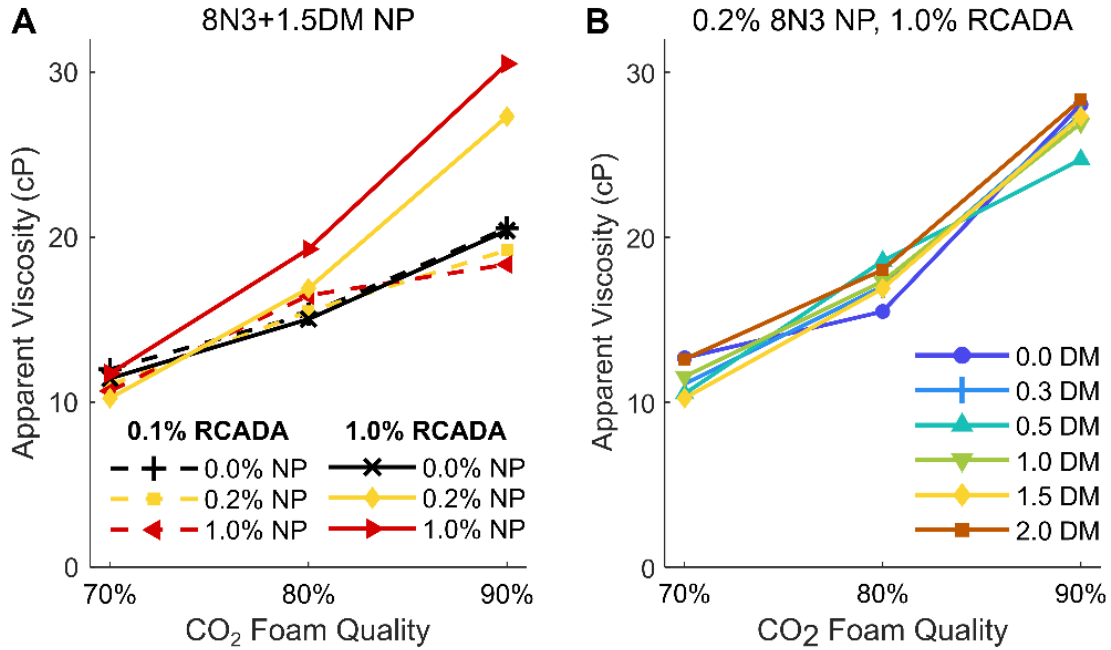


Fig. 5.5. (a) Apparent viscosity of 8N3+1.5DM NP CO₂ foams plotted as a function of CO₂ quality for 0.1-1 v/v% RCADA and 0-1 w/v% NP. (b) Apparent viscosity of 8N3+0-2DM NP CO₂ foams, plotted as a function of CO₂ foam quality with 1 v/v% RCADA and 0.2 w/v% NP. All foams were generated with 22 wt% brine at 80 °C and 2200 psi.

Fig. 5.5 (a) plots the apparent viscosities of foams with 0 to 1 w/v% 8N3+1.5DM NP, 0.1-1 v/v% RCADA, and 70-90% CO₂ quality. The foams exhibit viscosities ranging from 10-30 cP, well above the viscosities of water (0.358 cP, slightly higher for brine) or CO₂ (0.0325 cP) at the same conditions, and sufficient for mobility control. Apparent viscosity increased significantly when NP were used in conjunction with 1 v/v% RCADA. We observed an increase in apparent viscosity with increasing CO₂ foam quality, consistent with similar foams reported in the literature that exhibit maximum apparent viscosities at CO₂ of at least 90% [44,180]. The increase can be explained by an increased number of lamellae per unit length [197].

Fig. 5.5 (b) plots the apparent viscosity of 0.2 w/v% 8N3+0-2DM Pickering foams with 1 v/v% RCADA as a function of CO₂ foam quality. We again observed apparent viscosities ranging from 10-30 cP. DM ligands did not significantly affect the apparent viscosity, consistent with the small increase in θ_w with added DM silane. Fig. F.3, F.4, and F.5 in the appendices plot the variance of apparent viscosity for each combination of NP and surfactant at 70%, 80%, and 90% foam quality, respectively.

5.3.4 Long-term CO₂ foam stability

Having demonstrated apparent viscosity for all foams, we trapped some of the flowing foam in a view cell maintained at 80°C and 2200 psi and measured the long-term stability by analyzing microscope images. Fig. 5.6 displays selected microscope images at different timesteps.

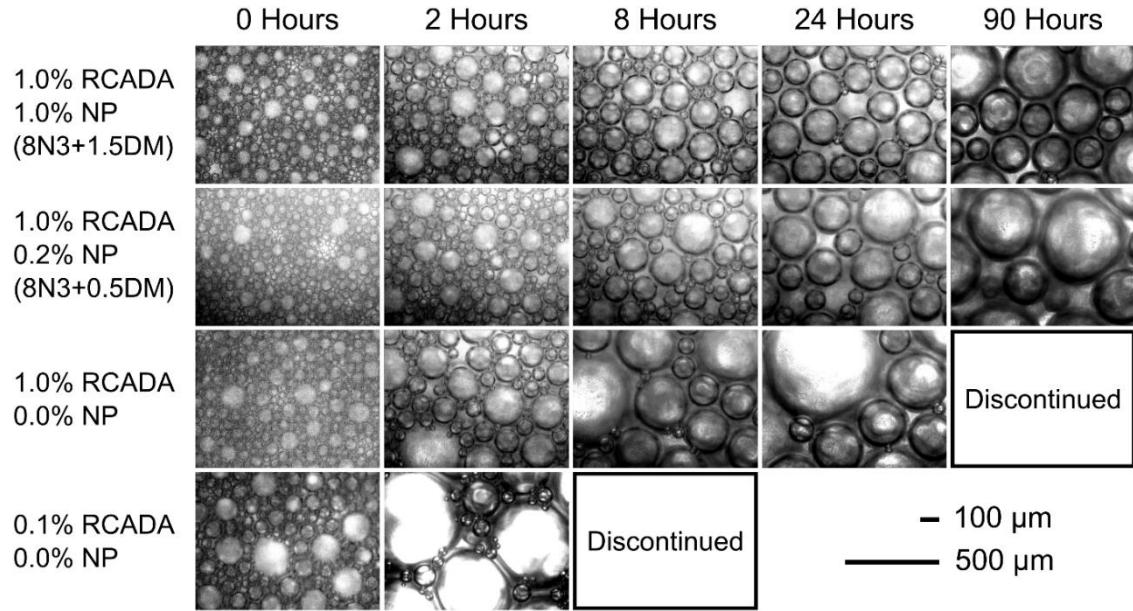


Fig. 5.6. Microscope images of selected CO₂ foams isolated in the view cell at 80 °C and 2200 psi over time. “Discontinued” indicates that the droplets grew too large to properly image at the same scale; at this point, the microscope was shut off. The scale bars are consistent for all images.

Similar to past work, we did not observe coalescence events after a few minutes from foam generation [42,180]; rather, as seen in Fig. 5.6, the foam bubbles coarsened and grew larger throughout the imaging period (we discontinued imaging when bubbles grew too large to properly analyze at the same magnification). The coarsening rate follows Eq. (5.4) [120-122]:

$$\frac{dD_M^3}{dt} = \frac{64\gamma D_{diff} S V_m}{9RT} F, \quad (5.4)$$

where γ is the CO₂-brine interfacial tension, D_{diff} is the molecular diffusion coefficient, S is the CO₂ solubility in the aqueous phase, V_m is the molar volume of dispersed CO₂, R is the gas constant, T is temperature, and F is a correction factor. We assume that the

righthand side of the equation (the coarsening rate) is constant; therefore, Eq. (5.4) suggests that cube of the foam bubble D_{SM} should increase linearly with time.

Fig. 5.7 (a) plots the cube of the foam bubble D_{SM} as a function of time for CO₂ foams generated with 0-1 w/v% 8N3+1.5DM NP, 0.1 v/v% RCADA, and 80% CO₂ foam quality. Fig. 5.7 (b) plots D_{SM}^3 for equivalent foams with 1 v/v% RCADA. Complete images of the foam bubbles from Fig. 5.7 (a) and (b) at different timesteps are displayed in Fig. F.6 in the appendices.

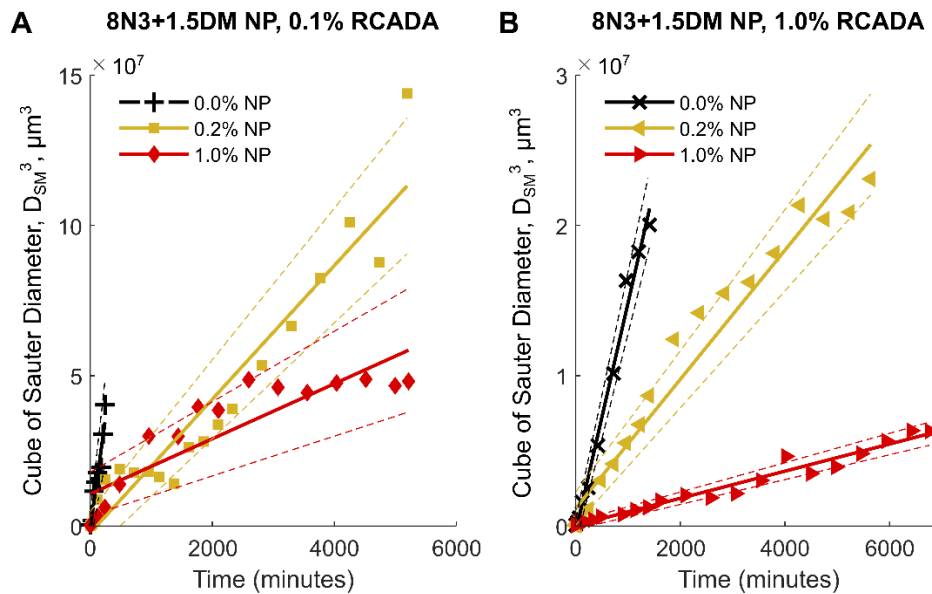


Fig. 5.7. (a) D_{SM}^3 of CO₂ foams with 0.2-1 w/v% 8N3+1.5DM NP and 0.1 v/v% RCADA, plotted against time. (b) D_{SM}^3 of CO₂ foams with 0.2-1 w/v% 8N3+0-2DM NP and with 1.0 v/v% RCADA, plotted against time. All foams were generated at 80% CO₂ quality with 22 wt% brine and maintained at 80 °C and 2200 psi. The linear slopes of these data series are the coarsening rates ($\mu\text{m}^3/\text{min}$). The dotted regions indicate two standard deviations of uncertainty in the coarsening rate.

The plots in Fig. 5.7 (a) and (b) are approximately linear, with their slopes equaling their respective coarsening rates. The coarsening rates and extrapolated D_{SM} after one month are listed in Table 5.1. Table 5.1 includes some of the most comparable results from the 4N3+4N2 system reported by Chen et al. [180] using RCADA surfactant at the same temperature, pressure, and salinity.

Foam system	NP concentration (w/v%)	RCADA concentration (v/v%)	Coarsening rate $\times 10^{-4}$ ($\mu\text{m}^3/\text{min}$)	Extrapolated foam bubble DSM at one month (μm)
RCADA only	0.0	0.1	15 ± 4	1800 ± 200
8N3+1.5DM	0.2	0.1	2.2 ± 0.3	990 ± 50
8N3+1.5DM	1.0	0.1	0.92 ± 0.26	740 ± 80
RCADA only	0.0	1.0	1.5 ± 0.1	870 ± 20
8N3	0.2	1.0	2.5 ± 0.4	1000 ± 50
8N3+0.3DM	0.2	1.0	1.1 ± 0.1	780 ± 30
8N3+0.5DM	0.2	1.0	0.24 ± 0.02	470 ± 10
8N3+1.0DM	0.2	1.0	0.28 ± 0.05	490 ± 30
8N3+1.5DM	0.2	1.0	0.43 ± 0.04	570 ± 20
8N3+1.5DM	1.0	1.0	0.090 ± 0.008	340 ± 10
8N3+2.0DM	0.2	1.0	0.55 ± 0.03	620 ± 10
4N3+4N2 (Chen et al., 2022)	0.2	0.1	1.0018	756
4N3+4N2 (Chen et al., 2022)	0.5	0.1	0.1626	413
4N3+4N2 (Chen et al., 2022)	0.5	1.0	0.1772	425
4N3+4N2 (Chen et al., 2022)	1.0	0.1	0.0408	260

Table 5.1: Summary of CO₂ foam stability measurements at 80 °C, 2200 psi, and 22 wt% brine, including comparable results from Chen et al. [180].

Foam stability improved with both increased NP and surfactant concentrations. With 0.1 v/v% RCADA, the coarsening rate improved from 1.5×10^5 to $9.2 \times 10^3 \mu\text{m}^3/\text{min}$ with 1.0 w/v% NP, an approximately 16x reduction (Table 5.1). With 1.0 v/v% RCADA, the coarsening rate improved from 1.5×10^4 to $9.0 \times 10^2 \mu\text{m}^3/\text{min}$ with 1.0 w/v% NP, an approximately 17x (Table 5.1). Increasing the concentration of RCADA from 0.1 to 1.0 w/v% in 8N3+1.5DM NP foam coarsening rate by 5-10x, with or without NP. We were unable to generate foams using 0 v/v% RCADA, even at 1 w/v% NP concentration.

Fig. 5.8 (a) plots the cube of the foam bubble D_{SM} of CO_2 foams as a function of time with 22 wt% brine, 0.2 w/v% 8N3+0-2DM NP, and 1.0 v/v% RCADA at 80 °C. The linear slopes of these plots are again the coarsening rates, which are plotted against the quantity of added DM silane in Fig. 5.8 (b), along with the coarsening rates of the foams plotted in Fig. 5.7 (a) and (b). Complete images of the foam bubbles from Fig. 5.8 (a) at different timesteps are displayed in Fig. F.7 in the appendices.

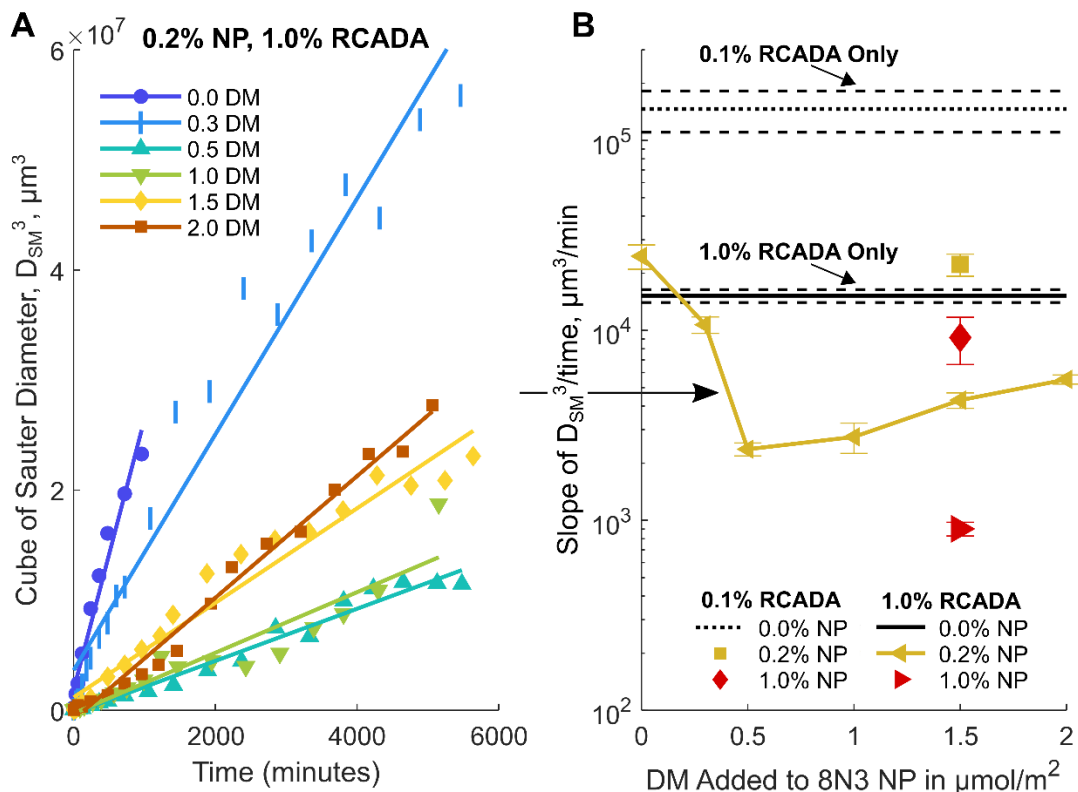


Fig. 5.8. (a) Cube of the D_{SM} of CO_2 foams with 0.2 w/v% 8N3+0-2DM NP and 1 v/v% RCADA, plotted against time. (b) Slope of linear fits to the data (coarsening rates) from both Fig. 5.6 and Fig. 5.8 (a), plotted as a function of DM silane added to the 8N3 NP. Error bars indicate two standard deviations of the coarsening rate. The horizontal solid lines indicate the coarsening rates of 0.1 v/v% RCADA and 1 v/v% RCADA foam without NP at equivalent operating conditions. The horizontal dashed lines are two standard deviations of uncertainty of the coarsening rate in RCADA-only foams.

As shown in Fig. 5.8 (a) and (b), the addition of $0.5 \mu\text{mol}/\text{m}^2$ DM silane to 8N3 NP reduced the coarsening rate from 2.5×10^4 to $2.4 \times 10^3 \mu\text{m}^3/\text{min}$, an approximately 10x reduction (Table 5.1). The 0.2 w/v% 8N3 NP and 8N3+0.3DM NP foams with 1 v/v% RCADA had similar coarsening rates to 1 v/v% RCADA foam without NP, suggesting that some DM ligands were required to better engage the NP at the interface and stabilize the

CO₂ foam. Above 0.5 μmol/m² DM silane added, the coarsening rate slowly increased, although it remained well below the rate of 1 v/v% RCADA foam without NP. The coarsening rates in Fig. 5.8 (b) covered a factor of 167x difference from the least stable (0.1 v/v% RCADA) to the most stable (1 w/v% 8N3+1.5DM + 1 v/v% RCADA) foam. This increase was a product of the coarsening rate reduction from increased NP (16-17x) and the coarsening rate reduction from increased surfactant (10x). This increase took place independently of the need for adsorption of the like-charged surfactant on the NP surface as the NP itself was interfacially active.

The increase in foam stability with increased surfactant and NP concentrations was consistent with past work [42,180]. The contributions of the surfactant and NP to foam stability reduced the coarsening rates independently, suggesting that surfactants and NP were engaging with the CO₂ interface independently. Previous studies have shown that as the surfactant stabilizes foams by reducing interfacial tension, NP attached to the interface can sharply increase E' , the interfacial elastic dilational modulus, slowing coarsening according to the Gibbs criterion [42,123]. Large E' has been reported for other like-charged NP and surfactant systems with air as the gas phase [42]. Unfortunately, we did not have equipment to measure E' at high pressure. The addition of at least 0.5 μmol/m² DM silane was necessary for NP to contribute to foam stability. 8N3 NP likely did not interact with the CO₂ phase strongly enough to provide additional stability to RCADA-stabilized foams. While we did measure an increase in the NP-brine-CO₂ θ_w with increased DM ligands – associated with increased NP affinity with CO₂ – there may be additional mechanisms that also account for the large difference in foam stability. DM ligands may have higher solvation with CO₂ than N3 ligands, increasing the attachment energy of N3+DM NP to the CO₂ foam interface. They may influence E' . Future work will go into better understanding chemistry behind DM ligand-CO₂ interactions.

While not ultra-stable, CO₂ foams with N3+DM and RCADA are stable for several days with low coarsening rates, an improvement over many past studies at similar conditions [126-129,132,168-170] and comparable to the N3+N2 and RCADA system at 80°C described by Chen et al. [180]. While Chen et al. reported lower coarsening rates with 1 w/v% NP than we do here (coarsening rate of 408 vs 900 μm³/min), their 0.2 w/v% NP foam had a higher coarsening rate than ours by up to a factor of four (10018 vs 2400 μm³/min). Our N3+DM system benefited greatly from high RCADA concentrations, whereas the foams reported by Chen et al. were seemingly unaffected by RCADA concentration above some threshold. As seen in Table 5.1, 0.5 w/v% 4N3+4N2 NP foam had similar stability from 0.1 to 1 v/v% RCADA (1626 and 1722 μm³/min, respectively). Stability at low NP concentration is economically advantageous, because NP are generally far more expensive to prepare than surfactants. Overall, the N3+DM and RCADA system demonstrated relatively high stability in difficult reservoir conditions, and is a promising candidate for developing CO₂ foams in higher temperatures.

5.4 CONCLUSIONS

8N3+DM NP and RCADA generated viscous, stable CO₂ foams in 22 wt% brine at 80 °C and 2200 psi. These foams demonstrated long-term stability with low coarsening rates relative to analogous CO₂ foams in the literature [126-129,132,168-170], including studies with foam half-lives ranging from 0-6 hours at similarly challenging conditions [126,128,129]. The N3+DM system had better stability at low NP concentration (0.2 w/v%) than 80°C foams described by Chen et al. [180], which is especially useful given the high cost of producing NP. The presence of DM ligands did not interfere with colloidal stability provided by the N3 ligands, and DM ligands had no measurable effect on foam viscosity, which exhibited similar values to previously reported foams [44,180]. While

amine-coated particles without specific hydrophobic modification have previously been reported to have low θ_w at the water-air interface [180,194], we found that θ_w increased significantly at the water-liquid CO₂ interface, explained by acid-base interactions between amine groups and CO₂ increasing the ligand compatibility with the CO₂ phase. DM ligands functioned as a wettability modifier, further increasing θ_w and greatly reducing the foam coarsening rate, although the full mechanisms of this increased stability are not completely understood.

The addition of DM ligands to 8N3 NP did not change the zeta potential or likewise the protonation behavior necessary for colloidal stability. 8N3+DM NP were colloiddally stable for at least 4 weeks in 22 wt% brine at 80 °C and pH 4 for nearly all tested conditions. The addition of 2 $\mu\text{mol}/\text{m}^2$ DM silane increased the three-phase θ_w of the NP by an average of 9°, tested for all tested conditions. A maximum θ_w of 53° was measured for 8N3+2DM for liquid CO₂ as the nonaqueous phase. Notably, the θ_w of 8N3+DM NP at the brine-liquid CO₂ interface was an average of 21° higher than at the brine-air interface and 37° higher than at the DIW-air interface, indicating high NP CO₂-phillicity. All foams tested exhibited apparent viscosities between 10 and 30 cP across a wide range of conditions – well above the apparent viscosities of water and pure supercritical CO₂, and suitable for CO₂-EOR and storage. The addition of 1 w/v% 8N3+1.5DM NP reduced the coarsening rate of RCADA-only foams by 16-17x at the tested conditions; similarly, increasing the RCADA concentration from 0.1 to 1 v/v% in foams with 8N3+1.5DM NP reduced the coarsening rate by 5-10x. Addition of at least 0.5 $\mu\text{mol}/\text{m}^2$ DM silane was necessary for the N3+DM NP to reduce the coarsening rate. The most stable overall foam (1 w/v% 8N3+1.5DM, 1 v/v% RCADA) exhibited a coarsening rate of 900 $\mu\text{m}^3/\text{min}$ in 22 wt% brine at 80 °C, which extrapolates to an average bubble size of 340±10 μm at one month. The most stable NP foam at 0.2 w/v% NP concentration (8N3+0.5DM, 1 v/v% RCADA) exhibited a

coarsening rate of $2400 \mu\text{m}^3/\text{min}$ in 22 wt% brine at 80°C , which extrapolates to an average bubble size of $470 \pm 10 \mu\text{m}$ at one month.

Overall, these results show that N3+DM at unusually low concentrations and RCADA is an effective system for generating stable CO_2 foams at high-temperature, high-salinity conditions common to reservoirs, and that DM ligands are an excellent additive to improve the affinity of colloidally stable NP to the CO_2 interface.

Chapter 6: Conclusions

6.1 SUMMARY

The purpose of this dissertation was to use nanoparticle surface modification as a tool to manipulate particle properties - both to understand the influence of particle-particle and particle-interface interactions on emulsion stability, and to develop stable Pickering emulsions and foams for reservoir applications at low nanoparticle concentrations. I first grafted silica particles with [3-(2,3-dihydroxypropoxy)propyl]-trimethoxysilane (GLYMO) and generated emulsions in deionized water (DIW) and brine. By measuring the difference in stability as a function of salinity while controlling for relevant factors such as droplet size, I demonstrated that reducing the electrostatic potential (Φ_E) could greatly increase emulsion stability, likely via interparticle networks. I secondly generated emulsions with polyethyleneglycol (PEG)-coated nanoparticles at various surface-grafting densities. By a similar framework, I showed that emulsion stability was maximized at an optimum steric potential that promoted particle-particle interactions without leading to rapid aggregation. Finally, using silica particles coated with both (3-trimethoxysilylpropyl)diethylenetriamine (N3 silane) and dimethoxydimethylsilane (DM silane), I developed nanoparticles stable to aggregation at harsh reservoir conditions and interfacially active with the CO₂ interface. Using these particles, I generated stable CO₂ foams with low nanoparticle concentrations.

6.1.1 Examining the role of salinity on the dynamic stability of Pickering emulsions

One of the biggest considerations for deploying Pickering emulsions and foams in a reservoir is the effect of salinity, and consequently changes in Φ_E , on the stability and performance of both the Pickering mixture and the particles themselves. A reduction in Φ_E increases particle-particle attraction and can cause aggregation. Φ_E has also been linked to

increased Pickering emulsion stability, although the stability itself is dependent on other factors that change with Φ_E (such as droplet diameter). Φ_E can be lowered or increased with the addition or removal, respectively, of salt ions, which surround charged nanoparticles and screen electrostatic forces.

To quantify the effect of lowering Φ_E and increasing particle-particle attraction, I generated decane-in-DIW and decane-in-brine emulsions with GLYMO-coated silica nanoparticles at various particle concentrations. GLYMO ligands added salt tolerance and steric stability, preventing particle aggregation. I measured the relative stability of the emulsions with centrifugation at a fixed condition (30 g of emulsion, 5000 g's of acceleration, 15 minutes). By sweeping across a range of particle concentrations, I identified transition points where emulsion stability curves would shift from completely unstable (releasing all decane as coalesced droplets) at low concentration to completely stable (releasing no decane) at high concentration. This transition occurred at 12x lower concentration in brine than in DIW, indicating improved emulsion stability at lower Φ_E .

To control for changes in emulsion droplet diameter (larger droplets are generally less stable to coalescence), I used microscopy to measure the volume-weighted “Sauter” diameter (D_{32} or D_{SM}), and found that emulsions in DIW had 50-80% larger droplet diameters than emulsions in brine. Accounting for this difference, I determined that brine emulsions matched the stability curve of DIW emulsions with 4.3 ± 0.5 x lower diameter, and calculated that brine emulsions exhibited 78 ± 23 x lower rates of coalescence. This increased stability likely resulted from inter-droplet particle-particle networks favored by the reduction of Φ_E in brine, a promising result for high-salinity reservoir applications. Fig. 6.1 illustrates a hypothetical arrangement of nanoparticles between oil droplets in deionized water and in brine.

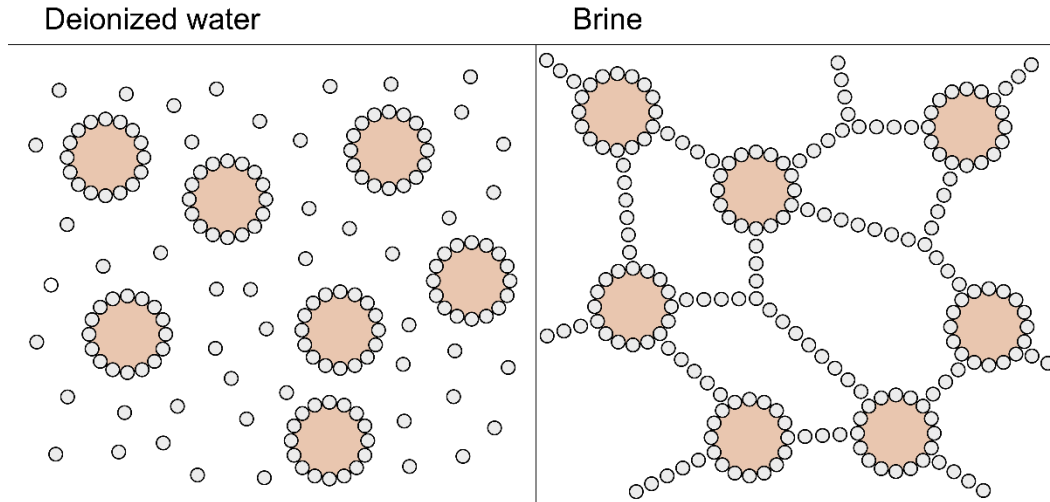


Fig. 6.1. Illustration of particle-particle networks between oil droplets in deionized water (left) and brine (right). This figure is identical to Fig. 3.6, and provided here as reference.

In deionized water, the particles were likely unassociated, and did not contribute to emulsion stability as particle networks. In brine, however, the particles were attracted, giving additional stability to the emulsions.

6.1.2 Effect of interparticle forces on the stability and droplet diameter of Pickering emulsions stabilized by PEG-coated silica nanoparticles

While the particle-particle networks hypothesized in the previous study were effective for improving emulsion stability, Φ_E is not easily modified in practice. Φ_E is influenced by the concentration of salt ions – this property is often environment specific, and is already quite low in most reservoirs. A more flexible approach to potentially increase emulsion stability even further would reproduce the same effect by manipulating a particle parameter, rather than by changing the aqueous phase salinity. For this purpose, I investigated the effects of Φ_S and Φ_{vdW} on emulsion stability.

I silanized silica nanoparticles of different diameters (to modify Φ_{vdw}) with varying concentrations of PEG silane (to modify Φ_S). Using thermogravimetric analysis, I measured the surface density of PEG ligands with high resolution and calculated the subsequent value of Φ_S (Φ_S increases with increasing PEG surface concentration). I showed with dynamic light scattering that particle attraction and aggregation was sensitive to the PEG concentration: from 0-0.5 $\mu\text{mol}/\text{m}^2$ PEG at the silica surface, particles aggregated near-instantly in brine (“Type I” particles); from 0.5-1 $\mu\text{mol}/\text{m}^2$ PEG, particles aggregated in brine at some measurable rate between one minute and one year (“Type II” particles); above 1 $\mu\text{mol}/\text{m}^2$, particle aggregation was negligible in brine and could not be reliably measured. I generated emulsions with these particles in brine and measured the stability with centrifugation. Type II emulsions demonstrated the highest stability, requiring the fewest number of nanoparticles ($1-3 \times 10^{15}$ particles / cm^3) to be stable to centrifuge; Type III emulsions, despite being the most stable, required $6-7 \times 10^{15}$ particles / cm^3 for stability; Type I particles aggregated too quickly to form stable emulsions. Type II particles likely struck a balance between too much aggregation (leading to particle precipitation and failure to stabilize an emulsion) and not enough particle-particle attraction (no inter-droplet particle networks). This concept is illustrated in Fig. 6.2, which displays possible arrangements of Type I (aggregated), Type II (attracted), and Type III (unattracted) particles.

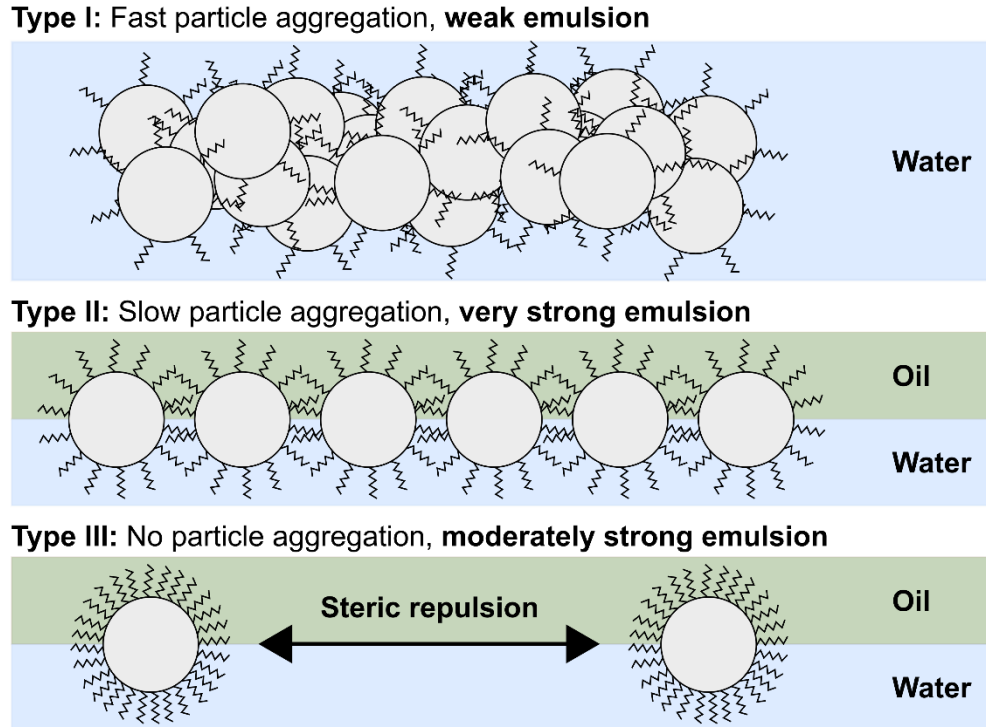


Fig. 6.2. Illustration of particle-particle interactions for Type I, Type II, and Type III systems at an oil-water interface. This figure is identical to Fig. 4.1, and provided here as reference.

Type I particles, as shown in Fig. 6.2, have a low surface concentration of PEG and aggregate quickly in the bulk water phase. Type II particles, with an intermediate surface concentration, are active at the interface and form particle-particle networks, increasing stability. Type III particles, with the highest surface concentration of PEG, are illustrated as sterically repelled and separated. While Type III particles still stabilize emulsions, the emulsions are not as stable as those using Type II nanoparticles. I unfortunately did not measure any significant effect from varying particle diameter and Φ_{vdw} .

For every emulsion generated in this study, I took microscope images and calculated a Sauter diameter. From this large dataset, I observed that droplet diameter

increased with increasing particle size, reduced salinity, and decreasing particle concentration. With an energy balance model based on particle-particle and particle-interface interactions, I calculated droplet diameters for all of the emulsions and fit them to the data. I found that, while emulsion stability was heavily influenced by particle-particle interactions, droplet diameter was influenced by only particle-interface interactions.

Altogether, these findings demonstrate an optimal surface coating based on manipulation of Φ_S to induce the formation of inter-droplet particle networks. Because of the versatility of modifying the surface density of ligands, these findings can be applied to a variety of applications as a new method of designing nanoparticles to generate stable emulsions. Together with the previous study, I show that Pickering emulsion systems can be tuned in different ways to increase particle-particle attraction (without inducing aggregation) and greatly increase emulsion stability.

6.1.3 Stable CO₂/water foam stabilized by dilute surface-modified nanoparticles and cationic surfactant at high temperature and salinity

Having explored particle-particle interactions from all three constituent potentials, I focused on particle-interface interactions to generate stable CO₂ Pickering foams. Thanks to their high viscosity and favorable mobility ratio, CO₂ foams have application for enhanced oil recovery and CO₂ storage, but particle and foam stability is difficult at the high salinity, temperature, and pressure common to reservoirs. CO₂ is especially challenging because of its high solubility to water (increasing the foam coarsening rate, dD_{SM}^3/dt) and unique chemistry. For CO₂ foam, my goal was to develop particles that were both resistant to aggregation (by tuning the particle-particle interaction) and active at the brine-CO₂ interface (by tuning the particle-interface interaction).

To meet these goals, I grafted silica particles with N3 and DM ligands. The former was a ligand already understood to provide steric stability at reservoir conditions; the latter was a known wettability modifier intended to improve particle CO₂-phillicity. I first verified that hydrophobic DM did not compromise the stability of particles to aggregation with measurements of the zeta potential, titration curves, and DLS size at representative conditions over time; I then measured the system contact angle as a function of DM concentration for DIW-air, brine-air, and brine-liquid CO₂. From these measurements, I found that DM was an excellent additive to the N3 system.

Using these N3+DM particles in conjunction with a cationic surfactant (RCADA), I generated stable foams with suitable viscosities. At 80°C, 2200 psi, 0.2 w/v% particle concentration, and 1 v/v% RCADA concentration, I reported a foam with a coarsening rate of 2400 μm³/min (extrapolated bubble diameter of 400 μm³ at one month) – an unprecedented stability at such a low particle concentration. This finding is favorable for most applications given the relatively high cost of nanoparticles compared with surfactants. I measured a 16-17x decrease in the coarsening rate by adding 1w/v% N3+DM particles to RCADA-only foam. The high stabilities were likely a result of the high contact angles (43-53°) measured for the particle surface at the interface of brine and liquid CO₂, greatly increasing the particle-interface interaction. The addition of some DM was necessary to increase foam stability; while DM did increase the contact angle by up to 9° on average for the measured conditions, there may be other mechanisms simultaneously increasing the foam stability.

6.2 FUTURE WORK

There are a few directions that future researchers could take to extend these topics. For Pickering emulsions, I think that the effect of Φ_S could be explored by other ligands. I

observed an optimal Φ_S at a specific PEG coverage. The optimal value, if reproduced for other ligands, may be at a different surface coverage; we may be able to derive this value for other ligands from Eq. (3.8-10). Optimizing Φ_S for other ligands would not only tell us more about particle-particle interactions, but may allow us to find co-optimize Φ_S and θ , which could further improve emulsion stability. This problem could be explored using multi-ligand coverage, which I used for CO₂ Pickering foam experiments but not with oil-and-water Pickering emulsions.

Future work could additionally go into applying lessons from Pickering emulsions to the CO₂ Pickering foams. It would be interesting to investigate whether increasing particle-particle attraction would increase the stability of CO₂ foams. This could be carried out by reducing the surface coverage of N3 at the silica surface and measuring for an optimum value. CO₂ foams could also be tested at higher temperatures – many reservoirs are still above 80°. In the long term, the best CO₂ foams should be applied to core floods and eventually pilot tests, paving the way for commercial deployment of CO₂ storage.

On the topic of CO₂ Pickering foams, one loose end from Chapter 5 is the grafting reaction and TGA response of DM silane on the N3-coated silica surface. The organic fraction of N3 particles reliably decreased with added DM. The magnitude of decrease was approximately equal to the mass of one DM and N3 molecule – in other words, if the addition of one molecule of DM prevented both itself and a molecule of N3 from detaching at high temperature, it could explain the unusual signal. This behavior could indicate DM oligomerization at the particle surface. While DM did increase the contact angle of N3 particles at the brine-liquid CO₂ interface, the increase (9°) seemed small relative to the increase in foam stability. DM oligomerization could be altering the particle-interface interaction by other means (possibly by increasing CO₂ solvation forces or increasing the interfacial elastic dilational modulus). The N3+DM particles could be tested with other

gases (N₂) to determine if CO₂ is uniquely stable, and interfacial rheology could be measured.

There are other approaches to extend these research topics. I report measurements of static foam stability and dynamic emulsion stability to compressive forces, but it would be interesting to investigate flowing stability in a beadpack or core under the conditions that we expect particle-particle networks to form. Future researchers could try mixing particles with different diameters to increase polydispersity and reduce the void fraction at the fluid-fluid interface, possibly increasing the stability of densely-packed emulsions. Surface modification could be carried out at very high silane concentrations to measure the limit of concentration and its effect on particle zeta potential and contact angle (this could also help clarify the particle surface OH⁻ density and specific mechanism of the grafting reaction). I'm especially curious about why the grafting reaction of PEG has approximately 50% efficiency for 0-2 μmol/m² silane added – for every two PEG molecules, I was able to attach at most one to the silica surface. Nanoparticles could be prepared at diameters below 6 nm – smaller diameters are associated with improved stability (filtration could become an issue). Finally, future work could explore controlled aggregates. Given our control over Φ_S and aggregation over time, future researchers could prepare aggregates at a given size and see the effects on emulsion and foam stability. Transmission electron microscopy – especially with a liquid cell – could reveal the particle aggregation morphology.

Appendix A: Nanoparticle surface modification

In this section, I will describe the procedures that my colleagues and I used to perform surface modification of silica nanoparticles. I will discuss the selection of particle core and silanes, surface modification procedures, and the measurement of surface modification with thermogravimetric analysis (TGA). This section builds on work from past researchers in our departments [28,42,60,81,105,175,180,191,198].

A.1 MATERIALS

For all of our experiments, we used NexSil silica nanoparticles from Nyacol Nano Technologies, Inc. These particles are supplied as an aqueous dispersion at high pH, with a negative surface charge and dispersed Na_2O . The advantage of these particles is that they are spherical, monodisperse, and commercially available. We and others have done extensive characterization with NexSil particles. Figure A.1 is an image of the aqueous stock particles; Table A.1 lists some relevant properties (dynamic light scattering (DLS), TGA, and zeta potential measurements will be discussed later here and also in Appendix B).

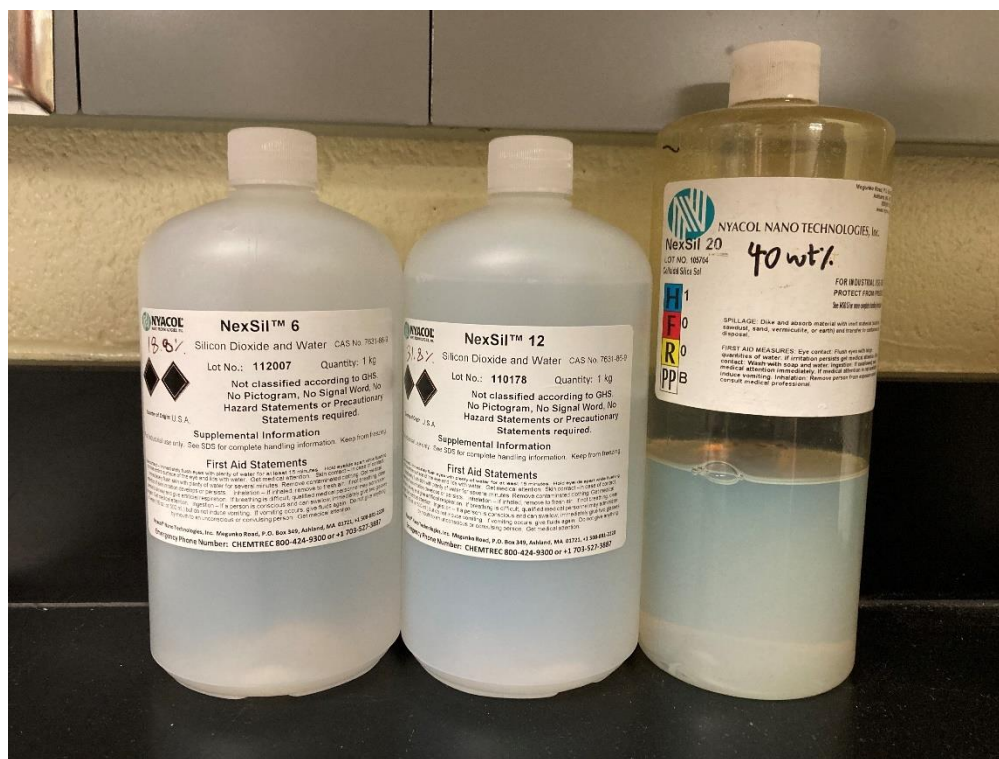


Fig. A.1. Left to right: NexSil 6, NexSil 12, and NexSil 20. Although difficult to see in opaque containers, the NexSil 6 and 12 particles are mostly clear. NexSil 125-40, not pictured, is even cloudier in appearance.

Name	Average surface area (m ² /g)	pH	Measured wt%	DLS average diameter (nm)	Z-TGA organic fraction	Zeta potential (mV)
NexSil 6	340-545	9.5 - 10.5	18.8	16.3	0.0290	-46
NexSil 12	195-273	8.8 - 9.5	31.8	23.8	0.0199	-47
NexSil 20	135	10	40.0	30.1	0.0175	-49
NexSil 125-40	25-50	9 - 10	43.0	110.4	0.0191	n/a

Table A.1: Properties of NexSil particles.

Fig. A.2 displays a transmission electron microscope (TEM) image of the larger NexSil 125-40 particles. TEM images of the other particles can be seen in Fig. 4.4.

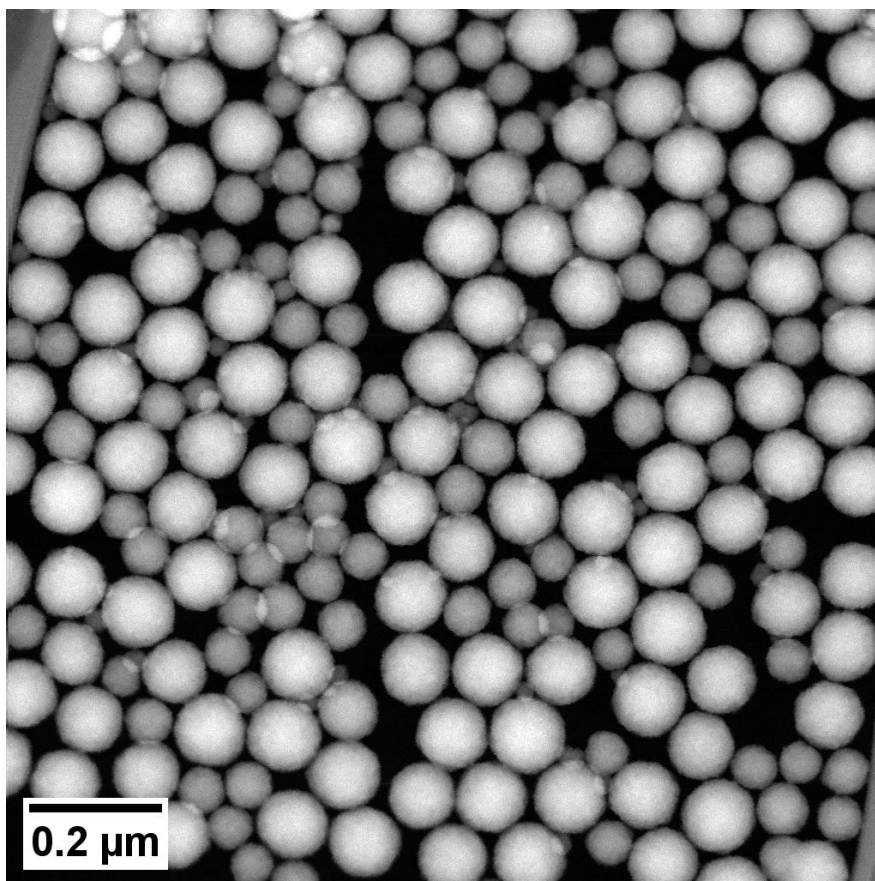


Fig. A.2. TEM image of NexSil 125-40 particles. These particles have been surface modified by PEG before imaging. Particles are spherical and monodisperse.

Silica particles can react with other molecules that have silanol groups (silanes). Several silanes can be purchased for surface modification. Table A.2 lists some silanes that we worked with, and Table A.3 displays some more information. Our choice of silane depended on ligand solubility, surface interactivity, and simplicity of reaction, as we will describe below.

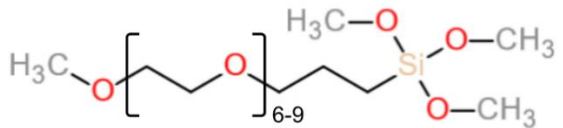
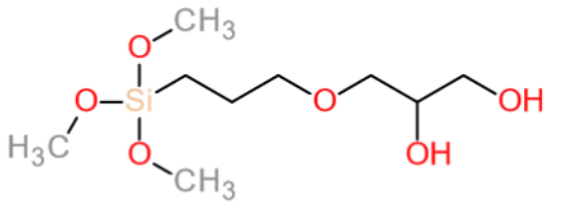
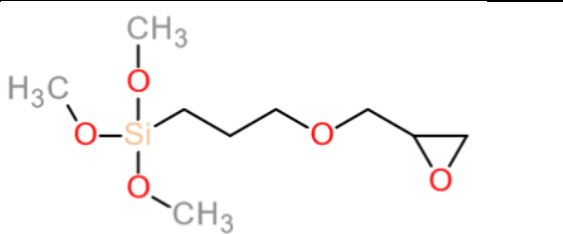
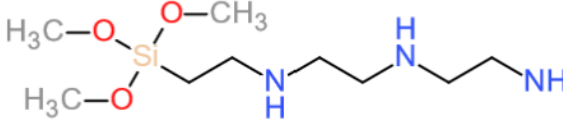
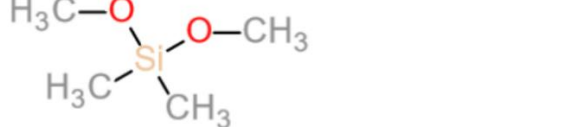
Name	IUPAC Names	Structure
PEG-silane	3-[methoxy(polyethyleneoxy)6-9]propyltrimethoxysilane	
GLYMO	[3-(2,3-dihydroxypropoxy)propyl]-trimethoxysilane 3-[3-(trimethoxysilyl)propoxy]-1,2-propanediol	
GPTMS	(3-glycidyloxypropyl)trimethoxysilane	
N3-silane	(3-trimethoxysilylpropyl)diethylenetriamine	
DM-silane	Dimethoxydimethylsilane	

Table A.2: Silane names and structures.

Name	Methanol cosolvent	Hydrolysis condition	MTGA (g/mol)	Molecular weight (g/mol)	Density (g/ml)	Purity
PEG-silane	No	Basic	404	459-591	1.076	>0.99
GLYMO	Yes	Basic	133	n/a	n/a	n/a
GPTMS	Yes	Basic	115	236.34	1.07	≥0.98
N3-silane	Yes	Acidic	144	265.43	1.030	0.95
DM-silane	No	Acidic	n/a	120.22	0.88	0.95

Table A.3: Properties of silane chemicals used in our experiments

All of the silanes listed in Tables A.2 and A.3 can be purchased commercially, except for GLYMO. GLYMO is produced by modifying GPTMS.

Another consideration when it comes to particle choice is the age of the batch of silica particles. Unfortunately, the quality of the particles appeared to degrade over a few years. Figure A.3 shows silica particles with various silane coatings after adding concentrated brine. These silica particles were over 5 years old, and were beginning to indicate some aggregation in DLS measurements. Naturally, we performed these simple DLS measurements after we had surface-modified all of the particles shown below. The same silane coatings applied to newer (1-2 years old) particles did not exhibit any aggregation in brine.



Fig. A.3. Various N3+DM and PEG particles reacted with an old batch of silica nanoparticles. Every batch failed, despite no changes in the procedures.

A.2 SURFACE MODIFICATION

The reaction between a silica particle and a silane is referred to as silanization [30,31]. The silanol group, Si-OH, is highly reactive with other silanol groups at high temperature via condensation to produce a covalent Si-O-Si bond (removing one water molecule). We use this reaction to coat the silanol-rich surface of our silica particles with

ligands that have desirable properties. This process is primarily done to either increase particle resistance to aggregation, or to modify particle wettability.

The silane molecules described in Table A.2 have with methanol groups “shielding” the silicon atom from reacting (some silanes have ethanol groups in this role). These groups must be removed by a hydrolysis reaction before silanol-silanol condensation can occur (Fig. 2.5). Hydrolysis can be catalyzed by acidic or basic conditions, and we used different conditions depending on the silane. Additionally, some silanes required the presence of significant amounts of methanol as a cosolvent in the aqueous phase to remain stable during the reaction. A more detailed description of the use of methanol to assist the silanization reaction of silica particles and GLYMO is given by former lab mate Chris Griffith [198].

Silanization was performed as a batch reaction in a glass vial or bottle. The mass of silica particles in the batch reaction, m_{silica} (not to be confused with the mass of the aqueous dispersion), was often chosen to be a multiple of 2 g. The total concentration of silica particles was set to 10 wt%. This concentration was high enough to produce significant yield, but low enough to prevent solubility and stability issues during the reaction. So, using 2 g of particles, the total reaction volume would be 20 g. If methanol was required for the reaction, then 20 wt% (20 v/v% is also acceptable) of the batch reaction would be methanol (4 g of methanol for every 2 g of silica particles). We calculated the appropriate quantity of silane to be added to the reaction with equation (A.1):

$$m_{silane}(g) = \frac{m_{silica}(g) * SA_{silica}\left(\frac{m^2}{g}\right) * coverage\left(\frac{mol}{m^2}\right) * MW_{silane}\left(\frac{g}{mol}\right)}{purity_{silane}}, \quad (A.1)$$

where m_{silane} is the mass of silane to be added to the reaction, SA_{silica} is the specific surface area of silica, $coverage$ is the “nominal” surface coverage of silane added to the reaction, MW_{silane} is the molecular weight of the silane, and $purity_{silane}$ is the purity of the silane chemical. Finally, DIW was added to the reaction to bring the total volume up to 20 g. We performed surface modification with each silane using this basic framework. Note that the reaction efficiencies were always less than 100%, and $coverage$ was not equivalent to the actual surface concentration of ligands at the silica.

A.2.1 GPTMS

GPTMS-coated silica nanoparticles are notable because of their steric stability at low molecular weight. The hydrolysis and condensation of GPTMS was performed at basic (unadjusted, pH ~10) conditions on a hot plate. GPTMS, particles, methanol, and DIW were added into a glass vial at the desired proportions and sealed with PTFE tape. As an example, to graft $8 \mu\text{mol}/\text{m}^2$ GPTMS to 2 g of NexSil 6 particles (18.8 wt% batch, $445 \text{ m}^2/\text{g}$), we required 1.7169 g of GPTMS, 4 g of methanol, 3.6431 g of DIW, and 10.64 g of aqueous particle dispersion. Stirred at basic conditions, we can expect GPTMS to hydrolyze into hydrolyzed-GPTMS, which has a molecular weight of 194.26 g/mol and can be described by a few names (trihydroxy-[3-(oxiran-2-ylmethoxy)propyl]silane, 3-glycidoxypropyl-silanetriol, [3-(Oxiranylmethoxy)propyl]silanetriol). The vial was heated on a hot plate overnight to promote silane condensation on the silica surface. Because we used methanol in the reaction, the methanol was then allowed to evaporate on the hot plate (removal of 4 g by this method took about 2 hours). The condensation and methanol evaporation are shown in Fig. A.4.



Fig. A.4. Left: nanoparticle condensation reaction of GPTMS and NexSil 6. While the temperature is not precisely controlled, we get excellent repeatability with this method. Right: evaporation of methanol after silanol condensation (also GPTMS and NexSil 6, but from a different batch).

If methanol is not added to the GPTMS reaction, then the reaction will not work, as shown in Fig. A.5. The produced particles will be cloudy and aggregated.



Fig. A.5. Left: GPTMS and NexSil 6 reacted without methanol. Right: GPTMS and NexSil 6 reacted with methanol.

Once the methanol was removed, the particles could then be transferred to a centrifuge filter.

A.2.2 GLYMO

GLYMO was used as a slightly more hydrophilic version of GPTMS. The procedure to graft GLYMO to the silica surface was similar to that of GPTMS, with one alteration. Before combining into a vial, GPTMS was first stirred in 0.01 M HCl (diluted from concentrated 12.1 M HCl) in a 1:6 ratio. Thorough stirring of GPTMS with acid for two minutes induced a ring-opening condensation reaction, converting the epoxy ring into a glycerol group as shown by Fig. A.6 [28]:

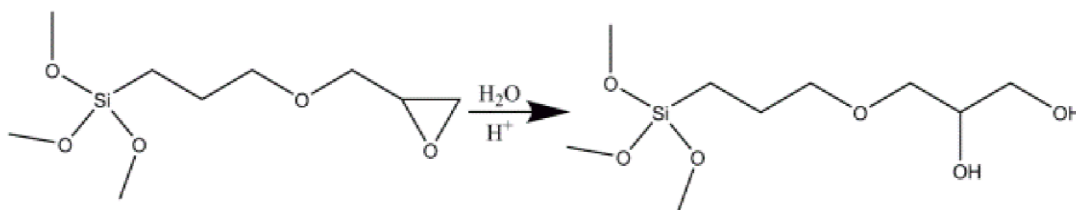


Fig. A.6. Acid-catalyzed ring opening of GPTMS (left) to form GLYMO (right), from Worthen et al [28]. The epoxy group is converted into a glycerol group by the addition of one water molecule.

Although not shown above, the methanol groups on GLYMO likely hydrolyze during the acid-catalyzed ring-opening step. The silane therefore converts from GLYMO ([3-(2,3-dihydroxypropoxy)propyl]-trimethoxysilane or 3-[3-(trimethoxysilyl)propoxy]-1,2-propanediol) to hydrolyzed GLYMO ([3-(2,3-dihydroxypropoxy)propyl]-silanetriol, 212.27 g/mol). Besides this step, the reaction of GLYMO to the silica was the same as that of GPTMS.

A.2.3 PEG

Perhaps the easiest ligand to graft to silica is PEG. PEG requires no methanol, and reacts well with NexSil particles at their unadjusted pH of 10. PEG is especially well studied in the literature, and excellent in room temperature brines (PEG has solubility problems in high-temperature brines). We performed the reaction with the following steps: (1) we mixed aqueous nanoparticles, DIW, and PEG-silane together (proportional to Eq. (A.1)) in a glass vial and sealed it with PTFE tape; (2) we stirred the vial overnight on a hot plate set to over 65°C; (3) after stirring, we filtered the particles to remove ungrafted ligands. As we will discuss below, the grafting reaction of PEG was predictable and repeatable.

A.2.4 N3

N3 was a good ligand to provide steric stability in low-pH, high-temperature, high-salinity brines (ideal for CO₂ foam applications). The reaction of N3-silane to silica was performed differently than the previous three ligands. Firstly, we performed the reaction in acidic conditions. In a glass vial, NexSil particles were adjusted to pH 5 with a small amount of 12 M HCl (in our experience, it took about 100 μ l of 12 M HCl to sufficiently protonate 10 ml of aqueous NexSil 6). We then added methanol and DIW (if necessary) to the particles. The quantity of materials used for this reaction was similar to above, but calculated volumetrically. For example, instead of 2 g silica per 20 g of reaction, we used 2 g silica per 20 ml of reaction, and 4 ml of methanol per 20 ml of reaction. Secondly, we pretreated the silane before the reaction. N3-silane was a challenging molecule to dissolve in water; the hydrolysis reaction was very exothermic, and could boil and rapidly solidify if combined too quickly. As such, we hydrolyzed N3-silane in a separate vial before reacting it with silica particles. We stirred DIW in a vial and (slowly, carefully!) added an equal volume of N3 dropwise. Once fully combined, we allowed the DIW and N3-silane to stir for 30 minutes before bringing it down to pH 5 with 12 M HCl (volume of HCl necessary to adjust pH was about 90% of the volume of N3-silane, in our experience), and then adding it to the vial containing particles. Finally, we stirred the (sealed) reaction vial in a temperature-controlled oil bath on a hot plate at 70°C. Evaporation of methanol and particle filtration.

A.2.5 DM

We used DM as a wettability modifier for nanoparticles grafted with N3. The addition of DM-silane to N3 particles was straightforward. After the removal of methanol, but before particle filtration, we simply added the appropriate amount of DM-silane to the

N3 particle batch (still stirring at 70°C), re-sealed the batch with PTFE tape, and reacted it overnight. This process could be done in separate vials to make several DM derivatives from a single large N3 batch. One note about DM is that it increased the particle hydrophobicity, and too much added DM-silane would cause the reaction to fail (possibly because of precipitation). For N3 particles with a *coverage* of 8 $\mu\text{mol}/\text{m}^2$ added to the reaction, we could generally add 2 $\mu\text{mol}/\text{m}^2$ DM-silane without issue. The permissible amount of DM-silane seemed to decrease with decreasing N3.

A.3 PARTICLE FILTRATION

Once the reaction was complete, it was necessary to filter our particles and remove ungrafted ligands. The presence of ungrafted ligands influenced many of our particle characterization methods, possibly with the exception of DLS size measurements in DIW. Unfiltered particles also struggled to produce stable emulsions in brine. We filtered the particles in an Eppendorf 5810R Centrifuge using Amicon Ultra-15 30k MWCO centrifuge filters, filtering the particles with DIW 4-8 times at 3000-5000 g for 15-30 min, depending on the experiment. The centrifuge filter was refilled to a total volume of 12 ml with DIW after each run. After performing many experiments, I think that 8 x 5000 g x 30 min was unnecessary – 4 or 5 washes seemed to work well. Filtered particles were extracted, placed in a vial at DIW, and bath or tip sonicated to disperse. Bath sonication was run for 30 minutes; tip sonication was performed five times for 60 seconds at 50% amplitude. The final particle concentration was either determined volumetrically (for certain experiments, assuming 100% recovery of particles from the filter), or by comparing the mass of a particle sample before and after drying in an oven at 120°C for 3 hours.

A.4 MEASUREMENT OF PARTICLE SURFACE MODIFICATION WITH THERMOGRAVIMETRIC ANALYSIS (TGA)

We measured the concentration of silanes at the silica surface with a Mettler Thermogravimetric Analyzer TGA/DSC 1. TGA is an excellent tool for nanoparticle characterization, and we've obtained repeatable, predictable results. We used 70 μl aluminum oxide crucibles (Mettler Toledo, ID 24123) with 5-10 mg of dried particles (dried from an aqueous dispersion) for the measurements. Particles in the crucible were weighed with a 0.01 mg precision scale. Fig. A.7 shows the TGA and crucible positioning.



Fig. A.7. Left: TGA instrument. Right: crucibles ready for TGA analysis. The crucibles in positions 16 and 17 contain particles already raised to 800°C, whereas the crucibles in positions 18-20 have yet to be analyzed.

The TGA measurements were fairly straightforward. We used a method that would ramp the particles from 35°C to 800°C at a rate of 10°C/min. The temperature was briefly held at 110°C for 20 min to remove residual water. Particles were kept under a constant 50 ml/min flow of N₂ gas during this process. The mass of the crucible was measured throughout the heating process, with the assumption that some of the surface ligand would detach and be removed from the crucible. The percent of mass loss was used to calculate

the coverage of silane at the silica surface, although the exact calculation is a little complicated.

The first consideration with analyzing TGA data was that ungrafted particles exhibited some mass loss at high temperature. Fig. A.8 plots the TGA mass of NexSil 6 particles as a function of temperature. Roughly 3% of the mass decreased by the end of the run. This mass is often attributed to dihydroxylation of the silica surface and possibly the silica matrix [86]. The total mass fraction lost at 800°C during TGA is referred to as the “organic fraction”, f_o . The organic fractions of ungrafted particles, $f_{o,np}$, are listed in Table A.1.

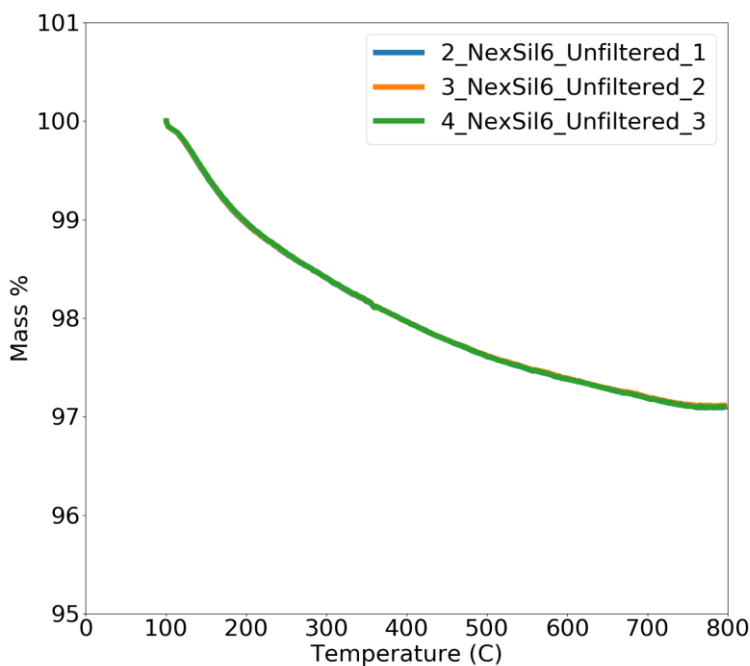


Fig. A.8. Mass fraction of NexSil 6 silica particles during TGA

Another consideration was that not all of the silane was removed from the particle surface during TGA. Some would be removed, and increase the organic fraction; however,

some of the silane likely remained attached to the silica surface and decreased the organic fraction. To illustrate this point, Fig. A.9 plots the TGA mass fractions of various silanes as a function of temperature. Please note that any GLYMO we used in experiments was always in its hydrolyzed form ([3-(2,3-dihydroxypropoxy)propyl]-silanetriol), because the process to create GLYMO also hydrolyzed GLYMO.

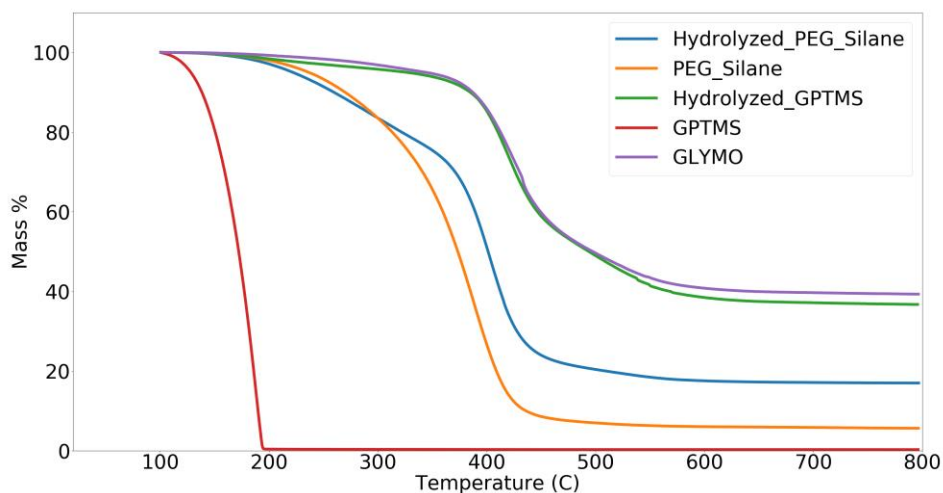


Fig. A.9. TGA mass fraction of various silanes up to 800°C.

PEG silane and hydrolyzed PEG silane exhibited organic fractions of 94% and 83%, respectively, at 800°C. The TGA curve for GPTMS quickly decreased to 0 at a relatively low temperature. This result is likely because unhydrolyzed GPTMS is volatile. Hydrolyzed GPTMS, on the other hand, decreased to an organic fraction of 63%. GLYMO exhibited an organic fraction of 60%. Figures A.10 through A.13 attribute the organic fractions and mass remaining (inorganic, f_i) fractions to different portions of the silane molecules, based on the percentage of the molar mass.

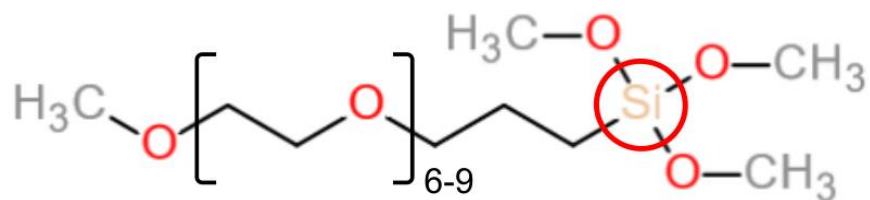


Fig. A.10. Diagram of PEG silane (525 g/mol, average), which has an organic fraction of 94% and an inorganic fraction of 6% (31 g/mol). The inorganic fraction is consistent with Si or SiH_x (28-32 g/mol, circled), which we suspect is left behind during TGA.

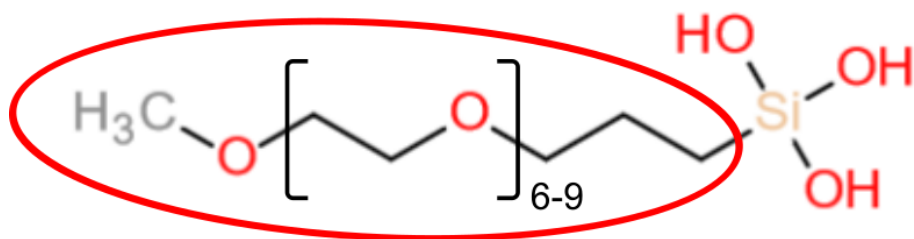


Fig. A.11. Diagram of hydrolyzed PEG silane (483 g/mol), which has an organic fraction of 83% (401 g/mol) and an inorganic fraction of 17%. The organic fraction is similar to the circled portion (404 g/mol), which we suspect is removed during TGA.

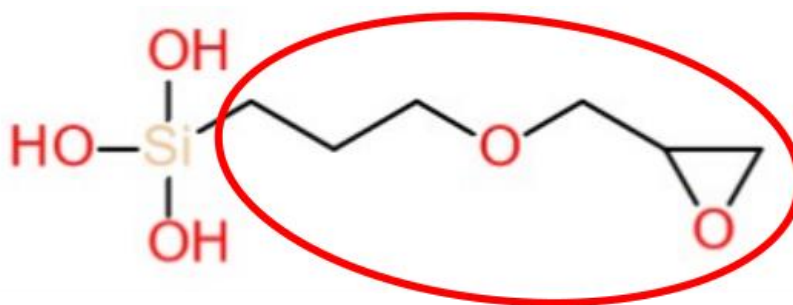


Fig. A.12. Diagram of hydrolyzed GPTMS (194 g/mol), which has an organic fraction of 63% and an inorganic fraction of 37%. The organic fraction is close to the circled portion (115 g/mol), which we suspect is removed during TGA.

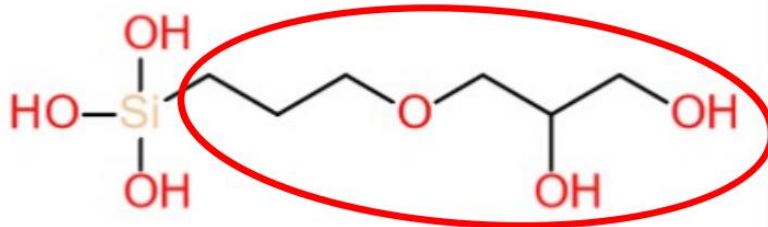


Fig. A.13. Diagram of hydrolyzed GLYMO (212 g/mol), which has an organic fraction of 60% (127 g/mol) and an inorganic fraction of 40%. The organic fraction is close to the circled portion (133 g/mol), which we suspect is removed during TGA.

Overall, hydrolyzed silanes in the form R-Si(OH)₃ appeared to lose the R group when brought to high temperature during TGA, while the mass of Si(OH)₃ remained behind. The molar mass of the R group removed by TGA and the molar mass of the portion left behind are referred to as M_{TGA} and M_{iTGA} , respectively. We note that, when attached to the silica particle surface, the silane group remaining after TGA has already lost one or two water molecules from the condensation reaction. As a result, we used a value of 52 g/mol for M_{iTGA} for our calculations. The M_{TGA} values that we used are all listed in Table A.3.

We used Eq. (A.2) to calculate the quantity of silane grafted to the silica surface while accounting for all of these observations. Eq. (A.2) is an expanded form of equations used in previous papers [28;81], which adds information about the TGA signal of the original particle ($f_{o,np}$) and about silane remaining (f_i , M_{iTGA}).

$$\varphi_l = \frac{f_o - f_{o,np}}{(1 - f_o - f_i + f_{o,np})S_A M_{TGA}}, f_i = \frac{(f_o - f_{o,np})M_{iTGA}}{M_{TGA}}, \quad (\text{A.2})$$

In Eq. (A.2), φ_l is the ligand coverage per area of particle surface, and S_A is the particle specific surface area.

Fig. A.14 displays the normalized mass change of TGA runs of three GLYMO-NP aquilots (the particles used in Chapter 3). The particles are NexSil 6 with a nominal coverage of $5 \mu\text{mol}/\text{m}^2$ added to the silanization reaction. The normalized mass is defined as the mass fraction with respect to 110°C – the temperature that residual water is removed.

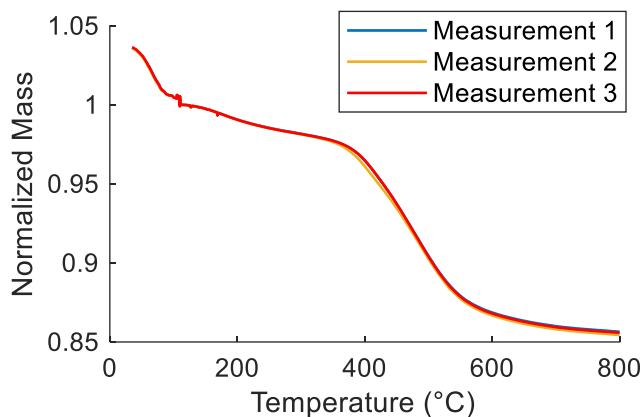


Fig. A.14. Mass change of three GLYMO-NP aquilots during TGA runs; normalized mass is defined as a mass fraction equal to one during the second ramp section (beginning at 110°C), when water is expected to be completely removed.

Normalized mass decreased from 1.04 to exactly 1 as temperature ramped up to and held at 110°C and residual moisture was removed from the dried nanoparticles. The discontinuity at 110°C in the plot represents this hold time. All three runs tracked closely together with low variance. The decrease of normalized mass as temperature increased from 110°C to 800°C was attributed to removal of GLYMO ligand and was used as the organic fraction, f_o , equal to 0.1445. Using Eq. (A.2), we calculated that these GLYMO particles had an actual surface concentration, φ_l , of $2.4 \mu\text{mol}/\text{m}^2$. This value represents 48% of the GLYMO added to the reaction and 32% of the total possible surface coverage (assuming $7.6 \mu\text{mol OH sites per square meter of silica surface}$) [86].

Fig. A.15 plots the TGA mass change of PEG-NP (from Chapter 4) with nominal coverage values of $16 \mu\text{mol}/\text{m}^2$ and $1 \mu\text{mol}/\text{m}^2$ PEG-silane added to the grafting reaction. This data is plotted starting at 110°C , omitting the discontinuity (related to removing residual water at fixed temperature) observed previously.

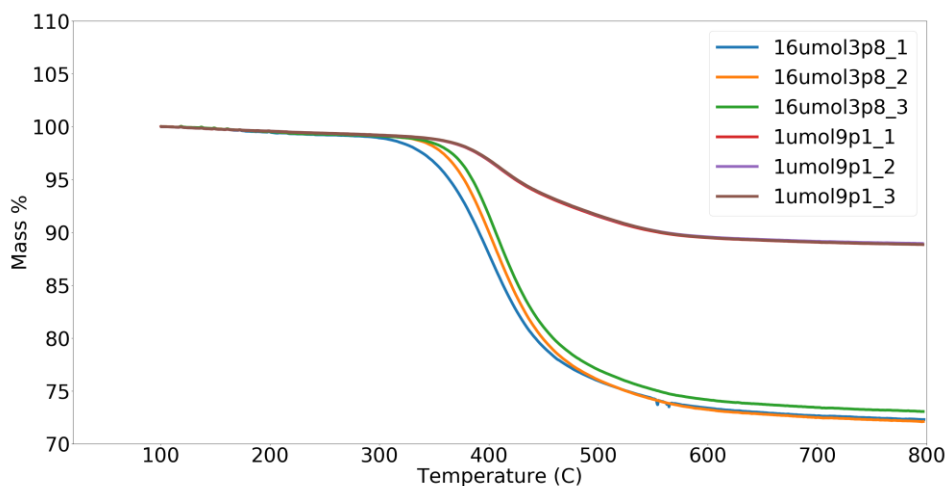


Fig. A.15. TGA mass curves of PEG-NP at $16 \mu\text{mol}/\text{m}^2$ and $1 \mu\text{mol}/\text{m}^2$ nominal coverage.

As expected, the higher grafting-density $16 \mu\text{mol}/\text{m}^2$ particles have a larger f_o of 0.275 than the lower $1 \mu\text{mol}/\text{m}^2$ particles (0.114), explained by the greater quantity of PEG ligands available to be removed. The organic fraction and corresponding PEG grafting densities (the actual surface coverage) for PEG particles ranging from 0 – $16 \mu\text{mol}/\text{m}^2$ PEG added to the reaction are listed in Table A.4. These values are plotted in Fig. 4.2.

Added to reaction ($\mu\text{mol}/\text{m}^2$)	Organic Fraction	Actual Coverage ($\mu\text{mol}/\text{m}^2$)
16	0.275	1.89
8	0.265	1.79
4	0.232	1.46
2	0.184	1.04
1.75	0.167	0.91
1.5	0.154	0.81
1.25	0.133	0.66
1	0.110	0.50
1	0.117	0.54
0.75	0.099	0.42
0.5	0.077	0.28
0	0.029	0.00

Table A.4: TGA data from PEG-NP series.

Appendix B: Nanoparticle Characterization

In this section, I discuss different particle characterization methods that my colleagues and I have used throughout various experiments. This section will discuss qualitative particle stability, dynamic light scattering (DLS), transmission electron microscopy (TEM), contact angle measurement, zeta potential measurement, and titration. The methods described in this section were adapted from multiple past studies.

B.1 PARTICLE STABILITY

A key motivation for particle surface modification was to increase the stability of the particles to aggregation in brine. The mechanism of particle stability is well described by extended DLVO theory and is discussed in detail in Section 3.3.2. Briefly, the total interaction (Φ_T) between two particles dispersed in the aqueous phase can be expressed as the summation of the van der Waals (Φ_{vdW}), electrostatic (Φ_E), and steric (Φ_S) potentials, given by Eq. (B.1):

$$\Phi_T = \Phi_{vdW} + \Phi_E + \Phi_S. \quad (\text{B.1})$$

As an example, Fig. B.1 plots the three constituent DLVO interaction potentials, plus the total interaction potential, for a system of 100-nm silica particles in either deionized water (DIW) or 4 wt% NaCl, 1 wt% CaCl₂ brine (5API brine). The particles are either bare and ungrafted, or coated with 1.5 $\mu\text{mol}/\text{m}^2$ of PEG-silane (actual coverage). This figure is identical to Fig. 2.8 and is shared here as reference.

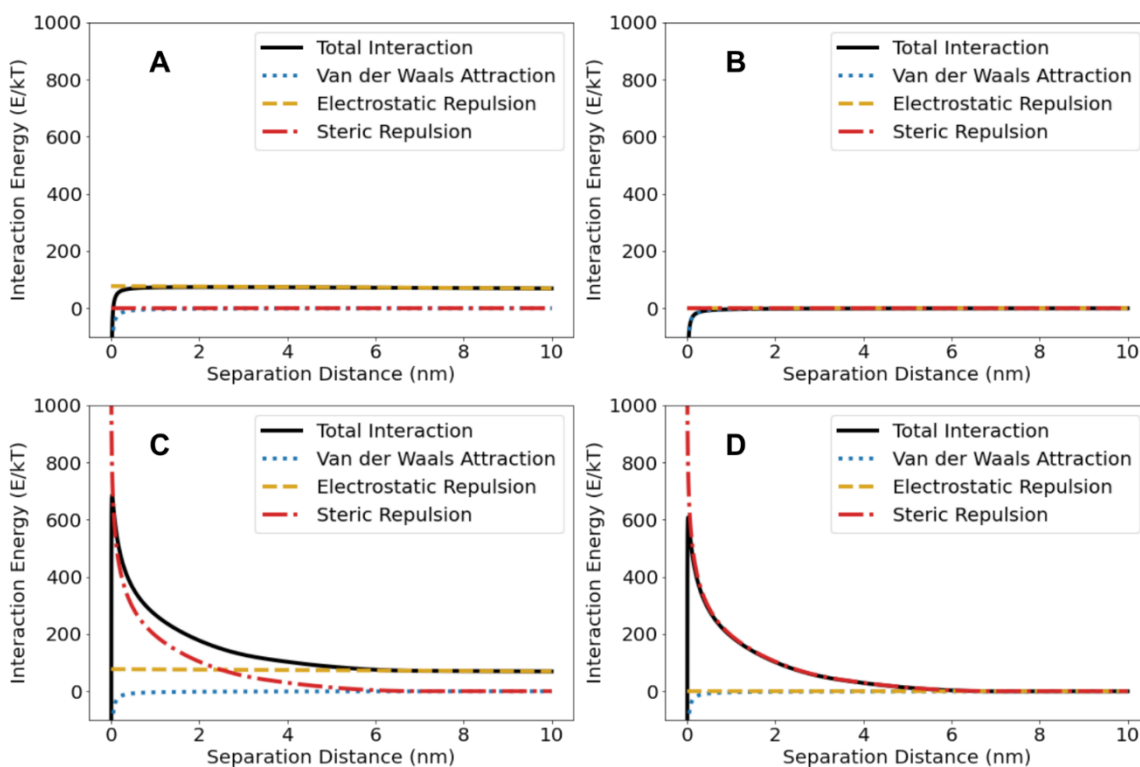


Fig. B.1. (a) DLVO interaction potential of bare, ungrafted silica in DIW; (b) DLVO interaction potential of bare, ungrafted silica in 5API brine; (c) DLVO interaction potential of PEG-coated silica in DIW; (d) DLVO interaction potential PEG-coated silica in 5API brine. Only (b) predicts particle aggregation.

A positive interaction potential over some distance indicates particle stability to aggregation. From DLVO calculations, we see that case (a) is stabilized via electrostatic interaction, (d) is stabilized via steric interaction, and case (c) is stabilized by both electrostatic and steric interaction. Only case (b) has a negative interaction potential for most distances, and as a result is expected to be unstable. As a qualitative test for particle stability, dispersions matching these four cases were mixed in cuvettes and imaged in Fig. B.2.



Fig. B.2. Qualitative stability test of silica particles. From left to right, the cuvettes contain (1) bare, ungrafted silica in DIW; (2) bare, ungrafted silica in 5API brine; (3) PEG-coated silica in DIW; and (4) PEG-coated silica in 5API brine. The second cuvette, (2), is analogous to case (b) from Fig. B.1.

All four of the cuvettes appear cloudy. This appearance is not due to instability, but due to the large particle diameter (100 nm) getting close enough to the wavelength of light to produce a Tyndall effect. The second cuvette, however, is clearly aggregated: the particles have settled to the bottom of the cuvette, whereas the liquid phase is conspicuously clear. While simple, qualitative tests like the one discussed above were useful for quickly assessing particle stability and silane grafting.

B.2 DYNAMIC LIGHT SCATTERING (DLS)

DLS was a useful measurement that we performed to determine particle diameter. We used two different DLS instruments throughout our experiments: a Malvern Zetasizer Nano ZS (Chapters 3 and 4) and a Brookhaven ZetaPals (Chapter 5). As we will discuss later, both instruments were used to measure zeta potential, as well. The operation of both instruments was similar. We pipetted 1 ml of 0.5-1 wt% particles in DIW or brine into a

DTS0012 cuvette. The concentration needed to be low enough that the count rate was less than 500 kcps (preferably under 300 kcps). The Malvern Zetasizer reported the particle diameter as the Z-average diameter (an intensity-weighted measure). The ZetaPals instrument was operated in the particle sizing mode, with the NNLS model in BI-MAS configuration [Da et al., 2018; Xiongyu et al., 2022]. For the ZetaPals instrument, we used the volume-average diameter.

Initial particle stability (a single measurement, usually particles dispersed in DIW) was useful for screening. Old batches of stock aqueous silica could degrade over time, and this degradation was identified with DLS. DLS measurements in DIW also worked well with unfiltered nanoparticles after a grafting reaction, and were convenient for testing the success of a grafting reaction before committing time to filter the particles. Broad particle size distributions and particle dispersity indices (reported by DLS), as well as unusually large particle diameters, were indicators that particles had partially aggregated.

DLS was especially useful for measuring long-term particle stability. We dispersed particles in glass vials at a desired particle and brine concentration (we sometimes adjusted other parameters, including pH and surfactant concentration). The particles were then kept for some length of time and periodically measured. We used the growth of particles over time to calculate a stability ratio, given by Eq. (B.2):

$$W = \frac{4k_B T N_o t_{1/2}}{3\mu}, \quad (\text{B.2})$$

where W is the stability ratio, k_B is the Boltzmann constant, T is temperature, N_o is the initial particle number concentration, $t_{1/2}$ is the half-life of the number of particles, and μ is the aqueous phase viscosity. The stability ratio, W , is dimensionless. To illustrate the calculation of W , Fig. B.3 plots the number concentration (N_p) divided by N_o of PEG-

coated silica dispersed in 5API brine for different PEG surface grafting densities. This ratio was calculated as the cube of the ratio in DLS-measured particle diameters.

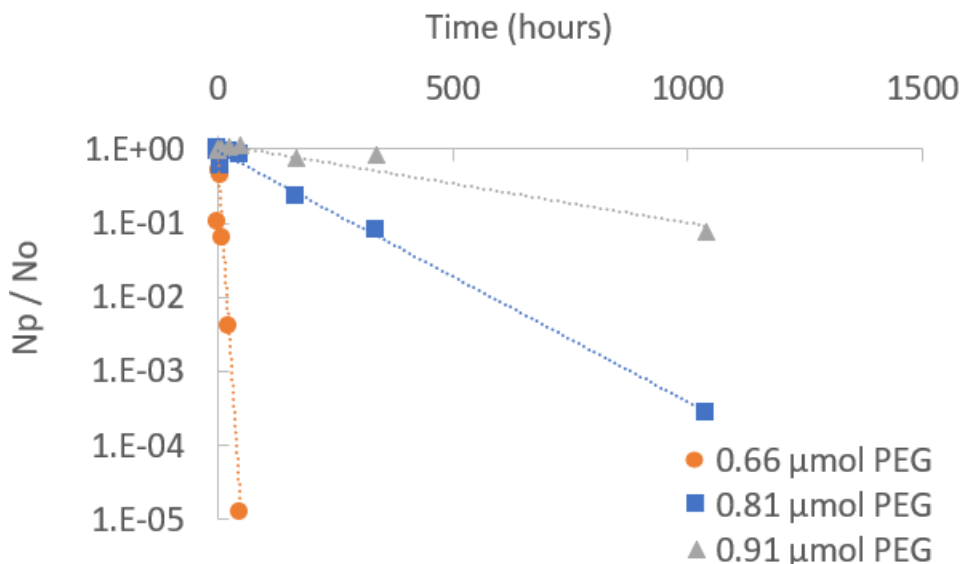


Fig. B.3. Particle number concentration divided by the initial particle number concentration (N_p/N_o) of PEG-coated NexSil 6 particles in 5API brine, plotted as a function of time (0.66-0.91 $\mu\text{mol/m}^2$ PEG coating).

The 0.66 $\mu\text{mol/m}^2$, 0.81 $\mu\text{mol/m}^2$, and 0.91 $\mu\text{mol/m}^2$ particles plotted in Fig. B.3 had exponential rate constants of -0.23448, -0.007877053, and -0.00224426, respectively; these values translate to half-lives of 88, 310, and 1100 hours. From these half-lives, we calculated W values of 9×10^6 , 3×10^8 , and 1×10^9 , respectively.

To measure DLS diameter at elevated temperature, we kept the glass vials in a temperature controlled hot water bath. Fig. B.4 displays the water bath and a metal block used to hold particle samples.

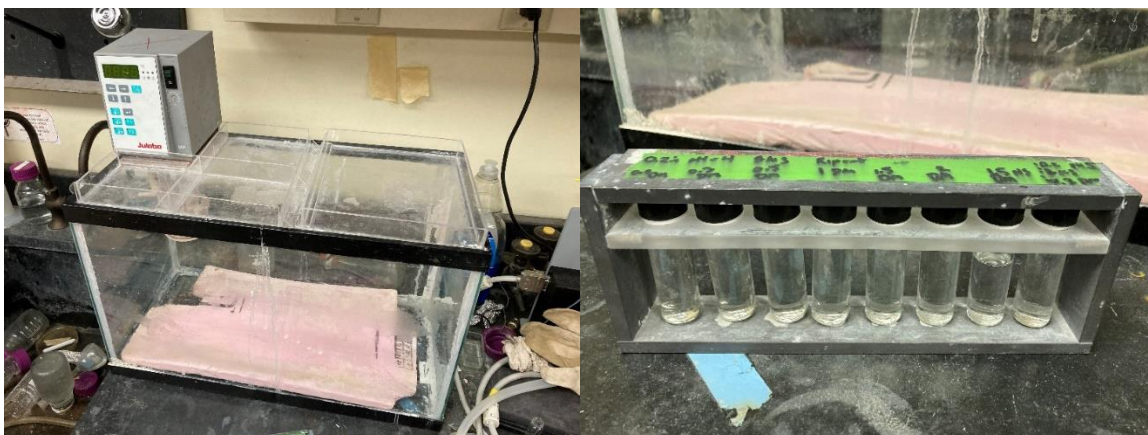


Fig. B.4. Left: image of the hot water bath used to store particle samples at high temperature for long-term stability measurements. Right: metal block used to hold and visualize particles during high-temperature storage.

The water bath was filled with tap water and maintained at 80°C. The pink foam was kept at the top of the water level as an insulator. We needed to add water every 3-4 days to maintain the water level. The glass vials were placed inside a specially-fitted metal block that could sink to the bottom of the water bath. This arrangement allowed us to easily visualize any signs of aggregation within the samples. The glass vials were sealed using PTFE tape, which we replaced weekly to ensure that tap water did not enter. By observing the water level in each sample, we confirmed that no vials had leaked throughout our experiments.

B.3 TRANSMISSION ELECTRON MICROSCOPY (TEM)

We used TEM to visualize the distribution and morphology of particles. We took aberration-corrected STEM images with a JEOL NEOARM at 80 kV. A small (20 μ l) droplet of particles diluted to 0.1-1 wt% was deposited onto the carbon side of a carbon-gold lacey grid (300-mesh, Ted Pella Inc). We dried the grid with particles in an oven for 30 minutes at 100°C to remove water and carbon contamination. Because of this drying

step, we could only perform imaging on grafted particles; bare, ungrafted silica would aggregate as the water was removed.

TEM imaging produced good images for all particles, but the quality was especially high for larger particles, such as the images of NexSil 125-40 displayed in Fig. B.5. These images show that, the time of imaging, the particles were bunched together at the edges of the lacey grid at low concentration and could stretch across gaps at higher concentrations. A similar image is shown for NexSil 12 particles in Fig. B.6.

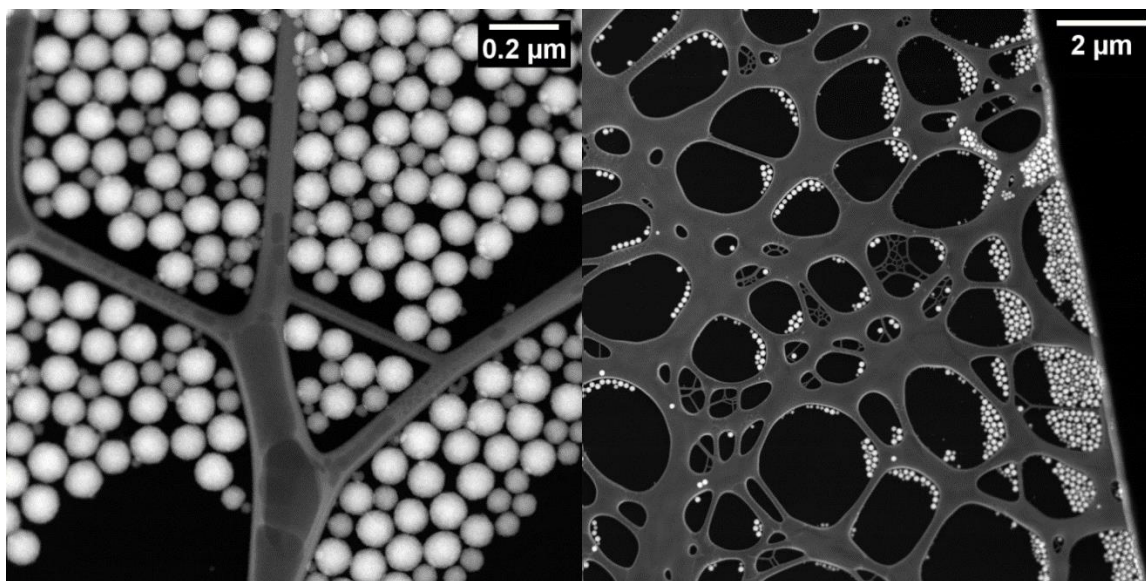


Fig. B.5. TEM images of $1.92 \mu\text{mol}/\text{m}^2$ PEG-coated NexSil 125-40 particles deposited on a carbon-gold lacey grid. After drying, particles grouped together and could be found along the edges of the carbon “web”.

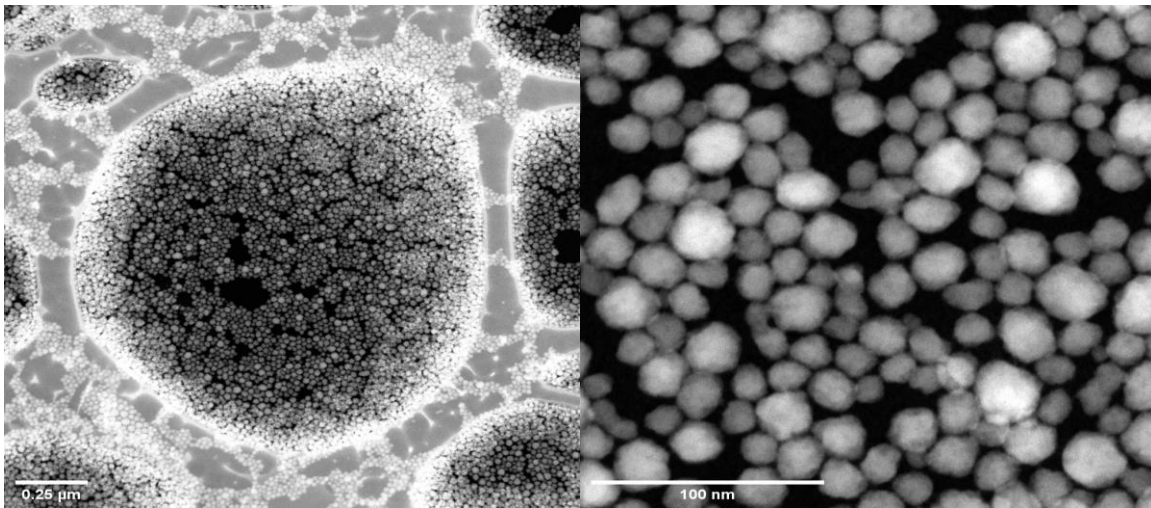


Fig. B.6. TEM images of $1.84 \mu\text{mol}/\text{m}^2$ PEG-coated NexSil 12 particles deposited on a carbon-gold lacey grid. Particles were widely distributed around the gaps.

B.4 CONTACT ANGLE MEASUREMENT

We measured the particle contact angle to determine the wettability of the particles with respect to the aqueous phase in the presence of decane, air, and liquid CO_2 . Wettability is important for particle-interface interactions, and can change significantly after surface modification. We measured the contact angles by spin-coating particles on a glass surface, depositing an aqueous droplet onto the glass, and imaging the droplet-glass interface in different non-wetting mediums.

B.4.1 Spin-coating

We performed spin-coating with a Laurell WS-650-23 spin-coater. This specific instrument was located inside a class 100 clean room at the University of Texas at Austin. The spin-coater has multiple attachments designed to hold different substrate geometries; we used the attachment designed to hold standard glass microscope slides for all of our experiments. Fig. B.7 shows an image of the spin-coater.



Fig. B.7. Laurell WS-650-23 spin-coater. This specific instrument is located inside a class 100 clean room.

We prepared the glass microscope slides for spin-coating by washing them overnight with dilute HCl. We put multiple microscope slides with a magnetic stir bar into a glass bottle filled with 0.01 M HCl. We then sealed the bottle with PTFE tape, placed it in an oil bath temperature-controlled at 70°C, and allowed it to stir overnight. Once complete, we extracted the glass slides, rinsed them with 2-propanol and DIW, and dried them with a high pressure air hose. In the clean room, we placed the slides into the spin-coater and pipetted 10 wt% particle solution (usually, the unmodified product of the particle silanization and filtration process) onto the slide, adding just enough to coat the entire surface. We then ran the spin-coater at 1000 rpm (1000 rpm/s acceleration) for 60 seconds. Once completed and outside of the clean room, we allowed the glass slides to air-dry in a fume hood overnight to remove residual water. The spin-coated slides were then ready for contact angle imaging.

B.4.2 Contact angle in air

The contact angle measurements of a particle-aqueous-air system were the easiest to perform. We placed the spin-coated glass on a viewing platform monitored by a Nikon camera. Using a pipette, we deposited a 7.5 μl aqueous droplet (either DIW or brine) onto the glass slide. The system was aligned such that the entire droplet, including its alignment with the glass, was in full view of the camera. Using the software OneAttention by Biolin operating in the sessile drop configuration, we calculated the contact angle of the particles with respect to the aqueous phase. We obtained nice droplet images using the following camera settings: exposure = 5141/10261; gain = 250/1023; gamma = 4073/10240; light intensity = 0.747/1.000.

Once deposited onto the glass surface, droplets immediately started to move and spread, effectively demonstrating a shrinking contact angle over time. We experimented with different standards for measuring the contact angle, including measuring the long-term behavior, taking an average contact angle for a select time period after deposition, and using the initial contact angle. The initial contact angle gave the most consistent results, and we reasoned that changes in the contact angle caused by droplet spreading represented movement and removal of particles from the spin-coated surface; as such, we used the first measurable contact angle as our standard for contact angle measurements. We took images at 76 FPS (or 7.6 FPS for decane measurements only, due to short-term issues with the camera), and selected the first image with a complete, non-deformed droplet on the glass surface. Each measurement was performed in triplicate by pipetting aqueous droplets onto different sections of the spin-coated glass. With this method, we obtained excellent contact angle measurements, exhibiting good repeatability and behavior consistent with expected trends, as shown in Figure 5.3.

B.4.3 Contact angle in decane

The procedure to measure contact angle in decane was similar to that in air, with a key difference in how the spin-coated slides were positioned for imaging. We used a plastic flask with vertical walls to contain a volume of decane, inside which we would image an aqueous droplet. The flask we used for measurements is shown in Fig. B.8. The uppermost face of the flask was removed with a saw so the glass slide and decane could be put inside. The clear, flat edges

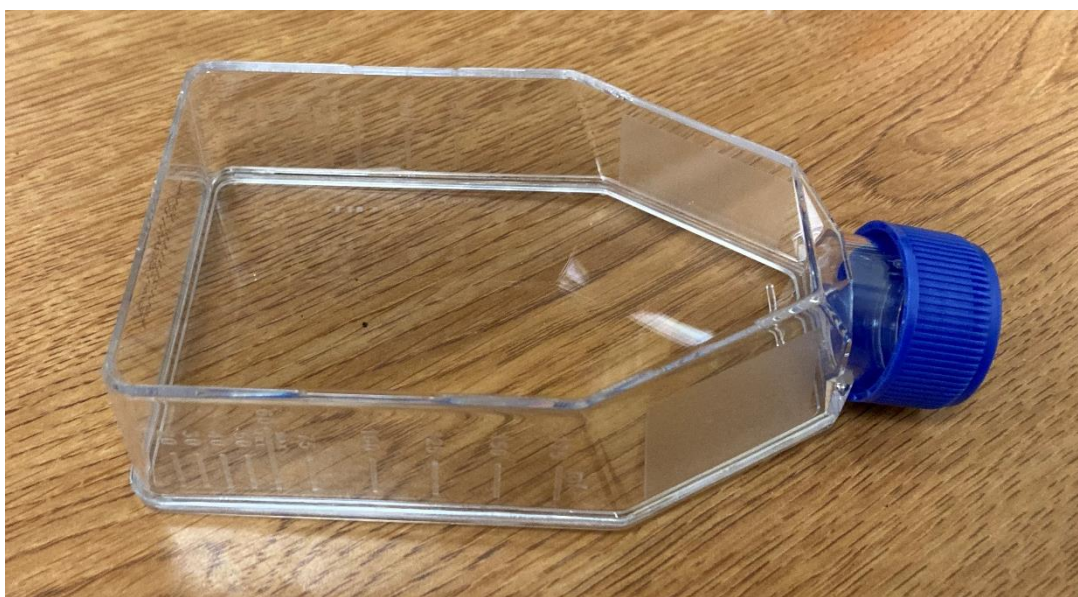


Fig. B.8. Plastic flask used to measure particle-aqueous-decane contact angle. The uppermost face was removed, and a spin-coated microscope slide was placed inside. The bottle was then filled with decane. The clear, flat edges allowed us to take clean, undistorted images of the droplet contact angle.

After placing the spin-coated glass down, we pipetted 50 ml of decane around the glass, raising the oil level to well above the height of a droplet. Using a pipette, we deposited a 7.5 μl aqueous droplet onto the glass surface and measured the contact angle in the same way as described above. Although we were concerned about the flow of decane

into the flask disrupting the particle surface, we saw no obvious noise or unusual trends in our results from these experiments.

B.4.4 Contact angle in liquid CO₂

Contact angle measurement in high-pressure liquid CO₂ required the use of a high-pressure vessel with three view cells (a front and back view cell for the camera, and a side view cell for visual observation during experiments). The specific vessel we used is shown in Fig. B.9, positioned such that the view of the Nikon camera intersected view cells on the front and back.

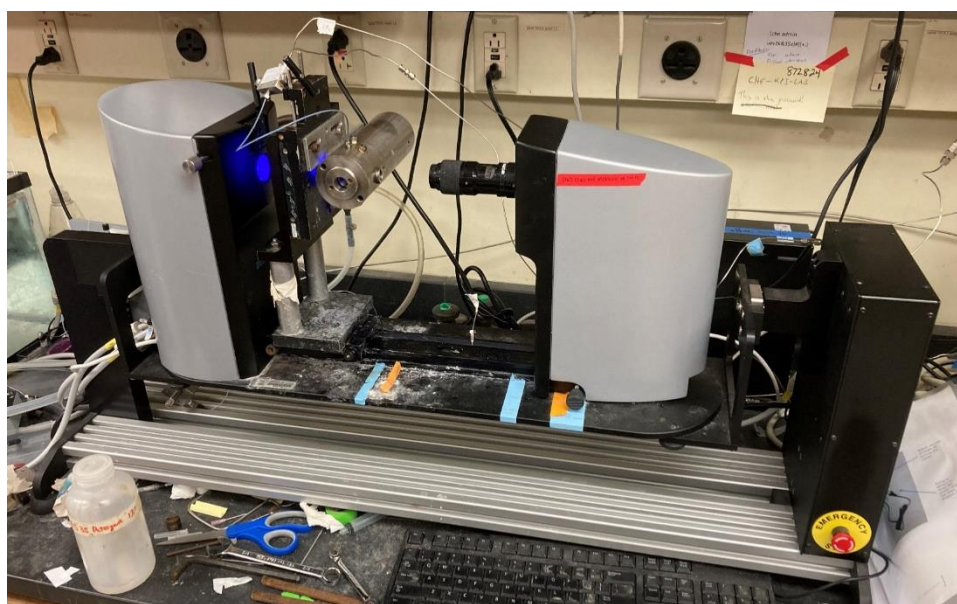


Fig. B.9. High-pressure contact angle measurement apparatus, including a metal high-pressure vessel and camera. The vessel and camera are mounted onto a tilt cradle.

A single line ran through a connection at the top of the high-pressure vessel. This line was swapped out as necessary to inject CO₂ or the aqueous phase into the vessel, and to vent CO₂ at the end of the experiment. The vessel included a piston for variable pressure

measurements, but we compressed it to its maximum extent to minimize the volume of CO₂ necessary for the imaging chamber. The backside of the piston was filled with water and sealed to apply back pressure.

We used a specially-cut glass piece to measure contact angle inside the high-pressure vessel. The glass piece is about one centimeter across and was designed to fit a small mount frame with two holes drilled into the sides for mounting screws. This glass piece is shown in Fig. B.10.



Fig. B.10. Left: specially-cut glass piece screwed in place on a mount. The mount plugged into the bottom of the high-pressure vessel, sealed with an o-ring. Right: view of glass piece in the direction perpendicular to the camera. The inlet line can be seen hovering closely above the glass surface.

The glass piece is normally too small to use with the spin-coater. Our workaround was to attach the glass piece to a (non spin-coated) microscope slide with double-sided tape (really, just single-sided tape wrapped around in a circle). It was necessary to tape the tape itself into place. Fig. B.11 shows an image of the glass piece correctly fastened to the microscope slide. The tape was cut off at the sides of the slide to prevent interference with the vacuum holding it to the spin-coater.

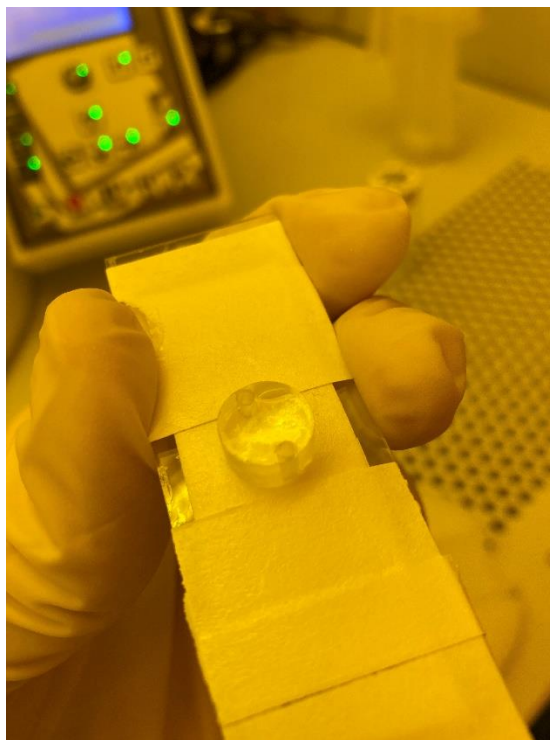


Fig. B.11. Glass piece attached to microscope slide in preparation for spin-coating.

Spin-coating was carried out with the glass piece in a similar way to the microscope slide. We usually noticed some residual liquid after spin-coating, so we ran the 60 second spin-coat method twice. At 1000 rpm and 1000 rpm/s acceleration, the glass piece did not detach from the base slide when attached with the above method. Following spin-coating, the glass piece was air-dried in the fume hood.

Once ready for imaging, the glass piece secured to the bottom mount and inserted into the high-pressure vessel. We injected CO₂ at a rate of 5 ml/min – a slow rate intended to not disturb the particle coating. CO₂ was injected with an ISCO pump over the course of an hour, usually in two or three stages. Pressurization was complete when liquid CO₂ filled a majority of the pressure vessel and submerged the glass piece, which occurred at a pressure of approximately 950 psi. We used 950 psi liquid CO₂ rather than 2200 psi liquid

CO₂ (the pressure of our foam system) for two reasons: firstly, at vapor-liquid equilibrium, the system pressure was held constant throughout the imaging process; and secondly, the density of 950 psi liquid CO₂ was closer to that of supercritical CO₂ at our foam conditions than the density of 2200 psi liquid CO₂.

Once fully pressurized, we switched the inlet line with a line feeding an aqueous phase (either DIW or brine adjusted to pH 4) from another ISCO pump. Using this second pump, we injected the aqueous phase into the vessel at 0.1 ml/min. Once the front of the aqueous phase was visible at the inlet line, we quickly dropped the flow rate to 0.01 ml/min. By carefully alternating between injection and refilling, we positioned a droplet just above the glass surface and allowed it to connect. Given the relatively low position of the inlet line, contact between the glass surface and droplet caused the droplet to snap off of the inlet line. The first frame of a fully-formed, non-distorted droplet after snap off was used to calculate the contact angle. We carried out this process three times in the same experiment, assuming that increasingly large droplets would wet a new perimeter on the glass surface and therefore provide multiple measurements of the contact angle.

B.5 ZETA POTENTIAL

We measured particle zeta potentials to determine the surface charge of our particles. Zeta potential is affected by particle material, pH, aqueous salinity, and surface modification. Zeta potential was measured by the aforementioned Malvern Zetasizer Nano ZS and ZetaPals instruments. When using the Malvern Zetasizer, particles were dispersed in DIW at a concentration of 1 wt%. We pipetted 800 μ l of particle dispersion into a DTS 1070 zetacell, ensuring that the liquid level was between the two fill lines. We tapped the zetacell several times to dislodge any air bubbles present when filling. Measurement with the Zetasizer was straightforward using built-in methods. After measurement, the zetacell

was emptied and washed eight times with a 10 ml syringe. We then injected air eight times with a new syringe, placed the zetacells in an oven tray, and heated them at 60°C overnight to remove residual water. We tracked the number of uses of each zetacell, and reused zetacells up to ten times (it has been reported that zetacells can be reused up to 40 times with good results).

When running the ZetaPals instrument in the ZetaPals mode, we dispersed particles at a concentration of 0.05 w/v% in 1 mM KCl solution. We titrated the solution with HCl or NaOH to bring it to a range of pH, using a Mettler Toledo Seven2Go pH meter S2. The pH meter is listed at ± 0.01 accuracy, and we took calibration measurements with pH 4, pH 7, and pH 10 standards before any measurements. We transferred 1.7 ml of the particle mixture at different pH intervals during titration into a DTS 0012 cuvette for measurement. We titrated two samples of particles for each series of zeta potential measurements – once from its natural pH of 5 up to pH 12 with NaOH, and again from pH 5 to 2 with HCl. Inserting and electrode connected to the ZetaPals instrument into the cuvette, we measured the samples with the Smoluchowski model. Given the large variance reported by zeta potential measurements, we had the instrument perform six runs and took an average as our reported value.

B.6 TITRATION

The final characterization method that we conducted was silane titration. The purpose of these experiments was to measure protonation curves of N3. N3 was capable of stabilizing particles in high-temperature, high-salinity conditions, but this stability was linked to its “switchable” ability to protonate at low pH. Titration curves allowed us to determine if N3 would sufficiently protonate at a given temperature, salinity, and pH threshold.

We performed titration in a three neck flask, shown in Fig. B.12. The flask was filled with 50 ml of brine (specific to the experiment) and 0.01 M of silane. When measuring multiple silanes, we used 0.01 M of each. The flask was equipped with a magnetic stir bar and stirred throughout the titration process. The central neck of the flask was connected to a burette containing 80 mM HCl, which we drained into the flask as necessary for titration. The rightmost neck was plugged with a stopper, leaving a small hole for the Mettler Toledo pH meter to enter and contact the liquid. The leftmost flask was left open for room temperature measurements.



Fig. B.12. Three-neck flask used for silane titration. The center neck connects to a burette administering dilute 80 mM HCl; the rightmost neck connects to the pH meter. The leftmost neck, unused in the image, was connected to a condenser for measurements at 80°C.

Titration were conducted and analyzed in accordance with Eq. (B.3):

$$\theta = \frac{C_a * V_{titrant} + (C_{OH^-} - C_{H^+}) * V_{titrand}}{C_{total} * V_{titrand,0}}, \quad (B.3)$$

where θ is the degree of protonation (fraction of amino groups on N3 successfully protonated at a given pH). θ was is determined by C_a , the molar concentration of HCl (80 mM), C_{OH^-} , the equilibrium molar concentration of OH^- (determined by pH), C_{H^+} , the equilibrium molar concentration of H^+ (determined by pH), C_{total} , the molar concentration of protonatable functional groups (in our case, triple the molar concentration of N3), $V_{titrant}$, the cumulative volume of 80 mM HCl added throughout the titration, $V_{titrand,0}$ is the volume of brine before the titration (50 mL), and $V_{titrand}$, the sum of $V_{titrant}$ and $V_{titrand,0}$.

We performed 80°C measurements in a fume hood. The leftmost neck, unused for room temperature measurements, was connected to a jacket condenser circulating cold tap water. The flask was lowered into an oil bath and maintained at 80°C with a temperature-controlled hot plate. With this arrangement, we were able to measure pH at elevated temperature without appreciable water evaporation.

Appendix C: Emulsion Generation and Measurements

In this section, I will review the methods of emulsion generation, imaging, and centrifugation that we used for our experiments. These procedures are largely based on work by Griffith and Daigle [60,81,105].

C.1 GENERATING EMULSIONS

We generated emulsions by sonicating mixtures of a particle-rich aqueous phase and oil. While the oil type and water-oil ratio can be adjusted to generate different emulsions, we always made 40 ml emulsions with 50:50 aqueous phase and decane in our experiments.

We prepared the aqueous phase in a 50 ml glass beaker. We mixed filtered nanoparticles with DI, NaCl, and CaCl₂ in desired proportions and stirred thoroughly. We often worked with 5API (4 wt% NaCl, 1 wt% CaCl₂) brine. Rather than weighing and mixing salts for each emulsion, we typically prepared this brine by diluting 20 wt% brine from a large, pre-mixed batch. Emulsions were sometimes generated with deionized water (DIW), in which case salts were omitted. We produced approximately 22 ml of aqueous phase for each emulsion; from this initial batch, we pipetted 20 ml into a separate 50 ml glass beaker. Into this new beaker, we added 20 ml decane. As a result, we had an exactly 50:50 water-oil ratio, as well as a carefully mixed aqueous phase with specific mass concentrations of nanoparticles, NaCl, and CaCl₂. We placed our second beaker – now containing 20 ml of aqueous phase and 20 ml of decane – inside a Branson 450 Digital Sonifier, shown in Fig. C.1.



Fig. C.1. Branson 450 Digital Sonifier for sonicating oil and water mixtures to form emulsions.

We positioned a 5 mm sonicator microtip just below the water-oil interface and set the amplitude to 50%. Sonication was run for ten seconds. After ten seconds, we removed the beaker and stirred the partially-emulsified mixture with a spatula. We performed two more ten-second sonications, stirring before and after, to fully emulsify the mixture. With this method, a freshly-generated stable emulsion had an opaque, white appearance and noticeably higher viscosity than water. Fig. C.2 displays two fully-emulsified mixtures.



Fig. C.2. Two batches of stable emulsion following the emulsification process.

C.2 EMULSION DROPLET IMAGING

We analyzed emulsion droplets using a Nikon Labophot-Pol microscope and Nikon Digital Sight DS-Fil camera connected to a computer. The purpose of emulsion microscopy was to determine the volume weighted diameter, D_{32} (also known as the Sauter diameter), given by Eq. (C.1).

$$D_{32} = \frac{\sum_i^n D_i^3}{\sum_i^n D_i^2}, \quad (\text{C.1})$$

D_{32} is equal to the sum of diameters (D_i) cubed, divided by the sum of diameters squared, from a set of n droplets.

We deposited 40 μl of emulsion onto a glass microscope slide, fixed the droplet with a cover slip, and imaged the droplets at different zoom scales. Based on observations of the focal planes above and below the glass slide and cover slip, respectively, we estimated that the cover slip lay 50 μm above the glass slide (we would eventually use this value when calculating average droplet diameters). For most images, it was necessary to

first dilute the emulsion in brine. The dilution factor required to produce good images ranged from 50x for the smallest (and therefore most concentrated by volume) emulsion droplets to 2-5x for the largest emulsion droplets. For each emulsion, we collected ten images at different locations of the microscope slide at 4x, 10x, and 40x magnification (if an emulsion was obviously too large or small for a given magnification, we omitted that magnification).

Emulsion images were analyzed with Fiji ImageJ to extract the set of individual droplet diameters, which we would later factor into a single value of D_{32} . We followed the following algorithm to determine droplet diameters:

1. The image was converted to 8-bit
2. Subtract a background image (8-bit) from the main image (unnecessary for 10x and 4x magnification)
3. Binarize the image
 - a. There are a few ways to do this, but our preference was to set minimum and maximum brightness to equal 5
 - b. Binary threshold with the Otsu method was another option
 - c. The binarization step was generally subjective
4. Crop a 400 by 400 pixel square from the top left corner of the image
5. If necessary, invert the image
6. If necessary, fill holes
7. Run particle analyzer with a minimum size of 10 pixels and circularity of 0.8-1.0

Normally, steps 4-7 were run through a macro in ImageJ. The stages of image processing – initial microscope image, binarized image, and identification of individual droplets from particle analysis – are shown in Fig. C.3.

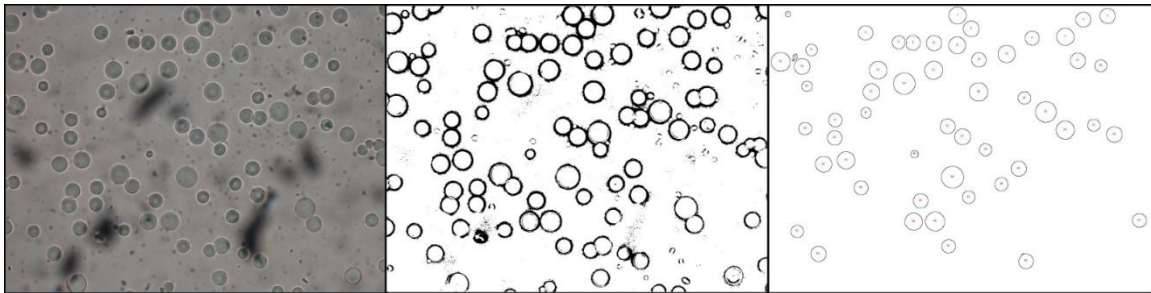


Fig. C.3. Left: initial microscope image of an emulsion. Center: binarized image, segmenting the droplet boundaries as black. Right: final result after running the particle analyzer in ImageJ.

Individual droplet diameter values were tabulated in Excel and processed in MATLAB. Emulsion droplet diameters were collected from 40x, 10x, and 4x magnifications. The distribution of droplet diameters from each image were weighted such that the different magnifications covered equal area on the microscope slide (for example, a droplet imaged from 40x magnification would have 100x the weight of an image from 4x magnification, because the latter represented 100x more area on the microscope slide). The same 400-by-400 pixel section in the corner of each image was analyzed by ImageJ to keep track of microscope slide areas for weighting purposes and to reduce the amount of variation in focus across the image.

To prevent noise, a cutoff value of 50 pixels of measured droplet area (stricter than the original 10 pixel cutoff from the particle analyzer) was used during processing as the minimum droplet size to be considered from each magnification, corresponding to diameters of approximately 2 μm at 40x magnification, 8 μm at 10x magnification, and 20

μm at 4x magnification. These different cutoff values divided the data into four brackets. Above 20 μm , all magnifications contributed to the dataset; above 8 μm to 20 μm , only the 40x and 10x magnification contributed (droplets from 4x magnification were now smaller than 50 pixels and dismissed as noise); above 2 μm to 8 μm , only the 40x magnification contributed; at or below 2 μm , all measurements were discarded. To prevent over-representation of outlier data during the weighting process, droplet diameters from 40x magnification in a given bracket were not used if they contained fewer than 25 droplets. The resulting combined dataset of all images and magnifications included several hundred unique droplets for each emulsion sample.

To demonstrate repeatability, Fig. C.4 plots individual histograms from four separately generated 0.25 wt% 5 $\mu\text{mol}/\text{m}^2$ (nominal concentration added to the grafting reaction) GLYMO-NP emulsions in 5API brine, which were independently imaged, as well as representative images of the three magnifications from one of the batches. This figure is a modification of Fig. 3.2.

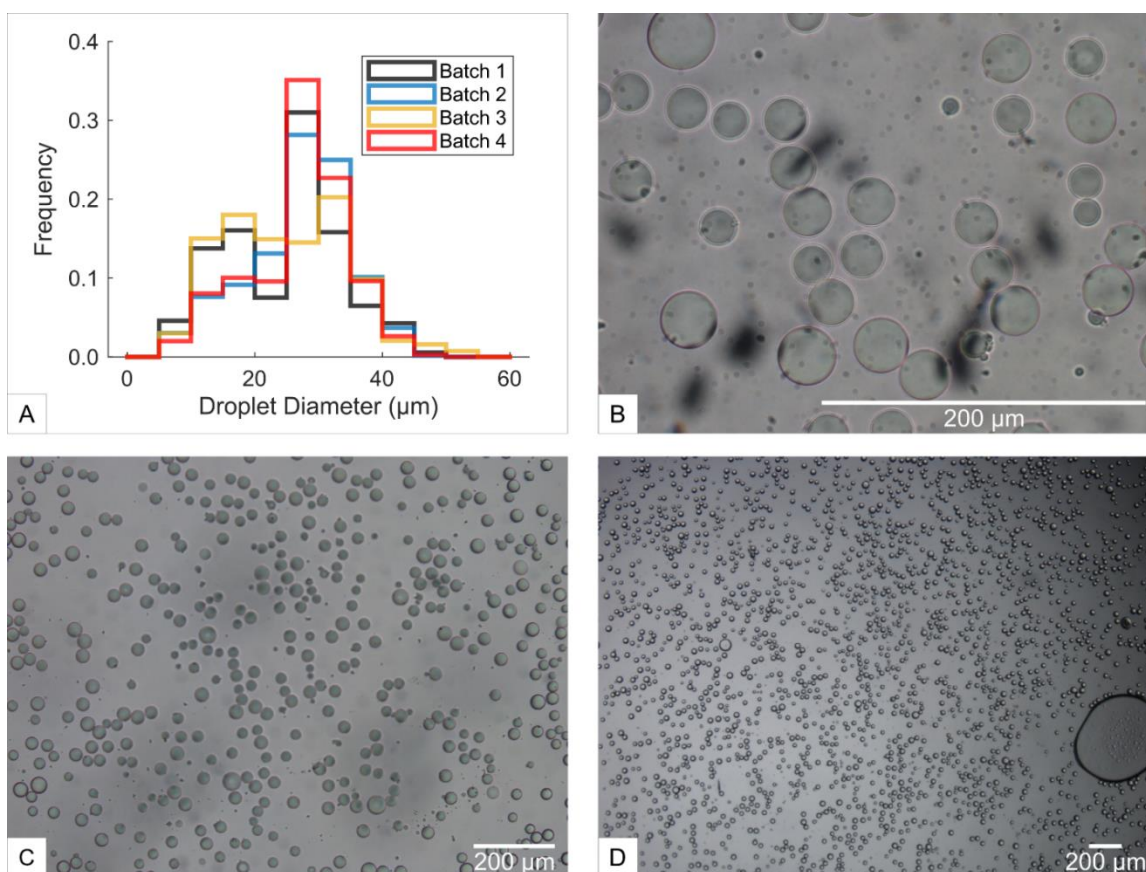


Fig. C.4. (a) Droplet size distributions of four independently generated, imaged, and analyzed 0.25 wt% GLYMO-NP-5API emulsions to demonstrate repeatability of the imaging process. The frequency of droplets at each diameter bin has been normalized to sum to a value of one for each batch. Images (b), (c), and (d) show the same 0.25 wt% GLYMO-NP-5API emulsion sample from one of the batches on a microscope slide imaged at 40x, 10x, and 4x magnification.

The final dataset of droplet diameters was fed into Eq. (C.1) to calculate the D_{32} of the emulsion.

C.3 EMULSION CENTRIFUGATION

We determined emulsion stability by centrifuging emulsions in an Eppendorf 5810R Centrifuge. We pipetted 30 g of freshly-generated emulsion into a 50 ml Falcon

conical centrifuge tube (polypropylene). Once placed in the centrifuge, we ran the samples at 5000 g acceleration for 15 minutes. The compressive forces caused by centrifugation stressed the individual droplets, destabilizing weaker emulsions. After centrifugation, the emulsions separated into three phases: an uppermost decane only phase caused by the coalescence and separation of unstable emulsion droplets; a central emulsion phase, composed of remaining emulsion droplets; and a bottommost aqueous phase, separated from the main emulsion by creaming. Stable emulsions would undergo few droplet coalescence events; as a result, stable emulsions would exhibit little if any of the decane-only uppermost phase. Unstable emulsions, on the other hand, would have little or none of the central emulsion-only phase. Creaming of the aqueous phase at the bottom of the centrifuge tube was observed in all emulsions, regardless of emulsion stability. Fig. C.5. shows an example of three emulsions after centrifugation – two with lower stability, and one with higher stability.

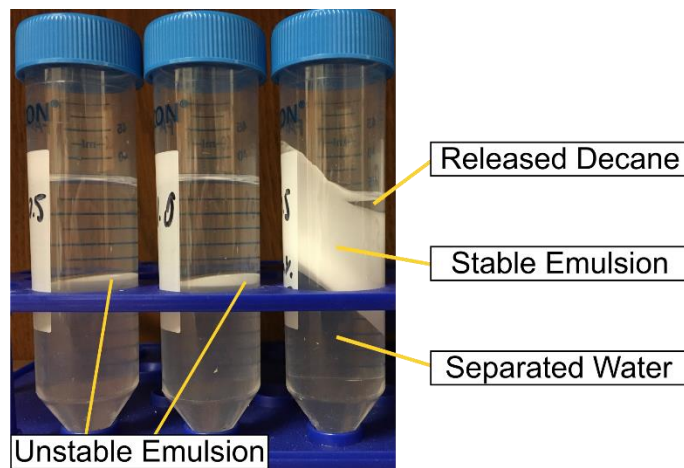


Fig. C.5. Three emulsions after centrifugation for 15 minutes at 5000 g of acceleration. The leftmost and middle emulsions were unstable and nearly fully coalesced after centrifugation; the rightmost emulsion was more stable, and separated into three distinct phases after centrifugation.

The two emulsions on the left and middle of Fig. C.5 were not stable to centrifugation, and coalesced into separate aqueous and oleic phases with some trace emulsion remaining at the interface. The emulsion on the right was more stable; while most of the continuous aqueous phase separated to the bottom, only a small amount of decane was released at the top of the emulsion.

We extracted and weighed the uppermost decane-only phase, converting it into a volume of separated decane. The fraction of decane released from the total decane inside the emulsion was our main metric for emulsion stability, with a higher decane fraction released corresponding to a weaker emulsion, and vice-versa. In order to compare stabilities between different types of emulsion, we carried out a “concentration sweep”. Because emulsions generated with lower nanoparticle concentrations are known to be less stable [80], we identified a concentration range across which an emulsion would transition from completely unstable to completely stable. The concentration of nanoparticles required for an emulsion to release 50% of the total decane was our point of comparison, with lower “50%” concentrations representing more effective nanoparticle emulsifiers.

Appendix D: CO₂ foam apparatus

We In this section, I will describe the operation of the CO₂ foam apparatus in detail. I'll review the flow diagram and give explanations of each section of the apparatus. I'll further discuss the measurement of apparent viscosity and long-term foam stability. Much of this section is based on work by several researchers over the past few years that helped to develop this foam apparatus.

D.1 CO₂ FOAM APPARATUS

We used an apparatus to pump CO₂ and an aqueous phase into a beadpack, shearing to produce CO₂ foam. Care was taken to ensure that the entire apparatus was kept at elevated temperature and pressure, using a combination of heaters and back-pressure regulators (BPRs). For simplicity, we can divide the system into four main sections: (1) the fluid pumps that deliver CO₂ and an aqueous nanoparticle-surfactant mixture into the oven; (2) the convection oven and connected pressure sensors, which shear the CO₂ and aqueous streams together at high temperature (used for apparent viscosity measurements); (3) the microscope assembly, which holds CO₂ foam for long-term storage at elevated temperature and pressure (used for imaging and stability measurements); and (4) the BPRs and surrounding convection bath, which maintain system pressure. Fig. D.1 displays a flow diagram of the CO₂ apparatus. This figure is identical to Fig. 5.1 and is shared here as reference.

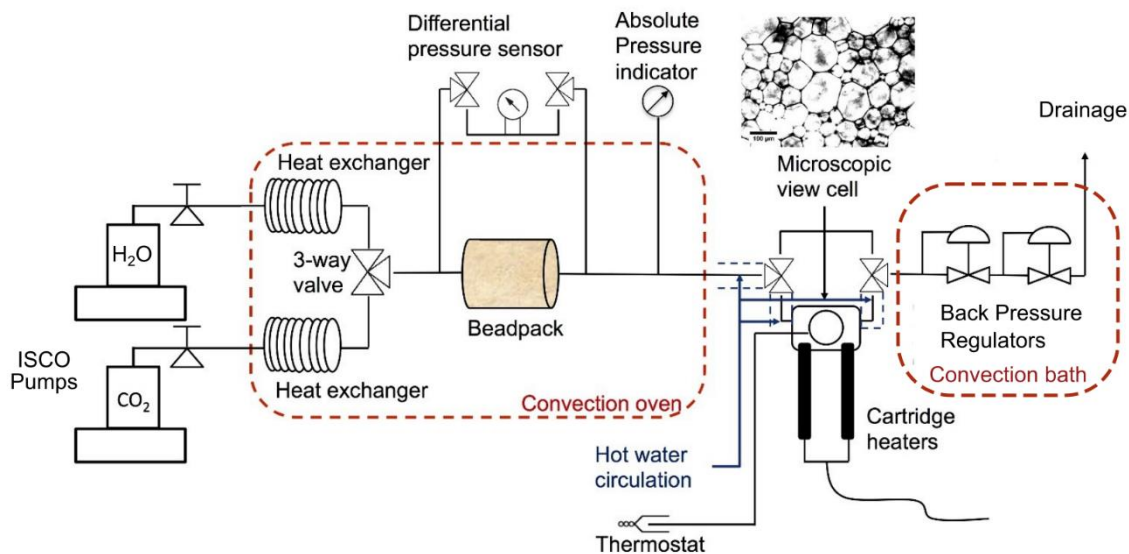


Fig. D.1. Flow diagram of the CO₂ foam apparatus. This figure is identical to Fig. 5.1 and shown here as a reference.

Fig. D.2 displays the first section: the CO₂ and aqueous phase pumps. The upper device was a Teledyne ISCO pump connected to a CO₂ gas cylinder. CO₂ was pressurized to 2250 psi (liquid state) before injection into the foam apparatus. The flow rate of this pump was set to equal 0.7, 0.8, or 0.9 ml/min of pressurized CO₂ at 80°C, giving us a 70%, 80%, or 90% quality foam at the operating conditions. The lower device was a Teledyne Series III HPLC pump, which we used to pump 0.3, 0.2, or 0.1 ml/min of an aqueous phase, respectively, to generate the target foam qualities. We also injected 1-5 ml/min of DIW for apparatus cleaning and permeability measurements. The contents of the aqueous phase depended on the specific experiment, and the conditions are specified in greater detail in Chapter 5. The outlet waste container – the final drainage point indicated in Fig. D.1 – is also imaged.

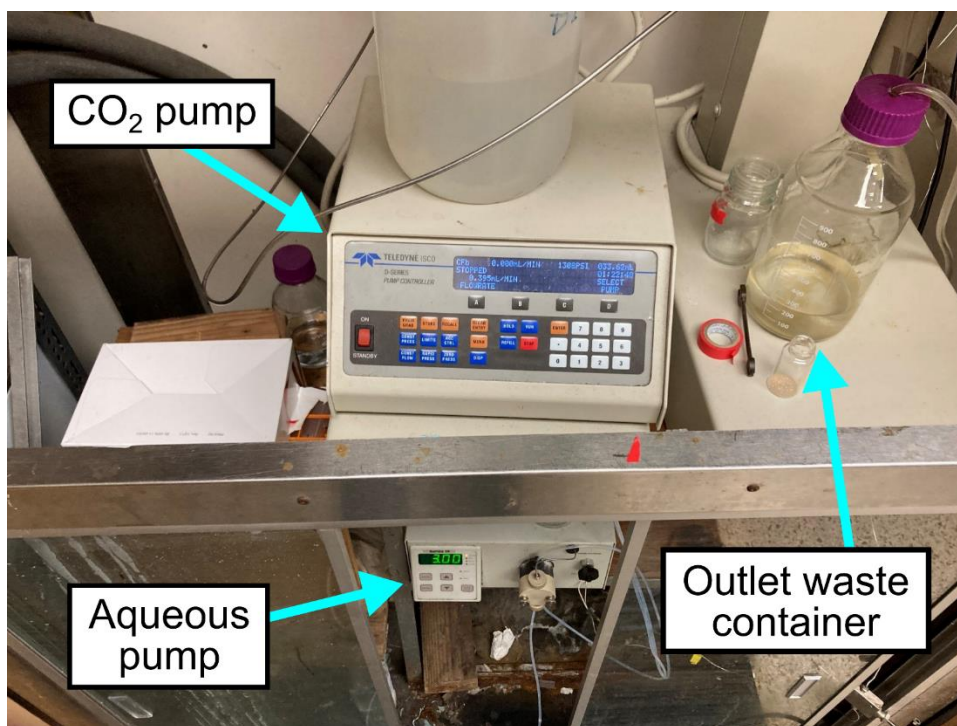


Fig. D.2. Teledyne ISCO and Series III HPLC pumps were used to flow CO₂ and the aqueous phase into the foam apparatus. Also imaged is the outlet waste container, which is downstream of the BPRs.

The two fluid streams entered the second section, a Thermo Scientific Lindberg/Blue M convection oven (set to 80°C). The interior of this oven is shown in Fig. D.3. The two fluids circulated multiple times before joining at the indicated connector. From here, they traveled together towards the beadpack, where they sheared to generate foam. Tubing before and after the beadpack connected to a differential pressure transducer, which we used to measure pressure drop and to calculate foam apparent viscosity. Another line, downstream of the beadpack, connected to an absolute pressure sensor. The flow paths of the two streams and the combined foam are indicated by red arrows. I'll discuss the preparation of the beadpack in more detail in a later section.

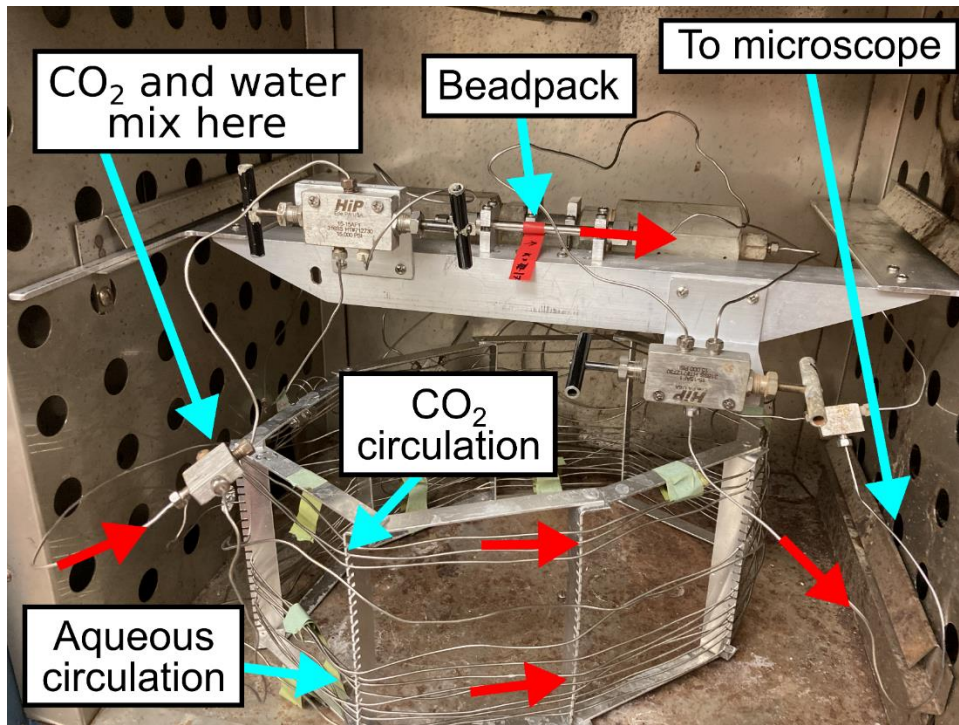


Fig. D.3. Interior of the Thermo Scientific Lindberg/Blue M convection oven. CO₂ and aqueous lines circulate to bring the fluids up to 80°C, before combining at the indicated connector and shearing in the beadpack. Red arrows indicate the critical flow path.

Leaving the oven, the foam flowed towards the third section, the microscope assembly. Fig. D.4 displays the microscope and neighboring flow paths; Fig. D.5 gives a better look at the view cell and internal lines with some of the insulation removed.

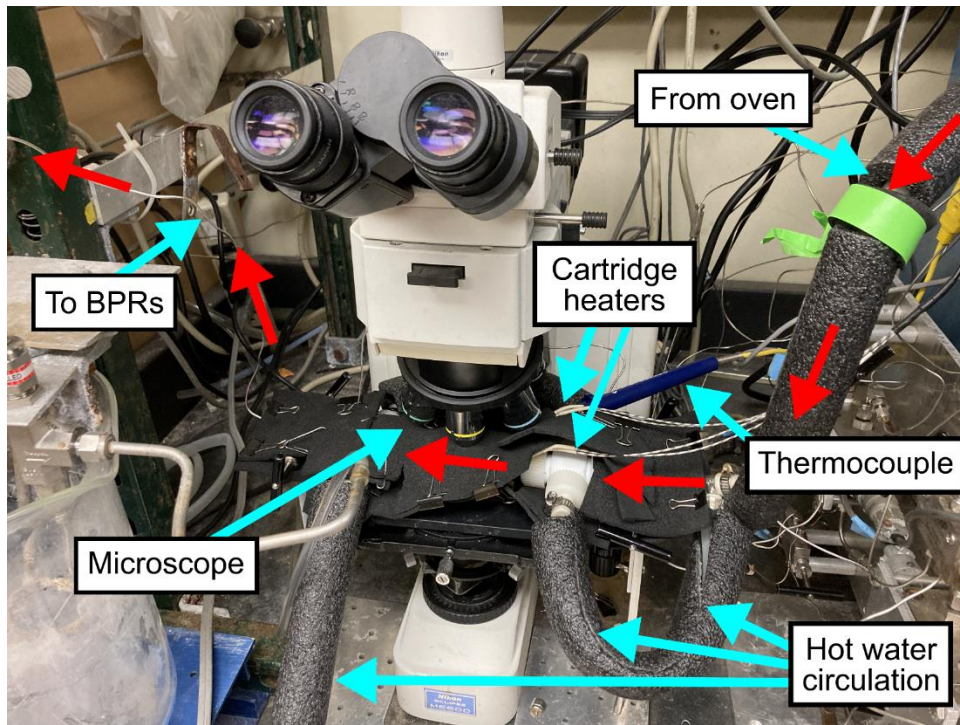


Fig. D.4. Microscope assembly. The foam flowed from the convection oven (out of image to the right) to the BPRs (out of image to the left), passing through the microscope. Layers of insulation maintain the 80°C environment generated by cartridge heaters and hot water circulation. Red arrows indicate the critical flow path.

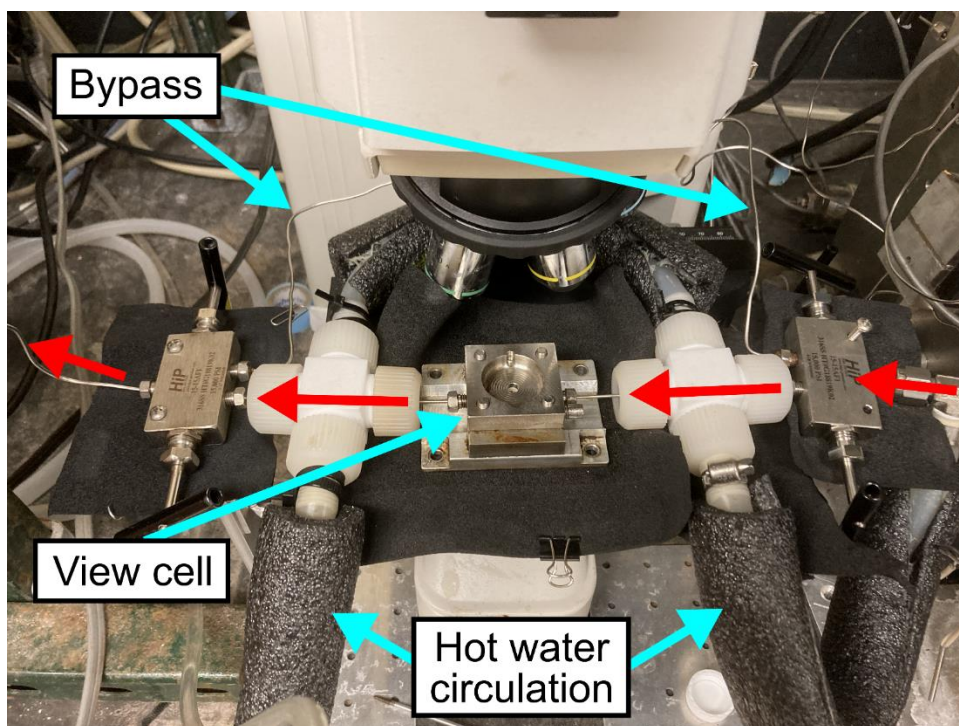


Fig. D.5. Interior of the microscope assembly, with some insulation and cartridge heaters removed. Foam passed through a view cell under the microscope. For long-term foam observation, the view cell could be isolated from the rest of the system by operating the valves, rerouting foam through a bypass line. Red arrows indicate the critical flow path.

Great care was taken to keep the foam at 80°C outside of the oven. The line connecting the oven to the microscope view cell was surrounded by an annular tube circulating hot (80°C) water. The foam flow path was jacketed in this way until it reached the view cell. The view cell itself was heated by two cartridge heating elements, controlled by a thermocouple plugged into the view cell. In this way, any foam section leading to or at the view cell was maintained at 80°C. Insulation was used extensively throughout this section. Areas downstream of the view cell, as well as the bypass line around the view cell, were not directly heated. The hot water circulation tubes looped around back to an insulated

hot water bath (80°C), where they were pumped back into the system. Fig. D.6 displays the pump and water bath for hot water circulation.

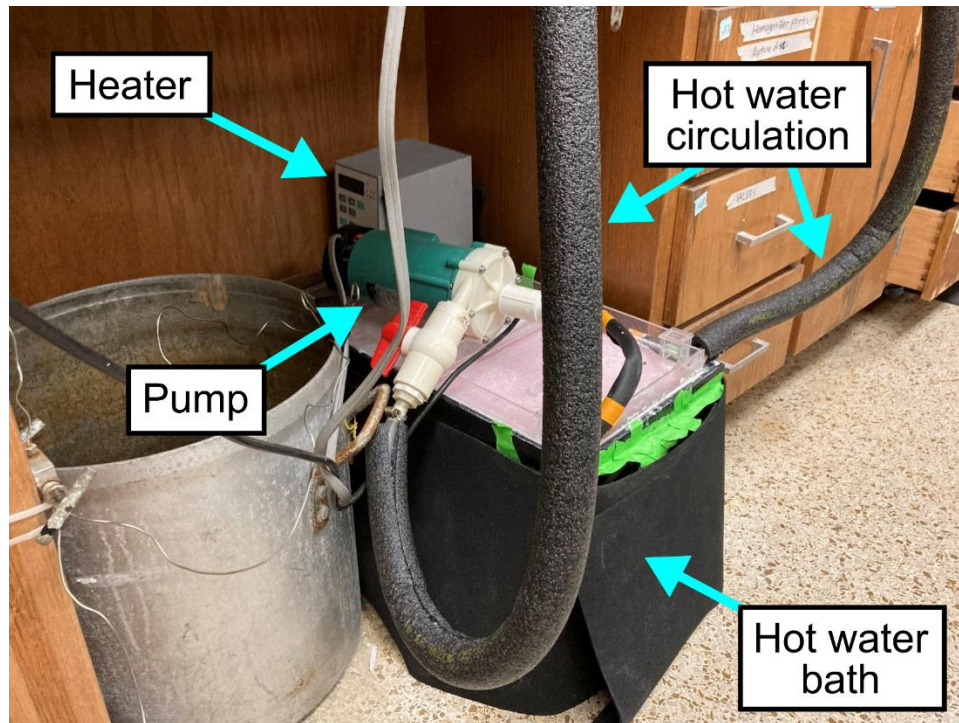


Fig. D.6. Hot water bath and pump. A water bath was kept at 80°C and continually pumped through annular tubing that jacketed the critical flow path. The bath and hot-water circulation lines were extensively insulated.

Leaving the microscope assembly, the foam finally arrived at the final section, the BPRs. Foam flowed through two Swagelok BPRs connected in series. The o-rings in the BPRs were sensitive to damage, so we equipped an in-line filter with 400 mesh screen to catch any stray beads from the beadpack. The lines surrounding the BPRs were kept at 80°C with a convection bath to prevent any freezing upon CO₂ expansion. The BPRs are displayed in Fig. D.7. The outlet from the second BPR fed back into the outlet waste container imaged in Fig. D.2.

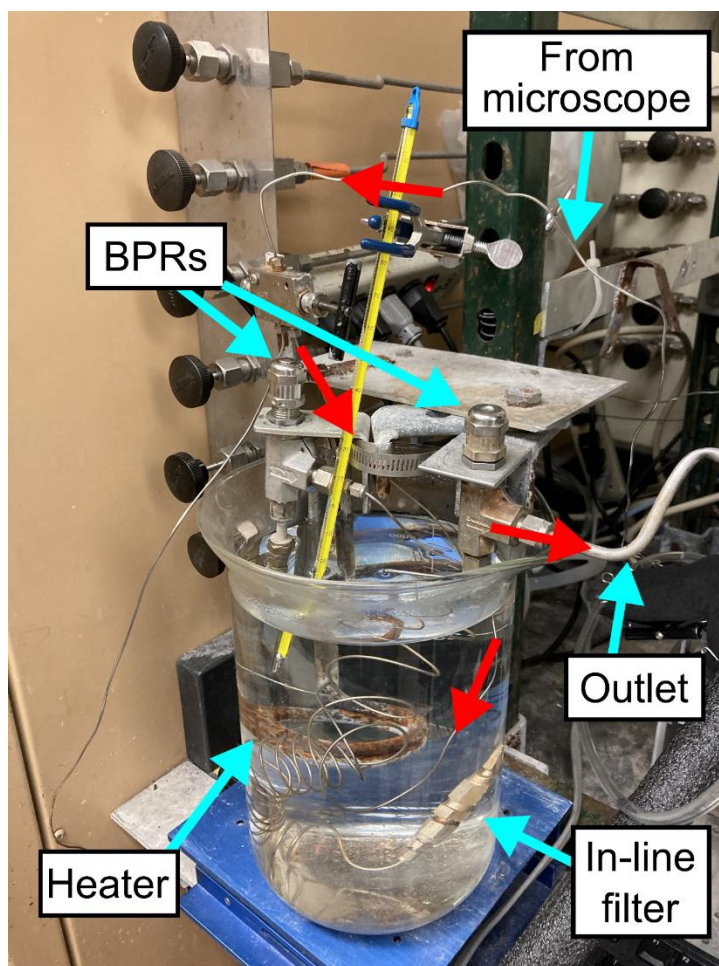


Fig. D.7. BPRs and convection bath. We connected two BPRs in series to maintain the system pressure and heated the tubing to 80°C in a water bath. The in-line filter was positioned upstream of the BPRs. The red arrows indicate the critical flow path, leading to the outlet.

Fig. D.8 shows the controller for the BPR convection bath heater, as well as the absolute pressure sensor.

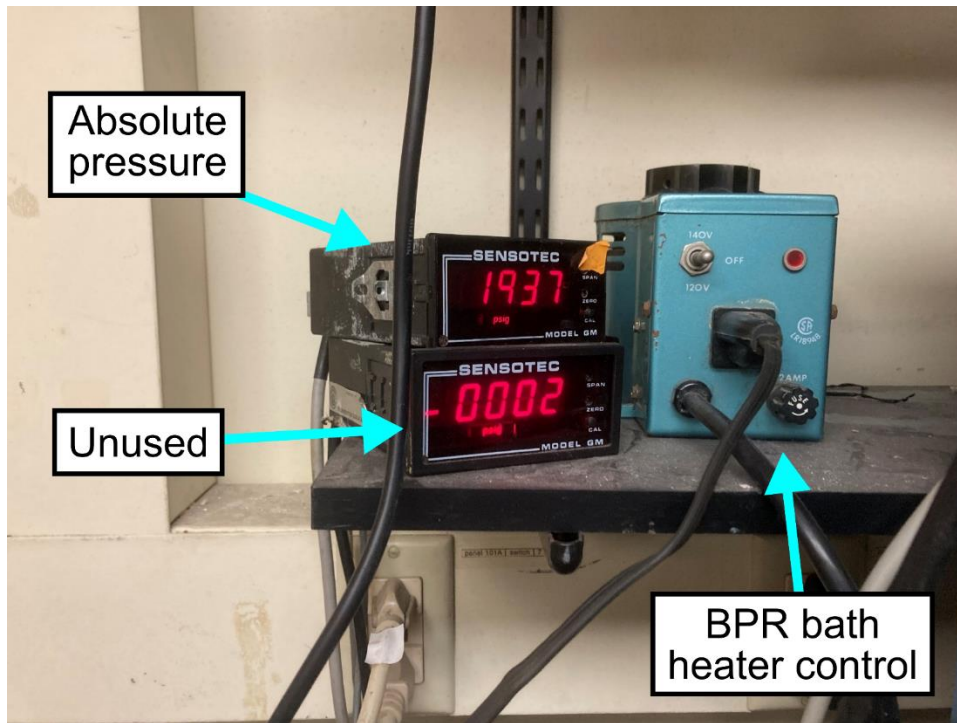


Fig. D.8. Absolute pressure sensor and BPR water bath temperature controller.

D.2 LEAK TESTING

The CO₂ foam apparatus operated at high salinity, high temperature, and high pressure – unfortunately, all excellent conditions for developing leaks. Two types of leaks needed to be addressed: major leaks anywhere in the system, and minor leaks in the view cell. We considered a leak “major” if it was large enough to affect the system pressure when not flowing, and “minor” if the effect on system pressure was negligible (but CO₂ was still being slowly emitted).

The presence of a major leak was identified by pressurizing the system with CO₂, stopping flow, and monitoring the absolute pressure sensor. Rapid drops in absolute pressure (really, any decrease in pressure that was noticeable without consulting time-series pressure data) indicated the presence of a major leak that could affect apparent

viscosity measurements. Note that temperature changes throughout could also lead to absolute pressure drops resembling a leak, so this testing was best performed at room temperature. We searched for leaks by applying a 1% solution of RBS 35 (ThermoFisher) to joints throughout the apparatus. A major leak would generate CO₂ bubbles on contact with the surfactant solution. Once found, we could fix the leak by tightening the joint or by replacing parts. This process could be simplified by strategically isolating different sections of the apparatus by closing valves. We checked for major leaks between every foam experiment.

While RBS solution was effective for finding major leaks, it struggled at identifying minor leaks. Luckily, outside of the view cell, minor leaks were not an issue. The tubing outside of the view cell was continually repressurized by flowing fluid into the BPRs, and as long as the flow rate through a leak was not the same order of magnitude as the internal 1 ml/min foam flow rate, then the leak was likely negligible for the purposes of measuring apparent viscosity. Given the large number of possible leakage sites throughout the apparatus, quick screening with RBS solution was a good solution.

Minor leaks were unacceptable, however, at the view cell. The view cell itself was designed to maintain 2200 psi for several days, even when isolated from the pressurized apparatus during long-term measurements. Because the residence volume of the isolated view cell was relatively small, it was vital to ensure that CO₂ was not leaking out of the view cell. Even a small leak could lead to depressurization in such a small volume over several days. We lost two months of foam experiments because of a particularly insidious leak in the view cell, which we didn't discover until a damaged ferrule causing the leak critically failed and audibly depressurized. To diagnose for minor leaks, we isolated the view cell at high pressure and submerged it under water. If no CO₂ bubbles were spotted

after a few minutes, the view cell was considered free of leaks. Fig. D.9 shows the leak test process and an example of a (major) leak near the view cell.

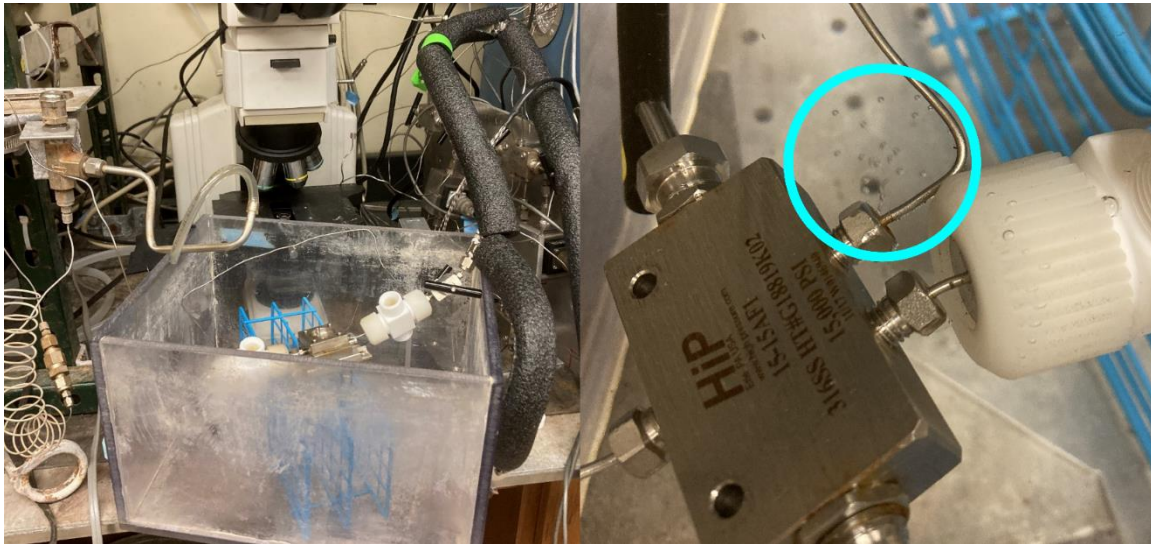


Fig. D.9. Leak testing of the view cell. While fully connected to the flow lines, we lowered the view cell into a large container (left) and filled the container with water. We then filled the view cell and neighboring lines with pressurized CO₂ and looked for CO₂ bubbles (right) to identify leakage points.

We checked for leaks in the view cell with this method every four or five foam experiments. Over the course of the experiments discussed in Chapter 5, we did not observe any new leaks in the view cell.

D.3 BEADPACK PREPARATION AND MEASUREMENT OF FOAM APPARENT VISCOSITY

Foam apparent viscosity was calculated from the pressure drop across the beadpack. This calculation required a beadpack of known permeability to shear the foam and generate flow resistance.

The beadpack, itself, was constructed using 180 μm spherical beads. Beads were poured in stages into a 10.6 cm long, 3.05 mm diameter Swagelok tube. Roughly one tenth of the required beads were poured inside at a time and the tube was tapped against a lab bench to settle. The beads were then packed in with the tip of a hexagonal screwdriver to compress them. Packing continued this way layer by layer. Once fully packed, the tube was closed on each end to hold the beads in place. 400 mesh screens were fitted to each end to prevent the flow of beads throughout the rest of the system.

Beadpack permeability was measured by flowing room temperature water at known flow rates (usually 1-5 ml/min) and measuring the pressure drop. We determined the beadpack permeability with Darcy's law, Eq. (D.1):

$$Q = \frac{kA}{\mu_{app}L} \Delta p, \quad (\text{D.1})$$

where Q is the volumetric flow rate, k is the permeability, A is the cross-sectional area of the beadpack, μ_{app} is the viscosity of the fluid (if solving for this parameter, it would be the apparent viscosity), L is the length of the beadpack, and Δp is the pressure drop. We calculated an initial permeability measurement of the pristine beadpack of 17 darcy. After some initial test runs of the foam apparatus, the permeability dropped down to 8-9 darcy (average of 8.6 darcy), where it remained constant throughout all of the foam experiments discussed in Chapter 5. We do not know if the initial measurement was an error, or if some changes occurred early in the operation of the beadpack (e.g., reduction of the packing fraction, plugging of the mesh screen) to reduce the permeability to a lower steady-state value. We measured the beadpack permeability multiple times throughout our foam experiments to confirm that it did not change.

Using the beadpack permeability and Eq. (D.1), we calculated the foam apparent viscosity at different foam qualities. We allowed foam to flow for 20 minutes at each condition, and took the average pressure drop after the development of steady-state flow to calculate the apparent viscosity. Fig. D.10 plots the pressure drop over time of room temperature water flow for permeability measurement (left) and 80°C, 2200 psi foam flow for apparent viscosity measurement (right). The beadpack permeability calculated from this data was 9.1 darcy. The foam plotted by Fig. D.10 contained 0.1 v/v% surfactant without nanoparticles, and had average apparent viscosities of 11.4, 15.0, and 20.4 cP at 70%, 80%, and 90% foam quality, respectively.

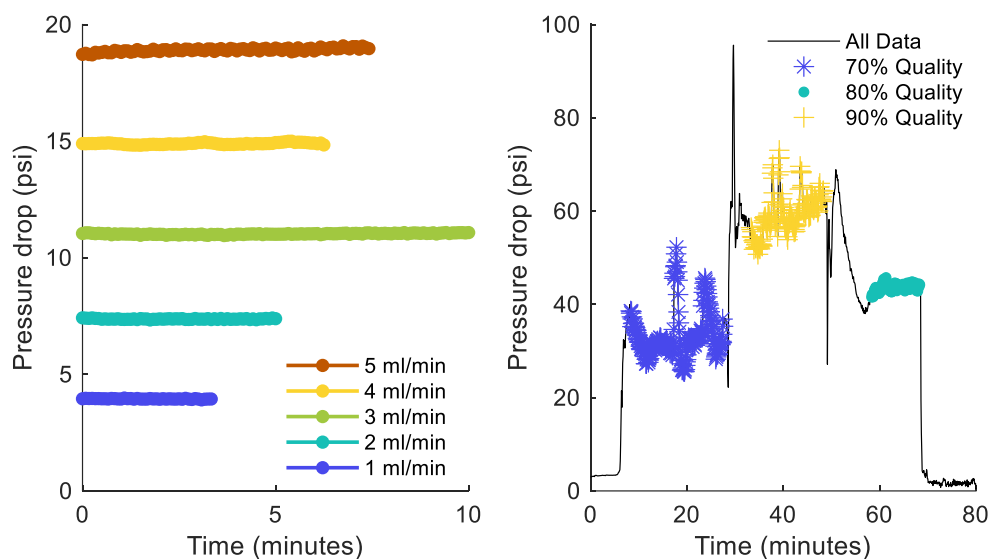


Fig. D.10. Left: pressure drop versus time for room temperature water flowed at different flow rates, used to calculate a beadpack permeability of 9.1 darcy (average: 8.6 darcy). Right: pressure drop of 0.1 v/v% surfactant only foam at 80°C and 2200 psi at different foam qualities.

D.4 MEASUREMENT OF FOAM COARSENING

Once trapped in the isolated view cell, foam images were monitored over time. Screenshots were taken every two seconds for the first 30 minutes, and every 15 or 30 minutes after that. Foam bubble sizes were calculated manually. In Fiji ImageJ, the circle tool was used to outline each foam bubble. The average diameter of the circle drawn was taken as the bubble diameter. A set of bubble diameters for each image was converted into the Sauter mean diameter, D_{SM} , using Eq. (D.2):

$$D_{SM} = \frac{\sum_i^n D_i^3}{\sum_i^n D_i^2}, \quad (\text{D.2})$$

where D_i represents each individual foam bubble diameter, from a total of n foam bubbles. Fig. D.11 gives an example of a manually-analyzed foam image, taken at four hours from the 0.2 w/v% 8N3+1.5DM and 1 v/v% surfactant foam at 80% foam quality, 80°C, and 2200 psi. For this image, we calculated a D_{SM} of 111 μm .

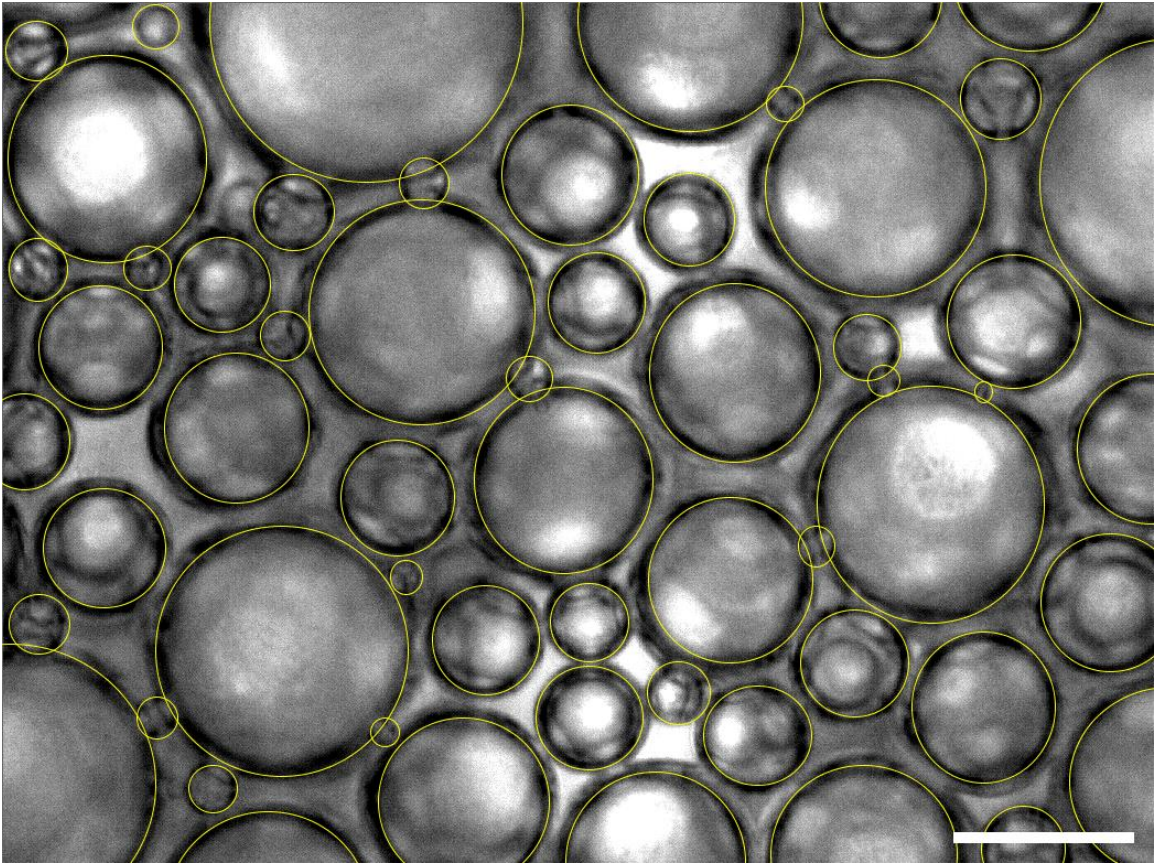


Fig. D.11. Example of manual bubble selection for calculating foam D_{SM} . The pictured foam is 0.2 w/v% 8N3+1.5DM NP with 1 v/v% surfactant after four hours at 80% foam quality, 80°C, and 2200 psi. The calculated D_{SM} for this image was 111 μm (scale bar is 100 μm).

Appendix E: Supporting information for Chapter 4 - Effect of interparticle forces on the stability and droplet diameter of Pickering emulsions stabilized by PEG-coated silica nanoparticles³

E.1 PROPERTIES OF NYACOL NEXSIL NANOPARTICLES

Table E.1 displays properties of the nanoparticles, given by Nyacol. We measured wt% by drying the nanoparticle dispersion at 120 °C and measuring the dry mass.

Name	Diameter (nm)	Average surface area (m ² /g)	pH	Measured wt%
NexSil 6	5 – 7.5	445	9.5- 10.5	18.8
NexSil 12	10 - 14	234	8.8 – 9.5	31.8
NexSil 20	20	135	10	40.0

Table E.1: Properties of unmodified silica nanoparticles.

Table E.2 lists the PEG grafting density, DLS-measured particle diameter, ζ potential, and particle-decane-water contact angle for each filtered batch of PEG-NP and stock NexSil particles [149].

³ A version of this appendix was published in the Journal of Colloid and Interface Science as supplemental material to: Hatchell, D., Song, W., & Daigle, H. (2022). Effect of interparticle forces on the stability and droplet diameter of Pickering emulsions stabilized by PEG-coated silica nanoparticles. Journal of Colloid and Interface Science, 626, 824-835.

*Average of two or more sets of reactions and measurements

^Imaged with TEM

Original Particle	PEG grafting density ($\mu\text{mol}/\text{m}^2$)	Z-average diameter in DIW (nm)	ζ potential in DIW (mV)	Contact angle to DIW ($^\circ$)	Contact angle to brine ($^\circ$)
NexSil 6	1.90	10.0	-35 ± 6	78	68
NexSil 6^ [^]	1.79	14.0	-41 ± 6	72	69
NexSil 6	1.47	11.5	-38 ± 6	53	63
NexSil 6	1.05	12.5	-41 ± 7	49	62
NexSil 6	0.91	13.5	-43 ± 8	55	56
NexSil 6	0.81	13.2	-42 ± 8	53	48
NexSil 6	0.65	16.6	-43 ± 8	39	46
NexSil 6*	0.52	13.6	-43 ± 9	49	41
NexSil 6	0.42	14.4	-44 ± 7	41	47
NexSil 6	0.28	21.3	-43 ± 6	30	33
NexSil 6	0.00	16.3	-46 ± 6	19	25
NexSil 12* [^]	1.65	17.3	-29 ± 8	42	55
NexSil 12	0.00	23.8	-47 ± 9	n/a	n/a
NexSil 20* [^]	1.85	24.9	-31 ± 11	62	57
NexSil 20	0.00	30.1	-49 ± 10	n/a	n/a
Plain Glass	0.00	n/a	n/a	36	37

Table E.2: Selected properties of modified silica nanoparticles.

E.2 DLVO PAIRWISE INTERACTIONS FOR PARTICLES DISPERSED IN THE AQUEOUS PHASE

Total DLVO interaction energies, Φ_T , are plotted as a function of particle pair separation distance and PEG coverage at the silica surface in Fig. E.1. Φ_T is calculated from Eq. (4.2) using Eq. (2.2) through (2.7) in Section 2.3.2. Specific variables used in these calculations are given in the supplemental material of Hatchell et al. [187].

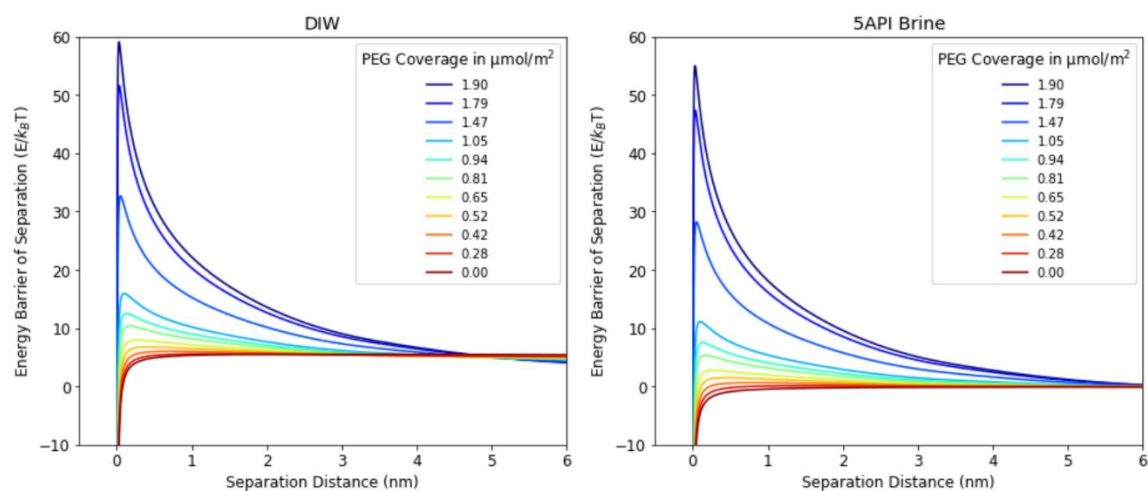


Fig. E.1. DLVO total interaction energy (Φ_T) vs separation distance plotted for 6 nm silica particles in deionized water (left) and 5API brine (right) with varying amounts of PEG coverage at the surface.

E.3 EFFECT OF NANOPARTICLE DIAMETER AND AQUEOUS PHASE SALINITY ON EMULSION STABILITY

We used the second set of PEG-NP (constant PEG grafting density, variable particle diameter) to examine the influence of electrostatic repulsion and vdW attraction on emulsion stability. Using 6, 12, and 20 nm particles grafted with approximately 1.75 $\mu\text{mol}/\text{m}^2$, we generated emulsions in both 5API brine and DI. Similar to the experiments presented in Fig. 4.6 (a), we generated and centrifuged emulsions, and measured the volume of released decane (a proxy for emulsion stability). Fig. E.2 (a) plots the results of these emulsion stability measurements, and Fig. E.2 (b) summarizes them by slicing the data horizontally at 50% decane released, analogous to Fig. 4.6 (b) [149].

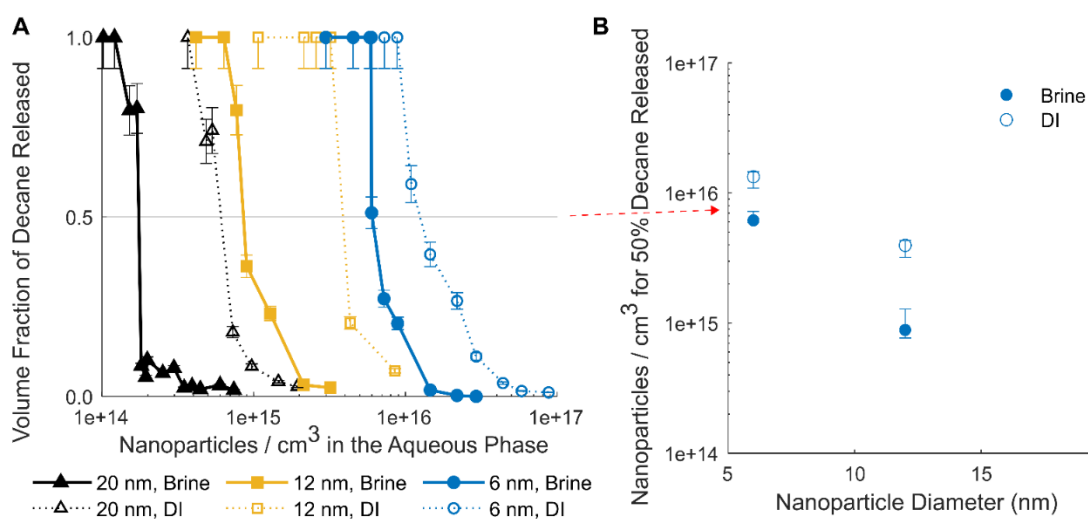


Fig. E.2. (a) Volume fraction of decane released from emulsion after centrifugation as a function of nanoparticle number concentration in the aqueous phase, plotted for 6, 12, and 20 nm $\sim 1.75 \mu\text{mol}/\text{m}^2$ PEG-NP in both 5API brine and DI. (b) Nanoparticle number concentration in the aqueous phase required to produce an emulsion that releases 50% of its decane by volume after centrifugation, plotted as a function particle diameter for both 5API brine and DI emulsions. This plot is constructed from the horizontal line drawn across (a).

Fig. E.2 (a) plots the volume fraction of decane released as a function of nanoparticle concentration for 6, 12, and 20 nm particles in both DI and 5API brine. Nanoparticle concentrations were calculated by dividing the mass of particles in the aqueous phase by the anticipated mass of a single nanoparticle. Error bars represent two standard deviations in decane volume, based on past experiments of similar emulsions, and emulsions with over 0.95 fraction of decane released were considered to be fully unstable and adjusted to a volume fraction of 1. Fig. E.2 (a) displays two trends: first, that smaller particle diameters required a larger number concentration of particles to stabilize an emulsion against coalescence; and second, that emulsions in DI required more particles to stabilize an emulsion against coalescence than particles in 5API brine. These findings are

consistent with past work. Larger particles are expected to occupy a greater area at the droplet interface and create a larger barrier to droplet coalescence; therefore, fewer large particles are necessary to achieve the same stability (although, given difference in particle mass, this corresponds to a larger particle mass concentration) [84,99,148]. Additionally, the presence of salt ions in the aqueous phase is expected to reduce interparticle electrostatic repulsion and promote the formation of interparticle networks, strengthening emulsions against coalescence [80,105,107,115-118,144].

Fig. E.2 (b) summarizes the data from Fig. E.2 (a) by plotting the nanoparticle concentration required for 50% of decane to be released as a function of nanoparticle diameter, with error bars representing the particle concentrations of the nearest more-stable ($> 60\%$ decane released) and less-stable ($< 40\%$ decane released) emulsions. The 6 nm particles required 1.3×10^{16} particles / cm^3 for 50% stability in DI and 6.2×10^{15} particles / cm^3 for 50% stability in 5API brine; 12 nm particles required 3.9×10^{15} and 8.8×10^{14} particles / cm^3 for DI and 5API brine, respectively; and 20 nm particles required 6.6×10^{14} and 1.8×10^{14} particles / cm^3 for DI and 5API brine, respectively. By dividing the DI concentration by the 5API brine concentration for each particle, we calculated ratios of 2.2 (error interval of 1.5-2.4) for 6 nm particles, 4.5 (2.5-5.6) for 12 nm particles, and 3.7 (2.7-4.3) for 20 nm particles.

By summarizing the data in this way, we controlled for the two aforementioned trends from Fig. E.2 (a) and isolated the influence of vdW forces on emulsion stability. When emulsions are formed in DI, we expect that electrostatic repulsion is the dominant particle interaction, and that vdW attraction is negligible. When emulsions are formed in 5API brine, however, electrostatic repulsion is significantly reduced and vdW attraction may become more important. If vdW attraction has a significant effect on emulsion stability (for example, if vdW attraction leads to increased formation of interparticle

networks), that effect might be observed by examining the change of emulsion stability from DI to 5API brine as a function of particle diameter (with the expectation that larger particles exert larger vdW interactions). Of the three particle diameters, the 6 nm PEG-NP had the smallest change in emulsion stability, with a ratio of only 2.2. The 12 and 20 nm PEG-NP had significantly larger ratios of 4.5 and 3.7, respectively, and while their error interval overlapped with each other, they were completely outside the interval of the 6 nm particles. It's possible that the smaller change in emulsion stability exhibited by 6 nm particles was a result of their relatively smaller vdW forces contributing to fewer interparticle networks and less emulsion stability in 5API brine. However, the similarity between the emulsions generated from 12 and 20 nm particles makes this trend inconclusive. Future work will examine the role of vdW attraction in greater detail.

E.4 ENERGY BALANCE EQUATIONS TO MODEL EMULSION DROPLET DIAMETER

The calculation of Eq. (4.6), the energy balance model, is described by Eq. (2.8) through (2.23) in Section 2.4. The parameters used in these calculations are given in the supplemental material of Hatchell et al. [187].

Table E.3 lists the parameters used for each model fit. Values of r were derived from DLS measurements, where $r + L$ was equated to an average of measurements of the z-average radius in DIW or brine, respectively. For 6 nm particles in brine, only unaggregated initial measurements were considered in the average. The particle interface fraction is a fitting parameter used to assign some fraction of the total particles to the droplet interface. A is the coefficient in the power law equation $D_{32} = A(\text{wt}\%/100)^{-1}$ derived from the energy balance model.

Particle	Aqueous phase	r (nm)	Interface Fraction: AF_{DIW} or AF_{Brine}	$A \times 10^7$
NexSil 6	DI	4.12	13.7%	2.259
NexSil 6	5API Brine	6.40	85.8%	0.7456
NexSil 12	DI	5.75	13.7%	3.4951
NexSil 12	5API Brine	12.27	85.8%	1.691
NexSil 20	DI	9.55	13.7%	7.358
NexSil 20	5API Brine	15.86	85.8%	2.263

Table E.3: Parameters for energy balance model for $\sim 1.75 \mu\text{mol}/\text{m}^2$ PEG-NP emulsions ($L = 2.89 \text{ nm}$)

E.5 ENERGY BALANCE MODEL PROCEDURE

The following steps describe the energy balance model in detail:

1. The following parameters are updated to reflect the specific emulsion being modelled: nanoparticle concentration, c_{NaCl} , c_{CaCl_2} , r , AF_{DIW} , AF_{Brine} , and θ .
2. Starting condition: the entire decane phase (in our case, 20 mL of decane) is split into droplets measuring $1 \mu\text{m}$ in diameter. These droplets are dispersed throughout the aqueous phase. Every nanoparticle currently sits in the aqueous phase.
3. We transfer a small number of nanoparticles to the droplet interface. The number of particles we transfer at each step depends on our desired resolution and computational time.
4. The nanoparticles are distributed equidistantly in a hexagonal pattern throughout all available surface area. We calculate the distances d and S for particles with this arrangement. We neglect any effects of droplet swelling, which we expect to have a negligible effect on droplet diameter at our conditions.
5. We calculate E_{Total} using Eq. (4.6) and (E.8) through (E.21). Presumably, at this step, E_{Total} is negative.

6. We transfer more nanoparticles to the droplet interface, which reduces d and S .
7. We recalculate E_{Total} . $\Delta_{demix}G$ increases. Φ_{vdW}^{int} decreases and Φ_E^{int} increases, although these energies are often not significant. Φ_S^{int} either increases or remains zero. $\Delta_{int}G$ is constant and does not change as we update d and S . As a result, E_{Total} should have increased.
8. We repeat the previous two steps as needed until we determine the point at which E_{Total} goes from negative to positive. The fraction of particles that we allow to transfer depends on the fitting parameters AF_{DIW} and AF_{Brine} .
9. Once the equilibrium E_{Total} is known, we determine the interfacial area occupied by our adsorbed nanoparticles, assuming each nanoparticle occupies a circle with radius $r + L$ at the droplet interface, with a 2D hexagonal packing density of 0.9069.
10. If the above interfacial area is larger or equal to the interfacial area of the oil droplets we considered in the starting condition, then our output droplet diameter is equal to the original droplet diameter (1 μm). This is an exception for very high nanoparticle concentrations (particle-rich).
11. If the above interfacial area is smaller than the interfacial area of the oil droplets, then we calculate a new droplet diameter (using our original 20 mL volume) that would make the two values equal. The new droplet diameter is the output of the energy balance model.

Appendix F: Supporting information for Chapter 5 - Stable CO₂/water foam stabilized by dilute surface-modified nanoparticles and cationic surfactant at high temperature and salinity

F.1 EXTENDED MATERIALS AND METHODS

F.1.1 Brine recipe

Brine was made from DIW with the following recipe: 169.02 g/L sodium chloride (NaCl, CAS: 7647-14-5, ≥99% purity, Fischer Scientific), 67.34 g/L calcium chloride dihydrate (CaCl₂-2H₂O, CAS: 10035-04-8, ≥99% purity, Fischer Scientific), 20.75 g/L magnesium chloride hexahydrate (MgCl₂-6H₂O, CAS: 7791-18-6, ≥99% purity, Fischer Scientific), 0.325 g/L sodium sulfate (Na₂SO₄, CAS: 7757-82-6, ≥99% purity, Fischer Scientific), and 0.084 g/L sodium bicarbonate (NaHCO₃, CAS: 144-55-8, ≥99.7% purity, Fischer Scientific). The final brine concentration and density were 22 wt% TDS and 1.155 g/mL, respectively, and included divalent Ca⁺⁺ and Mg⁺⁺ cations.

F.1.2 Particle grafting reaction and filtration

The grafting reaction and filtration was carried out similarly to past work [42,144,180,187], with the main change being the use of NexSil 6 NP. We first hydrolyzed the N3 silane by pipetting it dropwise into a vial containing an equal volume of DIW and stirred for 30 minutes. In a separate vial or reagent bottle, we adjusted our NP (originally pH 10) to pH 5 with 12 N HCl, and added methanol. After stirring, we adjusted the pH of the N3-DIW mixture to pH 5 with 12 N HCl and added it to the NP. Additional DIW was added as necessary. The volumes of each chemical used throughout this process were chosen to meet the following criteria: (1) the final mixture was 10 w/v% silica NP ; (2) the final mixture was 20 v/v% methanol; and (3) we hydrolyzed and added 8 μmol N3 silane per m² of silica surface (445 m²/g). The container was sealed with PTFE tape and stirred

overnight in an oil bath at 70°C. Once completed, we evaporated the methanol and added DIW to bring the NP concentration back up to 10 w/v%. DM silane was added directly to the batch at the desired concentration, and the batch was resealed with PTFE tape and stirred overnight at 70°C.

Following the reaction with DM silane, 5 mL of NP were pipetted with 7 mL DIW into an Amicon Ultra-15 30k MWCO centrifuge filter. The filters were centrifuged four times for 15 minutes at 4000 rpm, adding additional DIW between runs to wash out ungrafted ligands. Retentate volume decreased from 12 mL to 2-3 mL as filtrate passed through the filter; occasionally the centrifuge speed needed to be increased to 6000 rpm to maintain at least this much filtration (approximately a 5x dilution) at each stage. Filtration by this method reduced ungrafted ligands to approximately 0.01 $\mu\text{mol}/\text{m}^2$. Filtered NP were then extracted and bath-sonicated with DIW (enough to bring the volume back to 5 mL per filter) for 30 minutes to disperse at 10 w/v% concentration.

F.1.3 Silane titration

Titration of N3 and DM silane were carried out following past work [165,180,188]. In a three-neck glass flask, N3 and DM silane were added to 50 mL of 22 wt% brine at 0.01 M concentration each. The initial silane and brine mixture recorded a basic pH of approximately 8-10, depending on the temperature. While stirring the container, we used a burette to add 80 mM HCl dropwise. pH readings were taken throughout and converted into C_{OH^-} and C_{H^+} , the molar concentrations of hydroxide and hydrogen ions, respectively, dissociated in the aqueous phase. The fraction of switchable amino groups protonated, Θ , was calculated with the following equation [188]:

$$\Theta = \frac{C_a * V_{titrant} + (C_{OH^-} - C_{H^+}) * V_{titrand}}{C_{total} * V_{titrand,o}}, \quad (\text{F.1})$$

where C_a is the molar concentration of H^+ introduced by the acid (80 mM HCl), C_{total} is the molar concentration of protonatable amino groups, $V_{titrant}$ is the volume of acid added, $V_{titrand}$ is the combined volume of acid and initial brine, and $V_{titrand,0}$ is the initial volume of the brine (50 mL). We measured silane titration at both room temperature and 80°C. For measurements at elevated temperature, the flask was heated in an oil bath. A condenser jacket circulating cold water was connected to one of the flask necks to prevent evaporation during the measurement. Other openings and connections were sealed with stoppers.

F.1.4 Contact angle and spin-coating

Aqueous contact angles (θ_w) were measured in two steps: first, spin-coating a glass surface, and second, imaging the droplet-glass interface. We stirred microscope slides overnight with 0.1 N HCl at 70°C to remove residue, rinsed the cleaned glass with 2-propanol and DIW, and air-dried the glass. In a clean room, we pipetted enough 10 w/v% NP dispersion to fully coat the glass surface and spun the glass slides for 60 seconds at 1000 rpm and 1000 rpm/s acceleration with a Laurell WS-650-23 spin-coater. The coated glass surface was imaged at 76 FPS using the Biolin OneAttention software. A 7.5 μ L droplet of either DIW or 22 wt% brine (the latter adjusted to pH 4 with HCl) was deposited onto the glass, and θ_w was calculated by the software using sessile drop analysis. The first frame of contact between a fully-formed droplet and the glass surface was used for these measurements. Each measurement was performed in triplicate.

We further performed three-phase θ_w measurements in liquid CO_2 to more closely emulate the foam operating conditions. We used a high-pressure vessel with multiple sapphire view-cells for imaging. A small glass piece (approximately one cm in diameter) was cut to the shape of a holder that could fit into the high-pressure vessel at the correct viewing height. We prepared the glass piece for spin-coating by the above cleaning process

and attached it to a microscope slide with double sided tape for use with the spin-coater. The spin-coating process proceeded as above. The glass piece was positioned inside the vessel, and the vessel was slowly injected with 100 psi CO₂ from an ISCO pump. The injection rate was kept below 5 mL/min to not disturb the NP coating on the glass piece. The pressure was raised to 950 psi, at which point the glass surface was submerged in liquid CO₂ with a density close to that of supercritical CO₂ at reservoir conditions. With another ISCO pump, a droplet of 22 wt% brine (pH 4) was carefully deposited onto the glass piece and imaged. We performed a triplicate measurement by depositing increasingly large droplets onto the glass surface, ensuring that the perimeter of each droplet contacted untouched glass each time.

These methods to measure θ_w were based on past work [44,187].

F.1.5 CO₂ foam apparatus

The following foam apparatus procedures were similar to past studies [42,180]. During foam operation, an aqueous stream was injected into the system at 2200 psi with an ISCO pump. This stream contained N3+DM NP and RCADA dispersed in 22 wt% brine at desired concentrations, as well as 15 ppm of Na₂SO₃ as an oxygen scavenger. The aqueous stream circulated in a Thermo Scientific Lindberg/Blue M convection oven set to 80°C, where the fluid was equilibrated to high temperature and combined with a CO₂ stream. Flow rates were set to total 1 mL/min at the desired CO₂ volume fraction (foam quality) at in-situ conditions. The combined fluids entered a 180 μm layer-packed beadpack (10.6 cm long and 3.05 mm internal diameter) and sheared to generate foam. Leaving the oven, the foam flowed down a heated pipe into a view cell, where it was trapped for long-term imaging. The flow path was maintained at 80°C by a surrounding annular tube circulating water pumped from a heated water bath. The view cell was

maintained at 80°C with heating cartridges PID-controlled by a thermocouple. A bypass valve rerouted foam around the view cell through two back pressure regulators run in series and into a waste container. The back pressure regulators were maintained at 80°C with a convection water bath to prevent tubing freezing upon CO₂ expansion. The system was purged and washed with DIW between runs, with a constant permeability of roughly 8.6 darcy maintained from run to run. Mesh screens were positioned around the beadpack and back pressure regulators to prevent beads from flowing throughout the system and damaging components.

F.1.6 Thermogravimetric analysis

Thermogravimetric analysis (TGA) measurements were conducted similar to past work [28,144,187]. A 10 mg sample of dried NP was heated in the TGA to 800°C, and the mass change was recorded.

The mass loss from 110°C to 800°C was attributed to the surface ligands on the particle surface by the following equation:

$$\varphi_l = \frac{f_o - f_{o,np}}{(1 - f_o - f_i + f_{o,np})S_A M_{TGA}}, f_i = \frac{(f_o - f_{o,np})M_{iTGA}}{M_{TGA}}, \quad (\text{F.2})$$

where φ_l is the ligand coverage per area of particle surface, f_o is the “organic fraction”, the removeable mass lost to TGA from 110 to 800°C, $f_{o,np}$ is the analogous TGA mass loss for an ungrafted particle, f_i is the “inorganic fraction”, which represents unremoveable mass added to the particle during silanization, S_A is the particle specific surface area, M_{TGA} is the molecular weight of the removeable, “organic” portion of the ligand (144 g/mol for N3), and M_{iTGA} is the molecular weight of the unremoveable, “inorganic” portion of the ligand (52 g/mol for N3).

F.1.7 NP-CO₂ dispersity

Dispersity of NP in the CO₂ phase was measured with the same high-pressure vessel used for contact angle measurements. A small dried NP sample was placed on a raised platform within the vessel for viewing with a camera, and the vessel was pressurized with CO₂ to as high as 4000 psi. The vessel was heated to 80°C with heating elements connected to a temperature controller. Dispersity was determined by comparing NP images at different conditions and looking for mass loss into the CO₂ phase.

F.2 SUPPORTING RESULTS

F.2.1 Thermogravimetric analysis results

TGA mass profiles for 8N3+0-2DM NP are plotted in Fig. F.1.

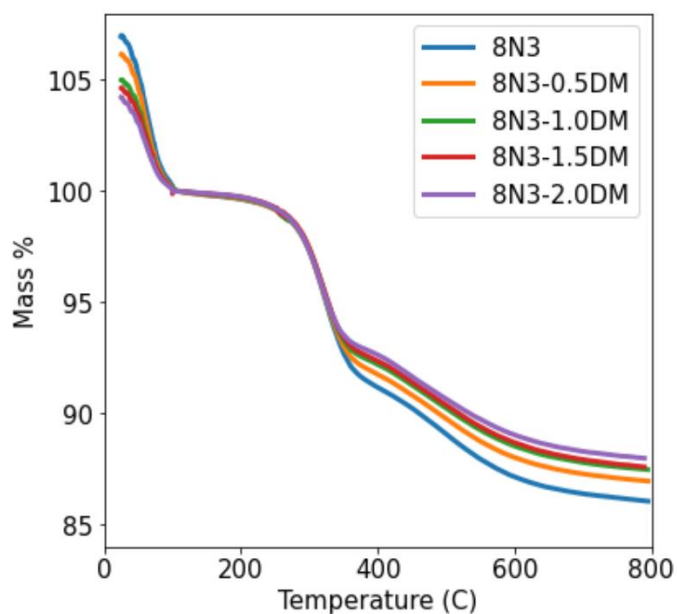


Fig. F.1. Mass fraction measured by TGA plotted as a function of temperature for 8N3+0-2DM NP. The mass fraction is normalized to equal one when the temperature increases beyond 110 °C (all residual water removed).

The discontinuity at 110°C represents a 20-minute holding period where water was removed from the sample. Following the TGA curve of 8N3 NP and using Eq. (F.2), the reaction of silica particles with 8 $\mu\text{mol}/\text{m}^2$ N3 yields 2.0 $\mu\text{mol}/\text{m}^2$ of N3 grafted. Counterintuitively, the addition of DM results in less mass removeable from particle by TGA. This result is difficult to interpret quantitatively, but is consistent with past work [44,193], and serves as a qualitative indicator that DM has been attached to the particle surface.

F.2.2 Contact Angle Measurement

In addition to the measurements reported in Fig. 5.4, we measured the θ_w of our NP dispersed in pH 4 brine and 1 v/v% RCADA, with respect to air. These results are plotted in Fig. F.2.

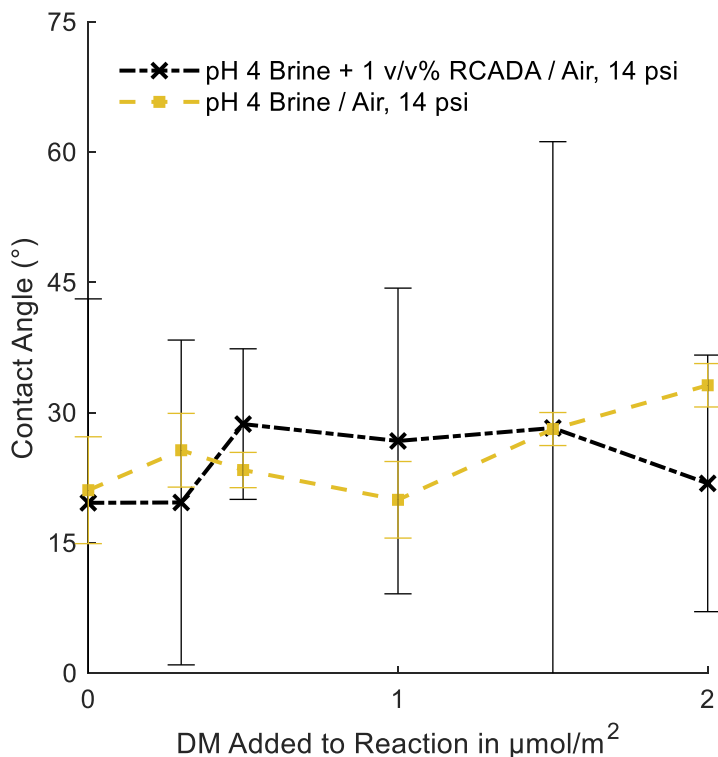


Fig. F.2. Three-phase θ_w of 8N3 NP in pH 4 brine (with or without 1 v/v% RCADA), plotted with respect to air as a function of DM silane added to the NP grafting reaction. Each data point is an average of measurements from three images.

As seen in Fig. F.2, contact angle measurements exhibited considerably greater variance when RCADA was present, and the error bars (twice the standard deviation) were too high to draw a meaningful trend. On contact with spin-coated glass, droplets begin to spread and appear to transfer particles from the glass into the aqueous phase. Droplets containing RCADA spread much more quickly onto the spin-coated surface, making it more difficult to get a high-quality image and leading to the variance in θ_w values. However, the values of θ_w were similar with and without RCADA.

F.2.3 NP-CO₂ Dispersivity Results

0.73 mg of 8N3+2DM NP were loaded onto a viewing platform within the high-pressure vessel. The mass of NP was approximately equal to 0.01 wt% of the mass of condensed CO₂ in the vessel at most conditions. The following procedures were attempted in order to disperse the particles: (1) bringing the vessel to 4000 psi at room temperature; (2) heating the vessel to 80°C and 4000 psi; (3) reducing to room temperature and holding 4000 psi overnight; (4) heating the vessel to 80°C and holding 4000 psi for two hours; (5) reducing pressure and temperature to ambient conditions. Throughout these procedures, there was no evidence of measurable particle dispersion into the CO₂ phase. The NP did not noticeably change appearance throughout the experiment.

F.2.4 CO₂ foam apparent viscosity

Fig. F.3, F.4, and F.5 are box plots of the apparent viscosities displayed in Fig. 5.5 (a) and (b). These box plots show the typical variance of each apparent viscosity measurement, itself calculated from mostly steady-state but occasionally fluctuating time-series data.

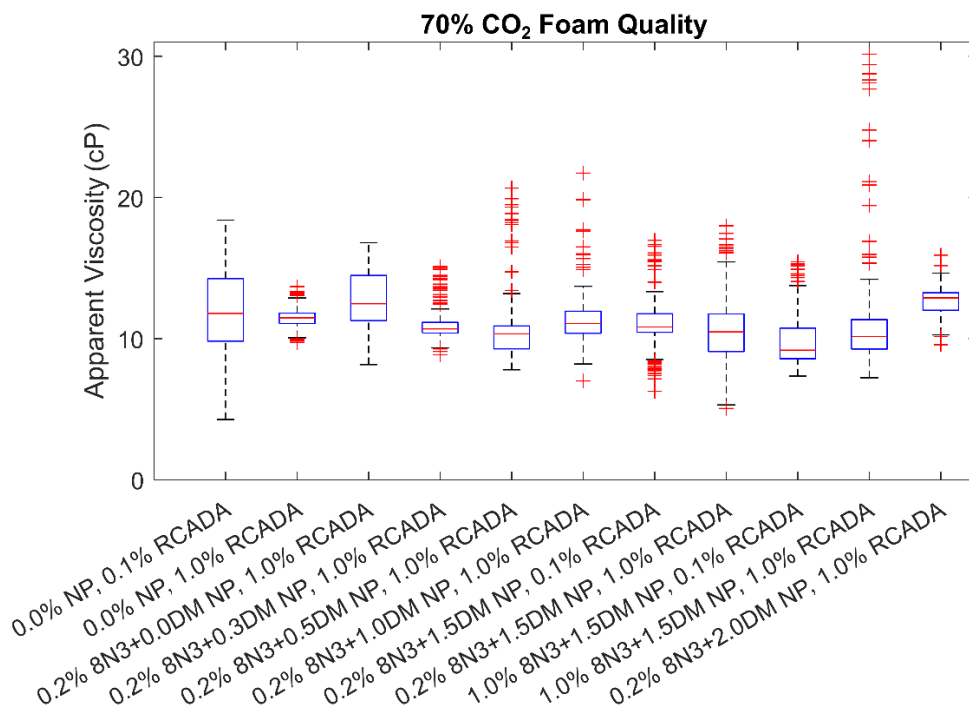


Fig. F.3. Box plot of CO₂ foam apparent viscosities for all particle-surfactant combinations at 70% CO₂ foam quality, 80 °C, and 2200 psi. The box indicates the 25th, 50th, and 75th percentiles with red markers representing outliers (1.5 times the 75th-25th distance removed from the edge of the box).

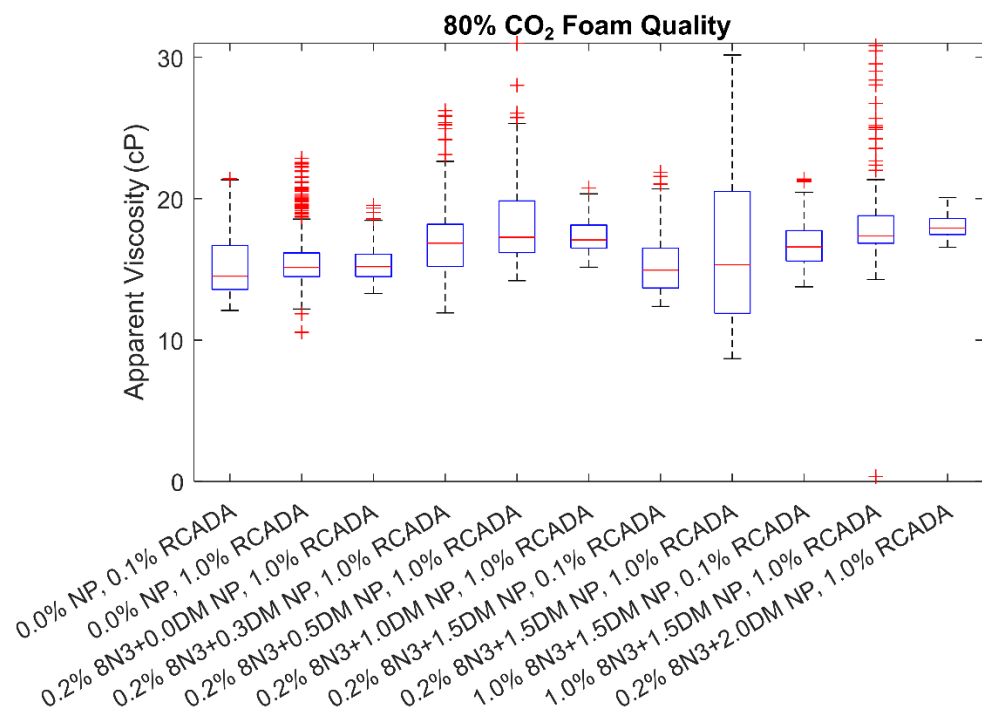


Fig. F.4. Box plot of CO₂ foam apparent viscosities for all particle-surfactant combinations at 80% CO₂ foam quality, 80 °C, and 2200 psi. The box indicates the 25th, 50th, and 75th percentiles with red markers representing outliers (1.5 times the 75th-25th distance removed from the edge of the box).

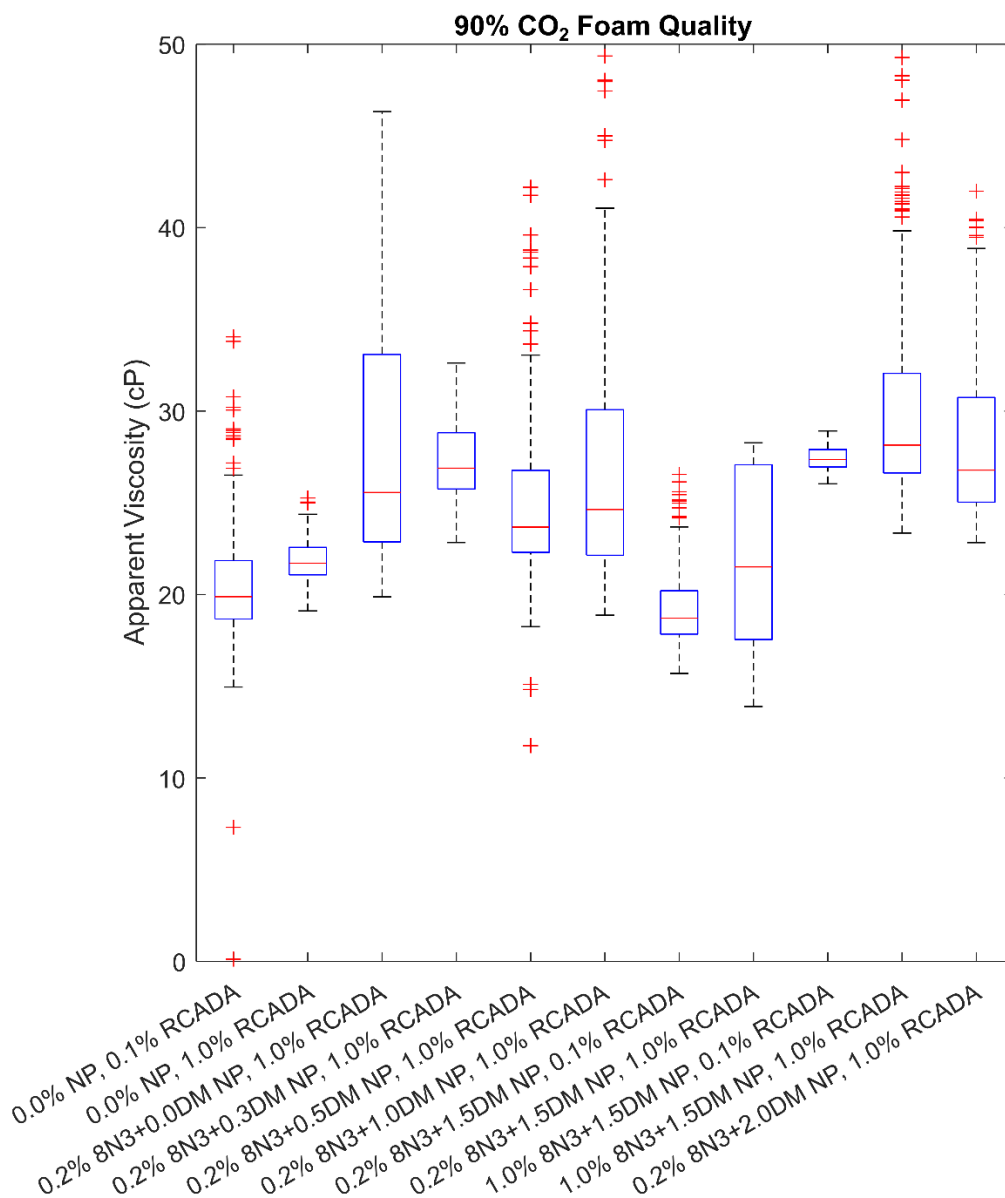


Fig. F.5. Box plot of CO₂ foam apparent viscosities for all particle-surfactant combinations at 90% CO₂ foam quality, 80 °C, and 2200 psi. The box indicates the 25th, 50th, and 75th percentiles with red markers representing outliers (1.5 times the 75th-25th distance removed from the edge of the box).

F.2.3 CO₂ foam stability images

Fig. F.6 and F.7 show CO₂ foam bubbles in the view cell at 80°C and 2200 psi for various foam formulations. All foams presented are at 80% foam quality. The images are presented at different time-steps representing the elapsed time since the foam entered the view cell. Because of small differences in each foam experiment, the images do not exactly correspond to the listed time, but most are very close and all are within 5% of the listed time. The two scale bars are equivalent for each image.

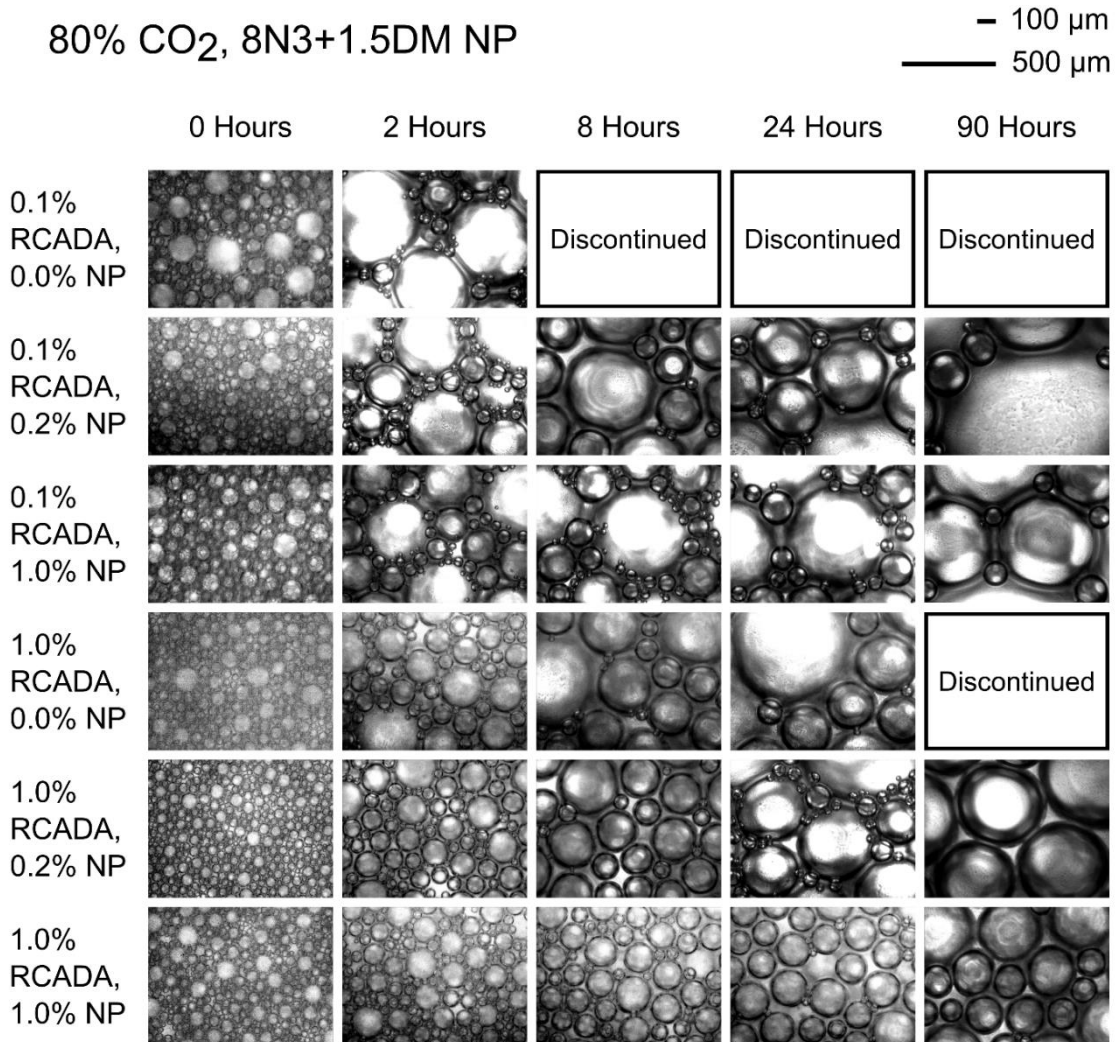


Fig. F.6. Microscope images of CO₂ foam bubbles (8N3+1.5DM NP, various particle and RCADA concentrations, 22 wt% brine) growing in the foam apparatus view cell at 80 °C and 2200 psi over time. “Coalesced” indicates that the droplets grew too large to properly image at the same scale; at this point, the experiment was discontinued. The scale bars are consistent for all images.

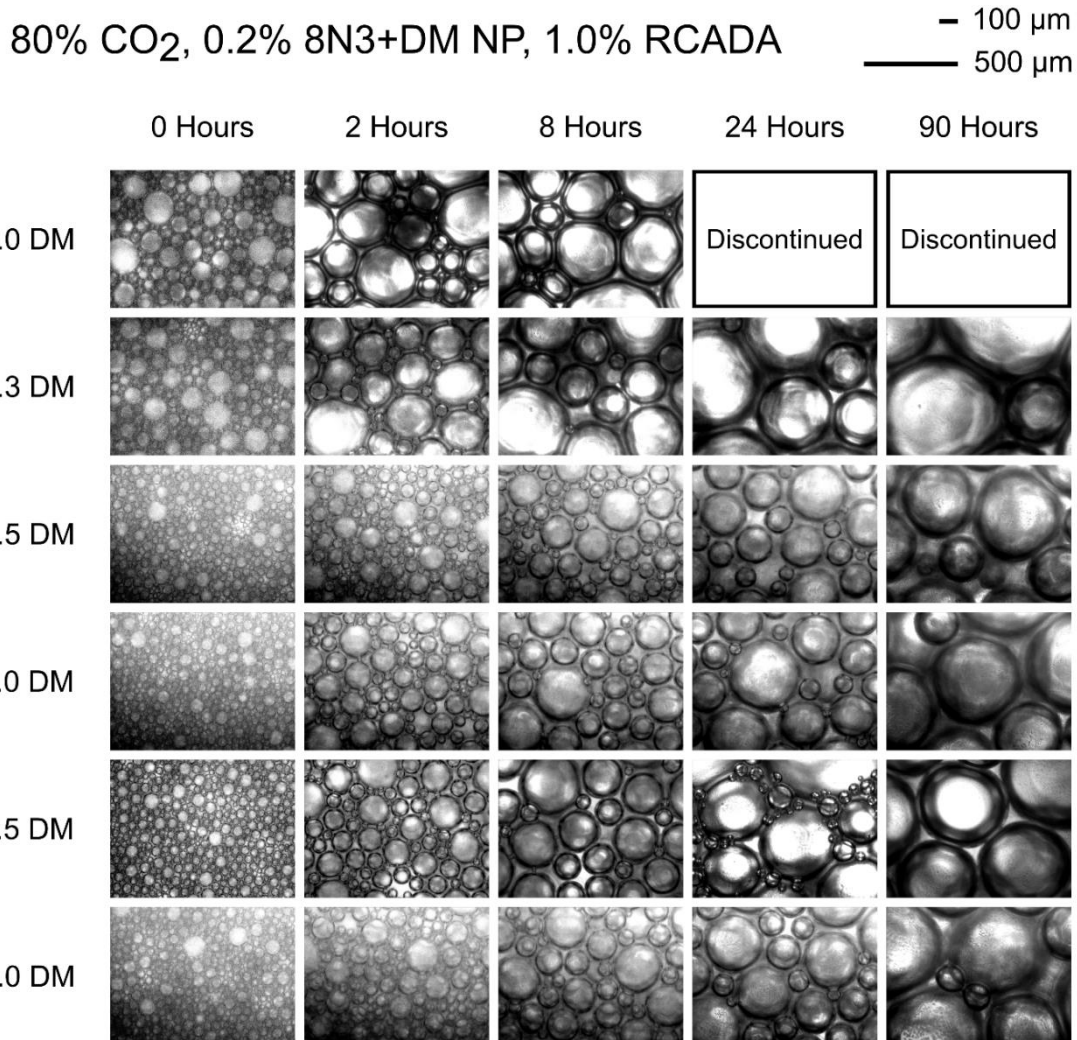


Fig. F.7. Microscope images of CO₂ foam bubbles (0.2 w/v% 8N3+0-2DM NP, 1 v/v% RCADA, 22 wt% brine) growing in the foam apparatus view cell at 80 °C and 2200 psi over time. “Coalesced” indicates that the droplets grew too large to properly image at the same scale; at this point, the experiment was discontinued. The scale bars are consistent for all images.

References

- [1] Ramsden, W. (1904). Separation of solids in the surface-layers of solutions and ‘suspensions’ (observations on surface-membranes, bubbles, emulsions, and mechanical coagulation).—Preliminary account. Proceedings of the royal Society of London, 72(477-486), 156-164.
- [2] Pickering, S. U. (1907). Cxcvi.—emulsions. Journal of the Chemical Society, Transactions, 91, 2001-2021.
- [3] Vert, M., Doi, Y., Hellwich, K. H., Hess, M., Hodge, P., Kubisa, P., ... & Schué, F. (2012). Terminology for biorelated polymers and applications (IUPAC Recommendations 2012). Pure and Applied Chemistry, 84(2), 377-410.
- [4] Binks, B. P. (2002). Particles as surfactants—similarities and differences. *Current opinion in colloid & interface science*, 7(1-2), 21-41.
- [5] Wu, J., & Ma, G. H. (2016). Recent studies of Pickering emulsions: particles make the difference. *Small*, 12(34), 4633-4648.
- [6] Albert, C., Beladjine, M., Tsapis, N., Fattal, E., Agnely, F., & Huang, N. (2019). Pickering emulsions: Preparation processes, key parameters governing their properties and potential for pharmaceutical applications. *Journal of Controlled Release*, 309, 302-332.
- [7] Harman, C. L., Patel, M. A., Guldin, S., & Davies, G. L. (2019). Recent developments in Pickering emulsions for biomedical applications. *Current Opinion in Colloid & Interface Science*, 39, 173-189.
- [8] Murray, B. S. (2019). Pickering emulsions for food and drinks. *Current Opinion in Food Science*, 27, 57-63.
- [9] Weiss, J., Ahmad, T., Zhang, C., & Zhang, H. (2020). A review of recent progress on high internal-phase Pickering emulsions in food science. *Trends in Food Science & Technology*, 106, 91-103
- [10] Ribeiro, E. F., Morell, P., Nicoletti, V. R., Quiles, A., & Hernando, I. (2021). Protein-and polysaccharide-based particles used for Pickering emulsion stabilisation. *Food Hydrocolloids*, 119, 106839.

- [11] Peito, S., Peixoto, D., Ferreira-Faria, I., Martins, A. M., Ribeiro, H. M., Veiga, F., ... & Santos, A. C. (2022). Nano-and microparticle-stabilized Pickering emulsions designed for topical therapeutics and cosmetic applications. *International Journal of Pharmaceutics*, 121455.
- [12] Wei, Y. S., Niu, Z. C., Wang, F. Q., Feng, K., Zong, M. H., & Wu, H. (2020). A novel Pickering emulsion system as the carrier of tocopheryl acetate for its application in cosmetics. *Materials Science and Engineering: C*, 109, 110503.
- [13] Cao, H., Escamilla, M., Anas, M., Tan, Z., Gulati, S., Yun, J., ... & Green, M. J. (2021). Synthesis and Electronic Applications of Particle-Templated Ti₃C₂T_x MXene–Polymer Films via Pickering Emulsion Polymerization. *ACS Applied Materials & Interfaces*, 13(43), 51556-51566.
- [14] Bian, Z., Xu, J., Zhang, S., Zhu, X., Liu, H., & Hu, J. (2015). Interfacial growth of metal organic framework/graphite oxide composites through Pickering emulsion and their CO₂ capture performance in the presence of humidity. *Langmuir*, 31(26), 7410-7417.
- [15] Bragg, J. R. (1999). *U.S. Patent No. 5,855,243*. Washington, DC: U.S. Patent and Trademark Office.
- [16] Kaminsky, R. D., Wattenbarger, R. C., Lederhos, J., & Leonardi, S. A. (2010, January). Viscous oil recovery using solids-stabilized emulsions. *SPE Annual Technical Conference and Exhibition*. Society of Petroleum Engineers.
- [17] Chaturvedi, K. R., & Sharma, T. (2021). In-situ formulation of pickering CO₂ foam for enhanced oil recovery and improved carbon storage in sandstone formation. *Chemical Engineering Science*, 235, 116484.
- [18] Ab Rasid, S. A., Mahmood, S. M., Kechut, N. I., & Akbari, S. (2022). A review on parameters affecting nanoparticles stabilized foam performance based on recent analyses. *Journal of Petroleum Science and Engineering*, 208, 109475.
- [19] Ko, S., Kim, E. S., Park, S., Daigle, H., Milner, T. E., Huh, C., Bennetzen, M. V., & Geremia, G. A. (2017). Amine functionalized magnetic nanoparticles for removal

- of oil droplets from produced water and accelerated magnetic separation. *Journal of Nanoparticle Research*, 19(4), 132.
- [20] Zhao, X., He, F., Yu, G., Feng, Y., & Li, J. (2021). High-viscosity Pickering emulsion stabilized by amphiphilic alginate/SiO₂ via multiscale methodology for crude oil-spill remediation. *Carbohydrate Polymers*, 273, 118492.
- [21] Amani, P., Miller, R., Javadi, A., & Firouzi, M. (2022). Pickering foams and parameters influencing their characteristics. *Advances in Colloid and Interface Science*, 102606.
- [22] Ko, S., & Huh, C. (2019). Use of nanoparticles for oil production applications. *Journal of Petroleum Science and Engineering*, 172, 97-114.
- [23] Liu, J. X., Zhu, H. J., Wang, P., & Pan, J. M. (2021). Recent studies of Pickering emulsion system in petroleum treatment: The role of particles. *Petroleum Science*, 18(5), 1551-1563.
- [24] Ortiz, D. G., Pochat-Bohatier, C., Cambedouzou, J., Bechelany, M., & Miele, P. (2020). Current trends in Pickering emulsions: Particle morphology and applications. *Engineering*, 6(4), 468-482.
- [25] Derjaguin, B., & Landau, L. (1941). The theory of stability of highly charged lyophobic sols and coalescence of highly charged particles in electrolyte solutions. *Acta Physicochim. URSS*, 14(633-52), 58.
- [26] Verwey, E. J. W., Overbeek, J. T. G., & Van Nes, K. (1948). *Theory of the stability of lyophobic colloids: the interaction of sol particles having an electric double layer*. Elsevier Publishing Company.
- [27] Napper, D. H. (1983). *Polymeric stabilization of colloidal dispersions* (Vol. 3). Academic Press.
- [28] Worthen, A. J., Tran, V., Cornell, K. A., Truskett, T. M., & Johnston, K. P. (2016). Steric stabilization of nanoparticles with grafted low molecular weight ligands in highly concentrated brines including divalent ions. *Soft Matter*, 12(7), 2025-2039.

- [29] Metin, C. O., Baran, J. R., & Nguyen, Q. P. (2012). Adsorption of surface functionalized silica nanoparticles onto mineral surfaces and decane/water interface. *Journal of Nanoparticle Research*, 14(11), 1246.
- [30] Xie, Y., Hill, C. A., Xiao, Z., Militz, H., & Mai, C. (2010). Silane coupling agents used for natural fiber/polymer composites: A review. *Composites Part A: Applied Science and Manufacturing*, 41(7), 806-819.
- [31] Hubbe, M. A., Rojas, O. J., & Lucia, L. A. (2015). Green modification of surface characteristics of cellulosic materials at the molecular or nano scale: A review. *BioResources*, 10(3), 6095-6206.
- [32] Everett, D. H. (1972). Manual of symbols and terminology for physicochemical quantities and units, appendix II: Definitions, terminology and symbols in colloid and surface chemistry. *Pure and Applied Chemistry*, 31(4), 577-638.
- [33] Bikerman, J. J. (2013). *Foams* (Vol. 10). Springer Science & Business Media.
- [34] Pugh, R. J. (2016). *Bubble and foam chemistry*. Cambridge University Press.
- [35] Lake, L. W., Johns, R., Rossen, B., & Pope, G. A. (2014). *Fundamentals of enhanced oil recovery* (Vol. 1, p. 1). Richardson, TX: Society of Petroleum Engineers.
- [36] Haynes, W. (1860). Improvements for obtaining metals from their ores or matrices. *Great Britain Lett Patent*, (488).
- [37] Texter, J. (2022). Pickering emulsions and dispersions—an early perspective. *Colloid and Polymer Science*, 1-6.
- [38] Aveyard, R., Binks, B. P., & Clint, J. H. (2003). Emulsions stabilised solely by colloidal particles. *Advances in Colloid and Interface Science*, 100, 503-546.
- [39] Balakrishnan, G., Nicolai, T., Benyahia, L., & Durand, D. (2012). Particles trapped at the droplet interface in water-in-water emulsions. *Langmuir*, 28(14), 5921-5926.
- [40] Washburn, E. W. (1921). The dynamics of capillary flow. *Physical review*, 17(3), 273.

- [41] Zhou, J., Qiao, X., Binks, B. P., Sun, K., Bai, M., Li, Y., & Liu, Y. (2011). Magnetic Pickering emulsions stabilized by Fe₃O₄ nanoparticles. *Langmuir*, 27(7), 3308-3316.
- [42] Da, C., Chen, X., Zhu, J., Alzobaidi, S., Garg, G., & Johnston, K. P. (2022). Elastic gas/water interface for highly stable foams with modified anionic silica nanoparticles and a like-charged surfactant. *Journal of Colloid and Interface Science*, 608, 1401-1413.
- [43] Zhang, Y., Wang, S., Zhou, J., Zhao, R., Benz, G., Tcheimou, S., ... & Behrens, S. H. (2017). Interfacial activity of nonamphiphilic particles in fluid–fluid interfaces. *Langmuir*, 33(18), 4511-4519.
- [44] Alzobaidi, S., Da, C., Wu, P., Zhang, X., Rabat-Torki, N. J., Harris, J. M., ... & Johnston, K. P. (2021). Tuning Nanoparticle Surface Chemistry and Interfacial Properties for Highly Stable Nitrogen-In-Brine Foams. *Langmuir*, 37(17), 5408-5423.
- [45] Faraday, M. (1857). X. The Bakerian Lecture.—Experimental relations of gold (and other metals) to light. *Philosophical transactions of the Royal Society of London*, (147), 145-181.
- [46] Sciau, P. (2012). Nanoparticles in ancient materials: the metallic lustre decorations of medieval ceramics.
- [47] Rosen, M. J., & Kunjappu, J. T. (2012). *Surfactants and interfacial phenomena*. John Wiley & Sons.
- [48] Kundu, P., Agrawal, A., Mateen, H., & Mishra, I. M. (2013). Stability of oil-in-water macro-emulsion with anionic surfactant: Effect of electrolytes and temperature. *Chemical Engineering Science*, 102, 176-185.
- [49] Jiang, H., Sheng, Y., & Ngai, T. (2020). Pickering emulsions: Versatility of colloidal particles and recent applications. *Current opinion in colloid & interface science*, 49, 1-15.
- [50] Verma, M. K. (2000). The significance of field growth and the role of enhanced oil recovery. *US Geological Survey Fact Sheet FS-115-00*.

- [51] Zhang, T., Roberts, M., Bryant, S. L., & Huh, C. (2009, April). Foams and emulsions stabilized with nanoparticles for potential conformance control applications. In *SPE international symposium on oilfield chemistry*. OnePetro.
- [52] Pandey, A., Telmadarreie, A., Trifkovic, M., & Bryant, S. (2018, September). Cellulose nanocrystal stabilized emulsions for conformance control and fluid diversion in porous media. In *SPE annual technical conference and exhibition*. OnePetro.
- [53] Saikia, T., Khamidy, N. I., Sultan, A., & Patil, S. (2021). Rheological investigation of pickering invert emulsion system for conformance control in high temperature reservoirs. *Journal of Petroleum Science and Engineering*, 205, 108854.
- [54] Zhang, L., Abbaspourrad, A., Parsa, S., Tang, J., Cassiola, F., Zhang, M., ... & Weitz, D. A. (2020). Core-shell nanohydrogels with programmable swelling for conformance control in porous media. *ACS applied materials & interfaces*, 12(30), 34217-34225.
- [55] Soo, H., & Radke, C. J. (1984). Flow mechanism of dilute, stable emulsions in porous media. *Industrial & engineering chemistry fundamentals*, 23(3), 342-347.
- [56] Dressaire, E., & Sauret, A. (2017). Clogging of microfluidic systems. *Soft matter*, 13(1), 37-48.
- [57] Arab, D., Kantzas, A., & Bryant, S. L. (2018). Nanoparticle stabilized oil in water emulsions: A critical review. *Journal of Petroleum Science and Engineering*, 163, 217-242.
- [58] McAuliffe, C. D. (1973). Oil-in-water emulsions and their flow properties in porous media. *Journal of petroleum technology*, 25(06), 727-733
- [59] Yu, L., Ding, B., Dong, M., & Jiang, Q. (2018). Plugging ability of oil-in-water emulsions in porous media: experimental and modeling study. *Industrial & Engineering Chemistry Research*, 57(43), 14795-14808.
- [60] Griffith, C., & Daigle, H. (2018). On the shear stability of water-in-water Pickering emulsions stabilized with silica nanoparticles. *Journal of colloid and interface science*, 532, 83-91

- [61] Habermann, B. (1960). The efficiency of miscible displacement as a function of mobility ratio. *Transactions of the AIME*, 219(01), 264-272.
- [62] Kim, I., Worthen, A. J., Lotfollahi, M., Johnston, K. P., DiCarlo, D. A., & Huh, C. (2017, April). Nanoparticle-stabilized emulsions for improved mobility control for adverse-mobility waterflooding. In *IOR 2017-19th European Symposium on Improved Oil Recovery* (Vol. 2017, No. 1, pp. 1-13). European Association of Geoscientists & Engineers.
- [63] Song, Z., Li, Y., Song, Y., Bai, B., Hou, J., Song, K., ... & Su, S. (2020, October). A critical review of CO₂ enhanced oil recovery in tight oil reservoirs of North America and China. In *SPE/IATMI Asia Pacific Oil & gas conference and exhibition*. OnePetro.
- [64] Orr, F. M. (2007). *Theory of gas injection processes* (Vol. 5). Copenhagen: Tie-Line Publications.
- [65] Dicharry, R. M., Perryman, T. L., & Ronquille, J. D. (1973). Evaluation and design of a CO₂ miscible flood project-SACROC unit, Kelly-Snyder field. *Journal of Petroleum Technology*, 25(11), 1309-1318.
- [66] Sweatman, R. E., Parker, M. E., & Crookshank, S. L. (2009, November). Industry experience with CO₂-enhanced oil recovery technology. In *SPE international conference on CO₂ capture, storage, and utilization*. OnePetro.
- [67] Wright, I. W., Ringrose, P. S., Mathieson, A. S., & Eiken, O. (2009, November). An overview of active large-scale CO₂ storage projects. In *SPE International Conference on CO₂ Capture, Storage, and Utilization*. OnePetro.
- [68] Elmabrouk, S. K., Bader, H. E., & Mahmud, W. M. (2017, April). An overview of power plant CCS and CO₂-EOR projects. In *International Conference on Industrial Engineering and Operations Management*.
- [69] Kavscek, A. R., & Cakici, M. D. (2005). Geologic storage of carbon dioxide and enhanced oil recovery. II. Cooptimization of storage and recovery. *Energy conversion and Management*, 46(11-12), 1941-1956.

- [70] Bachu, S. (2008). CO₂ storage in geological media: Role, means, status and barriers to deployment. *Progress in energy and combustion science*, 34(2), 254-273.
- [71] Kelemen, P., Benson, S. M., Pilorgé, H., Psarras, P., & Wilcox, J. (2019). An overview of the status and challenges of CO₂ storage in minerals and geological formations. *Frontiers in Climate*, 1, 9.
- [72] Azar, C., Lindgren, K., & Andersson, B. A. (2003). Global energy scenarios meeting stringent CO₂ constraints—cost-effective fuel choices in the transportation sector. *Energy Policy*, 31(10), 961-976.
- [73] Godec, M. L., Kuuskraa, V. A., & Dipietro, P. (2013). Opportunities for using anthropogenic CO₂ for enhanced oil recovery and CO₂ storage. *Energy & Fuels*, 27(8), 4183-4189.
- [74] Zahasky, C., & Krevor, S. (2020). Global geologic carbon storage requirements of climate change mitigation scenarios. *Energy & Environmental Science*, 13(6), 1561-1567.
- [75] Riahi, K., R. Schaeffer, J. Arango, K. Calvin, C. Guivarch, T. Hasegawa, K. Jiang, E. Kriegler, R. Matthews, G.P. Peters, A. Rao, S. Robertson, A.M. Sebbit, J. Steinberger, M. Tavoni, D.P. van Vuuren, 2022: Mitigation pathways compatible with long-term goals. In IPCC, 2022: Climate Change 2022: Mitigation of Climate Change. Contribution of Working Group III to the Sixth Assessment Report of the Intergovernmental Panel on Climate Change [P.R. Shukla, J. Skea, R. Slade, A. Al Khourdajie, R. van Diemen, D. McCollum, M. Pathak, S. Some, P. Vyas, R. Fradera, M. Belkacemi, A. Hasija, G. Lisboa, S. Luz, J. Malley, (eds.)]. Cambridge University Press, Cambridge, UK and New York, NY, USA. doi: 10.1017/9781009157926.005
- [76] Bachu, S., Bonijoly, D., Bradshaw, J., Burruss, R., Holloway, S., Christensen, N. P., & Mathiassen, O. M. (2007). CO₂ storage capacity estimation: Methodology and gaps. *International journal of greenhouse gas control*, 1(4), 430-443.
- [77] Godec, M., Kuuskraa, V., Van Leeuwen, T., Melzer, L. S., & Wildgust, N. (2011). CO₂ storage in depleted oil fields: The worldwide potential for carbon dioxide enhanced oil recovery. *Energy Procedia*, 4, 2162-2169.

- [78] Szulczewski, M. L., MacMinn, C. W., Herzog, H. J., & Juanes, R. (2012). Lifetime of carbon capture and storage as a climate-change mitigation technology. *Proceedings of the National Academy of Sciences*, 109(14), 5185-5189.
- [79] Sabet, N., Hassanzadeh, H., & Abedi, J. (2017). Control of viscous fingering by nanoparticles. *Physical Review E*, 96(6), 063114.
- [80] Whitby, C. P., Fischer, F. E., Fornasiero, D., & Ralston, J. (2011). Shear-induced coalescence of oil-in-water Pickering emulsions. *Journal of colloid and interface science*, 361(1), 170-177.
- [81] Griffith, C., & Daigle, H. (2018). Manipulation of Pickering emulsion rheology using hydrophilically modified silica nanoparticles in brine. *Journal of colloid and interface science*, 509, 132-139.
- [82] Hoxha, B. B., van Oort, E., & Daigle, H. (2019). How do nanoparticles stabilize shale?. *SPE Drilling & Completion*, 34(02), 143-158.
- [83] Yang, H., Hou, Q., Wang, S., Guo, D., Hu, G., Xu, Y., ... & Wang, J. (2018). Magnetic-responsive switchable emulsions based on Fe₃O₄@SiO₂-NH₂ nanoparticles. *Chemical Communications*, 54(76), 10679-10682.
- [84] Binks, B. P., & Whitby, C. P. (2005). Nanoparticle silica-stabilised oil-in-water emulsions: improving emulsion stability. *Colloids and Surfaces A: Physicochemical and Engineering Aspects*, 253(1-3), 105-115.
- [85] Zhuravlev, L. T. (1993). Surface characterization of amorphous silica—a review of work from the former USSR. *Colloids and Surfaces A: Physicochemical and Engineering Aspects*, 74(1), 71-90.
- [86] Zhuravlev, L. T. (2000). The surface chemistry of amorphous silica. Zhuravlev model. *Colloids and Surfaces A: Physicochemical and Engineering Aspects*, 173(1-3), 1-38.
- [87] Chevalier, Y., & Bolzinger, M. A. (2013). Emulsions stabilized with solid nanoparticles: Pickering emulsions. *Colloids and Surfaces A: Physicochemical and Engineering Aspects*, 439, 23-34.

- [88] Estephan, Z. G., Jaber, J. A., & Schlenoff, J. B. (2010). Zwitterion-stabilized silica nanoparticles: toward nonstick nano. *Langmuir*, 26(22), 16884-16889.
- [89] Zhuravlev, L. T. (1987). Concentration of hydroxyl groups on the surface of amorphous silicas. *Langmuir*, 3(3), 316-318.
- [90] Israelachvili, J. N. (2011). *Intermolecular and surface forces*. Academic press
- [91] Vincent, B., Edwards, J., Emmett, S., & Jones, A. (1986). Depletion flocculation in dispersions of sterically-stabilised particles (“soft spheres”). *Colloids and Surfaces*, 18(2-4), 261-281.
- [92] Aveyard, R., Clint, J. H., & Horozov, T. S. (2003). Aspects of the stabilisation of emulsions by solid particles: Effects of line tension and monolayer curvature energy. *Physical Chemistry Chemical Physics*, 5(11), 2398-2409.
- [93] Levine, S., Bowen, B. D., & Partridge, S. J. (1989). Stabilization of emulsions by fine particles II. capillary and van der Waals forces between particles. *Colloids and surfaces*, 38(2), 345-364.
- [94] Aveyard, R., Clint, J. H., Nees, D., & Paunov, V. N. (2000). Compression and structure of monolayers of charged latex particles at air/water and octane/water interfaces. *Langmuir*, 16(4), 1969-1979.
- [95] Overbeek, J. T. G., Verhoeckx, G. J., De Bruyn, P. L., & Lekkerkerker, H. N. W. (1987). On understanding microemulsions: II. Thermodynamics of droplet-type microemulsions. *Journal of colloid and interface science*, 119(2), 422-441.
- [96] Robins, M. M. (2000). Emulsions—creaming phenomena. *Current opinion in colloid & interface science*, 5(5-6), 265-272.
- [97] Lee, G. J., Am Son, H., Cho, J. W., Choi, S. K., Kim, H. T., & Kim, J. W. (2014). Stabilization of Pickering emulsions by generating complex colloidal layers at liquid–liquid interfaces. *Journal of colloid and interface science*, 413, 100-105.
- [98] Frelichowska, J., Bolzinger, M. A., & Chevalier, Y. (2009). *Pickering emulsions with bare silica*. *Colloids and Surfaces A: Physicochemical and Engineering Aspects*, 343(1-3), 70-74.

- [99] Nan, F., Wu, J., Qi, F., Liu, Y., Ngai, T., & Ma, G. (2014). Uniform chitosan-coated alginate particles as emulsifiers for preparation of stable Pickering emulsions with stimulus dependence. *Colloids and Surfaces A: Physicochemical and Engineering Aspects*, 456, 246-252.
- [100] Yang, F., Liu, S., Xu, J., Lan, Q., Wei, F., & Sun, D. (2006). Pickering emulsions stabilized solely by layered double hydroxides particles: The effect of salt on emulsion formation and stability. *Journal of Colloid and Interface Science*, 302(1), 159-169.
- [101] Briggs, N. M., Weston, J. S., Li, B., Venkataramani, D., Aichele, C. P., Harwell, J. H., & Crossley, S. P. (2015). Multiwalled carbon nanotubes at the interface of Pickering emulsions. *Langmuir*, 31(48), 13077-13084.
- [102] Maaref, S., Kantzas, A., & Bryant, S. L. (2019). The effect of silanization assisted nanoparticle hydrophobicity on emulsion stability through droplet size distribution analysis. *Chemical Engineering Science*, 201, 175-190.
- [103] Yoon, K. Y., Son, H. A., Choi, S. K., Kim, J. W., Sung, W. M., & Kim, H. T. (2016). Core flooding of complex nanoscale colloidal dispersions for enhanced oil recovery by in situ formation of stable oil-in-water pickering emulsions. *Energy & Fuels*, 30(4), 2628-2635.
- [104] Katepalli, H., John, V. T., Tripathi, A., & Bose, A. (2017). Microstructure and rheology of particle stabilized emulsions: Effects of particle shape and inter-particle interactions. *Journal of colloid and interface science*, 485, 11-17.
- [105] Griffith, C., & Daigle, H. (2020). A comparison of the static and dynamic stability of Pickering emulsions. *Colloids and Surfaces A: Physicochemical and Engineering Aspects*, 586, 124256.
- [106] Frelichowska, J., Bolzinger, M. A., & Chevalier, Y. (2010). Effects of solid particle content on properties of o/w Pickering emulsions. *Journal of colloid and interface science*, 351(2), 348-356.

- [107] Saha, A., Nikova, A., Venkataraman, P., John, V. T., & Bose, A. (2013). Oil emulsification using surface-tunable carbon black particles. *ACS applied materials & interfaces*, 5(8), 3094-3100.
- [108] Kruglyakov, P. M., Nushtayeva, A. V., & Vilkoval, N. G. (2004). Experimental investigation of capillary pressure influence on breaking of emulsions stabilized by solid particles. *Journal of colloid and interface science*, 276(2), 465-474.
- [109] Maurice, L., Maguire, R. A., Schofield, A. B., Cates, M. E., Clegg, P. S., & Thijssen, J. H. (2013). Squeezing particle-stabilized emulsions into bicontinuous foams—equation of state. *Soft Matter*, 9(32), 7757-7765.
- [110] Binks, B. P., & Lumsdon, S. O. (1999). Stability of oil-in-water emulsions stabilised by silica particles. *Physical Chemistry Chemical Physics*, 1(12), 3007-3016.
- [111] Binks, B. P., Desforges, A., & Duff, D. G. (2007). Synergistic stabilization of emulsions by a mixture of surface-active nanoparticles and surfactant. *Langmuir*, 23(3), 1098-1106.
- [112] Binks, B. P., Rodrigues, J. A., & Frith, W. J. (2007). Synergistic interaction in emulsions stabilized by a mixture of silica nanoparticles and cationic surfactant. *Langmuir*, 23(7), 3626-3636.
- [113] Binks, B. P., & Rodrigues, J. A. (2007). Enhanced stabilization of emulsions due to surfactant-induced nanoparticle flocculation. *Langmuir*, 23(14), 7436-7439.
- [114] Liu, L., Pu, X., Zhou, Y., Zhou, J., Luo, D., & Ren, Z. (2020). Smart Pickering water-in-oil emulsion by manipulating interactions between nanoparticles and surfactant as potential oil-based drilling fluid. *Colloids and Surfaces A: Physicochemical and Engineering Aspects*, 586, 124246.
- [115] Song, W., & Kovescek, A. R. (2015). Functionalization of micromodels with kaolinite for investigation of low salinity oil-recovery processes. *Lab on a Chip*, 15(16), 3314-3325.
- [116] Varanasi, S., Henzel, L., Mendoza, L., Prathapan, R., Batchelor, W., Tabor, R., & Garnier, G. (2018). Pickering emulsions electrostatically stabilized by cellulose nanocrystals. *Frontiers in chemistry*, 6, 409.

- [117] Song, W., & Kavscek, A. R. (2019). Spontaneous clay Pickering emulsification. *Colloids and Surfaces A: Physicochemical and Engineering Aspects*, 577, 158-166.
- [118] Zhu, Y., McClements, D. J., Zhou, W., Peng, S., Zhou, L., Zou, L., & Liu, W. (2020). Influence of ionic strength and thermal pretreatment on the freeze-thaw stability of Pickering emulsion gels. *Food chemistry*, 303, 125401.
- [119] Horozov, T. S., Binks, B. P., & Gottschalk-Gaudig, T. (2007). Effect of electrolyte in silicone oil-in-water emulsions stabilised by fumed silica particles. *Physical Chemistry Chemical Physics*, 9(48), 6398-6404.
- [120] Lifshitz, I. M., & Slyozov, V. V. (1961). The kinetics of precipitation from supersaturated solid solutions. *Journal of physics and chemistry of solids*, 19(1-2), 35-50.
- [121] Wagner, C. (1961). Theorie der alterung von niederschlägen durch umlösen (Ostwald-reifung). *Zeitschrift für Elektrochemie, Berichte der Bunsengesellschaft für physikalische Chemie*, 65(7-8), 581-591.
- [122] Adkins, S. S., Chen, X., Chan, I., Torino, E., Nguyen, Q. P., Sanders, A. W., & Johnston, K. P. (2010). Morphology and stability of CO₂-in-water foams with nonionic hydrocarbon surfactants. *Langmuir*, 26(8), 5335-5348.
- [123] Stocco, A., Drenckhan, W., Rio, E., Langevin, D., & Binks, B. P. (2009). Particle-stabilised foams: an interfacial study. *Soft Matter*, 5(11), 2215-2222.
- [124] Enick, R. M., & Klara, S. M. (1990). CO₂ solubility in water and brine under reservoir conditions. *Chemical Engineering Communications*, 90(1), 23-33.
- [125] Chapoy, A., Mohammadi, A. H., Tohidi, B., & Richon, D. (2004). Gas solubility measurement and modeling for the nitrogen+ water system from 274.18 K to 363.02 K. *Journal of Chemical & Engineering Data*, 49(4), 1110-1115.
- [126] Li, W., Wei, F., Xiong, C., Ouyang, J., Shao, L., Dai, M., ... & Du, D. (2019). A novel supercritical CO₂ foam system stabilized with a mixture of zwitterionic surfactant and silica nanoparticles for enhanced oil recovery. *Frontiers in chemistry*, 7, 718.

- [127]Kang, W., Jiang, H., Yang, H., Li, Z., Zhou, B., He, Y., ... & Gabdullin, M. (2021). Study of nano-SiO₂ reinforced CO₂ foam for anti-gas channeling with a high temperature and high salinity reservoir. *Journal of Industrial and Engineering Chemistry*, 97, 506-514.
- [128]Wang, Y., Zhang, Y., Liu, Y., Zhang, L., Ren, S., Lu, J., ... & Fan, N. (2017). The stability study of CO₂ foams at high pressure and high temperature. *Journal of Petroleum Science and Engineering*, 154, 234-243.
- [129]Eide, Ø., Føyen, T., Skjelsvik, E., Rognmo, A., & Fernø, M. (2018, November). Nanoparticle stabilized foam in harsh conditions for CO₂ EOR. In *Abu Dhabi International Petroleum Exhibition & Conference*. OnePetro.
- [130]Zhang, X., Zhang, G., Ge, J., & Wang, Y. (2020, December). CO₂ Foam Stabilized with Switchable Surfactants and Modified Nanoparticles Effected by PH and Salinity. In *SPE Europec*. OnePetro.
- [131]Zhang, X., Zhang, T., Jiang, P., Ge, J., & Zhang, G. (2020). Enhancement of CO₂ Foam Stability with Modified Silica Nanoparticles in High Salinity Brine. *CHEMICAL JOURNAL OF CHINESE UNIVERSITIES-CHINESE*, 41(5), 1076-1082.
- [132]Zhang, X., Wang, Y., Da, C., Ge, J., Zhang, G., Jiang, P., & Pei, H. (2020, August). The CO₂ Foam Stability Enhancement with Switchable Surfactant and Modified Silica Nanoparticles. In *SPE Improved Oil Recovery Conference*. OnePetro.
- [133]Yang, Y., Fang, Z., Chen, X., Zhang, W., Xie, Y., Chen, Y., ... & Yuan, W. (2017). An overview of Pickering emulsions: solid-particle materials, classification, morphology, and applications. *Frontiers in pharmacology*, 8, 287.
- [134]Levine, S., Bowen, B. D., & Partridge, S. J. (1989). Stabilization of emulsions by fine particles I. Partitioning of particles between continuous phase and oil/water interface. *Colloids and surfaces*, 38(2), 325-343.
- [135]Binks, B. P., & Clint, J. H. (2002). Solid wettability from surface energy components: relevance to Pickering emulsions. *Langmuir*, 18(4), 1270-1273.

- [136] Raghavan, S. R., Hou, J., Baker, G. L., & Khan, S. A. (2000). Colloidal interactions between particles with tethered nonpolar chains dispersed in polar media: direct correlation between dynamic rheology and interaction parameters. *Langmuir*, 16(3), 1066-1077.
- [137] French, D. J., Taylor, P., Fowler, J., & Clegg, P. S. (2015). Making and breaking bridges in a Pickering emulsion. *Journal of colloid and interface science*, 441, 30-38.
- [138] American Petroleum Institute (1960). Recommended practice standard procedure for the evaluation of hydraulic fracturing fluids. *API RP*, 39(1st Edition).
- [139] Luzinov, I., Julthongpiput, D., Liebmann-Vinson, A., Cregger, T., Foster, M. D., & Tsukruk, V. V. (2000). Epoxy-terminated self-assembled monolayers: molecular glues for polymer layers. *Langmuir*, 16(2), 504-516.
- [140] Chen, H., & Panagiotopoulos, A. Z. (2018). Communication: Modeling electrolyte mixtures with concentration dependent dielectric permittivity. *The Journal of chemical physics*, 148(4), 041102.
- [141] Maaref, S., & Ayatollahi, S. (2018). The effect of brine salinity on water-in-oil emulsion stability through droplet size distribution analysis: a case study. *Journal of Dispersion Science and Technology*, 39(5), 721-733.
- [142] Low, L. E., Siva, S. P., Ho, Y. K., Chan, E. S., & Tey, B. T. (2020). Recent advances of characterization techniques for the formation, physical properties and stability of Pickering emulsion. *Advances in colloid and interface science*, 277, 102-117.
- [143] Liu, L., Pu, X., Zhou, Y., Zhou, J., Luo, D., & Ren, Z. (2020). Smart Pickering water-in-oil emulsion by manipulating interactions between nanoparticles and surfactant as potential oil-based drilling fluid. *Colloids and Surfaces A: Physicochemical and Engineering Aspects*, 586, 124246.
- [144] Hatchell, D., Song, W., & Daigle, H. (2022). Examining the role of salinity on the dynamic stability of Pickering emulsions. *Journal of Colloid and Interface Science*, 608, 2321-2329.

- [145] Takae, S., Akiyama, Y., Otsuka, H., Nakamura, T., Nagasaki, Y., & Kataoka, K. (2005). Ligand density effect on biorecognition by PEGylated gold nanoparticles: regulated interaction of RCA120 lectin with lactose installed to the distal end of tethered PEG strands on gold surface. *Biomacromolecules*, 6(2), 818-824.
- [146] Elias, D. R., Poloukhine, A., Popik, V., & Tsourkas, A. (2013). Effect of ligand density, receptor density, and nanoparticle size on cell targeting. *Nanomedicine: nanotechnology, biology and medicine*, 9(2), 194-201.
- [147] Tran, E., & Richmond, G. L. (2021). Interfacial Steric and Molecular Bonding Effects Contributing to the Stability of Neutrally Charged Nanoemulsions. *Langmuir*, 37(43), 12643-12653.
- [148] Binks, B. P., & Lumsdon, S. O. (2001). Pickering emulsions stabilized by monodisperse latex particles: effects of particle size. *Langmuir*, 17(15), 4540-4547.
- [149] Hatchell, D., Song, W., & Daigle, H. (2021, September). Effect of Inter-Particle Van Der Waals Attraction on the Stability of Pickering Emulsions in Brine. In *SPE Annual Technical Conference and Exhibition*. OnePetro.
- [150] Hirasaki, G. J. (1991). Wettability: fundamentals and surface forces. *SPE formation evaluation*, 6(02), 217-226.
- [151] Dong, J., Chen, S., Corti, D. S., Franses, E. I., Zhao, Y., Ng, H. T., & Hanson, E. (2011). Effect of Triton X-100 on the stability of aqueous dispersions of copper phthalocyanine pigment nanoparticles. *Journal of colloid and interface science*, 362(1), 33-41.
- [152] Wiley, R. M. (1954). Limited coalescence of oil droplets in coarse oil-in-water emulsions. *Journal of Colloid Science*, 9(5), 427-437.
- [153] Golemanov, K., Tcholakova, S., Kralchevsky, P. A., Ananthapadmanabhan, K. P., & Lips, A. (2006). Latex-particle-stabilized emulsions of anti-Bancroft type. *Langmuir*, 22(11), 4968-4977.
- [154] Arditty, S., Whitby, C. P., Binks, B. P., Schmitt, V., & Leal-Calderon, F. (2003). Some general features of limited coalescence in solid-stabilized emulsions. *The European Physical Journal E*, 11(3), 273-281.

- [155] Van der Meer, L. G. H. (1995). The CO₂ storage efficiency of aquifers. *Energy conversion and management*, 36(6-9), 513-518.
- [156] Bachu, S. (2015). Review of CO₂ storage efficiency in deep saline aquifers. *International Journal of Greenhouse Gas Control*, 40, 188-202.
- [157] Blaker, T., Aarra, M. G., Skauge, A., Rasmussen, L., Celius, H. K., Martinsen, H. A., & Vassenden, F. (2002). Foam for gas mobility control in the Snorre field: the FAWAG project. *SPE Reservoir Evaluation & Engineering*, 5(04), 317-323.
- [158] Farzaneh, S. A., & Sohrabi, M. (2013, June). A review of the status of foam applications in enhanced oil recovery. In *EAGE Annual Conference & Exhibition incorporating SPE Europec. OnePetro*.
- [159] Lee, S., & Kam, S. I. (2013). Enhanced oil recovery by using CO₂ foams: fundamentals and field applications. In *Enhanced Oil Recovery Field Case Studies* (pp. 23-61). Gulf Professional Publishing.
- [160] Massarweh, O., & Abushaikha, A. S. (2021). A review of recent developments in CO₂ mobility control in enhanced oil recovery. *Petroleum*.
- [161] Rossen, W. R. (1996). *Foams in enhanced oil recovery*. Foams. Routledge.
- [162] Chen, Y. F., Yang, C. H., Chang, M. S., Ciou, Y. P., & Huang, Y. C. (2010). Foam properties and detergent abilities of the saponins from *Camellia oleifera*. *International Journal of Molecular Sciences*, 11(11), 4417-4425.
- [163] Moe, M. K., Huber, S., Svenson, J., Hagenaars, A., Pabon, M., Trümper, M., ... & Herzke, D. (2012). The structure of the fire fighting foam surfactant Forafac® 1157 and its biological and photolytic transformation products. *Chemosphere*, 89(7), 869-875.
- [164] Sangamithra, A., Sivakumar, V., John, S. G., & Kannan, K. (2015). Foam mat drying of food materials: A review. *Journal of Food Processing and preservation*, 39(6), 3165-3174.
- [165] Ma, L., & Liu, T. (2022). Effecting factor analysis to stability of ultra-dry CO₂-in-water foams stabilized with zwitterionic surfactants, polymers and nanoparticles. *The Journal of Supercritical Fluids*, 181, 105487.

- [166]Elhag, A. S., Da, C., Chen, Y., Mukherjee, N., Noguera, J. A., Alzobaidi, S., ... & Johnston, K. P. (2018). Viscoelastic diamine surfactant for stable carbon dioxide/water foams over a wide range in salinity and temperature. *Journal of colloid and interface science*, 522, 151-162.
- [167]Wang, J., Luo, X., Rogers, S., Li, P., & Feng, Y. (2022). Stabilization of CO₂ aqueous foams at high temperature and high pressure: Small-angle neutron scattering and rheological studies. *Colloids and Surfaces A: Physicochemical and Engineering Aspects*, 647, 129015.
- [168]Zhang, X., Zheng, W., Zhang, T., Ge, J., Jiang, P., & Zhang, G. (2019). CO₂ in water foam stabilized with CO₂-dissolved surfactant at high pressure and high temperature. *Journal of Petroleum Science and Engineering*, 178, 930-936.
- [169]Zhang, P., Diao, Y., Shan, Y., Pei, S., Ren, S., Zhang, L., & Yang, H. (2020). Experimental investigation of amine-surfactant CO₂ foam for smart mobility control during CO₂ flooding. *Journal of Petroleum Science and Engineering*, 184, 106511.
- [170]Ma, L., Zhu, M., & Liu, T. (2022). Effects of chain length of surfactants and their adsorption on nanoparticles on stability of CO₂-in-water emulsions. *Colloids and Surfaces A: Physicochemical and Engineering Aspects*, 644, 128877.
- [171]Worthen, A. J., Bagaria, H. G., Chen, Y., Bryant, S. L., Huh, C., & Johnston, K. P. (2013). Nanoparticle-stabilized carbon dioxide-in-water foams with fine texture. *Journal of colloid and interface science*, 391, 142-151.
- [172]Alzobaidi, S., Lotfollahi, M., Kim, I., Johnston, K. P., & DiCarlo, D. A. (2017). Carbon dioxide-in-brine foams at high temperatures and extreme salinities stabilized with silica nanoparticles. *Energy & Fuels*, 31(10), 10680-10690.
- [173]Ueno, K., Inaba, A., Kondoh, M., & Watanabe, M. (2008). Colloidal stability of bare and polymer-grafted silica nanoparticles in ionic liquids. *Langmuir*, 24(10), 5253-5259.
- [174]Hiemenz, P. C., & Rajagopalan, R. (2016). *Principles of Colloid and Surface Chemistry*, revised and expanded. CRC press.

- [175] Da, C., Zhang, X., Alzobaidi, S., Hu, D., Wu, P., & Johnston, K. P. (2021). Tuning surface chemistry and ionic strength to control nanoparticle adsorption and elastic dilational modulus at air-brine interface. *Langmuir*, 37(19), 5795-5809.
- [176] Kumar, S., & Mandal, A. (2017). Investigation on stabilization of CO₂ foam by ionic and nonionic surfactants in presence of different additives for application in enhanced oil recovery. *Applied Surface Science*, 420, 9-20.
- [177] Kim, I., Worthen, A. J., Johnston, K. P., DiCarlo, D. A., & Huh, C. (2016). Size-dependent properties of silica nanoparticles for Pickering stabilization of emulsions and foams. *Journal of Nanoparticle Research*, 18(4), 1-12.
- [178] Hu, N., Li, Y., Wu, Z., Lu, K., Huang, D., & Liu, W. (2018). Foams stabilization by silica nanoparticle with cationic and anionic surfactants in column flotation: Effects of particle size. *Journal of the Taiwan Institute of Chemical Engineers*, 88, 62-69.
- [179] Bashir, A., Haddad, A. S., & Rafati, R. (2019). Nanoparticle/polymer-enhanced alpha olefin sulfonate solution for foam generation in the presence of oil phase at high temperature conditions. *Colloids and Surfaces A: Physicochemical and Engineering Aspects*, 582, 123875.
- [180] Chen, X., Da, C., Hatchell, D., Daigle, H., & Johnston, K. (2022). Ultra-stable CO₂/water foam with ultralow concentration of amine-coated-nanoparticles and cationic surfactant. *Journal of Colloid and Interface Science*, *in preparation*.
- [181] Liggieri, L., Santini, E., Guzmán, E., Maestro, A., & Ravera, F. (2011). Wide-frequency dilational rheology investigation of mixed silica nanoparticle–CTAB interfacial layers. *Soft Matter*, 7(17), 7699-7709.
- [182] Yazhgur, P. A., Noskov, B. A., Liggieri, L., Lin, S. Y., Loglio, G., Miller, R., & Ravera, F. (2013). Dynamic properties of mixed nanoparticle/surfactant adsorption layers. *Soft Matter*, 9(12), 3305-3314.
- [183] Zhang, X., Zhang, T., Ge, J., Wang, Y., Ding, L., & Zhang, G. (2021). The CO₂-in-water foam stabilized with the mixture of CO₂-soluble surfactant and nonionic surfactant. *Journal of Petroleum Science and Engineering*, 198, 108117.

- [184] Singh, R., & Mohanty, K. K. (2015). Synergy between nanoparticles and surfactants in stabilizing foams for oil recovery. *Energy & Fuels*, 29(2), 467-479.
- [185] Zhu, J., Da, C., Chen, J., & Johnston, K. P. (2022). Ultrastable N₂/Water Foams Stabilized by Dilute Nanoparticles and a Surfactant at High Salinity and High Pressure. *Langmuir*, 38(18), 5392-5403.
- [186] Wu, D., & Honciuc, A. (2017). Design of Janus nanoparticles with pH-triggered switchable amphiphilicity for interfacial applications. *ACS Applied Nano Materials*, 1(1), 471-482.
- [187] Hatchell, D., Song, W., & Daigle, H. (2022). Effect of interparticle forces on the stability and droplet diameter of Pickering emulsions stabilized by PEG-coated silica nanoparticles. *Journal of Colloid and Interface Science*.
- [188] Chen, Y., Elhag, A. S., Reddy, P. P., Chen, H., Cui, L., Worthen, A. J., ... & Johnston, K. P. (2016). Phase behavior and interfacial properties of a switchable ethoxylated amine surfactant at high temperature and effects on CO₂-in-water foams. *Journal of colloid and interface science*, 470, 80-91.
- [189] Dickson, J. L., Gupta, G., Horozov, T. S., Binks, B. P., & Johnston, K. P. (2006). Wetting phenomena at the CO₂/water/glass interface. *Langmuir*, 22(5), 2161-2170.
- [190] Li, Y., Pham, J. Q., Johnston, K. P., & Green, P. F. (2007). Contact angle of water on polystyrene thin films: Effects of CO₂ environment and film thickness. *Langmuir*, 23(19), 9785-9793.
- [191] Da, C., Jian, G., Alzobaidi, S., Yang, J., Biswal, S. L., Hirasaki, G. J., & Johnston, K. P. (2018). Design of CO₂-in-water foam stabilized with switchable amine surfactants at high temperature in high-salinity brine and effect of oil. *Energy & fuels*, 32(12), 12259-12267.
- [192] Schindelin, J., Arganda-Carreras, I., Frise, E., Kaynig, V., Longair, M., Pietzsch, T., ... & Cardona, A. (2012). Fiji: an open-source platform for biological-image analysis. *Nature methods*, 9(7), 676-682.

- [193]Li, Y., Zhang, L., & Li, C. (2020). Highly transparent and scratch resistant polysiloxane coatings containing silica nanoparticles. *Journal of colloid and interface science*, 559, 273-281.
- [194]Alzobaidi, S., Wu, P., Da, C., Zhang, X., Hackbarth, J., Angeles, T., ... & Johnston, K. P. (2021). Effect of surface chemistry of silica nanoparticles on contact angle of oil on calcite surfaces in concentrated brine with divalent ions. *Journal of Colloid and Interface Science*, 581, 656-668.
- [195]Jung, J. W., & Wan, J. (2012). Supercritical CO₂ and ionic strength effects on wettability of silica surfaces: Equilibrium contact angle measurements. *Energy & Fuels*, 26(9), 6053-6059.
- [196]Kilic, S., Wang, Y., Johnson, J. K., Beckman, E. J., & Enick, R. M. (2009). Influence of tert-amine groups on the solubility of polymers in CO₂. *Polymer*, 50(11), 2436-2444.
- [197]Hirasaki, G. J., & Lawson, J. B. (1985). Mechanisms of foam flow in porous media: apparent viscosity in smooth capillaries. *Society of Petroleum Engineers Journal*, 25(02), 176-190
- [198]Griffith, C. A. (2019). Colloidal particles at fluid interfaces: from stabilizing emulsions to destabilizing them (Doctoral dissertation).